Gaseous Detonation-Driven Fracture of Tubes

Thesis by

Tong Wa Chao

In Partial Fulfillment of the Requirements

for the Degree of

Doctor of Philosophy

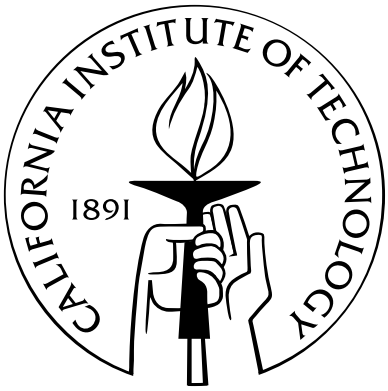

California Institute of Technology

Pasadena, California

2004

(Submitted March 2004)

Abstract

An experimental investigation of fracture response of aluminum 6061-T6 tubes under internal gaseous detonation loading has been carried out. The pressure load, with speeds exceeding 2 km/s, can be characterized as a pressure peak (ranging from 2 to 6 MPa) followed by an expansion wave. The unique combination of this particular traveling load and tube geometry produced fracture data not available before in the open literature. Experimental data of this type are useful for studying the fluid-structure-fracture interaction and various crack curving and branching phenomena, and also for validation for multi-physics and multi-scale modeling.

Axial surface flaws were introduced to control the crack initiation site. Fracture threshold models were developed by combining a static fracture model and an extensively studied dynamic amplification factor for tubes under internal traveling loads. Experiments were also performed on hydrostatically loaded preflawed aluminum 6061-T6 tubes for comparison. Significantly different fracture behavior was observed and the difference was explained by fluid dynamics and energy considerations. The experiments yielded comparison on crack speeds, strain, and pressure histories.

In other experiments, the specimens were also pre-torqued to control the propagation direction of the cracks. Measurements were made on the detonation velocity, strain history, blast pressure from the crack opening, and crack speeds. The curved crack paths were digitized. The Chapman-Jouguet pressure, initial axial flaw length, and torsion level were varied to obtain different crack patterns. The incipient crack kinking angle was found to be consistent with fracture under mixed-mode loading. High-speed movies of the fracture events and blast wave were taken and these were used in interpreting the quantitative data.

Numerical simulations were performed using the commerical explicit finite-element software LS-Dyna. The detonation wave was modeled as a traveling boundary load. Both non-fracturing linear elastic simulations and elastoplastic simulations with fracture were conducted on three-dimensional models. The simulated fracture was compared directly with an experiment with the same conditions. The overall qualitative fracture behavior was captured by the simulation. The forward and backward cracks were observed to branch in both the experiment and simulation.

Acknowledgements

My parents had always worried about my working with explosives, but working in Professor Joseph Shepherd's Explosion Dynamics Labs has been too much fun. I thank him for this memorable opportunity. I also thank him for teaching me how to safely run experiments that are dangerous by nature, and for inspiring me to achieve engineering feats that I had not thought possible for myself. His trademark loud and upbeat personality kept up my spirits on several occasions when my experiments did not work well. Always full of constructive ideas and possessing an uncanny ability to correctly foresee what works and what does not, he is truly a good advisor. If I had to do a PhD again, I would be happy to choose his lab.

I must thank two mentors who have been helping me since the beginning of my graduate career and have never asked for anything back. First is Professor Wolfgang Knauss, who guided me in the solid and fracture mechanics aspects of my experiments. He is like a sorcerer holding an incandescent torch for me in a long and dark tunnel. He can almost always accurately predict fracture behavior with complicated loading just by briefly thinking about it. I have always wondered how he does that, but I hope I can be like him one day. Talking to the gentle professor about solid and fracture mechanics has been pure joy.

Second is Professor Guruswami Ravichandran, who has been of invaluable help to my graduate career. He was the one who introduced me to Professor Shepherd and also to my future employer. Without Professor Ravichandran's help, my career path would have been much different. He once said, 'my door is always open to Tony,' and every time I went to him I would benefit greatly from his encyclopaedic knowledge of solid and fracture mechanics, which is matched only by his overwhelming modesty.

I would also like to thank Professor James Beck and Professor Kaushik Bhattacharya for generously serving on my thesis committee, taking time to read my thesis, and constructing an interesting discussion during my defense.

My thanks also go to Professor Ares Rosakis and David Anderson for lending me the circuit for conditioning crack detection gage signals.

Florian Pintgen and Patrick Hung have been of immense technical help on experimental and numerical aspects, respectively, of my graduate work. Without these two, I would have taken much longer time to accomplish what I have done. I would also like to thank Daniel Lieberman for his help with the experiments in Chapter 3 and for teaching me how to use the high-speed Phantom digital camera. I would also like to thank other past and present group members Marco Arienti, Joanna Austin, Marcia Cooper, Scott Jackson, Eric Schultz, and Eric Wintenberger for their help. Suzy, who has been so efficient in handling my paperwork, conference travel plans, purchase orders, and proofreading[1], nearly spoiled me with her amazing secretarial skills.

I would like to thank Joe Haggerty, Larry Frazier, Ali Kiani, and Brad St. John for machining and technical assistance throughout my graduate stay.

My gratitude goes to many fellow students at GALCIT for their valuable friendship. I would like to thank especially Wei-Jen Su, Kumar Bobba, Jimmy Fung, and Matt Fago.

Life without music for me is meaningless. I must thank my Caltech music teachers Delores Bing and Allen Gross for teaching me chamber music. I am grateful to the Caltech chamber music students I most frequently worked with: Ryan Merle (piano), Nick Guise (clarinet), Possu Huang (violin), Lance Christensen (cello), Brian Aydemir (violin), Andrew Hsieh (viola), and Victor Kam (piano). Performing music with them has been a truly wonderful experience.

All the people who are closest to me have been far away through my graduate years. I thank my parents, my sister, and my grandmother across the Pacific for their

[1]The verb 'Suzify' has been affectionately coined by our group to indicate excellent writing quality control by Suzy.

loving support, without which I would lose the heart to carry on. I am also grateful to Louisa[2], for her love and understanding while we are physically separated during our college and graduate years, which although seemed painfully like an ocean of time, are indelibly marked by sweet and intense moments of reunions. We have never been closer since we first met when we were ten, through music.

This research was sponsored in part through the Office of Naval Research (ONR) contract N00014-99-1-0744 and by the U. S. DOE through the Caltech ASCI project.

[2]who explained the reason why I have loved her and only her in my whole life was that 'there is no other girl in the world who would want to be with you.'

Contents

List of Figures

List of Tables

Nomenclature

E	Young's modulus	N/m^2
G	shear modulus	N/m^2
G_c	fracture propagation toughness	J/m^2
I	moment of inertia	m^4
K_I	mode-I stress intensity factor	$MPa\sqrt{m}$
K_{Ic}	mode-I critical stress intensity	$MPa\sqrt{m}$
K_{II}	mode-II stress intensity factor	$MPa\sqrt{m}$
K_s	isentropic compressibility	m^2/N
L	initial notch length	m
M	bending moment	N-m
P	pressure	N/m^2
P_{cj}	Chapman-Jouguet pressure	N/m^2
P_{init}	Initial pressure	N/m^2
R	gas constant	J/(kg K)
R_1	inner radius	m
R_2	outer radius	m
T	T-stress	N/m^2
U_{cj}	Chapman-Jouguet velocity	m/s
V	volume	m^3
V_s	transverse shear	N/m
$2a$	initial notch length	m
c	sound speed	m/s
c_s	shear wave speed	m/s
c_d	plane strain dilatational wave speed	m/s
c_p	specific heat at constant pressure	J/(kg K)
c_v	specific heat at constant volume	J/(kg K)
d	initial notch depth	m
h	shell thickness	m

s	specific entropy	J/(kg K)
t	time	s
u	elastic energy per unit mass	J/kg
v	specific volume	m^3/kg
v_{c0}	first critical speed	m/s
v_{c1}	second critical speed	m/s
v_{c2}	third critical speed	m/s
v_{c3}	fourth critical speed	m/s
v_d	plane stress dilatational wave speed	m/s
w	traveling load speed	m/s
ΔE	energy per unit mass	J/kg
ΔU	elastic energy	J
Φ	dynamic amplification factor	
Φ_s	dynamic shear amplification factor	
α	inclination of neutral plane	degrees
γ	ratio of specific heats	
ϵ	strain	
θ	angle of rotation	degrees
κ	shear correction factor	
ν	Poisson's ratio	
ρ	density	kg/m^3
τ	shear stress	N/m^2
τ_i	fracture initiation time	s

Chapter 1

Introduction

1.1 Overview

The problem of tube fracture due to internal pressure loading (static or dynamic) has continued to attract attention because of its engineering importance and the intellectual challenge and reward it offers. The challenge lies in that this is a strongly coupled fluid-structure-fracture problem. The internal pressure induces the structural deformation, which provides the driving force for crack extension. The opening crack(s) and large structural deformation in turn govern the gasdynamics. The problem has wide civilian and military applications such as oil, gas, and water transmission and distribution pipeline systems, pressurized aircraft fuselages, rocket casings, space station modules, and gun tubes.

This study is about gaseous detonation-driven fracture of tubes. The specific problem studied here, differing from traditional detonation-driven tube fragmentation, involves a tube that has been deliberately preflawed axially on the surface. The preflaw is made to control the crack initiation site. If there was no preflaw, cracks could start anywhere on the tube and the resultant stochastic rupture would be intractable to deterministic fracture mechanics analysis. A gaseous detonation wave is sent through this preflawed tube, and the crack is initiated due to the oscillating hoop stress set up by the traveling detonation wave. The crack grows into the inner wall, creating a through-wall crack. The breach allows gaseous reactants to escape, sending a shock wave into the ambient air and expansion waves into the tube which

relieves the dynamic stresses. Two crack fronts run upstream and downstream in straight paths for some distance. Depending on the crack driving force, these cracks may or may not branch. The cracks then turn along helical paths and are arrested.

There has been no existing study in the literature on such a problem. Substantial efforts have been made on studying initially quasi-statically pressurized tube fracture with preflaws or fragmentation of tubes due to explosions or detonations without preflaws. Combining preflaws and traveling loads to make the detonation-driven tube fracture problem tractable to fracture mechanics analysis is an innovation in this study.

1.2 Motivation

There are strong motivations for this study both in science and applications. Scientifically, studying detonation-driven tube fracture leads to insights into poorly understood phenomena such as crack branching and crack curving, both fundamental problems in fracture mechanics. The experimental data obtained from the complex fluid-structure-fracture also serve as a touchstone for validation of multi-physics and multi-scale numerical simulations. Applications ranging from novel applications such as the design of pulse detonation engines (PDEs) to classical engineering applications such as pipeline explosion hazard analysis and blast response of aircraft fuselages will also benefit from this research.

1.2.1 Pulse Detonation Engines

Pulse detonation engines are novel unsteady aerospace propulsion devices that generate quasi-steady thrust by high-frequency cycling of gaseous detonations. PDEs operate only on test-stands at the time of this writing. No PDE has yet flown, and it is not clear what type of material is suitable for PDEs. However, like any other light-weight, load-bearing aerospace component, pre-existing and/or propagating flaws could exist as (1) cracks due to external damage, (2) voids as a result of the manufacturing process, (3) interfacial cracks between layers of composites (if a PDE

is made of layered composites), or (4) fatigue, oxidation, and corrosion as a result of the punishing operating environment. The existence of flaws necessitates a fracture mechanics approached design and safety analysis.

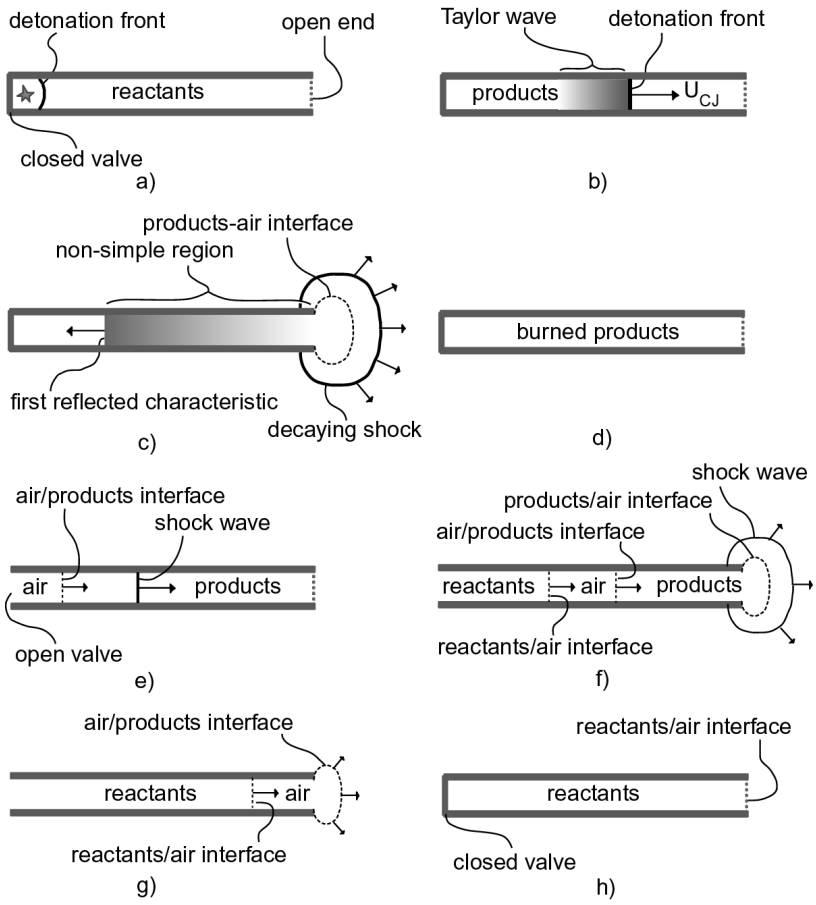

Figure 1.1: An air-breathing PDE cycle (Wintenberger and Shepherd, 2003).

A typical PDE cycle is shown in Fig. 1.1. The traveling impulsive loading and the high temperature excursions impose a significant challenge to the structure in the form of high-cycle thermomechanical impulsive fatigue. PDE fatigue fracture accidents occurred at a test site on the Wright-Patterson Air Force Base (Schauer, 2003), and some fatigue experiments have been performed to study fatigue crack propagation in PDE tubes (Chao et al., 2003). In PDEs, multi-cycle stress-fields are complicated and it is important to first understand the problem in simpler single-cycle fracture experiments.

1.2.2 Pipeline Explosions

Examples of explosive pipeline fracture can be found in recent nuclear power plant accidents. Two such accidents occurred in Hamaoka, Japan (see Fig. 1.2) and Brunsbrettel, Germany in 2001. In both accidents, sections of the carbon steel steam pipes were fragmented due to combustion events in hydrogen-oxygen mixtures created by radiolysis. Fortunately, there were no injuries or loss of life. One of the most important questions that arose during the accident investigation was whether one can deduce the type of accidental combustion (deflagation, detonation, or deflagation-to-detonation transition) from the fracture patterns. No one seemed to have sufficient knowledge to give a conclusive quantitative answer, although the pressure profiles of different combustion events are distinctly different and should cause different fracture patterns.

Figure 1.2: Two ends of a ruptured section of a steam pipe from the Hamaoka Nuclear Power Plant accident (2001).

These accidents highlighted the need to study fracture events due to traveling loads in pipes. The understanding, in addition to leading to safer piping system design in nuclear power plants, can also assist accident investigators in learning what type of combustion was responsible.

1.2.3 Blast Loading in Aircraft

Blast loading in commerical aircraft has been highlighted by recent terrorist events with enormous loss of life (e.g., Lockerbie 1989). While detection procedures can

ensure that the quantities of explosive smuggled on board will not be very large, small amounts of explosive can still have devastating effects (Kanninen and O'Donoghue, 1995). The chances of aircraft survivability can be increased if designated panels can be strategically fractured in response to the traveling load brought on by the explosive products and ensure safe decompression.

1.2.4 Dynamic Crack Curving and Branching in Tubes

Dynamic crack curving and crack branching in tubes are perhaps two of the most extensively reported yet least understood problems in fracture mechanics. The reason is perhaps that there is not much practical use of crack curving and branching in tubes, except as a means of crack arrest in long pipes or for predicting crack paths in multiple site damage (MSD) scenarios in aircraft fuselages.

In axial crack propagation of pressurized tubes, mode I loading clearly dominates, but cracks seldom run straight. Crack curving and branching have been widely observed in metal and polymeric pipes, but the cause behind the crack path instability in pipes is not well understood. A worthy challenge for the fracture community is to develop a complete and rigorous model that could predict the crack paths (Kanninen and O'Donoghue, 1995).

1.2.5 Validation for Multi-Physics and Multi-Scale Numerical Simulations

Detonation-driven tube fracture is one of the few problems that truly involves strong coupling of combustion, fluid mechanics, structural mechanics, and fracture mechanics. As a validation experiment, it provides a rich variety of data that challenge simulation experts. This type of data is well suited to validating the virtual test facility (VTF) that has been developed at Caltech to explore software development issues in simulating response of solids to detonation loading under the sponsorship of the U. S. Department of Energy through the Accelerated Strategic Computing Initiative (Aivazis et al., 2001).

1.3 Background Concepts

To understand the detonation-driven tube fracture problem, one must understand some basic concepts involving gaseous detonations, dynamic strain amplification due to traveling pressure loads, some preliminary fracture mechanics, and the effect of flap bulging on the stress intensity factor. A brief discussion on the concepts and vocabulary necessary for understanding this study will be provided.

1.3.1 Gaseous Detonations

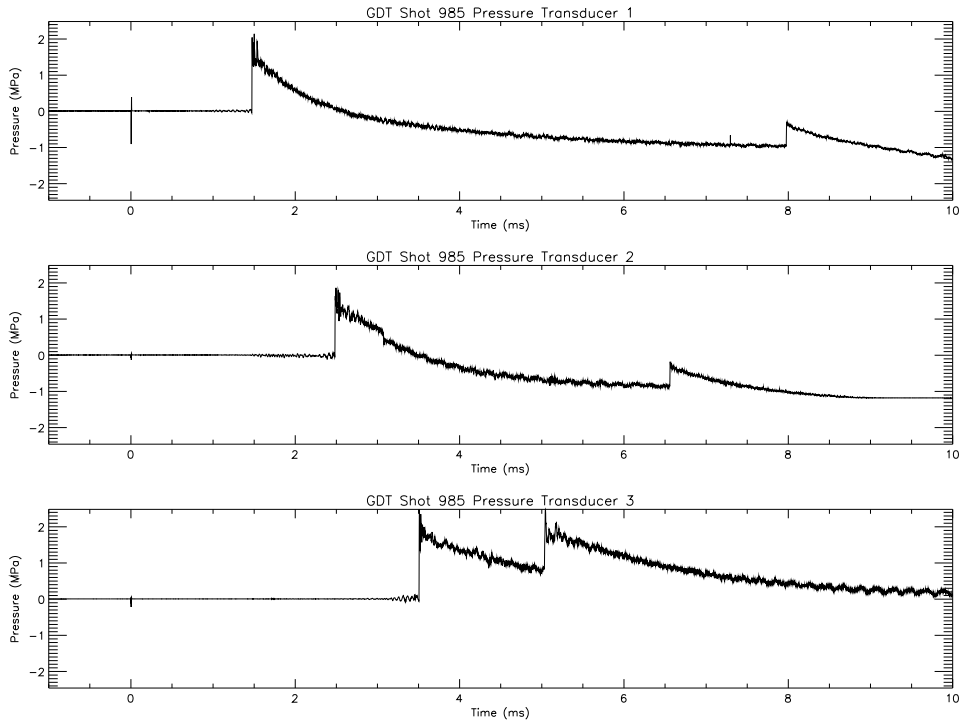

Figure 1.3: A typical detonation pressure trace measured in the 280-mm inner diameter closed-end GALCIT Detonation Tube. The pressure transducers were mounted at different locations along the length of the tube. The first pressure rise of each trace was the detonation wave front, while the second rise was the shock wave reflected from the closed end.

A gaseous detonation is a supersonic combustion wave consisting of a leading shock and a reaction zone. The shock and the reaction are tightly coupled. The

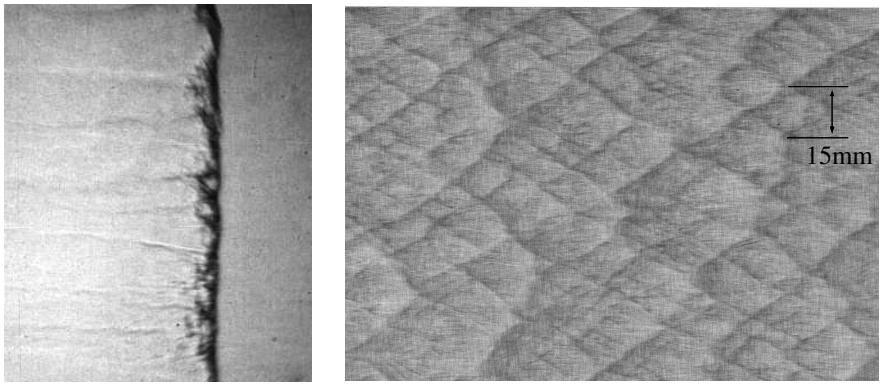

(a) (b)

Figure 1.4: (a) Shadowgraph of detonation front propagating from left to right through a C_2H_4-$3O_2$-$6N_2$ mixture with initial pressure P_1=20 kPa. Image height is 82 mm. (b) Soot foil from detonation in C_2H_4-$3O_2$-$5N_2$, P_1=20 kPa. The soot foil was mounted to the wall of a detonation tube while the detonation passed over it. The cellular pattern that remains is due to the three-dimensional inhomogeneities of the front. Image height is 75 mm. (Austin, 2003)

shock provides the thermodynamic conditions for the reaction zone, and the reaction zone releases energy to support the shock wave. General discussion on theory and phenomena of gaseous detonations can be found in textbooks by Strehlow (1984) and Fickett and Davis (2001). Gaseous detonation waves have characteristic speeds depending on mixture, called the Chapman-Jouguet (CJ) speed. The pressure loading is spatially non-uniform, characterized by an initial jump due to the shock. This is followed by a pressure decay due to expansion waves. Figure 1.3 gives an actual pressure trace from a detonation tube. There are three-dimensional inhomogeneities in the detonation wave front (Fig. 1.4), but for the mixtures used in the present study, these are small, and the detonation wave front can be approximated as planar and the traveling load as axisymmetric. For a fracturing detonation tube, the pressure profile is altered by the breach in the form of further decay due to additional expansions.

1.3.2 Dynamic Amplification Factor and Critical Speeds

The dynamic amplification factor is defined as the ratio of the dynamic strain amplitude to the equivalent static strain. The concept has practical use for estimating the

maximum dynamic stress by using only static formulas. The dynamic amplification factor for the hoop strain of a tube under internal traveling load is dependent on the traveling load speed.

Tang (1965) analyzed the motion of a tube under internal traveling pressure loads by starting from a linear elastic steady-state model and dynamic shell equations that accounted for rotatory inertia and shear deformation. He determined that there were four critical speeds. When the load traveled at any of these speeds, the solution became unbounded.

The speed v_{c0} is the first critical velocity and corresponds to a resonance between the group velocity of the structural waves and the phase velocity of the detonation (see the extensive discussion in Beltman and Shepherd (2002)). Each of the critical velocities can be calculated from the vanishing of the discriminant

$$A_2^2 - 4A_0A_4 = 0 \,, \tag{1.1}$$

where

$$\begin{aligned} A_4 &= \left[\left(\frac{w}{v_d}\right)^2 - 1\right]\left[\left(\frac{w}{c_s}\right)^2 - 1\right] \,, \\ A_2 &= \left(\frac{w}{v_d}\right)^2\left[1 + \beta^2\left(\frac{v_d}{c_s}\right)^2\right] - \beta^2\left(1-\nu^2\right)\left(\frac{v_d}{c_s}\right)^2 \,, \\ A_0 &= \beta^2 + \frac{\beta^2\nu^2}{\left[\left(\frac{w}{v_d}\right)^2 - 1\right]} \,, \end{aligned} \tag{1.2}$$

where the shell thickness parameter is

$$\beta = \frac{h}{\sqrt{12}R} \,. \tag{1.3}$$

The other critical velocities are v_{c1}, equal to the modified shear wave speed,

$$v_{c1} = \sqrt{\frac{\kappa G}{\rho}} \,; \tag{1.4}$$

the dilatational wave speed in a bar,

$$v_{c2} = \sqrt{\frac{E}{\rho}}\,; \tag{1.5}$$

and v_{c3}, equal to the plane stress dilatational wave speed

$$v_{c3} = \sqrt{\frac{E}{\rho\,(1-\nu^2)}}\,. \tag{1.6}$$

For a more detailed discussion on these cases, the reader is referred to Tang (1965).

A simpler model of the motion of a tube under internal traveling pressure load was given by Simkins (1987), whose analysis neglects rotatory inertia and shear deformation. In this model, there is a closed form solution for the first critical speed v_{c0}, which is sometimes useful for back-of-the-envelope engineering estimations, namely

$$v_{c0} = \left[\frac{E^2 h^2}{3\rho^2 R^2 (1-\nu^2)}\right]^{\frac{1}{4}}. \tag{1.7}$$

Beltman et al. (1999) and Beltman and Shepherd (2002) performed extensive experimental and numerical studies on the shock loading of an aluminum tube and detonation loading of a stainless steel tube. They verified the resonant behavior predicted by the Tang (1965) theory near the flexural wave speed (the first critical speed). Dynamic amplification factors as high as 3.9 were observed in these experiments near the first critical velocity. The amplification factor is plotted in Fig. 1.5 for three aluminum 6061-T6 tubes used in the present study.

No experimental study on the dynamic amplification factor at other critical speeds has been found in the literature. One chapter of this thesis will be devoted to studying the deformation behavior in the regime near the second (shear) critical speed experimentally and numerically.

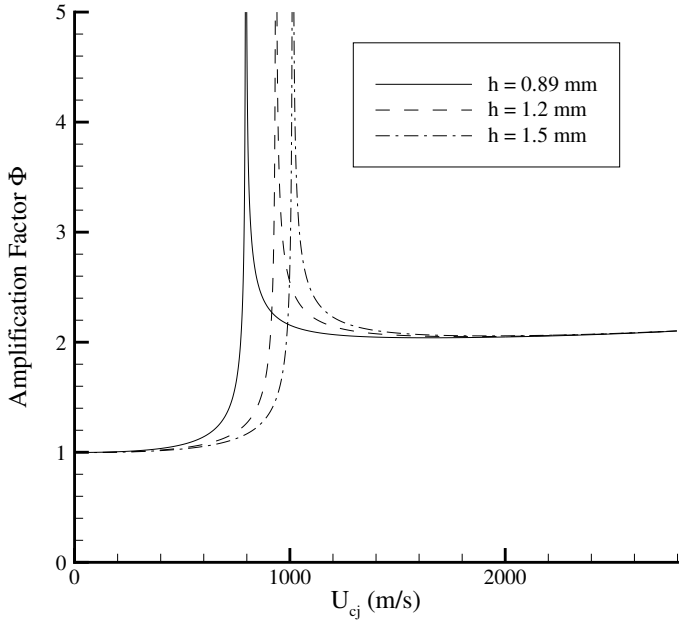

Figure 1.5: Steady-state dynamic amplification factor as a function of detonation wave speed according to the Tang (1965) model. Curves for Al6061-T6 tubes (R = 20.64 mm) of three different wall thicknesses are plotted for loads traveling near the first (flexural) critical speed.

1.3.3 Fracture Mechanics

Fracture mechanics is a wide and rich field of research. Excellent sources on fundamentals of cracks and fracture can be found in textbooks by Broek (1997), Kanninen and Popelar (1985), Broberg (1999), and Freund (1998). This section puts classical fracture mechanics in the context of the detonation-driven tube fracture problem.

1.3.3.1 Modes of Fracture

The three established modes for fracture analysis are shown in Fig. 1.6. Two-dimensional solids fracture is one or a combination of these mutually orthogonal modes. The three modes are symmetric in-plane (mode I), anti-symmetric in-plane (mode II), and anti-symmetric out-of-plane (mode III). For fracture problems with curved bodies and three-dimensional loading, these modes are insufficient and can

serve only as approximations. In the axially preflawed tube fracture problem, the initially straight crack propagation is dominated by mode I. As the crack begins to curve, mixed mode I and II conditions take over. As the crack runs further, the outward flapping and tearing motion causes the fracture to go into predominantly mode III. None of these modes take into account the shell curvature or the three-dimensional loading.

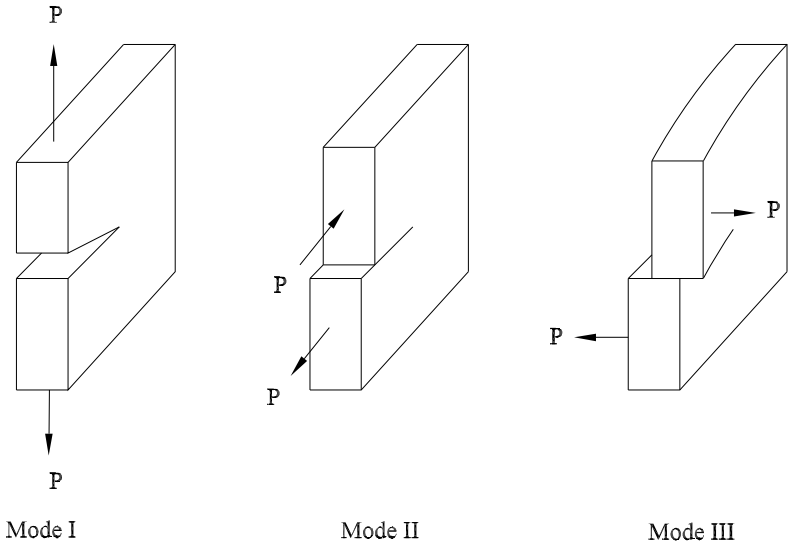

Figure 1.6: Fracture modes.

1.3.3.2 The Griffith Energy Criterion

As a crack extends through a stressed solid (a plate with a crack normal to far-field tension, for instance), the solid's compliance drops and so will its elastic energy content. The elastic energy released, G, is used to drive the crack. G is also called the 'crack driving force' because its dimensions of energy per unit plate thickness and per unit crack extension are also the dimensions of force per unit crack extension (Broek, 1997, Chapter 1). For crack extension to occur, G must equal or exceed a critical energy, G_c, required to form an incremental length of crack. This value is called the fracture toughness and is a material property. There are different values of G_c for initiation, propagation, and arrest.

1.3.3.3 The Stress Intensity Factor

The components of the near crack tip stress-field for an elastic body with reference to a rectangular coordinate system are (Freund, 1998, Chapter 2):

$$\sigma_{ij} = \frac{K(\sigma, a, t)}{\sqrt{2\pi r}} \Sigma_{ij}(\theta) + \sigma_{ij}^{(1)} + \mathcal{O}(1), \tag{1.8}$$

where r and θ are polar coordinates with respect to the usual crack tip coordinate system (Fig. 1.7), a is the crack length, and σ is some generalized far-field loading. $\Sigma_{ij}(\theta)$ is a dimensionless, universal function representing the angular variation and is independent of the body configuration, applied loads, and material. $\Sigma_{ij}(\theta)$ for different fracture modes are given in Freund (1998, Chapter 2).

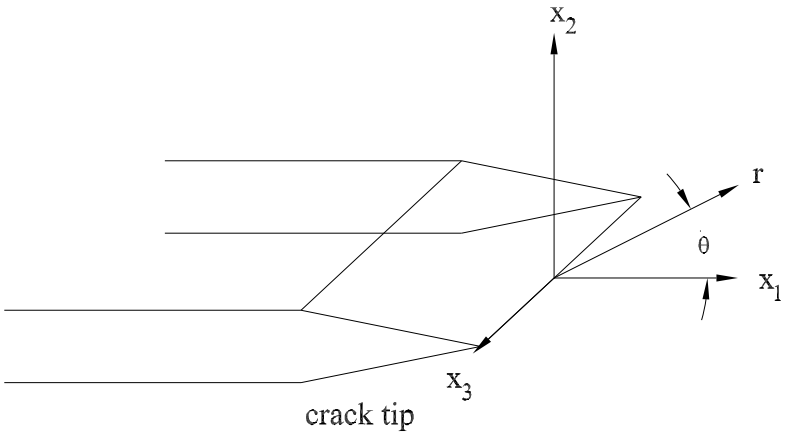

Figure 1.7: Crack tip coordinate system.

The time-dependent coefficient $K(\sigma, a, t)$ is called the stress intensity factor, which has physical dimensions of force/length$^{3/2}$. It is the only factor in the singular term that shows the influence of body geometry and loading. For crack initiation and propagation to occur, the stress intensity factor and the fracture toughness are related by (Kanninen and O'Donoghue, 1995):

$$K(\sigma, a, t) \geq K_c(\dot{a}, T, h), \tag{1.9}$$

where K_c is the fracture toughness, T is the temperature, and h is the characteristic

body thickness. This relation is valid for the linear elastic or small-scale yielding (SSY) condition, which says that the size of the plastic zone must be small enough so that the singular term (K-dominated field) can describe the near tip stress-field despite crack tip yielding.

So far, G_c and K_c (both dimensionally different) have been used for fracture toughness. There should be no confusion once it is pointed out that the crack extension stress intensity criterion $K \geq K_c$ and energy criterion $G \geq G_c$ are equivalent. For example, it can be shown for mode I that (Kanninen and Popelar, 1985, Chapter 1):

$$\frac{K^2}{E'} = G, \tag{1.10}$$

where $E' = E$ for plane stress and $E' = E/(1-\nu^2)$ for plane strain.

1.3.3.4 Salient Features of Mode I Dynamic Fracture

For the present detonation-driven tube fracture problem, crack initiation and early stages of crack propagation can be approximated by mode I dynamic fracture. Although there is no existing theoretical expression for the crack driving force of an axial through-wall crack of a tube under internal traveling internal load, there are derived expressions in the literature from which one can learn about some essential features of mode I dynamic fracture.

For a stationary, semi-infinite crack subjected to a suddenly applied crack face pressure of magnitude σ_0 and finite pulse duration t_0 under plane strain conditions, Freund (1998, Chapter 7) states that the dynamic stress intensity factor is

$$K_I^d(t) = \begin{cases} C_I \sigma_0 \sqrt{2\pi c_d t} & 0 \leq t \leq t_0, \\ C_I \sigma_0 \sqrt{2\pi c_d}(\sqrt{t} - \sqrt{t - t_0}) & t \geq t_0, \end{cases} \tag{1.11}$$

where

$$C_I = \frac{\sqrt{2(1-2\nu)}}{\pi(1-\nu)} \tag{1.12}$$

and c_d is the plane strain dilatational wave speed. This shows that during early stages of crack initiation, the stress intensity factor scales as the square root of time during the application of the pulse but falls once the pulse stops. Assuming fracture initiates at initiation time τ_i when the stress intensity reaches its critical value, $K_I^d(\tau_i) = K_{Ic}^d(\dot{K}_I(\tau_i))$, and the crack propagates at a steady speed, the stress intensity becomes (Freund, 1998, Chapter 7):

$$K_I^d(t, \dot{a}) = k(\dot{a}) K_I^d(t) \tag{1.13}$$

for $t \geq \tau_i$, where

$$k(\dot{a}) \approx \frac{1 - \dot{a}/c_R}{\sqrt{1 - \dot{a}/c_d}}. \tag{1.14}$$

This expression shows that the mode I dynamic stress intensity factor for crack propagation is a function of the crack speed $\dot{a}$ and decreases to zero as it approaches the Rayleigh wave speed c_R of the material. On the other hand, if the crack speed is much smaller than the Rayleigh wave speed, then $k(\dot{a})$ approaches unity and the dynamic stress intensity factors for the stationary crack and the running crack are practically the same. This situation applies to the present detonation-driven tube fracture problem for aluminum 6061-T6 specimens, where measured maximum crack speeds (about 250 m/s) are only 9 percent of the Rayleigh wave speed (about 2890 m/s).

1.3.4 Stress Intensity Amplification due to Bulging

Bulging refers to the radial, out-of-round distortion of the tube wall on either side of the crack. As a result of the bulging, the tube wall develops a radial component of displacement and velocity that depends on the extent of the bulging and the forward speed of the crack (Hahn et al., 1973). The bulging can cause a large contribution to the crack-driving force in addition to that provided by the hoop stress.

Perhaps the first to theoretically analyze in detail the stress intensity amplifica-

tion in a cracked cylindrical shell due to bulging is Folias (1965). The idea is that a cylindrical pressure vessel can be treated like a flat panel of the same material, thickness, and containing the same through-crack as the vessel. This equivalent flat panel is loaded in simple tension equal to the far-field hoop stress of the cylinder and multiplied by a 'Folias factor' which depends on the geometry of the cracked cylinder. Despite the two-dimensional analogy, the analysis was founded on static, linear elastic, three-dimensional shell equations. The 'Folias factor' has undergone some changes since its introduction. One recent version can be found in Folias (1998), where he states that flat plate behavior is correlated with axially-cracked cylindrical shells by

$$\frac{\sigma_{hoop}}{\sigma_{plate}} = \frac{1}{\sqrt{1 + 0.317\lambda^2}}, \tag{1.15}$$

where

$$\lambda^2 = \frac{a^2\sqrt{12(1-\nu^2)}}{Rh}. \tag{1.16}$$

The linear elastic mode I stress intensity of the analogous cracked plate under far-field loading σ_{plate} normal to a crack of length $2a$ is

$$K_{I(plate)} = \sigma_{plate}\sqrt{\pi a}. \tag{1.17}$$

Combining this with $\sigma_{hoop} = PR/h$, it is evident that the stress intensity factor of an axially-cracked cylindrical shell is

$$K_I = \frac{PR}{h}\sqrt{\pi a\left(1 + \frac{0.317a^2\sqrt{12(1-\nu^2)}}{Rh}\right)}. \tag{1.18}$$

1.4 Scope

This work involves primarily experiments on tubes ruptured by detonations with some numerical simulations. Topics explored include the strain, pressure, crack speed,

and crack path. This study allows for the variation of tube material (aluminum, carbon steel, and polycarbonate), tube geometry (radius to wall thickness ratio), flaw geometry (length and depth), prestress, and detonation pressure. Initial temperature was not varied.

Analytical modeling is not considered due to the complicated three-dimensional fracture dynamics coupled with gas dynamics. Nonetheless, fundamental aspects of fracture dynamics such as crack speed, stress intensity, and strain rate are discussed with aspects of gas dynamics.

Chapter 2

Literature Review

Literature on static and dynamic tube fracture due to internal pressure loading will be reviewed. This chapter is divided into experimental, numerical, and theoretical parts. These are further sub-divided by institutions when it is practical to do so. It is not intended to summarize the work of every paper that was selected. Only the information that is most relevant to this thesis will be briefly discussed. It includes data on crack speeds, strain and pressure histories, prestress, strain rates and loading rates, fracture criteria, fracture path (helical curving or branching), energy considerations, stress intensity factors, fluid-structure interaction during rupture, flap motion, and framing camera photographs.

The structural response of shells to shock or detonation loading was studied by researchers such as Tang (1965), Reismann (1965), de Malherbe et al. (1966), Brossard and Renard (1979), Simkins (1987), and Thomas (2002). Previous work was done at Caltech by Beltman et al. (1999) and Beltman and Shepherd (2002) to investigate the linear elastic structural response of unflawed cylindrical shells to internal shock and detonation loading. These analytical, numerical, and experimental studies demonstrated that the amplitude of the linear elastic strains is related to the speed of the shock or detonation wave. However, since these studies did not involve fracture, they will not be discussed in further detail. This chapter will focus on tube fracture.

2.1 Experimental Work

The bulk of the literature on experimental work on fracture of tubes has been motivated by the concern of gas-transmission pipeline safety. An impressive amount of work has been done on preflawed fracture of full-scale pipelines. Aircraft fuselage safety was another motivation for studying tube fracture.

2.1.1 Tube Fracture due to Static Loading

Strictly speaking, all processes become dynamic and unsteady once tube fracture begins. 'Static' means that before rupture, the internal pressure is quasi-static. Literature on gas transmission pipeline falls into this category. Since the 1960s, a number of studies were made to study fracture of long pipes. The focus has been on conditions of crack initiation, propagation, and arrest. Parameters studied included initial flaw size versus burst pressure, crack speed, strain, crack-opening area, pressure profile during crack propagation, and rate and amount of fluid lost.

2.1.1.1 Battelle Memorial Institute, Columbus, Ohio

A significant amount of pipeline research was done by the Battelle Memorial Institute. McClure et al. (1965), Duffy et al. (1969), Maxey et al. (1971), Kiefner et al. (1973), and Maxey et al. (1974) performed and studied full-scale burst tests at typical operating conditions and with materials of gas-transmission pipelines. A detailed description of some of these tests was included in McClure et al. (1965), who performed full-scale pipe experiments on 190 carbon steel specimens with different treatments and chemical properties. The specimens were typically 0.76 m in diameter and about 0.8 cm to 1.0 cm in wall thickness. Other diameters ranging from 0.4 m to 0.9 m and wall thickness ranging from 0.6 cm to 1.7 cm were also tested. The pipes were welded longitudinally and preflawed axially.

They observed two major kinds of fracture, shear and cleavage fracture. Shear fracture was characterized by high ductility, large plastic deformation, relatively low crack speeds (lower than 270 m/s), and usually resulted in only one long straight crack.

The fracture surfaces of shear fracture were dull, silky, and were generally inclined at 45° with respect to the shell surface. Shear fractures happened when the material was above the transition temperature. Below this temperature, cleavage fracture dominated. Cleavage fracture was characterized by relatively low ductility, less plastic deformation, relatively high crack speeds (greater than 460 m/s), and usually involved multiple cracks that traveled in the same front. The cracks usually traveled in a sinusoidal pattern. The fracture surfaces of cleavage fracture exhibited characteristic chevron marks which pointed in the reverse direction to the crack propagation.

It was pointed out that whether or not the cracks arrest depended on a competition between crack speed and decompression-front speed. When the cracks propagated slower than the decompression-front (the gas used was pumped in from a Texas Eastern pipeline nearby and had a sound speed of 410 m/s), the cracks propagated into a diminishing stress-field and tended to arrest quickly. This usually happened when the material was above the transition temperature. On the other hand, when the cracks propagated faster than the decompression-front, ahead of the crack tips there was a nominally constant stress-field and the cracks typically did not arrest easily. This usually happened when the material was below the transition temperature.

2.1.1.2 University of Washington, Seattle, Washington

A number of laboratory-scale pipe rupture experiments were performed by groups associated with A. S. Kobayashi at the University of Washington. In Emery et al. (1986), a 5.08-cm diameter thin-wall ($h/d = 1/60$) welded carbon steel pipe was pressurized with air to 7.4 MPa and fractured using a drop weight and a chisel. The crack was directed along a 0.2-mm deep longitudinal groove. Pressure histories were measured by pressure transducers mounted inside the tube, axial and circumferential strains were measured by strain gages, crack speeds were measured by crack wire gages, and crack-opening shapes were photographed by a framing camera. The average crack speed was determined to be 127 m/s. Photographs suggest a small depression or dimple at the tip of a crack, which had previously been observed by Shoemaker and McCartney (1974). Radial velocities of the flap were found to be

25 m/s near the crack tip to 18 m/s at 0.2 diameters behind the crack tip, decreasing nearly uniformly with distance. The flap circumferential velocity, over the same distance, was found to range from 13 to 15 m/s.

Kobayashi et al. (1988) performed similar experiments at different pressures and found that average crack velocity (ranging from 180 to 305 m/s) varied somewhat linearly with the groove depth. They used strain gage rosettes to determine the change in principal strain direction as the cracks ran. They also measured strains ahead of the propagating crack tip exceeding the yield limit for six pipe diameters. The cracks running into the ungrooved tube section curved and were arrested.

Experiments on cylinder fracture were recently performed by Shimamoto et al. (1998) and Kosai et al. (1999) to simulate idealized fuselages. The specimens were made of Al2024-T3, 360 mm diameter by 914 mm long by 0.3 mm wall thickness with one or two riveted and bonded lap or butt joint(s). The ends were clamped to steel cylinders. The specimens were riveted to tear straps. Upon pressurization by air, the initial axial crack was initiated, ran, kinked, and turned due to mixed mode I and II states set up by the internal pressure, crack flap, stringer, and tear straps. Strain gages, crack gages, and pressure transducers were used in this experiment.

2.1.1.3 U. S. Steel Research Laboratory, Monroeville, Pennsylvania

We return to full-scale gas transmission line pipe testing with U. S. Steel Research Laboratory. Here, Ives et al. (1974) and Shoemaker and McCartney (1974) studied the running fracture of 23 line pipes. The diameter ranged from 0.8 to 1.2 m, and the wall thickness ranged from 8 mm to 18 mm. Carbon steel line pipes were pressurized by air with pressures ranging from 4.5 to 11.2 MPa. The fracture lengths ranged from 6 to 27 m. The pipes were axially preflawed. Using crack detectors (fine wires cemented to the pipes), strain gages, and pressure transducers, they measured crack speeds, pipe deformation, strain fields, and pressure during fracture. They found that each of four different locations along the pipe length relative to the crack tip had a distinctive type of pipe deformation, which was described in detail. One aspect of this was that the circumferential strain was the most tensile near the crack tip, dropped

to compressive within a longitudinal distance of one diameter, and then rose again to tensile at two diameters away from the crack tip. Maximum crack speeds were measured to reach 300 m/s. They also compared the crack arrest conditions affected by the difference between sand backfill (crack was slower and shorter) and no backfill (crack was faster and longer). Close-up framing camera photographs of the crack running through a gridded section of the pipe were taken.

2.1.1.4 Berkeley Nuclear Laboratories, Berkeley, Gloucestershire, United Kingdom

Research at Berkeley Nuclear Laboratories on air-pressurized pipe fracture was associated with M. R. Baum. In a number of laboratory-scale experiments (Baum and Elston, 1981, Baum, 1982b,a), pipes of different materials were fractured. In the study by Baum and Elston (1981), 25-mm inner diameter initially-flawed glass pipes with 1.3-mm wall thickness were fragmented. The rupture pressures ranged from 0.3 to 4.6 MPa. The transient depressurization was measured by a pressure transducer mounted inside a metal pipe that was connected to the glass specimen, and the velocities of the fragments were measured by high-speed cine films.

The fracture of axially-preflawed mild steel pipes (102 mm diameter, 1.6 mm wall thickness) was presented in Baum (1982a). Rupture pressure was in the range of 5 to 12 MPa. The events were captured on high-speed cine films. The maximum crack speeds reached about 230 m/s. Breach areas and free edge velocities were also measured. It was found that crack speeds reached a peak steady value well before the breach was 'fully open', defined by a breach area equal to twice the pipe cross sectional area.

2.1.1.5 Other Researchers

There have been many vessel failure experiments performed at other institutions which are not as specialized as those mentioned above. The part of their contribution relevant to the present study is described in this section.

Cain and Hall (1994) performed full-scale pressure vessel burst tests of steel cylinders that were pressurized by water and nitrogen. The diameters varied from 0.6 to 0.9 m, and burst pressures varied from 10 to 49 MPa. The fragmentation was typically initiated with the help of grooves and shape charges. The ratio of fragment kinetic energy to isentropic expansion energy was calculated. The strength of the blast wave was measured in terms of the pressure rise caused by the shock and the impulse.

Laboratory-scale burst tests were performed by Hyde and Yaghi (1995) on Araldite CT200 (a brittle polymer) tubes. Unlike other experiments which had saw-cut blunt notches, these tubes (150-mm diameter, 10-mm wall thickness) were custom-made so that the axial preflaws were created by inclusion of sharp shims in the moulds used for casting the cylinders. The width of these flaw tips were as small as 0.02 mm. The specimens were pressurized with oil to pressures up to 2.6 MPa. Painted conductive grids were used to measure crack speeds which ranged from 260 to 564 m/s. Extensive crack branching and curving were observed and their paths documented in detailed diagrams. Fracture surfaces exhibited mirror, mist, and hackle regions. Although they did not measure strains, they attempted to deduce dynamic stress intensity factors from a theoretical relationship presented by Freund (1998).

The burst pressures and strain concentrations of water-pressurized aluminum 6063-TB pipes (100-mm diameter and 1.8-mm wall thickness) containing dents and gouges were studied (Lancaster and Palmer, 1996a,b). Using radially oriented linear voltage displacement transducers, strain gages, and photoelastic coating, they identified in detail the displacement and strain fields at different stages of pressurization. Ong et al. (1992) performed similar experiments on 18 mild steel pipe specimens and revealed the locations of maximum stresses for different kinds of dents.

There were a number of other cylinder fracture experiments aimed at validation of numerical simulations. For example, fatigue crack growth experiments on a generic narrow-body fuselage with tear straps, stringers, stringer clips, and frames were tested by the Boeing Commercial Airplane Group. The test data were detailed in Potyondy (1993) and compared with results from the FRANC3D/STAGS program. A cyclic

pressure of 53.8 kPa was applied to propagate the crack which curved within a 0.91-mm thick skin made of 2024-T3 clad aluminum alloy. Another set of unpublished validation experiments was performed in 1994 by M. F. Kanninen and co-workers. These results were summarized in Zhuang and O'Donoghue (2000a) for comparison with simulations by the PFRAC program. The Small Scale Steady State (S4) tests used polyethylene pipe specimens that were 0.25 m in diameter at 0 to 10°C. Cracks were initiated by a dropped chisel. The range of internal gas pressures were from 0.2 to 0.4 MPa, and axial crack speeds were from 125 to 225 m/s.

Failure of steel pipes under carefully controlled combined loading can be found in other studies. For example, Roy et al. (1997) described full-scale corroded pipe failure experiments performed by the Southwest Research Institute. These tests involved pipes that were artificially corroded and loaded under axial compression, bending, and internal pressure. Different failure modes (rupture and bending collapse) were tabulated for different failure pressures and bending moments. These data were compared with finite-element simulation results. Koundy et al. (1998) described tension-torsion fracture tests on thin-wall laboratory-size steel tube specimens. A photograph of a post-test specimen showed simultaneous buckling and helical crack propagation.

2.1.2 Tube Fracture due to Dynamic Loading

Recent work on gaseous detonation-driven fracture of preflawed metal and polymer tubes can be found in Chao and Shepherd (2002), Lam and Zielonka (2002), and Chao and Shepherd (2003). Experiments performed by the U. S. Air Force on explosive-induced blast loading of decommissioned B-52 aircraft were summarized in Kanninen and O'Donoghue (1995). The large body of research on tube fracture due to dynamic (non-fatigue) loads often does not involve a fracture mechanics approach (i.e., no deliberate preflaw). This research has typically focused on high strain rate (10^4 to 10^5 s^{-1}) loading of non-preflawed specimens. Examples of such experiments can be found in Slate et al. (1967), Ivanov et al. (1974), Wesenberg and Sagartz (1977), and Singh et al. (2002). In the study by Singh et al. (2002), crack speeds through

copper cylinders were found to range between 250 to 300 m/s for specimens with inner diameter of 52 mm and wall thickness from 1 to 7 mm that were loaded by high explosives such as RDX/TNT, TNT, Octol, and Baratol. Rupture strains were found to be as high as 300%. In Wesenberg and Sagartz (1977), dynamic fracture of 6061-T6 aluminum cylinders was studied by expanding ring specimens to strain rates of 10^4 s^{-1} by magnetic pressure pulses from a capacitor bank discharge. The fragmentation was analyzed using Mott's treatment of the bomb fragmentation problem (Mott, 1947).

2.2 Computational Work

Currently, there is no computer program that can simulate all the essential aspects of tube fracture. 'Essential' means that the code must accurately simulate the transient coupling of fluid dynamics, elastic-plastic structural dynamics, crack initiation from a surface flaw, crack propagation, crack branching, crack curving, and crack arrest. Each of these phenomena, when simulated in an uncoupled setting, requires significant effort to perform correctly. Some of these cannot be simulated at all with current computational capabilities. Adding gaseous detonations into the picture significantly increases the challenge. The following presents attempts to model various tube fracture problems. All required some degree of simplifying assumption. Much can be learned from each study about the validity of these assumptions.

2.2.1 Tube Fracture due to Static Loading

2.2.1.1 Southwest Research Institute, San Antonio, Texas

One of the most advanced tube fracture programs described in the literature is the proprietary Pipeline FRacture Analysis Code (PFRAC). PFRAC was first integrated at the Southwest Research Institute (O'Donoghue et al., 1991) and further developed by Zhuang (1995). Validation was made by comparison with full-scale gas transmission pipeline fracture test data. The package can be used to calculate the crack driving force G by node force release and energy balance methods for a propagating crack

in a gas pipeline. Key features include (i) three-dimensional non-steady gasdynamics description using finite differences, (ii) elastic-plastic shell structure deformation using finite elements, (iii) mechanisms to simulate dynamic crack advance, and (iv) coupling of fluid dynamics, structural dynamics, and fracture mechanics models. A typical result was shown in Kanninen and O'Donoghue (1995), where steady-state crack propagation (crack speed = 125 m/s) of a 1.42-m diameter steel gas transmission pipe, pressurized to 10 MPa, was simulated using 1260 shell elements and 14560 fluid cells. On a CRAY 2 computer, this took 40 minutes. This code was applied to determine fracture toughness (which could not be directly obtained from the full-scale experiments) in the crack propagation of a polyethylene pipe (Zhuang and O'Donoghue, 2000a). It was also used to evaluate pipeline crack arrest methodologies and designs (O'Donoghue and Zhuang, 1999, Zhuang and O'Donoghue, 2000b). Pressure profiles, strains, displacements, and crack speeds were calculated and compared with experiments.

Being a shell element code, PFRAC does not simulate surface cracks. Consequently, it does not deal with crack initiation problems (pipeline fracture initiation often requires a surface crack). Although PFRAC focuses on crack propagation and arrest, so far no PFRAC publication has been found on crack branching and crack curving, which are often encountered in pipe fracture.

2.2.1.2 University of Washington, Seattle, Washington

The numerical modeling of tube fracture associated with A. S. Kobayashi at the University of Washington can be categorized into two types. One involves simulating the axial crack propagation (no crack branching or crack curving) by a 'split-ring' model (Emery et al., 1981, 1986, Kobayashi et al., 1988, Emery et al., 1992). This model basically approximates the axially fracturing pipe with a train of axially split and discontinuous cylinders. The second type involves finite-element models (Shimamoto et al., 1998, Kosai et al., 1999). These are used to simulate crack branching and crack curving.

Depending on the type of research, different models were used. Studies on gas

transmission pipelines typically used the split-ring model because it could simulate running axial cracks and it was computationally much less expensive than the FEM. Fluid pressure could also be calculated because there was a coupling algorithm. On the other hand, FEM was used in studies of pressurized aircraft fuselage fractures because it was capable of modeling curving cracks under the influence of fuselage components such as tear straps and stringers. However, fluid pressure must be obtained from experimental data as input to the simulation.

The fluid pressure for the split-ring model was computed by a transient one-dimensional finite difference fluid program (Love et al., 1977a,b). The crack tip opening angle (CTOA) criterion (Newman et al., 2003) was used for crack extension by assuming that the opening gap of the split-ring was equal to the average crack opening over a characteristic distance (length of each ring). Fluid pressure, strain, and crack extension history for air-filled, cold water-filled, and hot water-filled pipes were computed and some of these results were compared with experimental data (Emery et al., 1981, 1986, Kobayashi et al., 1988, Emery et al., 1992).

The Aloha Flight 243 accident (NTSB, 1989) motivated studies on crack propagation, curving, and arrest criteria in pressurized fuselages. Two of these numerical studies can be found in Shimamoto et al. (1998) and Kosai et al. (1999). They used finite element models to simulate fuselages with tear straps and stringers. Static linear elastic fracture mechanics was used with a crack kinking criterion which depended on maximizing the crack tip circumferential stress and an experimentally measured 'length of attempted branch cracks associated with a rapidly propagating crack' (Kosai et al., 1999). Pressure data from fracture experiments were used as boundary values for the model. The mesh was constructed with smaller elements concentrated in a region along the anticipated crack path. The computed crack path and strain were verified against experimental data. Stress intensities were also calcuated.

2.2.1.3 Cornell University, Ithaca, New York

The structural integrity of aircraft fuselages motivated computational fracture studies at Cornell University (Potyondy, 1993, Potyondy et al., 1995, Chen et al., 1997, Chen,

1999, Chen et al., 2002). In Chen et al. (2002), simulations were performed using the FRANC3D/STAGS program[1]. The residual strength of a cracked KC-135 fuselage panel was calculated using the CTOA fracture criterion. The crack path was also calculated using a T-stress and fracture toughness orthotropy approach. Pressure was applied as a constant internal load on the shell structure and crack flap. Computed crack trajectories compared satisfactorily with experimental data. T-stresses and stress intensity factors were also computed.

2.2.1.4 Other Researchers

Baaser and Gross (2000) computationally analyzed the damage evolution in axially and circumferentially cracked ductile steel cylindrical shells subjected to uniform quasi-static internal pressure using finite continuum elements and a Gurson model. Stress and damage distribution across the wall thickness were represented. Crack initiation and growth were studied in a deformation-controlled condition. Contours of von Mises stress near the cracks were plotted.

Other finite element studies on failure of tubes were performed in conjunction with combined loading experiments that were mentioned in the Experimental section. These include studies by Roy et al. (1997), who used the ABAQUS code to simulate a corroded steel pipe under combined axial compression, bending, and internal pressure; and Koundy et al. (1998), who used the INCA code to simulate tension-torsion tests on steel tubes.

2.2.2 Tube Fracture due to Dynamic Loading

There are not many computational studies available in the open literature on fracture of preflawed tubes due to dynamic (non-fatigue) loads. One such recent study can be found in Tzeng (2000). In this study, he used the code DYNA2D to compute the dynamic response of a composite gun tube with an internal traveling load (to simulate the projectile) and a stationary interfacial crack between the composite and

[1]FRANC3D is available at the Cornell Fracture Group's website at www.cfg.cornell.edu

the liner. The tube was modeled with 4000 axisymmetric elements and the value of the J-integral was calculated. The critical velocity concept (Simkins, 1987) was applied and the traveling load speed was varied to study its dynamic amplification effects.

Another study on fracture of preflawed tubes under dynamic loading can be found in Popelar et al. (1981). They used a two-dimensional finite difference algorithm to simulate the cross-section of an infinitely long steel cylinder (radius = 305 mm and wall thickness = 26 mm) with an infinitely long internal, partially-through, axial flaw (depth = 6 mm). An impulsive shock loading was applied to the inner wall (radial velocity = 1 m/s), causing the crack to run under linear elastic fracture mechanics conditions. It was observed that 84 μs were required for the stress intensity to build up to the critical value and to initiate crack growth. After initiation, the crack propagated at 300 m/s and penetrated the outer surface.

Simulations were performed to analyze the blast-loading experiments on decommissioned B-52 aircraft done by the U. S. Air Force (Kanninen and O'Donoghue, 1995). In these simulations, the BLASTIN code was used to calculate the fuselage pressures, generating time of arrival, the peak pressure, and pulse duration. Southwest Research Institute's PFRAC code then used this traveling load data as input to simulate the structural response, and the equivalent plastic strain was calculated as a measure of the on-set of damage. Experimentally observed damage (ranging from minor internal damage to extensive, 3-m long cracking) was correlated with computed equivalent plastic strain (ranging from 0.58 $\times 10^{-2}$ to 5.55 $\times 10^{-2}$).

2.3 Theoretical Work

All studies on tube fracture involved some degree of theoretical analysis. Due to the complexity of the problem, a closed-form solution for the fracture of preflawed tubes due to internal pressure has never been attempted. Efforts have been made to study different facets of the tube fracture problem, often with many simplifying assumptions. These studies focused on the gasdynamics, structural deformations,

crack initiation stress intensity factors, plasticity corrections, crack propagation and arrest conditions, and energy balance considerations.

2.3.1 Tube Fracture due to Static Loading

Again, the literature on theoretical analysis of tube fracture due to static loading is far richer than that of dynamic loading, mainly due to economic drivers of the oil, gas, and aircraft industries.

2.3.1.1 Gasdynamics

Analytical attempts at gasdynamics of rupturing tubes have been limited to one-dimensional or two-dimensional treatments. One-dimensional gasdynamics was used by authors such as Kanninen et al. (1976), Love et al. (1977a), and Love et al. (1977b) to model the pressure distribution in the vicinity of the opening axial fracture of a long pipe based on the classical theory of compressible flow through a nozzle where mass exits through the opening crack at the local sound speed. In these models, the local mass outflow rate was equal to that of a nozzle whose opening area was the same as that of the crack.

Implicitly assumed in these one-dimensional models was that the crack opening was much smaller than the pipe diameter. However, as pointed out by Freund et al. (1976) and Freund and Parks (1976), in order to obtain realistic values of pressure decay length, crack openings on the order of one pipe diameter were required. This violated the assumption that the crack opening was much smaller than the pipe diameter. To attain a more realistic model, Parks and Freund (1978) presented a gas escape model based on a two-dimensional flow field. The flow was assumed to be steady, adiabatic, isentropic, and irrotational. Equations of motion for a perfect gas were used. It was also assumed that the flow was supersonic and a curved shock was present. Their results compared favorably with experimental data.

The gasdynamics of fragmentation of pressurized pipes was considered by Baum and Elston (1981). They used one-dimensional assumptions where the flow was isen-

tropic and steady (valid when fragment velocities were very much less than the sound speed of the gas and the breach area was initially small). Taking the flow between fragments to be choked, the classical theory of compressible flow through a nozzle was used to model the pressure transient after rupture. A parametric study was performed to fit the model to experimental data. A similar analytical one-dimensional exercise was performed on the axial crack propagation of a gas-pressurized steel pipe to determine the pressure profile of the rarefaction waves (Baum, 1982b).

2.3.1.2 Structural Deformations

One of the simplest models of structural deformations of axially-cracked pipes was considered by Hahn et al. (1973), where it was assumed that the bulging of the pipe wall on either side of the crack was similar to the deflection of classical cantilevered beams subjected to a uniformly distributed load corresponding to the pipe pressure. Photographic pipe fracture evidence (Duffy et al., 1969) was used to determine some of the unknown parameters in this beam model.

Starting with cylindrical shell equations, Kanninen et al. (1976) deduced the equation of motion for a cracked and pressurized pipeline using the following assumptions: (1) neglect axial displacement (this was later argued to be invalid based on energy balance considerations by Emery et al. 1986), (2) neglect circumferential pressure variations, (3) a fully plastic hinge develops at a finite distance behind the crack, and (4) the crack opening displacement at any cross section is equal to the circumferentially integrated radial displacement. The analysis led to the derivation of the dynamic energy release rate for a propagation crack.

More sophisticated structural models were considered by the University of Washington group (Emery et al., 1976, Love et al., 1977a,b). In these papers, a cracked structural shell model which considers transverse shear and rotatory inertia was used to calculate the deflections of a rupturing pipe. The calculations were performed using finite difference methods. In later studies (Emery et al., 1986), structural deformations were considered in a more simple manner by approximating the pipe-wall shape behind the crack front with straight flaps in order to get quick estimates of the

strain energy.

2.3.1.3 Crack Initiation

The theoretical foundation for calculating the static crack initiation stress intensity factor of a cracked cylinder was provided by Folias (1965) (see previous chapter). However, it was only a linear elastic (brittle) and through-wall crack analysis. For application to more practical problems, many subsequent studies have incorporated plasticity corrections (e.g., Hahn et al. 1969) and partially-through-wall crack corrections (e.g., Kiefner et al. 1973) to the Folias factor.

2.3.1.4 Crack Propagation and Arrest

One of the main concerns of pipeline researchers has been the conditions for crack propagation and arrest. Kanninen (1970) predicted a limiting speed for rapid crack propagation based on an analogy between the deformation of an axisymmetrically-loaded cylinder and the deflection of a beam on elastic foundation. The results agreed with full-scale test data from Maxey et al. (1974). In Hahn et al. (1973), the steady-state crack speed in full-scale pipelines was modeled by considering a crack extension criteria associated with the COD (critical crack opening displacement). While they admitted that their assumptions were not on very firm ground, they attempted to compare this model with measured crack speeds. Maxey et al. (1971) and Maxey et al. (1974) developed an analytical expression that related the Charpy energy and other material properties of the pipe to the crack propagation and crack arrest conditions. The model compared well with full-scale tests done at Battelle.

Since the energy release rate for a propagating crack was a fundamental parameter determining crack propagation and arrest, some researchers have tried to model it. One example was Kanninen et al. (1976), who used an equation of motion to deduce the dynamic energy release rate. They used an approach based on a form of Hamilton's principle and a path integral on the surface of the shell analogous to the J-integral formulation (Rice, 1968). For the special case of a steady-state propagation crack, a maximum in the energy release rate as a function of crack speed was shown.

Freund (1998, Chapter 5) developed an expression for the energy flow into the crack tip which is propagating at an instantaneous speed. From this, the energy release rate was deduced for a special case of the steady-state crack.

Few analytical studies exist on crack speed variations in pressurized pipes. One such study can be found in Williams and Venizelos (1998). They assumed an analogy between the pressurized pipe and a beam with loads moving with constant velocity. The pressure was assumed to decay linearly with distance. The crack driving force as a function of crack speed was found to exhibit a maximum, which was verified by numerical studies. In the second part of their study, they attempted a perturbation and stability analysis on the crack length. This yielded oscillations in the crack speeds, which they speculated were related to the snaking crack paths that other researchers observed in full-scale pipeline rupture tests. Comparison of measured wavelengths with predicted wavelengths, however, showed large discrepancies.

2.3.1.5 Energy Balance

The analytical energy balance was used by Poynton et al. (1974) to identify the conditions for crack arrest. They considered an energy balance which included the work done by the gas, recoverable component of the elastic strain energy in the pipe wall, fracture energy (using Charpy energy data), and kinetic energy of the fractured pipe. The balance yielded an equation with some unknown constants to be determined by statistical fits with experimental data. After the constants were found, fracture arrest conditions were then established.

Emery et al. (1986) used the energy balance to study the validity of the assumptions for their numerical models. In Emery et al. (1986), a large discrepancy was found between measured axial crack speeds in long pipes and those values in their simulated split-ring model. This discrepancy motivated the derivation of an analytical energy balance equation for investigating the validity of previous assumptions made by the University of Washington group for the split-ring model (Emery et al., 1981). One of the simplifying assumptions made in Emery et al. (1981) was that there was no axial stretching in the pipe. By comparing pressure energy, kinetic energy,

bending energy, axial stretching energy, fracture energy, and crack elastic energy, the energy balance equation showed that this assumption was invalid by demonstrating that axial stretching of the crack flaps acted as a major source of energy dissipation.

2.3.2 Tube Fracture due to Dynamic Loading

No literature was found on theoretical study of tube fracture of preflawed tubes due to internal traveling loads. However, there have been a great number of studies on fragmentation of tubes due to explosive loads. Classical studies can be found in Taylor (1963), Gurney (1943), and Mott (1947). A recent analysis can be found in Singh et al. (2002).

Chapter 3

Linear Elastic Response Near the Modified Shear Wave Speed

3.1 Introduction

One of the interesting questions involving linear elastic response of tubes is what happens when the internal pressure load is traveling at $v_{c1} = \sqrt{\kappa G/\rho}$, the Tang (1965) second critical wave speed. This speed is also called the modified shear wave speed because of the application of the shell theory's shear correction factor, κ, to the shear speed of the material. According to the Tang (1965) model, the steady-state solution does not exist at this speed. Although it was well documented experimentally and numerically (Beltman et al., 1999, Beltman and Shepherd, 2002) that resonance in the hoop strains exists at the first critical speed, no study in the literature was found on whether a similar resonance near the second critical speed will occur. The first two critical speeds are of engineering importance to metal tubes because the CJ speeds of gaseous detonations are typically closer to the first two critical speeds than the third (bar) and fourth (dilatational) critical speeds.

In this chapter, experiments and numerical simulations will be presented for an aluminum 6061-T6 tube under internal gaseous detonation loading in the modified shear wave speed (v_{c1}) regime. The tube, 1.52 m long, 41.28 mm in outer diameter, and 1.5 mm in wall thickness was linearly elastically loaded. An explicit finite element code (LS-Dyna V.960) was used to compute the elastic response to a gaseous

detonation modeled as a traveling load. Since transverse shear is the focus of this chapter, the tube wall was simulated with axisymmetric solid elements as opposed to shell elements. In the experiments and simulations, detonation waves were used with various velocities. These range from velocities between 2187 m/s (above the first critical speed, v_{c0}, of the tube but below v_{c1}) and 3576 m/s (above v_{c1} but below the elastic bar wave speed, v_{c2}). These speeds were chosen to complement previous work by Beltman and Shepherd (2002) on the regime of speeds near v_{c0}. Table 3.1 lists the four critical speeds and the material shear wave speed (c_s) of this specimen. It will be shown experimentally and numerically that there is no resonance in the hoop strains near the modified shear wave speed. However, resonance in transverse shear will be demonstrated numerically.

	Speed (m/s)
v_{c0}	1013
v_{c1}	2847
c_s	3055
v_{c2}	4982
v_{c3}	5278

Table 3.1: Critical and characteristic speeds.

3.2 Experimental Setup

3.2.1 Detonation Tube Assembly

Figure 3.1 shows a schematic of the experimental setup for the detonation loading of a 1.524 m long, 1.47 mm wall thickness, and 41.28 mm outer diameter specimen tube. Figure 3.2 is a corresponding photograph showing the assembly aligned and bolted to aluminum plates, which were bolted to a plywood table. The setup consisted of two aluminum tubes connected together by a flange. The tubes were sealed at one end by a Teflon flange containing the spark plug, and the other end by a flange and an aluminum endplate. Inside the detonation tube, a spark first created a flame, which

then transitioned to a detonation wave after being accelerated through a Shchelkin spiral. The detonation wave propagated into the thin-walled specimen tube. Pressure transducers mounted on the detonation tube measured the pressure profile and wave speeds. Table 3.2 shows the properties of aluminum 6061-T6.

Property	Value
K_{Ic} (Static)	30 MPa$\sqrt{\text{m}}$
ρ	2780 kg/m^3
E	69 GPa
ν	0.33

Table 3.2: Aluminum 6061-T6 properties.

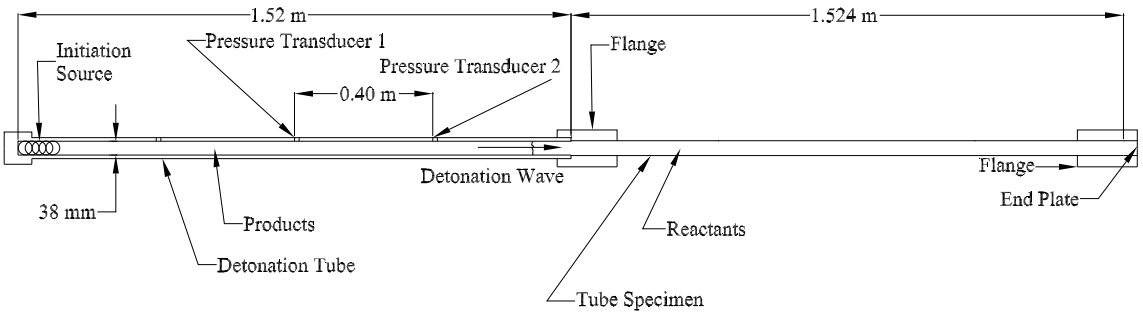

Figure 3.1: Tube assembly schematic for detonation experiment.

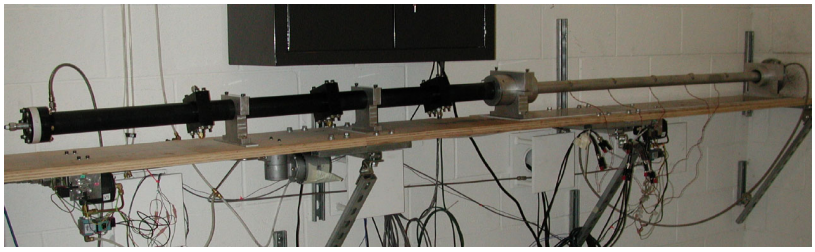

Figure 3.2: Tube assembly for detonation experiment.

3.2.2 Instrumentation

The velocity and pressure of the detonation wave were measured by two PCB piezoelectric pressure transducers. The pressure transducers were mounted 0.406 m apart

in the detonation tube.

Five Micro-Measurements strain gages (CEA-06-032UW-120, gage length = 0.81 mm) were bonded to different locations on the external surface of the tubes to measure circumferential strain. The axial locations of the strain gages measured from the left end of the specimen are shown in Table 3.3. The Trig-Tek amplifiers that amplified the signals from the Wheatstone bridges had a bandwidth of 100 kHz.

Gage	Axial location
SG1	30.38 cm
SG2	53.34 cm
SG3	76.20 cm
SG4	99.06 cm
SG5	121.9 cm

Table 3.3: Strain gage locations on specimen.

3.3 Test Mixture

Stoichiometric hydrogen and oxygen mixtures were used with various amounts of dilution by either nitrogen or helium. These mixtures were chosen to vary the CJ velocity without significantly altering the CJ pressure. Table 3.4 (can be found at the end of this chapter) shows the types of mixtures used and their corresponding parameters. The initial pressure for all these mixtures was 0.1 MPa.

3.4 Finite-Element Simulations

Finite-element simulations were performed to complement every experiment listed in Table 3.4. In addition, three more numerical runs were performed at CJ speeds that were of special interest. They are designated the S1, S2, and S3 runs, and were performed to reveal which CJ speed caused the greatest transverse shear stresses. S2 was computed with the CJ speed equal to the second critical speed of Tang (1965), S3 was computed with the CJ speed equal to the shear speed of aluminum, and S1 was

computed after a trial process to approximately locate the CJ speed for maximum shear amplification.

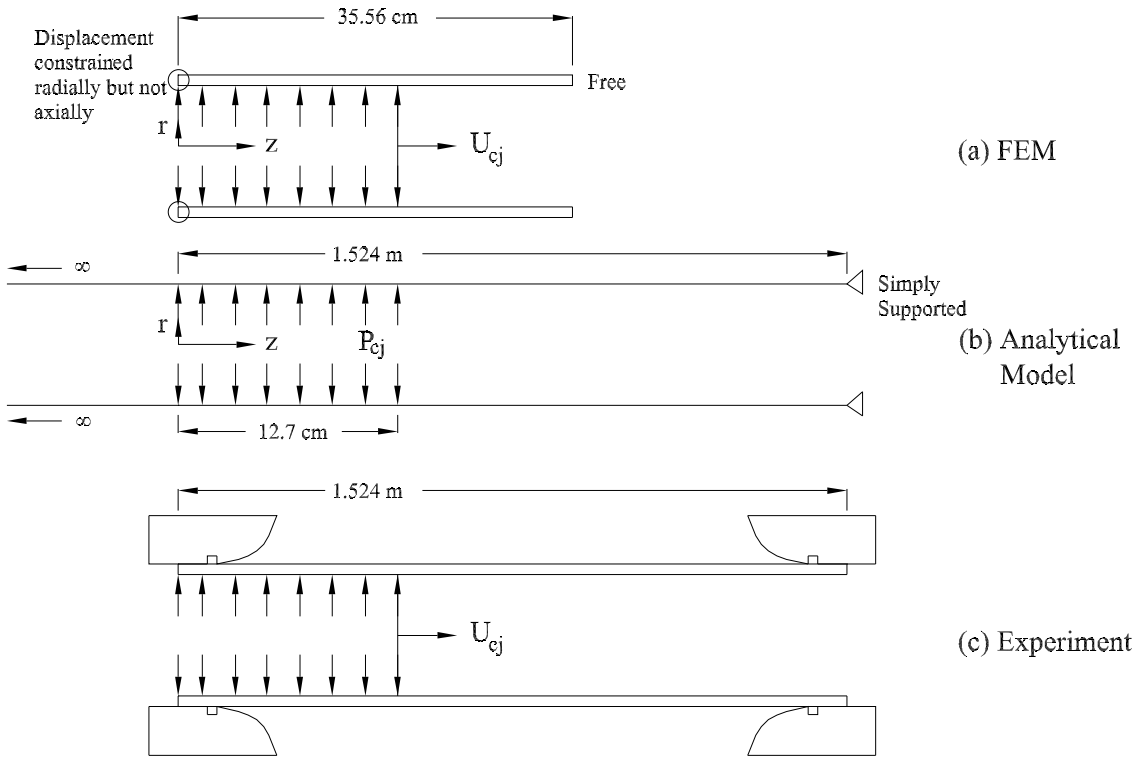

Figure 3.3: Comparison of boundary conditions.

3.4.1 Tube Model

The specimen tube was modeled with axisymmetric solid elements using the commercial explicit finite-element code LS-Dyna V.960. Full integration was used. To decrease computational costs, only 35.56 cm of the tube was modeled. The left end of the tube was simply supported radially but not axially (Fig. 3.3a). Twenty elements were used in the radial direction and 5039 elements in the axial direction. The whole model had 100780 elements. The choice of the large number of elements was made after a trial and error process at resolving the high-frequency shear stresses.

The location for recording stresses was at 12.7 cm from the left end and in the middle of the wall thickness. The location for recording radial displacements was at 12.7

cm from the left end and on the outside diameter of the wall. The choice of 12.7 cm avoided contamination by reflected dilatational waves and eliminated the influence of boundary conditions from the right end throughout the duration of the simulation. A comparison between the simulated and experimental boundary conditions is illustrated in Figs. 3.3a and 3.3c, respectively.

3.4.2 Pressure Distribution

The traveling pressure load model followed the one used in the study by Beltman and Shepherd (2002). The load was prescribed as a function of time at each node. The force history was a discrete version of the exponential approximation to the Taylor-Zeldovich model:

$$P(x,t) = \begin{cases} P_1 & 0 < t < t_{cj}, \\ (P_2 - P_3)\exp(-(t-t_{cj})/T) + P_3 & t_{cj} < t < \infty, \end{cases} \tag{3.1}$$

where t_{cj} is the arrival time of the detonation front, P_1 is the initial pressure, P_2 is the CJ pressure, T is the decay time, and P_3 is the pressure at the end of the expansion wave. Similar to Beltman and Shepherd (2002), P_3 and T were approximated as constants by curve-fitting the pressure trace from the second transducer. These values can be found in Table 3.4. The exponential decay from the CJ point was approximated by 5039 linear segments over 0.11 ms, which was the duration of the simulations. Both the tube mesh and the traveling load were constructed using the pre-processor LS-Ingrid. A comparison between a typical experimental pressure trace and a curve-fit for the FEM is shown in Fig. 3.4.

3.4.3 Mesh Size and Temporal Resolution Considerations

There is currently no model in the literature that can estimate the frequency content of transverse shear stresses for the current experiments. The numerical study first began with coarse meshes and low sampling rates. They were refined until the shear stresses were resolved reasonably well.

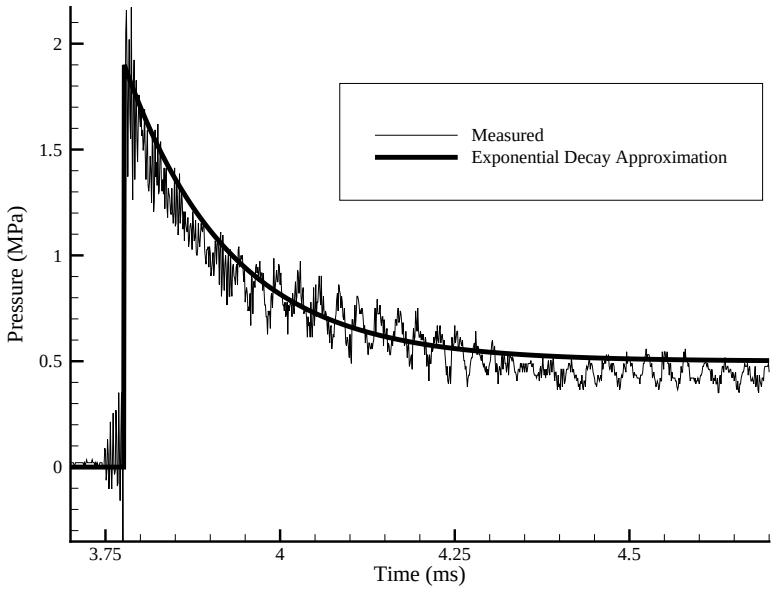

Figure 3.4: Comparison of measured (pressure transducer 2) and approximated pressure profiles for Shot 41. The apparent oscillations in the measured pressure trace were an artifact caused by the structural vibrations of the pressure transducer mounts.

3.4.3.1 Flexural Wavelength Considerations

To begin with, the simulations must be good enough to at least simulate the flexural (breathing mode) waves (in the form of hoop strains) so that they can be compared with the experimental strain signals. An upper bound of the mesh size could be estimated using flexural wavelength. Flexural waves for these experiments ranged from about 37 to 40 kHz, with wavelengths from 55 to 97 mm. Since this was much larger than the wall thickness of 1.5 mm, as long as the mesh size was smaller than the wall thickness, flexural waves could be more than adequately resolved. Note that since the flexural wavelengths were also much larger than the gage length of strain gages (0.81 mm), the experimental hoop strains were also adequately resolved.

3.4.3.2 Detonation Cell Size Considerations

Another way to think about the mesh size is to consider the detonation wave cell size. The detonation wave was modeled in this numerical study as a traveling load. This was a numerically planar front. However, real detonation wave fronts have three-

dimensional transverse disturbances with wavelengths known as the detonation cell size (see Fig. 1.4). For the current mixtures, the smallest cell size was 1.3 mm. This corresponded to a stoichiometric H2+O2 mixture with no dilution. Although these complicated three-dimensional features were not modeled in the loading, the mesh size must be chosen so that in terms of the detonation cell size, the structure was better resolved than the loading.

3.4.3.3 Chosen Resolution

It was found after several trials that considerations of flexural wavelengths and detonation cell sizes were insufficient in resolving transverse shear because higher-frequency components were being discovered as the mesh size went down and sampling rate went up. Down to a mesh size of 71 micron (axial) by 74 micron (radial) and up to a sampling rate of 91 megasample per second, the shear stress traces seemed to have converged, although a rigorous convergence study had not been attempted. At this spatial resolution, the mesh was capable of resolving transverse shear waves with frequency components up to 3.3 MHz traveling at a speed of 3576 m/s (highest in this study) with 15 elements per wavelength. The time step, automatically imposed by LS-Dyna V.960, was 10 ns.

3.4.4 Shear Stress Amplification Factor Scaling

One way to study shear resonance is to use a dynamic amplification factor similar to that used in flexural wave resonance studies. For this purpose, the dynamic shear amplification factor, Φ_s, is defined as:

$$\Phi_s = \frac{\tau_{dynamic}}{\tau_{static}}, \tag{3.2}$$

where $\tau_{dynamic}$ is the maximum dynamic transverse shear stress (acting perpendicular to the z-axis in Fig. 3.3) and τ_{static} is the static equivalent. τ_{static} had to be computed using linearly elastic shell theory. An approximate analytical static model is shown in Fig. 3.3b. It is a semi-infinite tube simply supported at the right end and internally

pressurized from $z = 0$ to $z = 12.7$ cm, where the data for FE analysis were recorded. It is well-known that the form of the equations for this model are the same as those for a semi-infinite beam on an elastic foundation. From the handbook by Young (1989, p.149, case 2), the transverse shear V_s is

$$\begin{aligned} V_s &= -\frac{P}{2\lambda}[(\sin\lambda B - \cos\lambda B)\exp(-\lambda B) - (\sin\lambda A - \cos\lambda A)\exp(-\lambda A)] \\ &\quad \times \cosh(\lambda(B-z))\cos(\lambda(B-z)) \\ &\quad + \frac{P}{2\lambda}[(\sin\lambda B + \cos\lambda B)\exp(-\lambda B) - (\sin\lambda A + \cos\lambda A)\exp(-\lambda A)] \\ &\quad \times \sinh(\lambda(B-z))\sin(\lambda(B-z)) \\ &\quad + \frac{P}{2\lambda}[\cosh\langle B-A-z\rangle \sin\langle B-A-z\rangle \\ &\quad + \sinh\langle B-A-z\rangle \cos\langle B-A-z\rangle \\ &\quad - \cosh\langle B-A-z\rangle \sin\langle B-A-z\rangle \\ &\quad - \sinh\langle B-A-z\rangle \cos\langle B-A-z\rangle], \end{aligned} \tag{3.3}$$

where

$$\langle B-A-z\rangle = \begin{cases} 0, & z > B-A \\ B-A-z, & z < B-A \end{cases} \tag{3.4}$$

and

$$\lambda = \left[\frac{3(1-\nu^2)}{R^2h^2}\right]^{1/4}, \; A = 0.127 \text{ m}, \; B = 1.524 \text{ m}. \tag{3.5}$$

The average shear stress τ_{static} is then

$$\tau = \frac{V_s}{h}. \tag{3.6}$$

The shear stress τ near the loading discontinuity is plotted in Fig. 3.5 for an example case where the internal pressure P was equal to a P_{cj} of 2.0 MPa. The τ_{static} used for normalization was taken to be the maximum τ, which was located at the loading dis-

continuity. This value (recalculated for each P_{cj}) was used to normalize the dynamic shear stresses in Fig. 3.9 (to be discussed in Section 3.5.2).

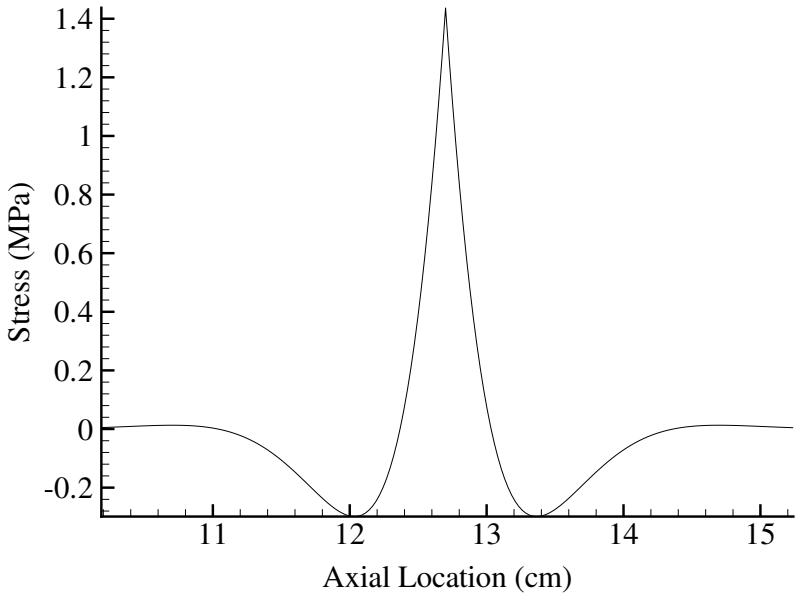

Figure 3.5: Static shear stress for the analytical model (pressure load discontinuity is at 12.7 cm).

3.5 Results and Discussion

3.5.1 Hoop Strain

Hoop strain amplification factors (defined as the ratio of the maximum dynamic hoop strain to the equivalent static hoop strain) close to two were obtained both in the present experiments and simulations. No resonance phenomena in the hoop strain was found near the modified shear wave speed such as that in previous studies for v_{c0} (Beltman et al., 1999, Beltman and Shepherd, 2002). This is consistent with the analytical model of linear elastic tubes under internal traveling load first presented by Tang (1965). Figure 3.6 shows a comparison between the experimental, numerical, and analytical hoop strain dynamic amplification factor. The maximum difference between experiment and simulation was about 24%. On the other hand,

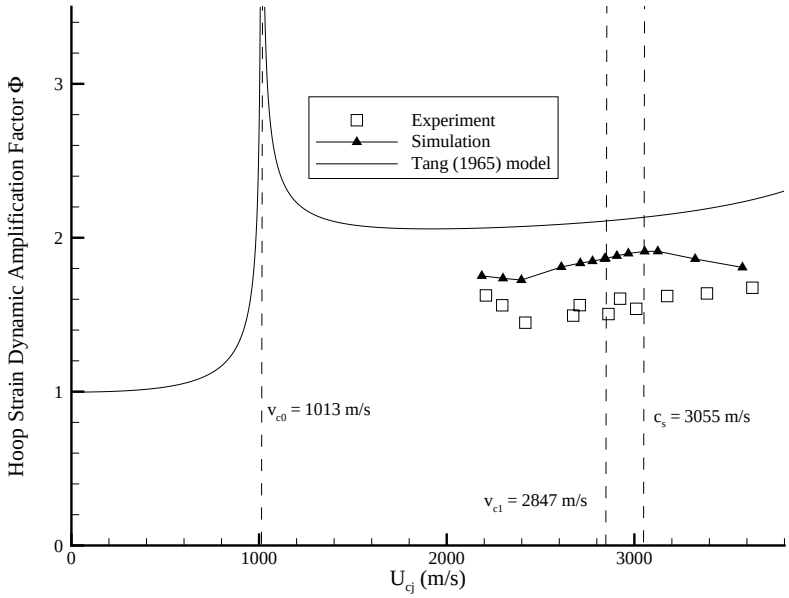

Figure 3.6: Dynamic amplification factor.

the Tang (1965) model differed from the experimental values by as much as 42%. This larger difference is perhaps mainly due to the approximating assumptions of the shell theory used in the steady-state model by Tang (1965). The FEM gave results closer to measurements because it used solid elements instead of shell elements and included transient effects. Moreover, both theory and simulations overestimated the hoop strains probably because no material damping effects were included in these calculations.

Figure 3.7 shows a typical set of measured hoop strain and pressure traces. For this experiment, the CJ speed was 2841 m/s. Although this was very close to the theoretical modified shear wave speed of 2847 m/s, the characteristic behavior of the oscillatory strains did not differ qualitatively from the measured strains of other CJ speeds. Figure 3.8 shows a comparison between measurement and simulation.

3.5.2 Transverse Shear Stress

Transverse shear stresses, on the other hand, showed drastically different behavior as the CJ speed was varied. Since there was no known way of directly measuring

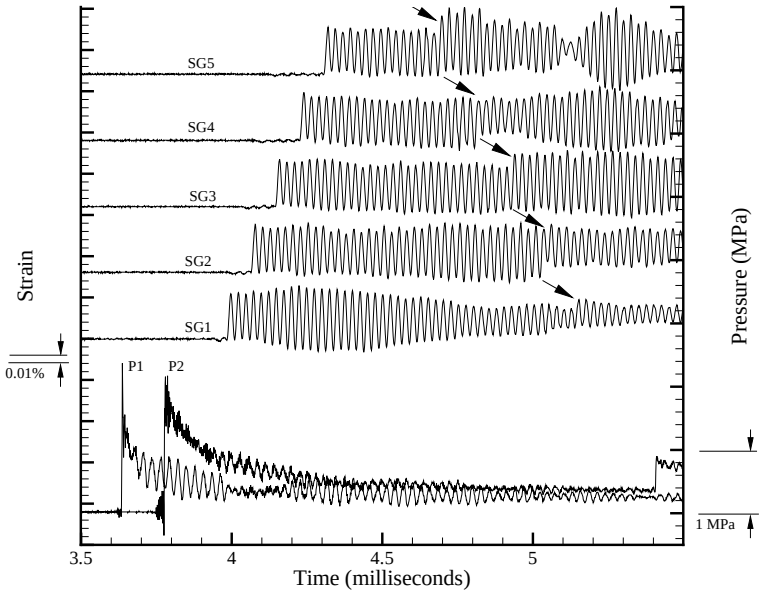

Figure 3.7: Shot 41, U_{cj} = 2841 m/s. Arrows indicate arrival of the shock wave reflected from the end plate. The strains after this reflected shock were disregarded when considering the maximum hoop strain for the dynamic amplification factor.

transverse shear stress and also no known theoretical solution of transverse shear stresses under these loading conditions, only numerical data were available.

The maximum frequencies of these shear stresses were two orders of magnitude higher than those for the hoop strains. Three kinds of behavior can be distinguished from the traces in Fig. 3.10. CJ speeds below that of S1 can be classified into the first type, those between that of S1 to S3 into the second, and those between Shots 45 to 46 into the third. The first and second types had bulk shear disturbances ahead of the traveling load (the circle denotes coincidence with the detonation wave front). The second type is characterized by a spike in shear stress which traveled with the detonation front, whereas in the first type, the tail of the bulk shear disturbance coincided with the detonation front. No bulk shear disturbance was observed to travel faster than c_s, the material shear wave speed, for type one and type two. The arrival time for the waves associated with c_s was 0.0416 ms. When the CJ speed was above c_s, the front of the bulk shear disturbance traveled with the detonation front.

Since all the test runs were performed with approximately the same loading mag-

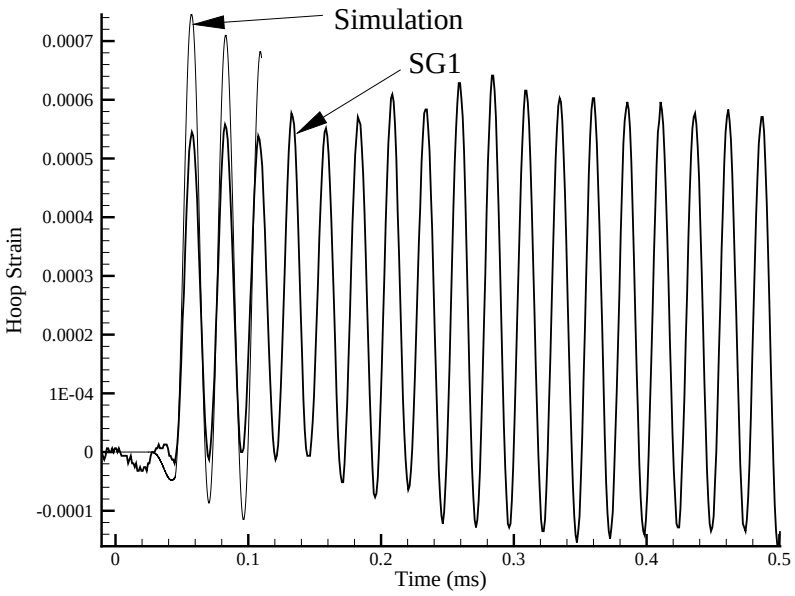

Figure 3.8: Comparison between simulation and experiment for Shot 41, $U_{cj} = 2841$ m/s. SG1 is plotted here because it was closest among all the strain gages to the recording location in the simulation. Simulation terminated at 0.11 ms. SG1 has been time-shifted so that the flexural wave front coincides with the simulated flexural wave front for comparison.

nitude, it is obvious that the group energy of the shear transverse waves had much to do with the speed of the traveling load. The first type certainly carried much more group energy than the other two types.

The dynamic shear amplification factor is shown in Fig. 3.9. It is somewhat reminiscent of the dynamic amplification curve for flexural waves in Fig. 3.6. The value of Φ_s starts from about 2 at Shot 35 and rises to about 4.5 at S1. It then drops to about 0.3 at Shot 44. If S1 is to be interpreted as the second critical speed, then it differs from the Tang (1965) theoretical speed by about 3%.

3.6 Conclusions

It was shown that there is no resonance in hoop strain in the second critical speed. This was verified experimentally and it also agrees with the model by Tang (1965). It has also been shown that shear resonance in the second critical speed did exist numer-

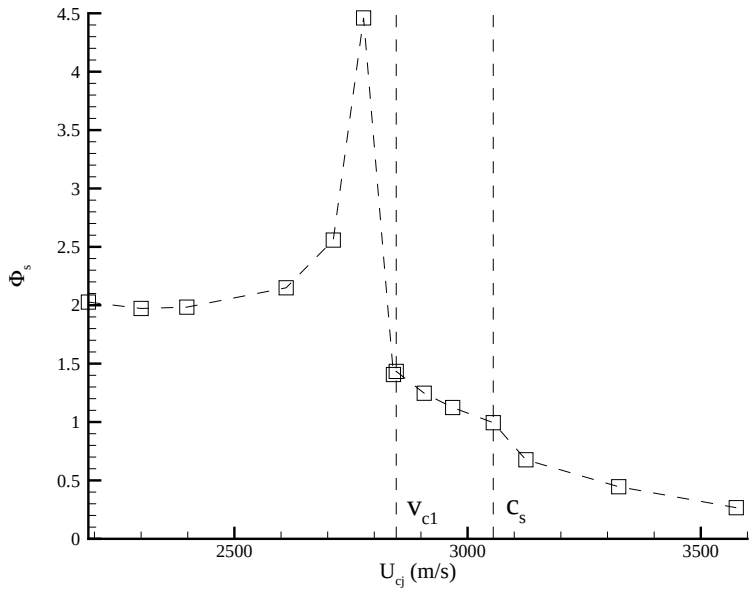

Figure 3.9: Shear amplification factor near the modified shear wave speed.

ically. Computed transverse shear stresses reach 4.5 times that of static equivalent transverse shear stresses. However, there is currently no conceivable way to verify this result experimentally because transverse shear transducers do not exist. Even if one could measure transverse shear, the probes and signal conditioners would have to be able to measure signals with frequency content that are on the order of 1 MHz. Such technical challenges can hopefully be overcome in the future. Since transverse shear stresses are small compared to hoop stresses (for example, the highest computed shear stress was 6 MPa compared to hoop stress of 49 MPa of S1), it is unlikely that plain tubes will fail in shear due to shear resonance. However, for tubes with other geometries and shear stress concentrators such as joints, elbows, notches, surface cracks, and interfacial cracks, transverse shear amplification may play a significant role in the design and hazard analysis of detonation tubes.

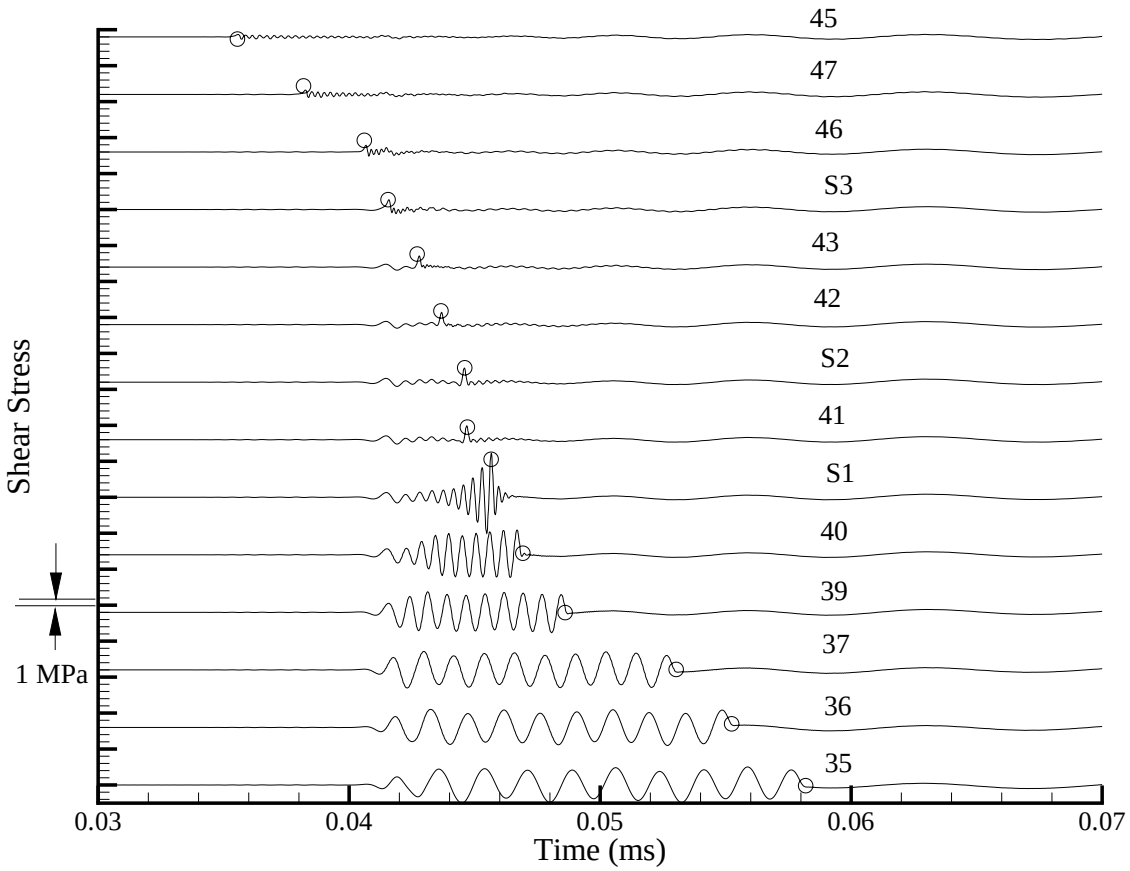

Figure 3.10: Transverse shear stress from simulations for different shots. Circles denote the detonation wave front.

Shot	Mixture	n	Stanjan U_{cj} (m/s)	Measured U_{cj} (m/s)	Stanjan P_{cj} (MPa)	Stanjan U_{refl} (m/s)	Curve-fit Parameters P_3 (MPa)	T (ms)
35	H2+0.5O2+nN2	1.0	2187	2209	1.72	850	0.5	0.15
36	H2+0.5O2+nN2	0.7	2300	2296	1.77	888	0.5	0.15
37	H2+0.5O2+nN2	0.5	2398	2419	1.80	923	0.5	0.15
39	H2+0.5O2+nN2	0.2	2611	2674	1.85	1000	0.5	0.15
40	H2+0.5O2+nN2	0.1	2712	2709	1.87	1037	0.5	0.15
S1	Simulation only	n/a	2777	n/a	1.90	n/a	n/a	n/a
41	H2+0.5O2+nHE	0.0	2841	2862	1.90	1087	0.5	0.15
S2	Simulation only	n/a	2847	n/a	1.90	n/a	0.5	0.15
42	H2+0.5O2+nHE	0.1	2907	2924	1.90	1115	0.5	0.15
43	H2+0.5O2+nHE	0.2	2968	3010	1.90	1142	0.5	0.15
S3	Simulation only	n/a	3055	n/a	1.90	n/a	0.5	0.15
46	H2+0.5O2+nHE	0.5	3125	3175	1.90	1212	0.5	0.15
47	H2+0.5O2+nHE	1.0	3324	3387	1.88	1306	0.5	0.10
45	H2+0.5O2+nHE	2.0	3576	3629	1.82	1440	0.5	0.10
44	H2+0.5O2+nHE	3.0	No Go	No Go	No Go	No Go	No Go	No Go

Table 3.4: Test matrix.

Chapter 4

Fracture Response without Applied Prestress

4.1 Introduction

This chapter[1] presents results from the first batch of detonation-driven fracture experiments. Since the specimens were not deliberately prestressed by any loading device, the cracks ran according to the stress-fields set up by the detonation wave and the boundary conditions of the tube assembly. The experiments in this chapter involve six aspects. The first is the qualitative behavior of the crack path of a fractured tube as a function of initial flaw length. The second deals with the quantitative measurements of strain history on the rupturing tube. The third is an estimate of the fracture threshold, which is of engineering value in determining what the residual strength of a tube will be if it is flawed. The fracture threshold divides a non-dimensional parametrized test space into rupture (i.e., surface notch becoming a through-wall crack) and no rupture zones. Given a detonation wave of certain magnitude and a flaw of certain size, one can use this threshold model to estimate whether a surface flaw will break through the wall. The fourth aspect concerns how crack branching could be related to the direction of propagation of a detonation wave. The fifth aspect studies the influence of static prestress on the crack curving direction. The sixth deals with the extent of the influence of the rupture event on the detonation wave.

[1] This chapter has been submitted as a paper to the International Journal of Fracture.

4.2 Analytical Models

There is currently no analytical model in the literature that can predict the burst pressure of an initially-flawed detonation tube. The motivation to predict the burst pressure is relevant to industrial applications and the present experiments. If a pressure vessel or pipe is flawed and is expected to withstand a detonation load, it is important to know its residual strength. In the present experiments, knowing the burst pressure or critical flaw size lets us predict which specimens will rupture and instrument them accordingly.

Two important aspects of the fracture threshold model are taken into account. The first consideration is Φ, the dynamic amplification factor that determines strain amplitude as a function of the speed of the traveling load. The dynamic amplification factor was discussed in Section 1.3.2. The second consideration is the stress intensity factor of a partially-through-wall cracked specimen. A static stress intensity factor is used because there is no existing dynamic derivation for traveling loads. Therefore, the only parameter that accounts for the dynamic effect is Φ, the dynamic amplification factor. Although this threshold model may be oversimplified, it can be compared to experimental data to ascertain its usefulness.

4.2.1 A Simple Fracture Threshold Model for Detonation Tubes

In linear elastic fracture mechanics, mode-I fracture initiates when the stress intensity factor K_I reaches the fracture toughness K_{Ic}. Since currently there is no analytical model for the dynamic stress intensity factor for a detonation tube with an external axial flaw, the well-known static relations will be used to estimate the stress intensity factor in our simplified model. To account for the dynamic strains, a dynamic amplification factor due to flexural wave excitation (see Section 2.1) was incorporated in this threshold model. 'Rupture' is identified with the notch breaking into a through-wall crack, and for simplification, it is assumed to be synonymous with K_I reaching K_{Ic} at the notch front.

The static model is based on the assumption that a thin-wall tube with an external axial notch under internal pressure can be treated, neglecting curvature, as a wide plate with a surface crack under far-field tension (Fig. 4.1). The following results of static three-dimensional finite-element analysis of a wide plate with a surface crack by Newman and Raju (1981) will be used:

$$K_I = \sigma\sqrt{\frac{\pi d}{Q}}H \tag{4.1}$$

where

$$H = M_1 + M_2\left(\frac{d}{h}\right)^2 + M_3\left(\frac{d}{h}\right)^4 , \tag{4.2}$$

$$Q = 1 + 1.464\left(\frac{d}{a}\right)^{1.65} , \tag{4.3}$$

and

$$M_1 = 1.13 - 0.09\left(\frac{d}{a}\right) , \tag{4.4}$$

$$M_2 = \frac{0.89}{\left[0.2 + \left(\frac{d}{a}\right)\right]} - 0.54 , \tag{4.5}$$

$$M_3 = 0.5 - \frac{1.0}{\left[0.65 + \left(\frac{d}{a}\right)\right]} + 14\left[1.0 - \left(\frac{d}{a}\right)\right]^{24} . \tag{4.6}$$

The K_I defined above describes the stress intensity at the deepest point of penetration for small values of d/a. The fracture condition is identified with

$$K_I = \sigma\sqrt{\frac{\pi d}{Q}}H \geq K_{Ic} . \tag{4.7}$$

Substituting $\sigma = \sigma_{dynamic\_max} = \Phi\Delta pR/h$ and rearranging, the rupture criterion is

$$\frac{\Phi\Delta pR\sqrt{\pi d}}{hK_{Ic}} \geq \frac{\sqrt{Q}}{H} \tag{4.8}$$

where Δp is the pressure difference across the shell. The right-hand side of this equation is plotted as a surface in Fig. 4.3. This surface divides the parameter space into a rupture regime above the surface and non-rupture regime below the surface.

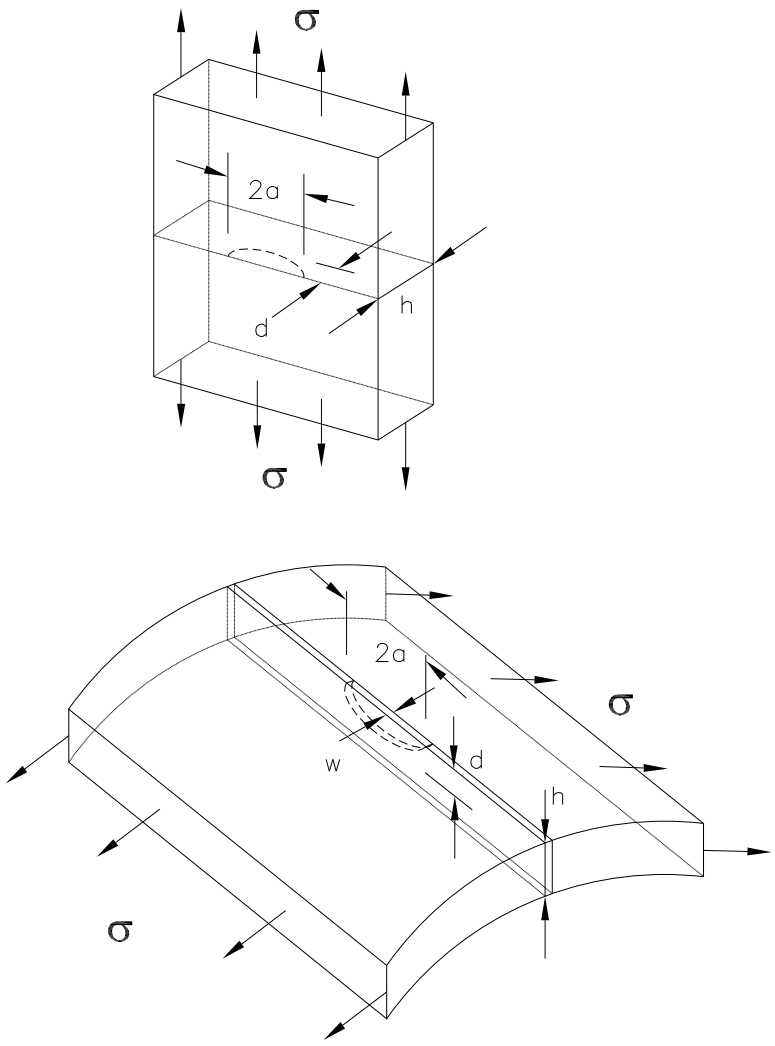

Figure 4.1: Flat plate model with mathematically sharp crack assumed by Newman and Raju (1981), above, compared to the tubes' actual surface notch with finite width w, below.

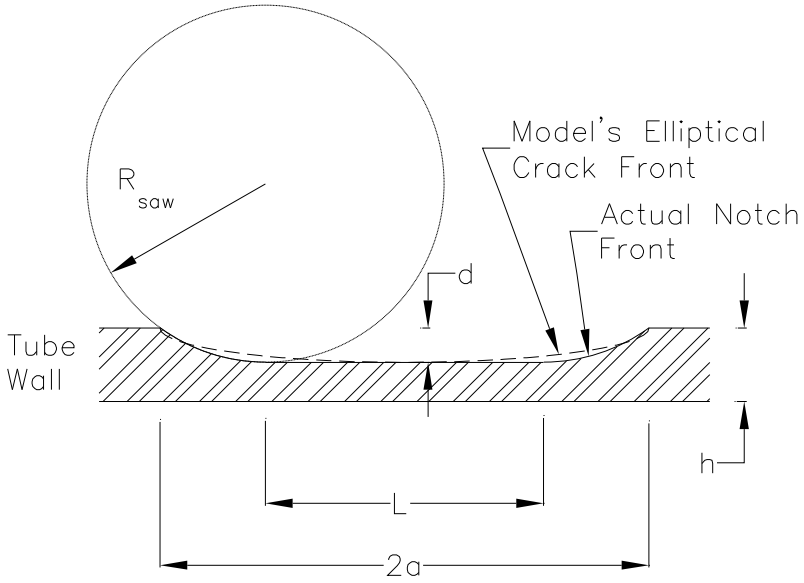

Figure 4.2: Flaw geometry.

4.3 Experimental Setup

4.3.1 Specimens

Two sets of experiments were performed on aluminum 6061-T6 tubes. In the first set, the notch depth (0.56 mm), notch width (0.3 mm), and tube size (0.89 mm in wall thickness, 41.28 mm in outer diameter, 0.914 m long) were kept constant for studying the fracture behavior by changing only the notch length (from 12.7 mm to 76.2 mm). The surface notch was oriented axially, located in the middle of the tube length, and cut by a CNC machine using a jeweler's slotting saw.

The second set was performed with shorter tubes (0.610 m) of the same outer diameter (41.28 mm), various flaw depth, flaw length, and wall thickness. The dimensions can be found in Tables 4.1 and 4.2.

Since the actual notch geometry (Figs. 4.1 and 4.2) was different from the elliptical crack geometry assumed by Newman and Raju (1981), an approximation was used to relate the model crack length, $2a$, and the 'actual' crack length, L, used in machining

$$2a = L + 2\sqrt{R_{saw}^2 - (R_{saw} - d)^2}\,, \tag{4.9}$$

Shot	d (mm)	w (mm)	L (mm)	$2a$ (mm)	$2R_{saw}$ (mm)	h (mm)	U_{cj} (m/s)	P_{cj} (MPa)	Fracture Behavior
2	0.56	0.3	76.2	85.4	38.1	0.89	2404	6.1	Forward bifurcation and backward curving
3	0.56	0.3	76.2	85.4	38.1	0.89	2404	6.1	Forward and backward bifurcation
4	0.56	0.3	25.4	34.6	38.1	0.89	2404	6.1	Forward straight (short) and backward curving
5	0.56	0.3	12.7	21.9	38.1	0.89	2404	6.1	Forward and backward curving
6	0.56	0.3	50.8	60.0	38.1	0.89	2404	6.1	Forward bifurcation and backward curving
7	0.56	0.3	50.8	60.0	38.1	0.89	2404	6.1	Forward bifurcation and backward curving
9	0.91	0.2	12.7	24.4	38.1	1.47	2351	2.0	No rupture
10	0.79	0.2	12.7	23.5	38.1	1.24	2370	3.0	No rupture
11	0.56	0.2	12.7	21.9	38.1	0.89	2384	4.0	No rupture
12	0.56	0.2	19.1	28.2	38.1	0.89	2384	4.0	No rupture
13	0.56	0.2	25.4	34.6	38.1	0.89	2384	4.0	No rupture
14	0.56	0.2	38.1	47.3	38.1	0.89	2395	5.1	Forward and backward curving
15	0.56	0.2	50.8	60.0	38.1	0.89	2384	4.0	No rupture
16	0.48	0.2	25.4	33.9	38.1	0.89	2399	5.4	Forward and backward curving
17	0.48	0.2	25.4	33.9	38.1	0.89	2388	4.4	No rupture
18	1.19	0.2	25.4	38.7	38.1	1.47	2388	4.4	No rupture
19	1.19	0.2	25.4	38.7	38.1	1.47	2388	4.4	No rupture
24	0.56	0.2	76.2	85.4	38.1	0.89	2404	6.1	Forward bifurcation and backward curving
25	0.71	0.2	25.4	35.7	38.1	1.24	2394	4.9	No rupture
26	0.71	0.2	25.4	35.7	38.1	1.24	2404	6.1	No rupture
28	0.84	0.2	25.4	36.6	38.1	1.24	2404	6.1	No rupture

Table 4.1: Test matrix. Shots 2 to 7 have tube lengths of 0.914 m, and those of Shots 9 to 118 are 0.610 m.

Shot	d (mm)	w (mm)	L (mm)	$2a$ (mm)	$2R_{saw}$ (mm)	h (mm)	U_{cj} (m/s)	P_{cj} (MPa)	Fracture Behavior
29	0.71	0.2	25.4	35.7	38.1	0.89	2376	3.3	Forward and backward curving
30	0.64	0.2	25.4	35.2	38.1	0.89	2384	4.0	Crack confined within notch
31	0.64	0.2	25.4	35.2	38.1	0.89	2365	2.6	No rupture
32	1.19	0.2	25.4	38.7	38.1	1.47	2404	6.1	No rupture
33	n/a	n/a	n/a	n/a	n/a	0.89	2365	2.6	No rupture, elastic strains
34	0.64	0.2	25.4	35.2	38.1	0.89	2404	6.1	Forward and backward curving
48	n/a	n/a	n/a	n/a	n/a	0.89	2365	2.6	Dynamic axisymmetry validation (0°)
49	n/a	n/a	n/a	n/a	n/a	0.89	2365	2.6	Dynamic axisymmetry validation (90°)
50	n/a	n/a	n/a	n/a	n/a	0.89	2365	2.6	Dynamic axisymmetry validation (180°)
51	n/a	n/a	n/a	n/a	n/a	0.89	2365	2.6	Dynamic axisymmetry validation (270°)
54	0.56	0.2	50.8	60.0	38.1	0.89	2404	6.1	Forward bifurcation and backward curving
90	0.56	0.2	25.4	37.8	69.9	0.89	2404	6.1	Forward and backward curving
108	1.16	0.2	25.4	43.4	69.9	1.47	2404	6.1	No rupture
109	0.56	0.2	25.4	37.8	69.9	0.89	2404	6.1	Forward and backward curving
110	0.56	0.2	25.4	37.8	69.9	0.89	2404	6.1	Forward and backward curving
113	0.56	0.2	25.4	37.8	69.9	0.89	2404	6.1	Forward and backward curving
114	0.56	0.2	25.4	37.8	69.9	0.89	2404	6.1	Forward and backward curving
115	0.56	0.2	25.4	37.8	69.9	0.89	2404	6.1	Forward bifurcation and backward curving
116	0.56	0.2	25.4	37.8	69.9	0.89	2404	6.1	Forward and backward curving
117	0.56	0.2	25.4	37.8	69.9	0.89	2404	6.1	Forward bifurcation and backward curving
118	0.56	0.2	25.4	37.8	69.9	0.89	2404	6.1	Forward bifurcation and backward curving

Table 4.2: Test matrix (continued).

where R_{saw} is the radius of the jeweler's slotting saw.

4.3.2 Detonation Tube Assembly

The experimental setup evolved during the course of the experimental study. There were two sets of experiments with two different specimen lengths. Figures 4.4 and 4.5 show a schematic and a photograph, respectively, of the experimental setup for the first set of experiments with 0.914-m long specimen tubes. The setup consisted of two aluminum tubes connected together by a flange. The tubes were sealed at one end by a Teflon flange containing the spark plug, and the other end by a flange and a Mylar diaphragm. Inside the detonation tube, a spark first created a flame, which then transitioned to a detonation wave after being accelerated through a Shchelkin spiral. The detonation wave propagated into the thin-wall and preflawed specimen tube. The Mylar diaphragm burst each time so that the effects of a reflected shock wave were minimized. Pressure transducers mounted on the detonation tube measured the pressure profile and wave speeds.

For the second set of tests with 0.610-m long tubes, an additional thick-wall extension tube with pressure transducers was connected by a flange to the aft end of the specimen tube. The pressure transducers were used to study the effects of rupture on the detonation wave. Figures 4.6 and 4.7 show a schematic and a photograph, respectively, of the experimental setup for the second set of experiments.

4.3.3 Instrumentation

The velocity and pressure of the detonation wave were measured by PCB piezo-electric pressure transducers. The pressure transducers were mounted 0.40 m apart in the detonation tube. The extension tube with additional pressure transducers was used only for the second set of experiments with 0.610-m long tubes.

Micro-Measurements strain gages were bonded to different locations on the external surface of the tubes to measure circumferential strain. The Trig-Tek amplifiers that amplified the signals from the Wheatstone bridges had a bandwidth of 100 kHz.

The spark and data acquisition system was triggered by a Stanford Research Systems digital pulse generator. Both the pressure traces and the strain history were digitized with Tektronix oscilloscopes at a rate of 1 MHz. The data were transferred into a computer through a LabVIEW program.

4.4 Results and Discussion

4.4.1 Crack Propagation Behavior As a Function of Initial Flaw Length

For the first set of experiments, all parameters except one were fixed. The flaw length L was varied and different fracture behaviors were observed. The CJ pressure, P_{cj}, and CJ velocity, U_{cj}, were nominally 6.1 MPa and 2.4 km/s, respectively. The mixture was stoichiometric ethylene-oxygen at an initial pressure of 1.8 bar and room temperature. Figure 4.8 shows a typical pressure signal.

Due to noise, the three-dimensional structure of the detonation wave front, and the finite size of the pressure transducer, the pressure peak recorded by the pressure transducer is not reliable as an average value for computing structural loads. It is generally recognized in the gaseous detonation literature that for loading computations, computed values instead are more dependable. The CJ velocity and pressure of each experiment were calculated with the STANJAN program of Reynolds (1986). The computed values depend on the initial thermodynamic conditions, and the initial temperature was taken to be 300 K in the computations although minor variations in this occurred between tests. A statistical analysis on the variation of U_{cj} showed that for 20 experiments which had identical initial thermodynamic conditions and a STANJAN U_{cj} of 2.40 km/s, the measured mean was 2.35 km/s with a standard deviation of 0.01 km/s.

Figures 4.9 to 4.12 show tubes of different notch lengths after fracture. The detonation wave traveled from left to right. As the wave propagated past the surface notch, the hoop stress opened the notch into a through-wall crack. Two crack fronts

then propagated–one in the forward (i.e., same direction as the detonation wave) and one in the backward direction (i.e., in the opposite direction as the detonation wave). We will refer to these two crack fronts simply as the "forward" and "backward" cracks.

Different fracture behavior was observed for the various notch lengths. For the L = 12.7 mm and L = 25.4 mm specimens (Fig. 4.9 and Fig. 4.10, respectively), both the forward and backward cracks propagated straight for some distance, then turned, ran helically around the tube, and were arrested. As the notch length increased, the cracks propagated further and severed the tube into two or three parts. Figure 4.11 displays a fractured 50.8 mm notch specimen. The backward crack behaved similarly to those of previous specimens, but the forward crack propagated straight for only a short distance and bifurcated. The two branch cracks then ran around the tube and met on the other side, cutting the tube in two. The L = 76.2 mm notch specimen (Fig. 4.12) resulted in bifurcation of both the forward and backward cracks, cutting the tube into three pieces. The middle piece was plastically deformed until it was bent inside-out.

4.4.1.1 Repeatability of Bifurcated Crack Paths

Another experiment on an L = 50.8 mm specimen was conducted to demonstrate repeatability. Figure 4.13 shows the resemblance of the forward bifurcated crack paths of two L = 50.8 mm specimens. Both specimens also exhibited similar helical and arrest behavior for the backward crack.

4.4.1.2 Sharp Turns for Branching Cracks vs. Smooth Turns for Single Curving Cracks

While bifurcated cracks tend to turn sharply with a very small turn radius (Fig. 4.14), single helical cracks tend to turn smoothly with a large turn radius. Cracks that bifurcated traveled straight for relatively short distances after leaving the notch tip before turning sharply. Cracks that did not bifurcate traveled straight for longer distances before turning smoothly.

4.4.1.3 Bifurcation "Favoring" the Forward Crack

Figure 4.15 shows cases for different tube lengths and initial flaw sizes, in which the forward cracks bifurcated and the backward cracks curved but did not branch. In these shots, the CJ pressures and detonation speeds were nominally held constant at 6.1 MPa and 2.4 km/s, respectively. These cases are interesting because this kind of asymmetry has not been observed the other way. That is, there has not been a single case in which the backward crack bifurcated and the forward crack did not branch. Crack bifurcation "favoring" the forward crack is perhaps due to the asymmetric profile of the traveling detonation load, which caused the forward crack to have a higher stress intensity.

4.4.1.4 Critical Crack Length for Bifurcation

Crack branching occurs because there is a sufficient energy release rate to support additional cracks. Since the energy release rate scales with the crack length, a valid question is whether or not there is a characteristic crack length for branching to occur. The distance a' between the forward notch tip and the forward bifurcation point was measured for several shots and the measurements are shown in Tables 4.3 and 4.4. In these shots, the CJ pressure and detonation speeds were nominally held constant at 6.1 MPa and 2.4 km/s, respectively. A reasonable choice for the characteristic crack length for branching is the sum of the half-notch length and bifurcation distance, $a+a'$, because it is a figure of merit for scaling the forward crack's energy release rate. The 0.914-m long specimens and 0.610-m specimens have to be analyzed separately because they contained different explosive mass and different energy content. The average critical bifurcation crack length was found to be 60 mm for the 0.914-m long specimens and 79 mm for the 0.610-m long specimens.

4.4.1.5 Crack Length for Non-Bifurcating Curved Cracks

Table 4.5 shows the distance between the notch tip to the arrested crack tip for shots that did not exhibit crack branching. No clear correlation has been found

Shot	$2a(mm)$	a' (mm)	$a + a'$ (mm)
2	85	24	67
3	85	22	65
6	60	21	51
7	60	29	59
Mean			60
Average of absolute deviation from mean			5

Table 4.3: Critical crack lengths for bifurcation for 0.914-m long tubes.

Shot	$2a(mm)$	a' (mm)	$a + a'$ (mm)
24	85	32	75
54	60	38	68
115	38	64	83
116	38	58	77
117	38	69	88
118	38	63	82
Mean			79
Average of absolute deviation from mean			6

Table 4.4: Critical crack lengths for bifurcation for 0.610-m long tubes.

amongst variables such as the stress intensity factor (based on the dynamic hoop stress and initial notch length), detonation pressure, initial notch length, and final crack length. Even for shots with apparently identical conditions (90, 113, 114), the crack length was not reproducible. It is suspected that uncontrolled variables such as prestress induced by tube misalignment and also dimensional and material variation between individual tubes were responsible for the apparent lack of correlation and reproducibility. The tubes were not all from the same lot of material. The outer diameter had an uncertainty of $\pm$ 0.3 mm, and the wall thickness had an uncertainty of $\pm$ 0.09 mm.

4.4.2 Strain Response

Just as the fracture behavior was studied by keeping all parameters constant except the notch length, the hoop strains near the notch were examined by keeping everything fixed except the pressure loading. Figure 4.16 shows the strains for three different specimens with the same tube and notch geometry but different detonation pressures

					Notch tip to crack tip distance	
	d	$2a$	l	P_{cj}	Backward	Forward
Shot	(mm)	(mm)	(m)	(MPa)	(cm)	(cm)
4	0.56	34.6	0.914	6.1	17.0	14.8
5	0.56	21.9	0.914	6.1	16.8	22.4
14	0.56	47.3	0.610	5.1	21.9	24.5
16	0.48	33.9	0.610	5.4	23.0	24.8
29	0.71	35.7	0.610	3.3	12.3	12.7
34	0.64	35.2	0.610	6.1	18.6	22.7
90	0.56	37.8	0.610	6.1	18.7	22.7
113	0.56	37.8	0.610	6.1	12.5	16.5
114	0.56	37.8	0.610	6.1	10.7	13.4

Table 4.5: Length of non-bifurcating curved cracks. All shots listed here have wall thickness $h = 0.89$ mm.

(Shots 30, 31, and 34). As a control experiment, an identical tube with no notch and undergoing only elastic deformation was also tested (Shot 33). Time $t = 3$ ms corresponded to the spark used to initiate detonation. Six strain gages were placed near the notch; their locations are shown in Fig. 4.17. Four of these were aligned with the notch, one was 90° from the notch, and one was 180°. Figure 4.18 shows a schematic of the crack propagation direction for Shot 24 and Fig. 4.19 shows a corresponding photograph. The strain rates ranged from 10^2 s^{-1} to 10^3 s^{-1}.

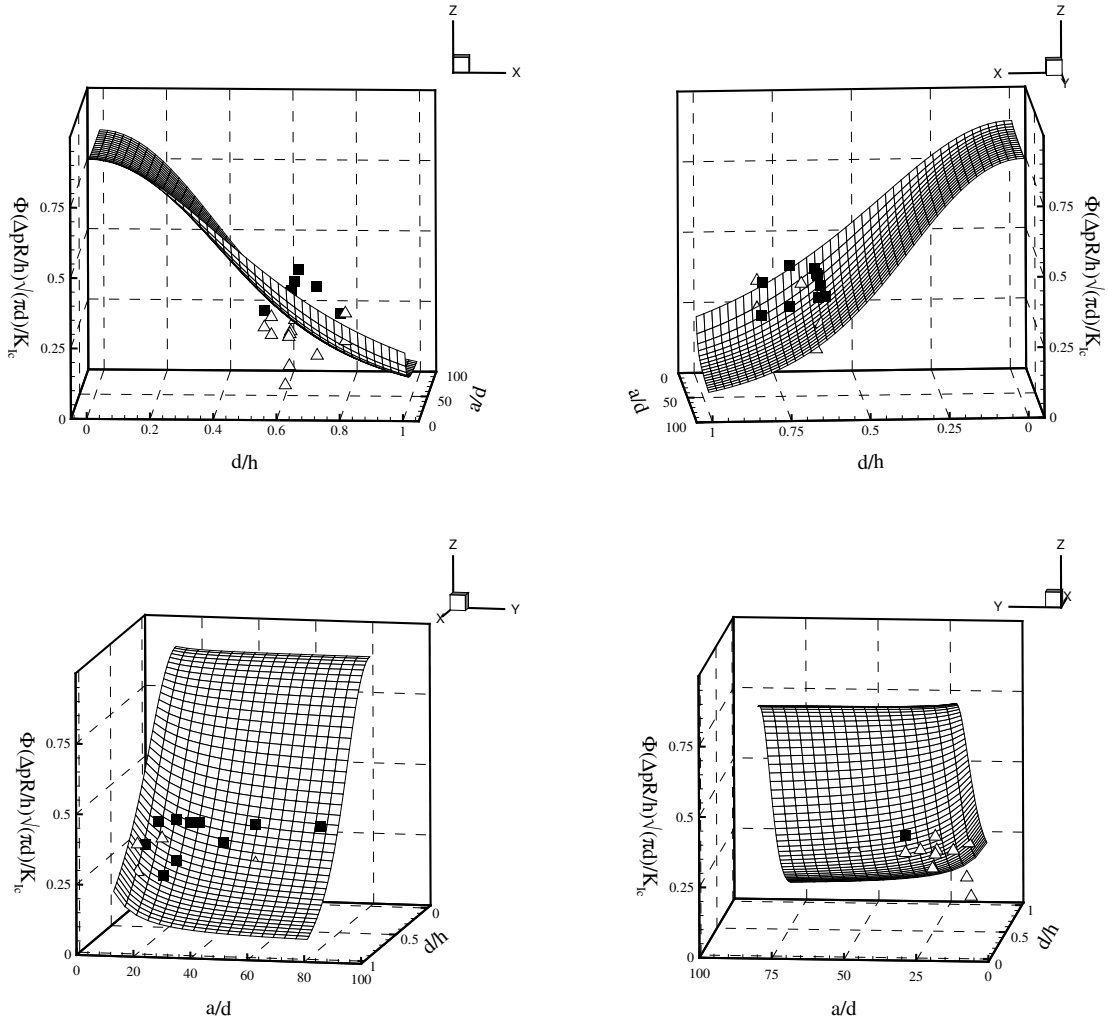

Figure 4.3: Different perspective views of the fracture threshold. The surface divides the space into theoretical rupture (above) and no rupture regimes (below) according to Eq. 4.8. Experimental data are presented as filled squares for ruptured tubes and open triangles for intact tubes.

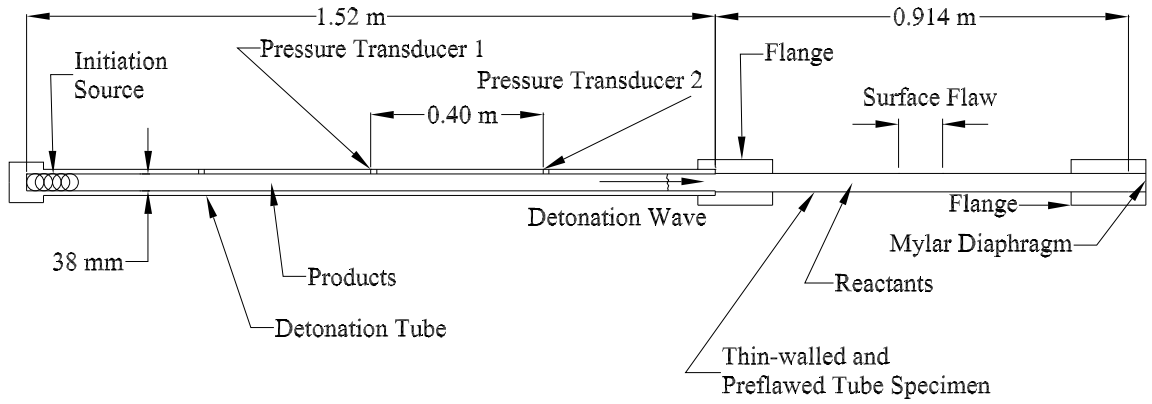

Figure 4.4: First tube assembly with 0.914-m long specimen.

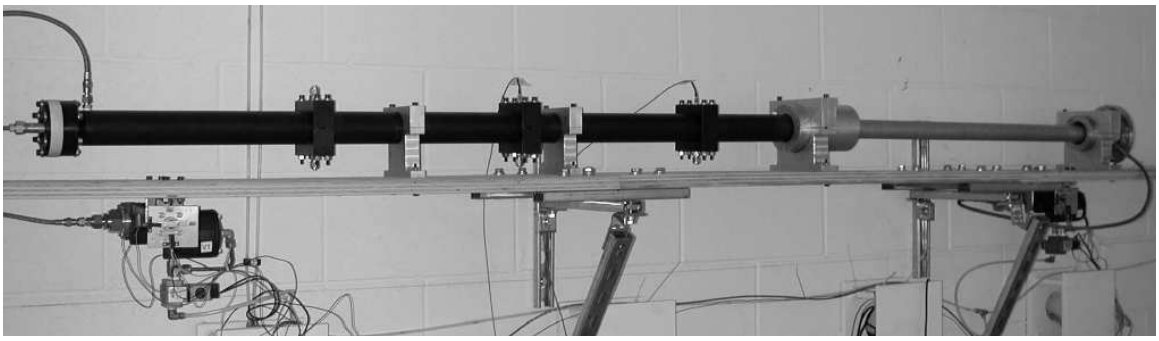

Figure 4.5: First tube assembly with 0.914-m long specimen.

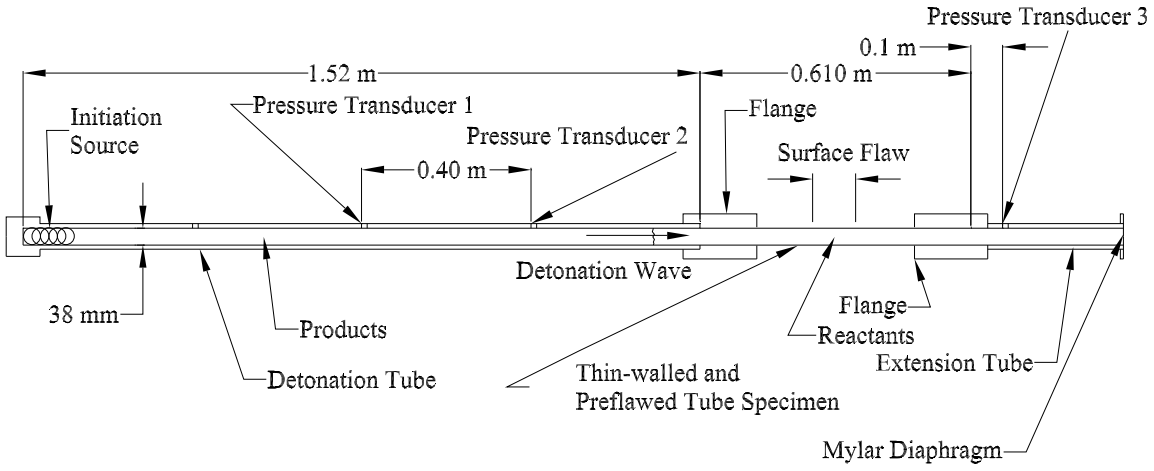

Figure 4.6: Second tube assembly with 0.610-m long specimen and a 0.305 m extension tube.

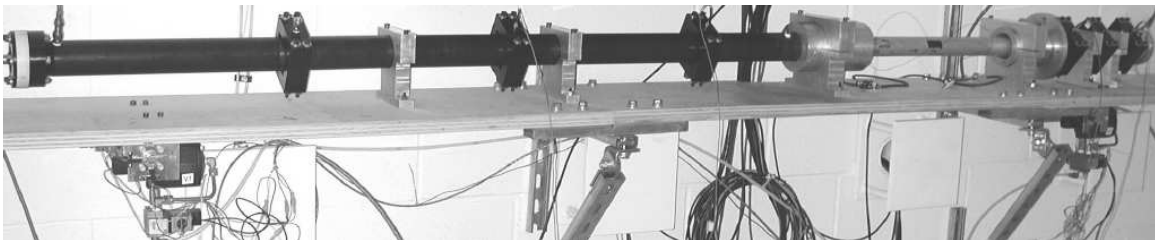

Figure 4.7: Second tube assembly with 0.610-m long specimen and a 0.305 m extension tube.

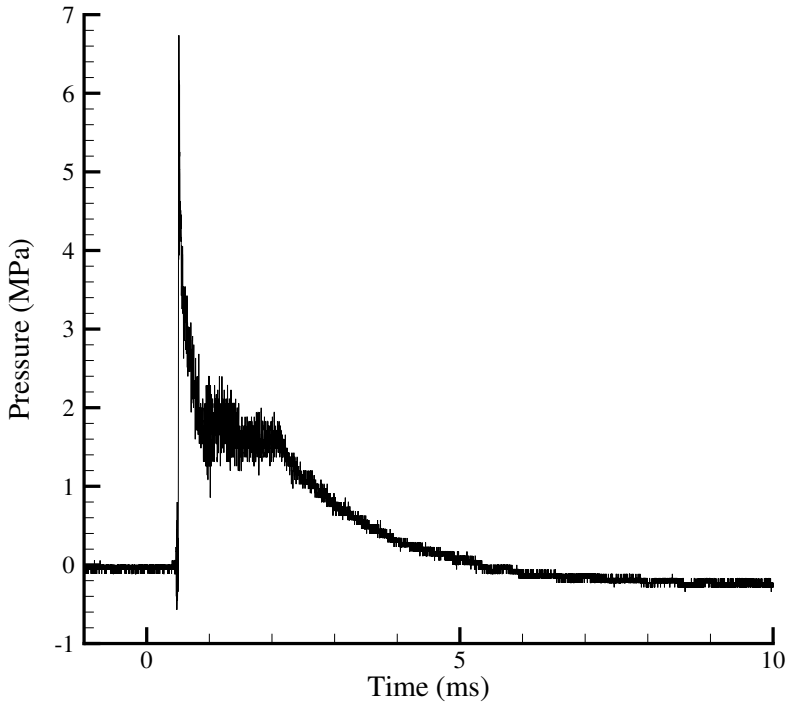

Figure 4.8: Typical detonation pressure trace recorded by the piezo-electric pressure transducer in the detonation tube.

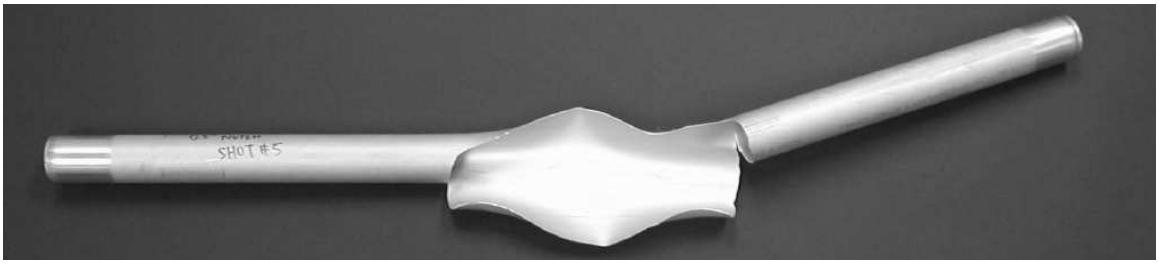

Figure 4.9: Ruptured tube with initial $L = 12.7$ mm notch (Shot 5).

Figure 4.10: Ruptured tube with initial $L = 25.4$ mm notch (Shot 4).

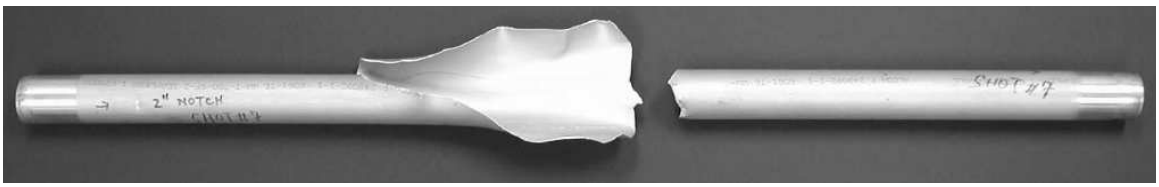

Figure 4.11: Ruptured tube with initial $L = 50.8$ mm notch (Shot 7).

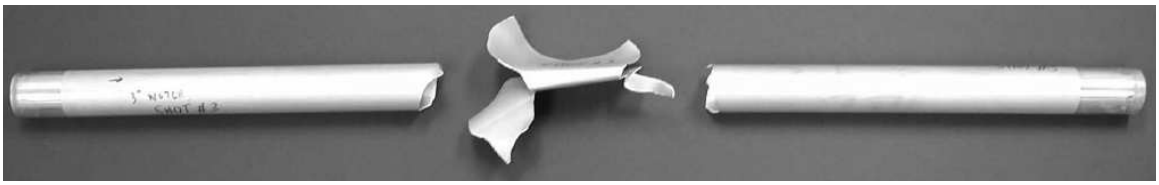

Figure 4.12: Ruptured tube with initial $L = 76.2$ mm notch (Shot 3).

Figure 4.13: Resemblance of the forward bifurcated crack paths of two $L = 50.8$ mm notch specimens. The repeated experiments were run to demonstrate reproducibility (Shot 7 on the left and Shot 6 on the right).

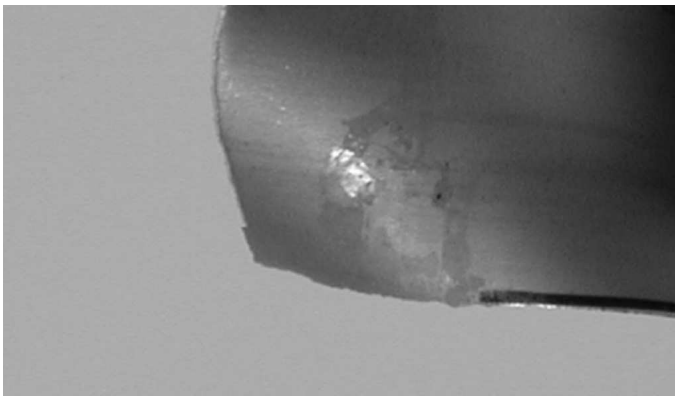

Figure 4.14: Sharp turn from a bifurcated crack. Darkened edge at the lower right indicates location of the initial notch. This branch of the crack traveled from right to left and then upwards.

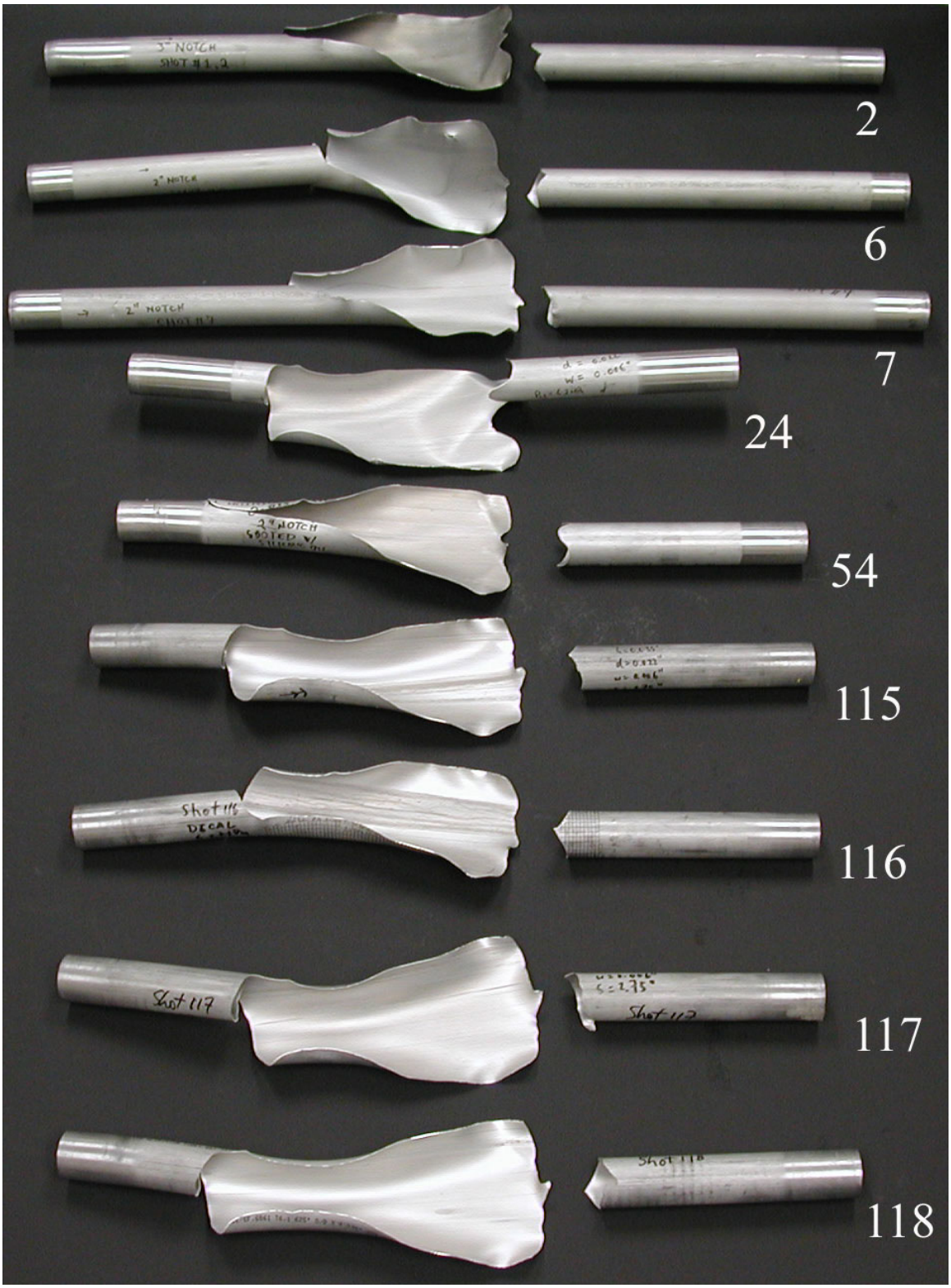

Figure 4.15: Post-test specimens with forward cracks bifurcating and single backward cracks curving, but never with forward single crack curving and backward crack bifurcating. This shows bifurcation favoring the forward crack. The detonation wave ran from left to right. Numbers denote shot numbers. CJ pressures and detonation speeds were nominally held constant at 6.1 MPa and 2.4 km/s, respectively. Refer to the test matrix for other shot conditions.

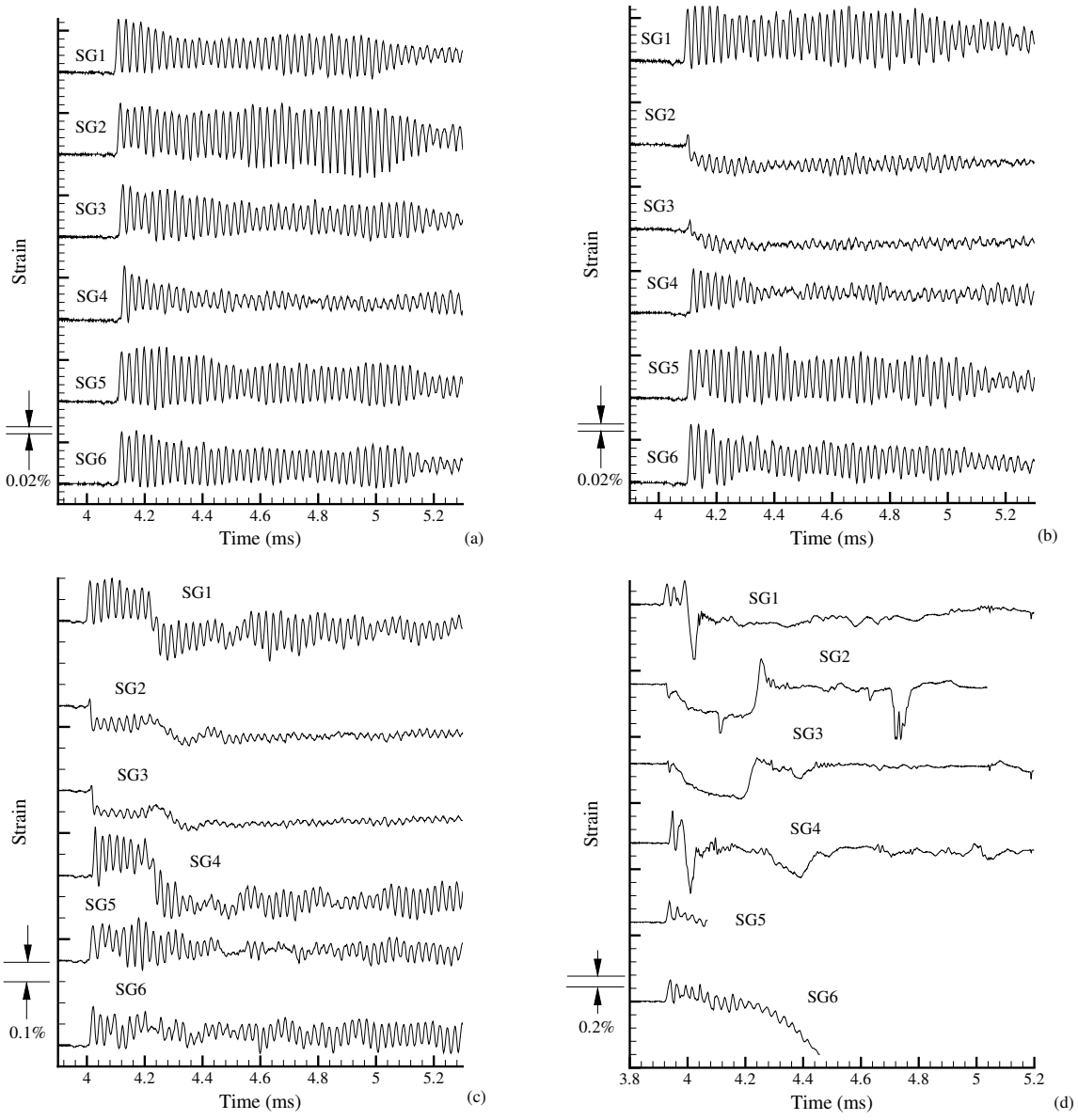

Figure 4.16: Hoop strain of four specimens with the same wall thickness and tube length but different CJ detonation pressure. The flaw sizes were also the same, except Shot 33, which had no notch. All strain traces start at zero strain. (a) Tube with no notch and no rupture (Shot 33). (b) Notched tube with no rupture (Shot 31). (c) Notched tube with rupture confined within the notch (Shot 30). (d) Notched and ruptured tube with forward and backward helical cracks (Shot 34).

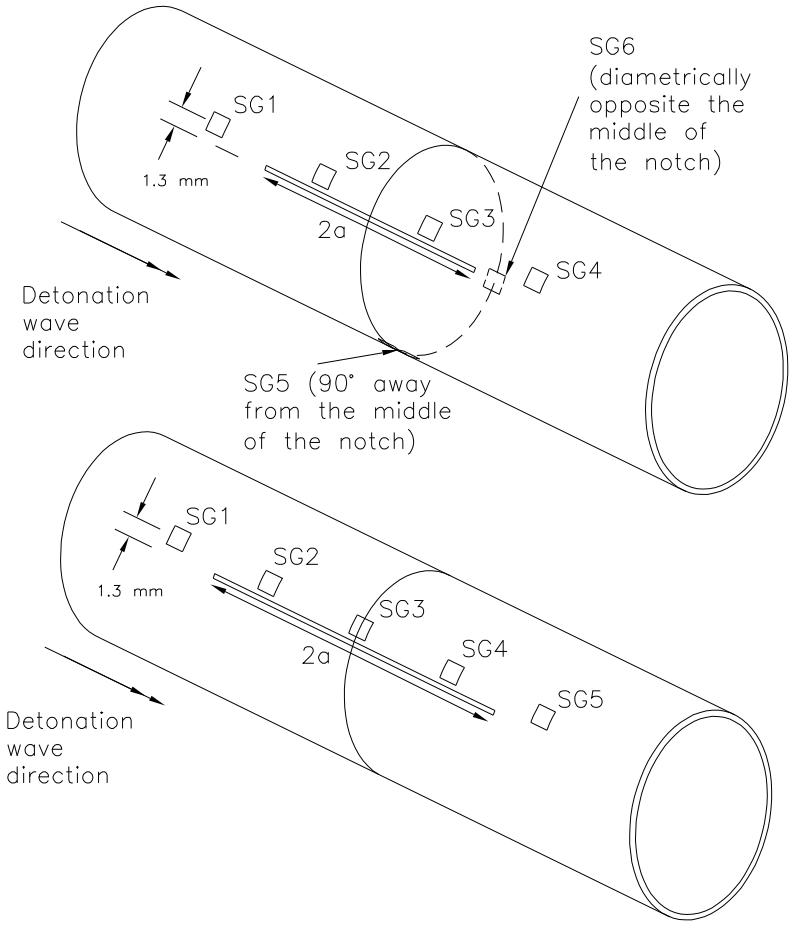

Figure 4.17: Strain gage locations for Shots 30, 31, and 34 (above) and Shot 24 (below). Distance between gages was 15.2 mm for gages 1 through 4 for Shots 30, 31, and 34. Distance between gages was 25.4 mm for Shot 24. The strain gage locations for Shots 33 and 48 to 51 follow that of 30, 31, and 34. Gage length was 0.81 mm and gage width was 1.52 mm. Drawing is not to scale.

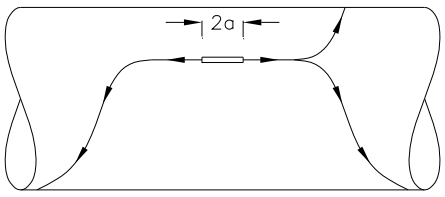

Figure 4.18: Schematic of crack paths of Shot 24. Detonation wave ran from left to right. Drawing is not to scale.

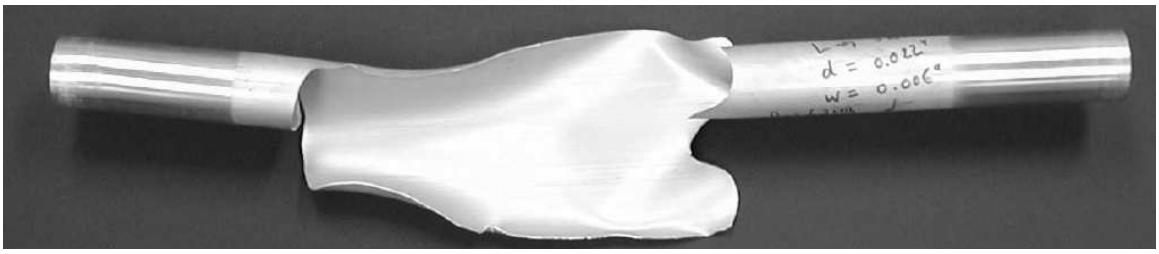

Figure 4.19: Shot 24 specimen. Detonation wave ran from left to right.

4.4.2.1 Dynamic Hoop Strain Characteristics of a Detonation Tube

Shot 33 shows typical elastic strains of flexural waves excited by detonation waves that travel above v_{c0} but below v_{c1}. While the reader is referred to Beltman and Shepherd (2002) for a more detailed discussion, several points are worth mentioning here. First, the strain front coincides with the detonation wave front. Second, the frequencies of the strains correspond closely to the Tang (1965) model's theoretical steady-state frequency, which is 39 kHz for this tube. Third, the measured Φ here is about 1.5, and thus, our assumed value of 2 for the fracture threshold model is apparently too high. Fourth, since the flexural waves were dispersive and the detonation wave was traveling above v_{c0}, precursor waves at frequencies over 1 MHz would travel ahead of the strain signals seen here. The reasons that they are invisible are that 1) they are of small amplitude compared to the main signal, and 2) the amplifiers, having a bandwidth of 100 kHz, attenuated the high-frequency precursors. Fifth, beating can be observed in all of the strain traces due to flexural wave reflections from the tube ends. Sixth, the disparity among individual strain signals is mainly caused by the gages' different, albeit close, axial locations on the tube and multiple wave reflections from the tube ends. As it will be shown in the next section, the differences in dynamic strain histories shown here are not primarily caused by tube misalignment or other non-axisymmetric boundary conditions.

4.4.2.2 Effect on Surface Hoop Strains due to Bulging Near the Notch

Comparison between Shots 31 (notched tube with no rupture) and 33 (no notch and no rupture) reveals that the presence of the notch reverses the sign of the hoop strains (gages 2 and 3) near the notch. This is expected because as the notch edges bulged under internal pressure, the local curvature of the shell changed and the local strain became compressive. Figure 4.20 shows an illustration. The compression is not unlike the one experienced by one side of a cantilever beam under distributed load. This effect was not experienced by gages 1, 4, 5, and 6 as they were further away from the notch.

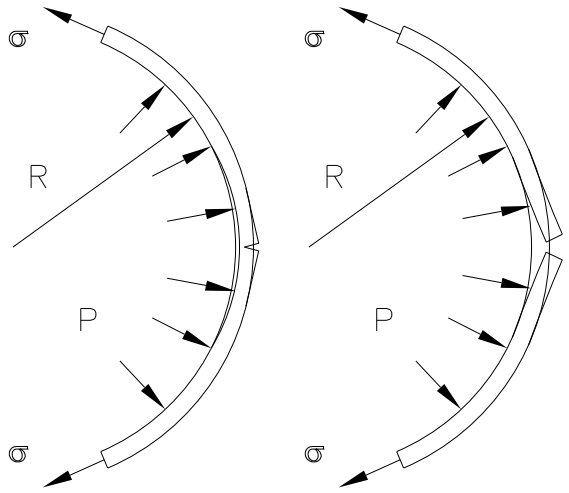

Figure 4.20: Bulging of the regions near the notch and the cracks caused the local shell curvature to change and thus, gave rise to local compressive strains recorded by strain gages. The compression is not unlike the one experienced by one side of a cantilever beam under distributed load.

In Shot 30, a higher pressure was used on a notched tube, which ruptured with the crack confined inside the notch. An abrupt change from tensile to compressive strains for gages 1 and 4 and the sudden increase in compression for gages 2 and 3 suggest that crack initiation occurred at about 4.2 ms, or 0.2 ms after the arrival of the detonation wave front. The change in sign for gages 1 and 4 is due to increased bulging after the loss of material continuity in the notch.

4.4.2.3 Hoop Strains for Catastropic Structural Failure

Shot 34 was an example of catastrophic structural failure in which cracks propagated both in the forward (following the detonation wave) and backward directions. The two cracks propagated in a helical fashion. Because of the emerging detonation products from the crack, some of the gages did not survive long enough to provide meaningful data. Gages 2 and 3 were put into compression, while gages 1 and 4 were in tension for about 0.1 ms and then abruptly went into compression when the cracks propagated past the gage location, causing the local shell surface to bulge. Note that strain gage 4 reverted from tension to compression slightly earlier than gage 1, suggesting that the forward crack was propagating faster than the backward crack.

Figure 4.21 shows strain signals for a specimen whose forward crack bifurcated and the backward crack ran helically. The five strain gages are all aligned with the notch (Fig. 4.17) and were located differently from those of Shots 30, 31, 33, and 34. The forward crack ran straight for a short distance, passing strain gage 1 before branching into two secondary cracks. The gage recorded tension for a brief period, but then transitioned to compression as did gage 1 in Shot 34. Strain gages 2 thru 4 in Shot 24 behaved similarly to gages 2 and 3 in Shot 34, while gage 5 in Shot 24 behaved similarly to gage 4 in Shot 34.

In all of the five cases just discussed, the detonation wave travelled at 2.4 km/s. This means that the detonation wave front took 0.1 ms to travel from the strain gages to the end of the specimen tube. The pressure traces in the initiator tube give the approximate duration from the detonation wave front's arrival at the pressure transducer to completion of venting of the detonation products (i.e., coming to atmospheric pressure). It was found that for all of the five cases above, this tube venting time was at least 5 ms.

Abrupt strain jumps at later times such as gage 2 at 4.7 ms for Shot 34, gage 1 at 5.1 ms, and gage 2 at 4.8 ms for Shot 24 were probably due to the flaps of tube material (created by fracture) impacting the support structure.

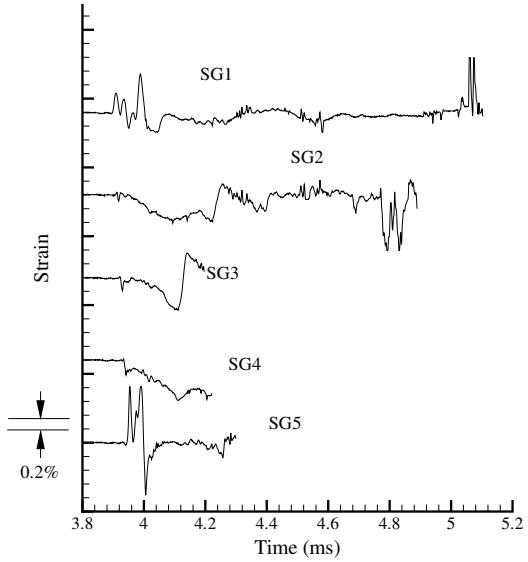

Figure 4.21: Notched and ruptured tube with forward bifurcated cracks and backward helical cracks (Shot 24).

4.4.3 Boundary Conditions, Non-Axisymmetry, and Crack Curving Direction

Figure 4.22 shows vividly the effect of non-axisymmetry. It shows specimens whose cracks either curved upwards or downwards for a range of pressures and flaw lengths. There are several potential causes of crack curving. One would expect that if the initial stress, detonation loading, and material properties had been perfectly axisymmetric, the cracks should have run straight. However, up to the time of this writing, no such straight detonation-driven cracks were found. What is more interesting is that, disregarding the bifurcation cases, both the forward and backward cracks always curved upwards or downwards, but never one upwards and another downwards. This phenomena of two cracks always curving towards the same direction causes one to suspect that the curving direction is not random. From this point on, the sign convention of Fig. 4.23 will be used to denote the curved crack path directions.

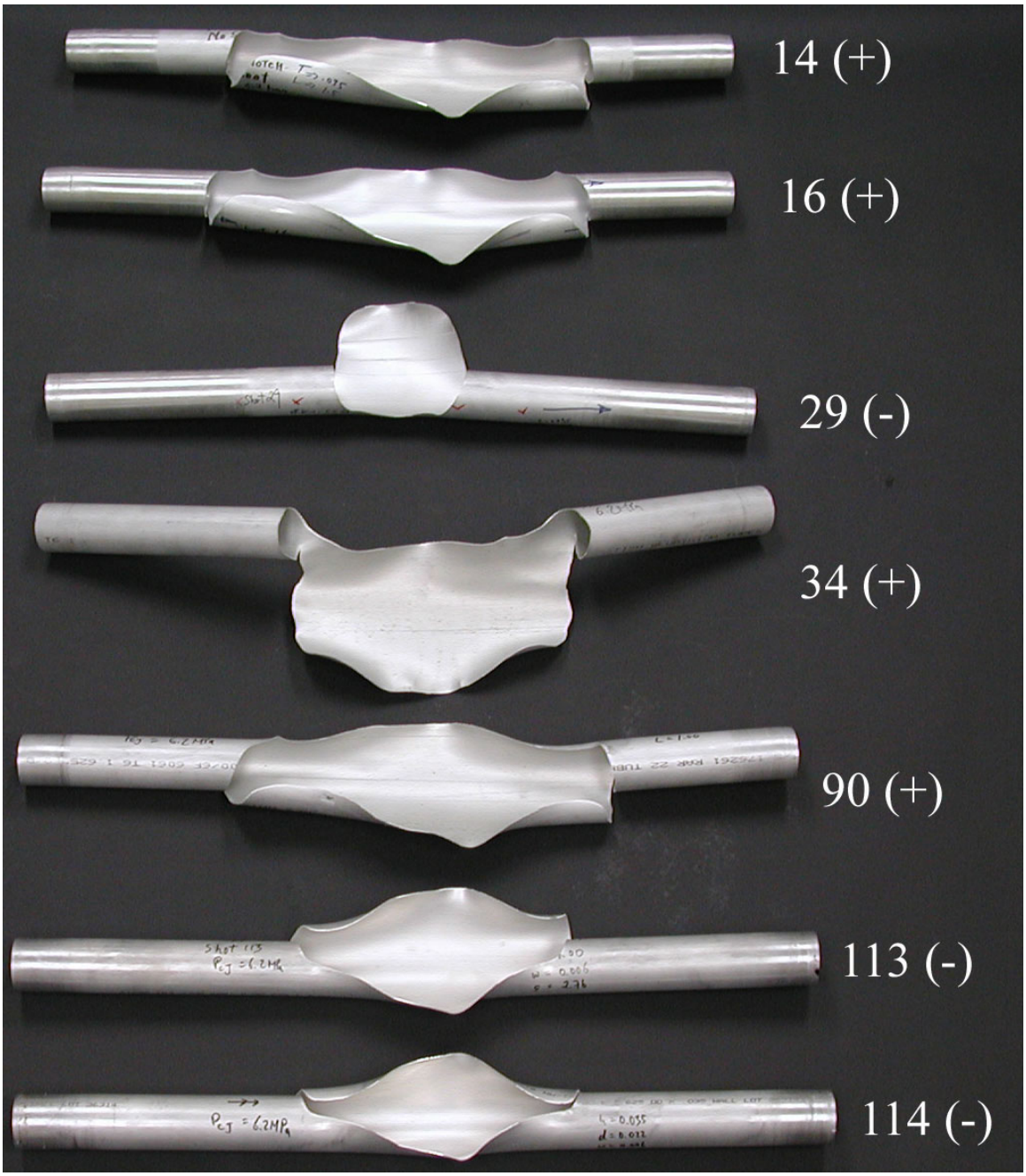

Figure 4.22: Post-test specimens with both forward and backward cracks directed upwards or both downwards, but never in different directions. This suggests that crack curving direction may not be random. The detonation wave ran from left to right. Numbers denote shot numbers. Positive and negative signs denote crack path directions. Refer to test matrix for shot conditions. See the next figure for crack path sign conventions.

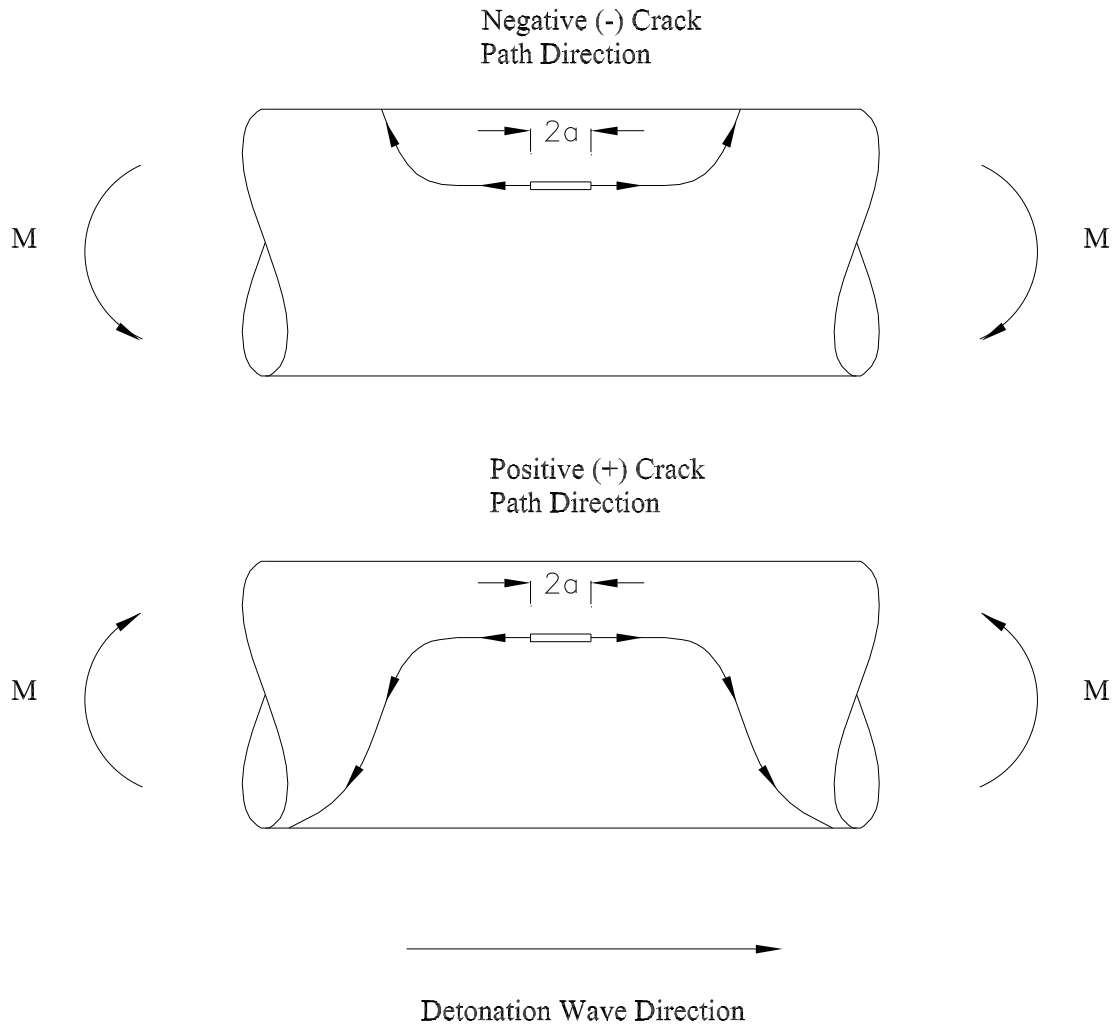

Figure 4.23: Crack path directions following the right-hand screw rule. The fact that the forward and backward cracks did not curve in opposite directions led us to believe that a bending moment M imposed unintentionally by the fixture was a contributing factor for crack curving. Cracks are attracted to the tensile side of the tube under bending.

4.4.3.1 Dynamic Axisymmetry

Strains were measured again with the specimen tube rotated about the fixture after each measurement to quantify the amount of non-axisymmetry. The total strain can be broken up into two parts:

$$\epsilon_{total}(t) = \epsilon_{static} + \epsilon_{dynamic}(t). \tag{4.10}$$

The static part is caused by prestress due to end conditions, and the dynamic part is the one superimposed by the detonation load. Static experiments measured the static prestrain, and dynamic experiments measured the detonation-induced dynamic strains.

A series of four experiments was designed to determine whether the dynamic hoop strains produced by the detonation were axisymmetric. Four experiments (Shots 48 to 51), repeating Shot 33 on the same specimen with only variation of initial axial rotation with respect to the fixture, were performed to measure the effects of boundary conditions on the tube. After Shot 48, the tube specimen was rotated 90 degrees axially with respect to the fixture after every shot until Shot 51. The goal was to see whether or not strain histories would significantly alter if the tube was turned. If they do, there would not be axisymmetry in the dynamic strains. The strain histories of Shots 48 to 51 are shown in Fig. 4.24 and can be compared to that of Shot 33 (Fig. 4.16). The strain amplitudes, frequencies, and beats are reproduced nicely.

4.4.3.2 Non-Axisymmetry due to Unintentional Static Preload

Next, the initial strains were examined to determine how much static preload was unintentionally imposed onto the specimen. Static strains in the axial direction were measured after the tube was mounted to the fixture. The rationale for examining the axial strains comes from flat-plate fracture literature, where it is well-known that the T-stress, a non-singular stress component acting parallel to the crack, is sometimes responsible for crack curving in a mode-I dominated fracture (Cotterell and Rice, 1980). A strain gage was mounted axially next to SG6 in the middle of the same specimen used for Shot 33 and Shots 48 to 51. As in the dynamic experiments, the tube was rotated 90 degrees axially with respect to the fixture after every measurement. The results are plotted in Fig. 4.25. It is clear from this plot that there is measurable prestress present. The fixture caused one part of the tube to go into longitudinal compression and the other into longitudinal tension, much like a beam being bent by end moments.

The Bernoulli-Euler beam theory can be used to curve-fit the measured static

strains and infer the bending moment imposed on the specimen by the fixture. The following assumptions are used:

$$\sigma = \frac{My}{I} = E\epsilon \ , \ y = R_2 \sin(\theta - \theta_0) \ , \ I = \frac{\pi(R_2^4 - R_1^4)}{4}, \tag{4.11}$$

where M is the bending moment, y is the perpendicular distance of the strain gage to the neutral plane, θ_0 is the angle of the neutral plane relative to the initial angle of rotation of the strain gage, θ is the angle of rotation of the strain gage, I is the moment of inertia of the tube, R_1 is the inner radius of the tube, and R_2 is the outer radius of the tube. Figure 4.26 shows a diagram of this model. Rearranging,

$$\epsilon = \frac{4MR_2}{\pi E(R_2^4 - R_1^4)} \sin(\theta - \theta_0). \tag{4.12}$$

This curve is plotted on Fig. 4.25 for $M = 8$ N-m and $\theta_0 = 195°$. It is known that T-stresses cause instability in crack paths from two-dimensional analysis (Cotterell and Rice, 1980). If this analysis can be extrapolated to the present three-dimensional situation so that crack directions are sensitive to these measured tensile stress distributions, this will explain why the curving cracks shown in Fig. 4.22 either both go up or both go down and not in random directions. When the tube is put into bending by the fixture, either side of the notch becomes locally tensile or compressive, and the cracks propagate into the tension side.

4.4.3.3 Effect on Crack Curving Direction due to Intentional Static Preload

To further justify that the paths of detonation-driven cracks do follow prestress fields, two experiments (Fig. 4.27) were performed by applying a wedge load F onto the middle of the tube on either side of the notch to create a deliberate initial bending moment. Figures 4.28 and 4.29 show the post-test specimens. The cracks curved as expected, to the tension side of the tube.

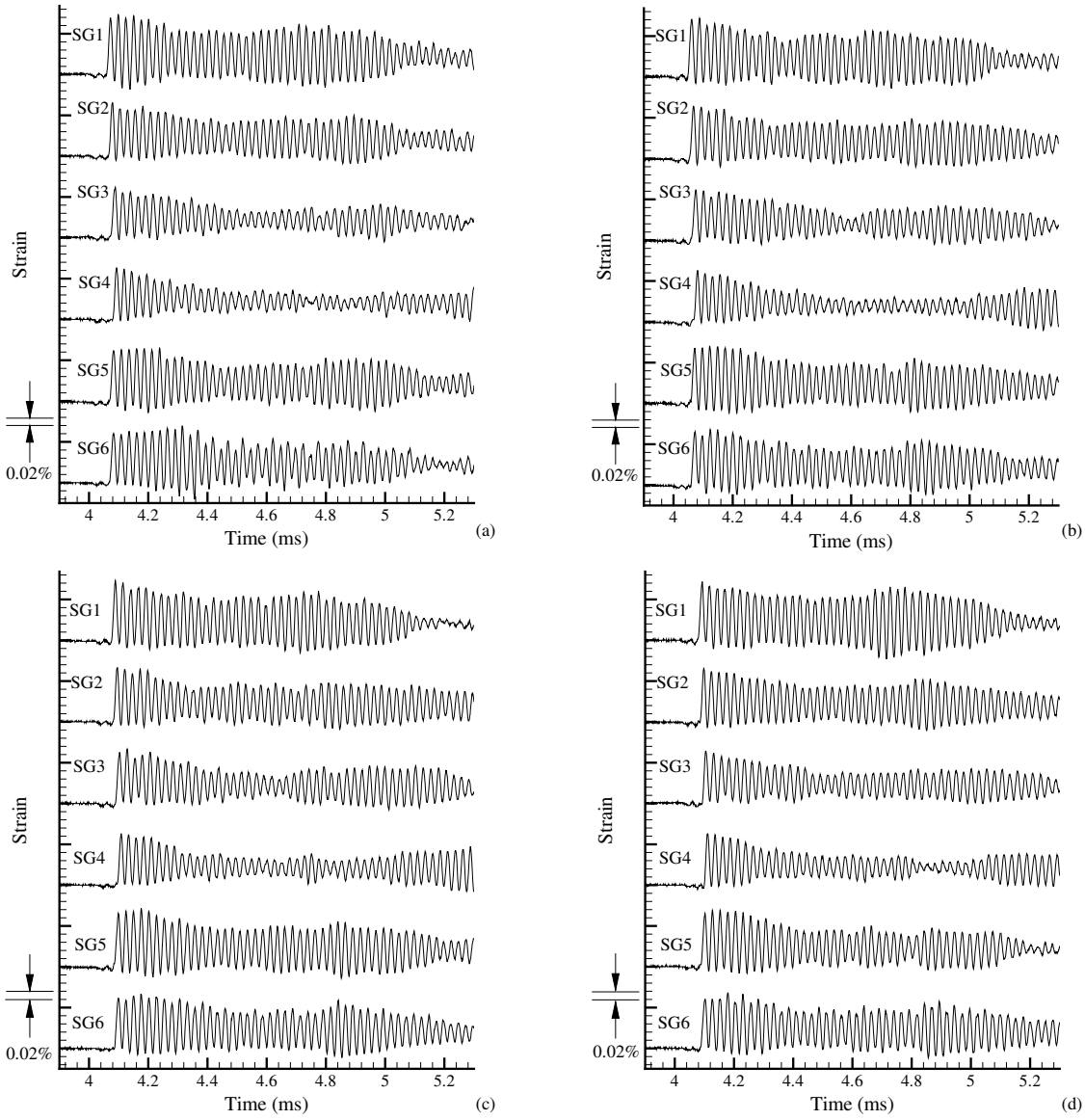

Figure 4.24: Dynamic axisymmetry validation: shots with same conditions but with the tube rotated 90 degrees with respect to the fixture after each successive shot. Conditions are same as Shot 33. (a) Shot 48. (b) Shot 49. (c) Shot 50. (d) Shot 51.

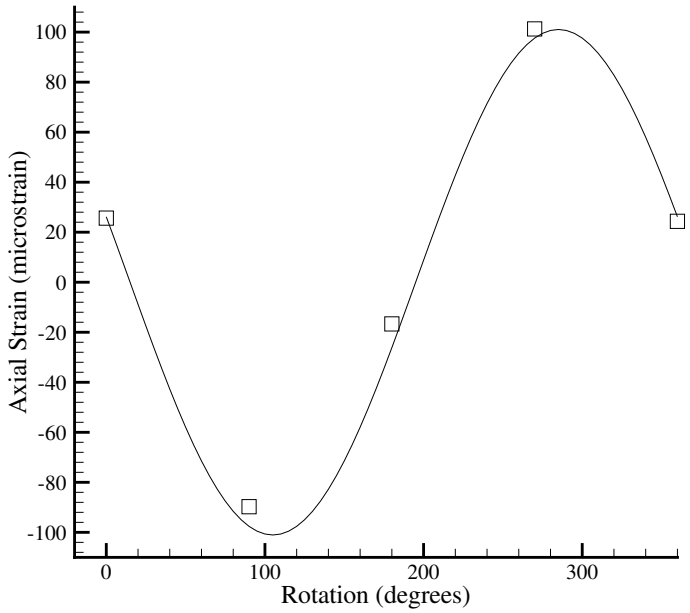

Figure 4.25: Static longitudinal axial strains (open squares) measured on a strain gage in the middle of the tube. The tube was rotated 90 degrees with respect to the fixture after each successive measurement. The solid line represents the theoretical strains for a fixture-induced bending moment of 8 N-m.

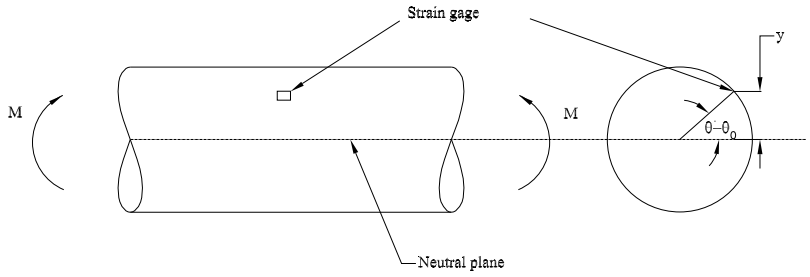

Figure 4.26: Bernoulli-Euler beam model used to infer the fixture-induced bending moment M from measured static longitudinal strains. y is the perpendicular distance from the strain gage to the neutral plane and $\theta - \theta_0$ is the angle between the strain gage and the neutral plane.

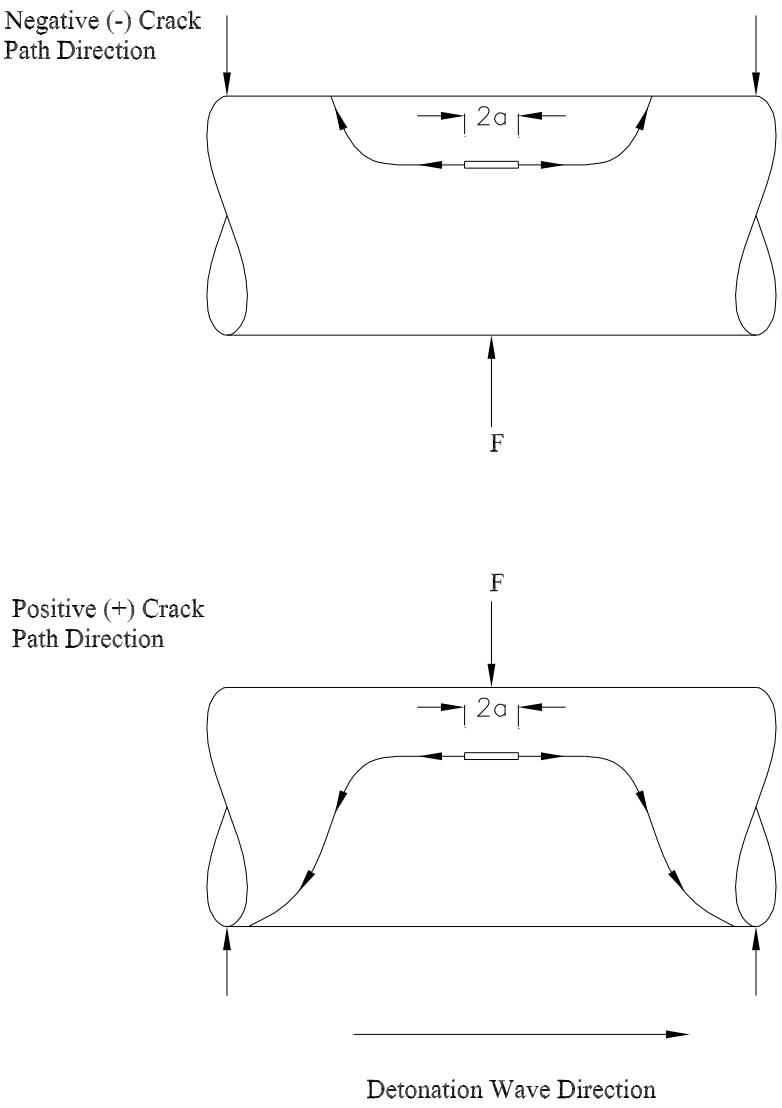

Figure 4.27: Wedge load setup schematic. The upper diagram shows the configuration and crack path for Shot 109, and the lower diagram shows those for Shot 110. The crack path directions are consistent with the induced bending moment.

Figure 4.28: Shot 109.

Figure 4.29: Shot 110.

4.4.4 Comparison of Fracture Threshold Model to Experimental Data

The second set of experiments used shorter tubes (0.610 m) and the parameters being varied included flaw depth, flaw length, wall thickness, and pressure. Experiments on Al6061-T6 tubes of this length were performed (see Tables 4.1 and 4.2 for loading and geometry). The results are plotted on Fig. 4.3 using the left-hand side of Eq. 4.8. The right-hand side of Eq. 4.8 is the theoretical threshold surface, plotted on the same figure for comparison.

Out of 38 experiments performed on preflawed tubes, only three experimental data points (Shots 16, 28, and 32) were on the 'wrong' side of the threshold surface. The worst case was Shot 32, which had a normalized stress intensity (parameter on the vertical axis) of 37% away from its predicted region. The agreement between theory and experiment is unexpectedly good for such a simple model. This is partly due to the fact that Al6061-T6 is a relatively brittle metal. Experiments have not

yet been performed on higher values of d/h because a shallower initial flaw requires higher detonation pressure to rupture.

4.4.5 Effect of Propagating Fracture on the Detonation Wave

The detonation wave may quench due to the rapid gasdynamic expansion associated with the flow out of the crack opening. If quenching happens in a rupture accident, this may mitigate the hazards of the detonation wave propagating into a piping system filled with combustible reactants. However, no detonation quenching has been observed so far for the three shots (14, 16, and 29) that involved fracture and pressure measurement at the extension tube. This is because the cracks traveled too slowly to catch up with the sonic plane of the detonation wave. However, the Taylor expansion wave was affected. Two example cases of the pressure history in the extension tube are shown. Figure 4.30 shows a case (Shot 14) in which the pressure in the Taylor wave region dropped more rapidly due to rupture. As a comparison, Fig. 4.31 shows a case (Shot 17, no rupture) in which the pressure in the Taylor wave region did not drop as quickly and did not reach atmospheric pressure in the time interval considered.

4.5 Conclusions

The key results in this chapter include 1) qualitative behavior of the crack path of a fracturing detonation tube as a function of initial flaw length, 2) quantitative measurements of strain history, 3) fracture threshold, 4) relation of detonation wave propagation direction to crack branching, 5) influence of static prestress on crack curving direction, and 6) influence of rupture on the pressure profile of the detonation wave. The present experiments and analyses demonstrate that the fracture mechanics approach is very useful in studying detonation-driven fracture of aluminum tubes.

Initial flaw depth has a stronger effect than flaw length on the threshold detonation pressure required to burst a tube. This was demonstrated by the fracture threshold model and experiments. While this is not a precise predictive capability, the fracture

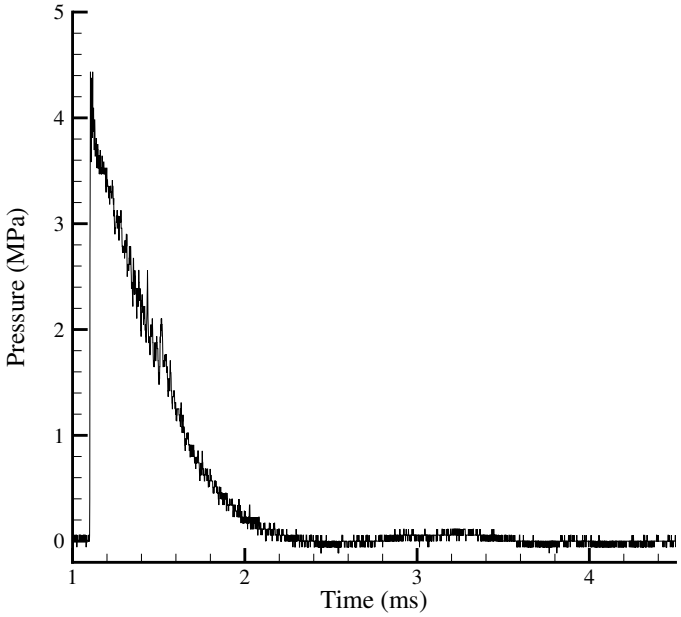

Figure 4.30: Pressure history of transducer 3 for Shot 14 that resulted in rupture. The propagating crack resulted in venting the explosion products and increased the rate of pressure decay over that associated with the Taylor wave in a rigid tube as shown in the next figure and discussed in the Appendix of Beltman and Shepherd (2002). The detonation was not quenched. Time zero corresponds to the spark in this case.

threshold model had been an extremely useful engineering tool in the design of our test matrix, correctly identifying trends and enabling the approximate sizing of test specimens and flaw geometry.

The current fracture threshold model, while being able to identify the trend for fracture threshold, needs improvement. A fully dynamic numerical model must be developed in the future to account for bending, shear, inertia, strain rate effects, and plasticity. Moreover, the specimens had blunt notches that are dissimilar from the mathematically sharp crack which the static model assumes. To ensure better agreement between experiment and analysis, one must either initiate a sharp crack (and know how deep it has penetrated) in the tube before each experiment, or develop a numerical method that accounts for the bluntness of the notch. The multi-cycle na-

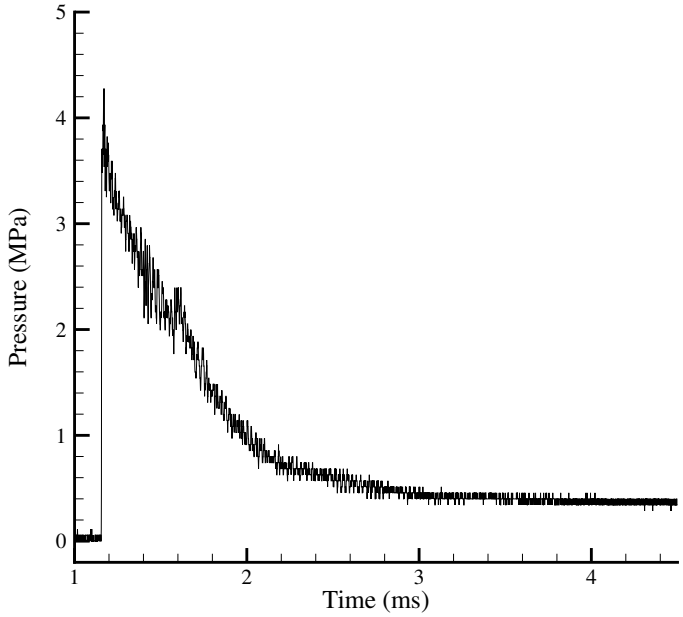

Figure 4.31: Pressure history of transducer 3 for Shot 17 that resulted in no rupture. Unlike the pressure profile in the ruptured case of Shot 14, the pressure here dropped at a lower rate and did not go to atmospheric pressure for the time interval considered. Time zero corresponds to the spark in this case.

ture of the stress is obvious from the strain signals. Numerical analysis that attempts to predict whether or not the initial crack has propagated through the wall thickness must account for not only the first cycle, but also multiple cycles of stress, and how, during that period, the dynamic stress intensity field evolves as a function of time.

The results of this study should be useful for forensic analysis in pressure vessel and pipeline detonation-driven fracture accidents. Given a portion of postmortem ruptured pipe from an accident, the fact that crack bifurcation favored the forward crack helps to decipher the propagation direction of the detonation wave. Moreover, the fact that initial bending stress causes cracks to curve in one direction helps to give some clues as to the initial stress state of a piping system. Furthermore, experiments have shown cases in which running cracks were unable to quench detonation waves, but the venting caused a quicker drop in loading on the crack flaps.

The fracture behavior can help in deducing the size of the initial flaw if one is

present. It was shown that initial flaw length strongly influenced the crack propagation behavior for aluminum tubes under detonation loading. This is expected because larger initial flaws mean higher stress intensity factors and greater crack driving force. Characteristic critical crack lengths for crack bifurcation were also found for different tube lengths. Strain traces measured at strategic positions on the tube were analyzed for different levels of rupture and plastic deformation. The present documentation of postmortem specimens and strain histories should be helpful for researchers who are simulating this type of fluid-structure-fracture interaction.

Chapter 5

Comparison of Detonation-Driven Fracture with Hydrostatically Loaded Fracture

5.1 Introduction

Detonation-driven tube fracture is distinguished from quasi-statically loaded tube fracture for two main reasons[1]. First, flexural waves set up by traveling loads (described in the previous two chapters) can cause dynamic strains that are oscillatory and have amplitudes several times higher than those predicted for static situations. These amplitudes and frequencies are dependent on the speed of the traveling load. Second, for quasi-statically loaded tubes, the stored elastic energy caused by prestress everywhere in the tube can provide a substantially higher crack driving force than in the case of traveling loads.

The experiments in this chapter are motivated by our interest in the forensic analysis of pipe rupture in accidental explosions and the fracture-based design of pressure vessels that withstand explosions. A key issue is the effect of the loading rate on fracture thresholds and fracture propagation. In the experiments described here, the flaw size and geometry, tube material, and nominal loading magnitude were kept invariant. The loading rate and pressure medium were varied. One case was static rupture by hydraulic oil; another, static rupture by gaseous nitrogen at room

[1]This chapter will appear as a paper in Journal of Pressure Vessel Technology.

temperature; and the third, dynamic rupture by an internal gaseous detonation. The specimen ruptured under hydraulic oil loading had the least damage. Much more substantial damage, i.e., crack propagation and plastic deformation, was observed in the cases with nitrogen and detonation loading. The nitrogen loading caused a substantially larger fracture than the detonation partially due to a difference in total stored energy, although the peak loading pressure was similar.

5.2 Experimental Setup

5.2.1 Specimens

The specimens were thin-walled, seamless aluminum 6061-T6 tube. The surface notch was oriented axially, located in the middle of the tube length, and cut by a CNC machine using a jeweler's slotting saw. The notch depth (0.56 mm), notch width (0.2 mm), tube size (0.89 mm in wall thickness, 41.28 mm in outer diameter, 0.610 m long), and notch length ($L = 25.4$ mm) were the same for all tests. Figure 4.2 shows the geometry of the flaw. $R_{saw} = 34.9$ mm is the radius of the jeweler's slotting saw.

5.2.2 Detonation Tube Assembly

Figure 5.1 shows a schematic of the experimental setup for the detonation loading. The assembly was aligned and bolted to aluminum plates, which in turn, were bolted to a plywood table. The setup was almost identical to that described in Section 4.3.2.

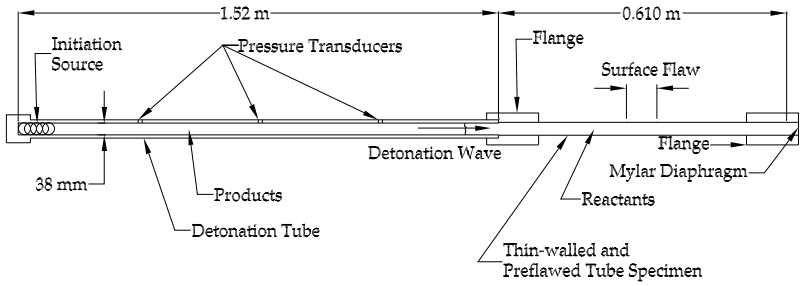

Figure 5.1: Tube assembly schematic for detonation experiment.

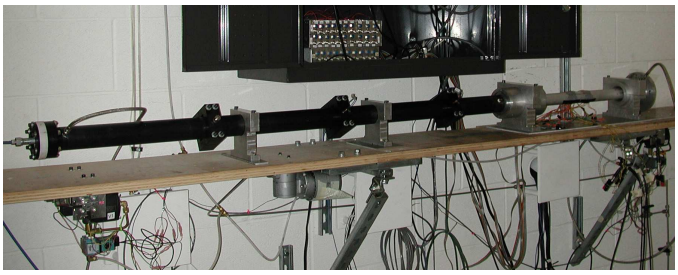

Figure 5.2: Tube assembly for detonation experiment.

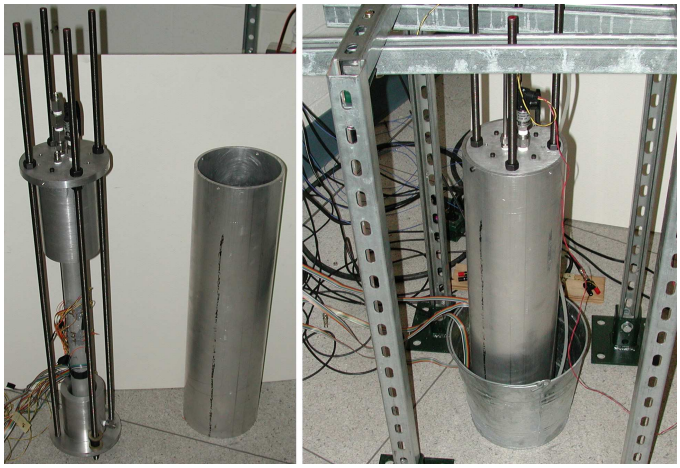

Figure 5.3: Tube assembly for hydraulic oil loading and gaseous nitrogen loading. Left: assembly separated from the blast shield. Right: with the blast shield. The flanges used in the hydraulic oil and nitrogen loading were the same ones as those in detonation loading.

For the gaseous nitrogen and hydraulic oil loading experiments, the specimen tube was connected to the same flanges used in the detonation experiments. The ends of the flanges were capped, threaded rods and nuts were used to counter the resulting hydrostatic axial force, and the assembly was fixed vertically rather than clamped down on a table. Figures 5.2 and 5.3 show the photographs for detonation and static loading experiments, respectively.

5.2.3 Instrumentation

The velocity and pressure of the detonation wave were measured by PCB piezo-electric pressure transducers. The pressure transducers were mounted 0.406 m apart in the

detonation tube.

Micro-Measurements strain gages and crack detection gages were bonded to the external surface of the tubes to measure circumferential strain and crack arrival times, respectively. Dow Corning 3145 RTV was used to protect the leads from premature destruction due to the blast wave. The Trig-Tek amplifiers that amplified the signals from the Wheatstone bridges had a bandwidth of 100 kHz.

In the detonation experiment, the spark and data acquisition system was triggered by a Stanford Research Systems digital pulse generator. The pressure traces, strain history, and crack arrival times were digitized with Tektronix oscilloscopes. The detonation experiment was recorded at a rate of 2.5 megasample per second, while the gaseous nitrogen and hydraulic oil experiments were recorded at a rate of 1 megasample per second. The data were transferred into a computer through a LabVIEW program.

In the gaseous nitrogen and hydraulic oil experiments, one of the crack detection gages was placed close to the surface notch tip to trigger the data acquisition system. The pressure was recorded with an Omega PX4100-3KGV pressure transducer attached to one of the endcaps.

In the gaseous nitrogen experiment, nitrogen was supplied to the tube assembly from a liquid nitrogen tank via a pressure regulator and an electro-pneumatic valve. The pressure was slowly increased by turning a lever on the regulator. Upon rupture, the electro-pneumatic valve was closed by a manual switch.

In the hydraulic oil experiment, an SFX PowerTeam handpump was used to pressurize the tube assembly with SFX PowerTeam no. 9638 hydraulic oil.

Figures 5.4 and 5.5 show a schematic and a photograph, respectively, of the crack detection gage and strain gage setup. Table 5.1 shows the locations for these gages.

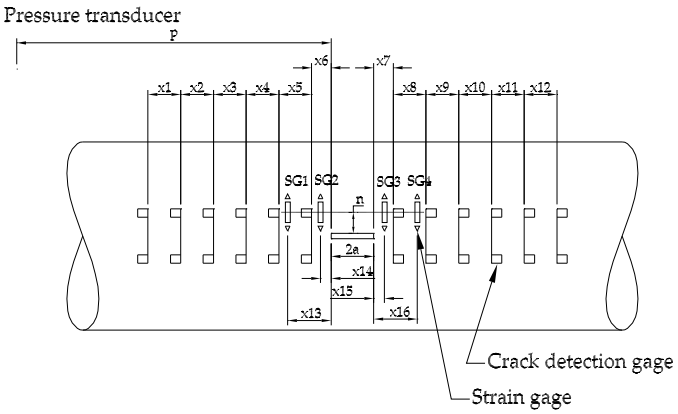

Figure 5.4: Schematic for crack detection gages and strain gages. In the detonation case, "pressure transducer" refers to the PCB transducer on the initiator detonation tube closest to the specimen tube.

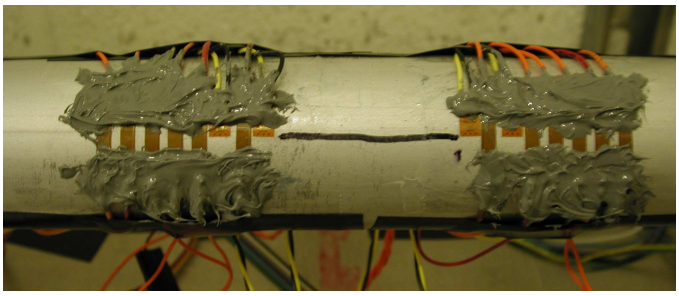

Figure 5.5: A pre-test photograph of crack detection gages and strain gages. The surface notch was marked in black with a pen (free hand).

5.3 Results and Discussion

5.3.1 Pressure Loading

For the detonation experiment, the mixture was stoichiometric ethylene-oxygen (C_2H_4+$3O_2$) at an initial pressure of 1.8 atm and room temperature. The pressure peak recorded by the pressure transducer is not reliable due to noise, the three-dimensional structure of the detonation wave front, and the finite size of the pressure transducer. For this reason, computed values of the CJ pressure were used to characterize the detonation. The calculated (Reynolds, 1986) CJ pressure and wave speed are 6.2 MPa and 2390 m/s. The detonation pressure history recorded on the pressure transducer closest to

	Detonation	Nitrogen	Oil
x1	-	5.41	-
x2	-	5.54	-
x3	-	4.95	-
x4	4.95	5.21	-
x5	9.40	9.75	-
x6	5.94	5.59	-
x7	5.61	5.49	-
x8	9.45	9.91	-
x9	5.08	5.36	-
x10	5.33	4.62	-
x11	5.38	5.38	-
x12	5.46	5.28	-
x13	12.2	12.0	12.1
x14	2.95	2.77	2.59
x15	2.92	2.79	7.85
x16	12.0	12.2	16.9
p	563	285	285
n	1.3	1.3	1.3
2a	38.1	37.4	37.5

Table 5.1: Crack detection gage and strain gage locations (all dimensions are in mm).

the flange is shown in Fig. 5.6. This is a typical gaseous detonation pressure trace with the initial CJ point (around 0.6 ms) coinciding with the shock front, immediately followed by a Taylor expansion wave. After the end of the Taylor expansion, there is a short plateau (1.2 to 1.6 ms) followed by the expansion wave that came from the rupture and the open end of the tube. The detonation wave speeds were measured just before entering the specimen tube and are typically within 5% of the computed values.

The burst pressures of the gaseous nitrogen experiment (5.5 MPa) and hydraulic oil experiment (6.0 MPa, see Fig. 5.6) were slightly lower than the CJ pressure of the detonation experiment. However, loading and unloading rates were quite different in the three cases. The pressure was increased very slowly in the static tests and the loading rate was zero for all practical purposes in the nitrogen and hydraulic oil experiments. The pressure transducer used in the nitrogen and hydraulic oil experiments was too slow (response time of 10 ms) to capture the initial fast pressure

transients during rupture (the original intention being only to capture the burst pressure). However, one can still obtain an estimate of the depressurization rate. In the hydraulic experiment, it took about 15 ms to drop to about 3 MPa, while in the nitrogen experiment, it took as long as about 25 ms. In the detonation experiment, the loading is essentially complete after a few μs, and the unloading occurs in two stages. Immediately following the detonation, it took only about 0.4 ms for pressure to drop from 6 MPa to 2 MPa and then a slower decay occurs over the next 5 ms. Note that these three pressure traces were recorded at different locations with very different gages so that the comparison is only qualitative.

5.3.2 Fracture Behavior As a Function of Loading

As can be seen in the post-test specimens in Fig. 5.7 (hydraulic oil), Fig. 5.8 (detonation), and Fig. 5.9 (gaseous nitrogen), the fracture behavior is a strong function of the applied loading.

In Fig. 5.8, the detonation wave traveled from left to right. As the wave propagated past the surface notch, the hoop stress opened the notch into a through-wall crack. Two crack fronts then propagated–one in the forward direction (i.e., same direction as the detonation wave) and one in the backward direction (i.e., in the opposite direction of the detonation wave). Both the forward and backward cracks propagated straight for some distance, then turned, ran helically around the tube, and were arrested.

Under initially static gaseous loading with nitrogen, the cracks ran straight and did not arrest until they propagated to the supports (Fig. 5.9). Both cracks began to turn as they approached the supports.

In the experiment with hydraulic oil, the cracks were arrested almost immediately after they left the notch (Fig. 5.7). The cracks were so short that they did not run past enough crack detection gages for crack arrival time measurements. This behavior is relatively benign and in stark contrast to the extensive fractures observed with the static nitrogen or detonation tests. These observations support the standard practice (ASME, 2000) of hydrostatic pressure testing using liquids as opposed to pneumatic

testing using gases.

5.3.3 Fractographs

Fractography is widely used in failure investigation and analysis (Thielsch, 1965, Engle and Klingele, 1981, Becker and Shipley, 2002), but at present, there are no published data on gaseous detonation-driven fracture. Light microscope pictures of fracture surfaces for the present experiments were taken and some of these are shown for detonation and nitrogen experiments in Figs. 5.8 and 5.9, respectively. The magnification was 30X with a Leica GZ4 light microscope which was coupled to a Nikon Coolpix 990 digital camera. The natural scale in these photos is the wall thickness of the tubes, which is 0.89 mm.

Two types of fractographs can be discerned in the detonation experiment shown in Fig. 5.8. Both the forward and backward cracks first propagated straight for some distance, turned helically, and were arrested. Arrows next to the fractographs indicate the direction of propagation for the detonation waves and the cracks. The approximate locations on the tube where these fractographs were taken and the location of the initial notch are also shown.

The first type is shown in Fig. 5.8 (a) and (b). These fracture surfaces are along the straight portion of the cracks. They are relatively rough because 1) they were caused by the predominantly mode-I (opening mode) fracture and 2) the specimen was ductile, being above its transition temperature. Since the wall was thin, the fracture surfaces were, in general, slanted at 45 degrees to the specimen's surfaces and were composed almost entirely of shear lips.

The second type, less frequently reported in the literature, is shown in Fig. 5.8 (e) and (f). These fracture surfaces are along the curved portion of the cracks. They are relatively smoother than the fracture surfaces of the straight portion of the cracks. The cracks have turned helically along the tube, and the fracture was predominantly mode-III (tearing mode) due to the large outward dynamic motion of the flaps. On some fracture surfaces, shallow striations that are almost perpendicular to the crack

path can be seen, such as those in Fig. 5.8 (e) and (f).

The fracture surfaces of the gaseous nitrogen experiment are less distinctive from one another because the fracture mode stayed the same throughout the course of crack propagation. Nonetheless, the fracture surfaces farther from the notch tend to be somewhat smoother than those near the notch.

5.3.4 Strain Response

Figure 5.10 shows the strain response of the specimen tubes within one or two milliseconds of rupture. In the detonation and gaseous nitrogen experiments, the strain gages and crack gages were located at the straight portions of the propagating cracks. The average crack speeds calculated from arrival times between consecutive crack gages are plotted in Fig. 5.11. The strain rates ranged typically from 10^2 s^{-1} to 10^3 s^{-1}.

The initial hoop strain patterns of the gaseous nitrogen and hydraulic oil experiments are qualitatively similar. They are on different time scales, but the strain histories of corresponding gages in the two experiments are generally of the same shape. In both plots, all strains start near the burst pressure. The initial drop in strain results from both the depressurization of the fluid and the motion of the flaps of material created by the propagating crack. The flaps fold outward and are hinged about the crack front; this motion compresses the material ahead of the crack. This hinge effect causes a drop in strain at a distance ahead of the crack and is common in flat-plate mode-I fractures. Since SG2 and SG3 were closer to the notch, as the cracks ran by, the crack tip stress concentrations along with the significant residual internal pressure caused sharp strain peaks. SG1 and SG4 were further from the notch, and one does not see such high strain peaks because the internal pressure had already been relieved quite significantly. Another point of interest is that although SG2 and SG3 in the hydraulic oil experiment are schematically symmetric about the notch, their signals look dissimilar because their actual locations were not symmetric about the notch.

5.3.4.1 "Static" Loading vs. "Dynamic" Loading

The first important difference is the magnitude of the initial strain. The initial strain of the nitrogen and oil experiments is about 0.2%, equal to the static cylindrical shell prediction using the burst pressure. The magnitude of the first strain cycle (uncontaminated by stress concentrations because the crack has not yet arrived) of the detonation experiment is about 0.3%, giving a dynamic amplification factor (ratio of dynamic strain to static prediction) of 1.5 using the CJ pressure. The traveling detonation load caused stresses and strains higher than static predictions. The steady-state Tang (1965) model predicts a dynamic amplification factor of 2 for the present situation. An extensive discussion of dynamic amplification factors as a function of detonation loading can be found in Beltman and Shepherd (2002). In that study, it was shown that the length of the tube and the location of the flanges can have a significant effect on the actual values of the amplification factor. If the amplification factor must be known exactly, then either detailed measurements or finite-element simulations are necessary.

The second important difference is the fatigue-like, oscillatory nature of the strain response caused by detonation load that is not observed in the static load cases. The first two or three cycles of strain that are shown by the strain gages on Fig. 5.10a show typical elastic strains of flexural waves excited by a detonation wave that traveled between the first two critical wave speeds of the structure. The characteristic strain response was discussed in detail in Section 4.4.2.1.

The third important difference is that the loading and unloading have a preferred direction in the detonation case. The detonation propagates along the tube, creating a spatially-dependent stress-field in the tube, sweeping over the notch, and setting up a flow field behind the wave. The crack initiation process will be asymmetric due to the interaction of the elastic waves created by the detonation passing over the notch and the strain field created by the fracture process itself. The expansion waves in the detonation interact with the flow field so that the subsequent stress field in the tube will be different upstream and downstream of the notch. This

asymmetry will be reflected in an asymmetric fracture process. The results are the higher stresses and higher stress intensity factors associated with the forward crack. This is evidenced in the consistently higher crack speeds of the forward crack than those of the backward crack (Fig. 5.11a). The asymmetry was also demonstrated in Section 4.4.1 on the fracture behavior as a function of initial flaw length using similar specimens. For short initial flaws, both the forward and backward cracks propagated helically without bifurcation. When the initial flaw size was increased, the forward crack bifurcated while a single backward crack propagated helically. This case was shown to be repeatable and was another indication of a higher stress intensity factor at the forward crack tip due to the asymmetry of the loading. For very long initial flaws, both cracks bifurcated.

5.3.5 Crack Speeds

Crack speeds deduced from crack arrival times for the gaseous nitrogen loading fluctuated between 200 to 400 m/s, while those of detonation loading fluctuated between 170 to 250 m/s (Fig. 5.11). The error bars show upper and lower bounds. Crack speeds for hydraulic oil loading were not measured because the cracks were arrested before reaching the crack gage locations. From the measured crack speeds, it appears that the gaseous nitrogen loading provided a slightly larger crack driving force than the detonation loading. In the nitrogen case, the tube was prestressed everywhere when rupture occurred and the stress state decayed slowly in comparison to the fracture propagation time. A 200 m/s crack tip would propagate 0.3 m from the notch to the tube end in 1.5 ms, and the pressure decays a neglible amount during this time (Fig. 5.6). In the detonation case, only the portion of the tube behind the detonation wave was loaded and the pressure decays substantially during the time the crack tips propagate towards the ends of the tube (Fig. 5.6). Figure 5.12 shows plots of crack and detonation trajectories in x-t diagrams. The detonation trajectories were predicted assuming that the fracture process did not affect the detonation velocity. The detonation wave speeds were obtained from the detonation front arrival times at the

pressure transducers in the detonation tube, and then extrapolating the detonation trajectory into the specimen tube. Figure 5.13 shows plots of crack trajectories in x-t diagrams.

Fluid	c (m/s)	v (m^3/kg)	K_s (m^2/N)
Detonation Products	1300	0.24	1.4×10^{-7}
Nitrogen Gas	354	0.016	1.3×10^{-7}
Hydraulic Oil	1154	0.0011	8.3×10^{-10}

Table 5.2: Properties of the fluids used for loading. Detonation products are evaluated at CJ state. Nitrogen is evaluated at burst pressure of 5.5 MPa and room temperature. Since the sound speed of the hydraulic oil was not available from the manufacturer, it was measured in our laboratory.

5.4 Effect of Fluid Properties

The differences in observed fracture behavior are quite striking and most apparent when comparing the hydraulic oil loading with either of the two gas loading cases. This immediately suggests that the large difference in physical properties of gases and liquids is responsible for the differences in fracture behavior. The properties of greatest interest are specific volume v and sound speed c, which can be combined to form the isentropic compressibility

$$K_s \equiv -\frac{1}{v}\frac{\partial v}{\partial P}\bigg|_s = \frac{v}{c^2}\,. \tag{5.1}$$

Values of these properties have been estimated for all three fluids used in present experiments and are given in Table 5.2. Inspection of these values indicates a two-order-of-magnitude difference between the gas and liquid compressibility. As shown below, the main consequence of this is that a much larger (three orders of magnitude) amount of energy can be stored at the same pressure in the compressed gases or detonation products than in the hydraulic oil. A secondary factor is that the crack speeds are comparable to the sound speeds in the nitrogen case but a factor of 5 lower

than the sound speed in the detonation products.

Three principle physical processes associated with the fluid-structure interaction that will influence the fracture process have been identified. First, the pressure will begin to drop in the tube once a through-crack has developed and fluid begins venting out of the crack opening. This will reduce the pressure in the vicinity of the crack, lowering the hoop stress in the tube and reducing the crack driving force. Second, the local reduction in pressure due to the fluid venting will propagate through the fluid as an expansion wave, the head of this wave moving at the sound speed in the static fluid and with the sum of sound and flow velocities in the moving fluid. This will reduce hoop stress near or ahead of the crack tip, reducing the crack driving force. Third, the fluid does work through plastic deformation and acceleration of the "flaps" of material created by the fracture process. The amount of work that can be done is limited by the amount of energy initially stored in the fluid. This energy can be estimated from thermodynamic principles and compared to the elastic energy in the tube as well as the energy required to create new fracture surfaces. Brief explorations of each of these issues are given in the subsequent sections.

5.4.1 Venting

For a small (isentropic) change in specific volume Δv, the pressure drop ΔP is

$$\Delta P = \left.\frac{\Delta P}{\Delta v}\right|_s \Delta v = \left.\frac{\partial P}{\partial v}\right|_s \Delta v = -\frac{1}{K_s}\frac{\Delta v}{v}. \tag{5.2}$$

Inspection of the values in Table 5.2 indicates that the liquid will depressurize much more rapidly than the gases, causing the hoop stress near the original notch to rapidly decrease once the fluid starts to vent. For example, venting 0.5% of the original volume of the hydraulic oil is sufficient to drop the average pressure in the tube from 6 MPa to zero. On the other hand, venting a similar amount from the compressed nitrogen reduces the pressure by only 38 kPa, a factor of 10^2 less.

5.4.2 Expansion Waves

Expansion waves generated by the venting of fluid out of the crack opening will travel fastest in the detonation products and hydraulic oil and slowest in the nitrogen (Table 5.2). The situation is complex in the detonation case because the fluid is moving behind the detonation wave, creating a spatially nonuniform pressure field (Beltman and Shepherd, 2002). However, it is clear from the measured crack propagation speeds that the expansion waves travel five times faster than the crack tips and the detonation wave travels ten times faster than the crack tips.

This means that the expansion waves travel faster than the crack tips in both the hydraulic oil and the detonation cases. This will result in a decrease in the hoop stress and decreasing crack driving force as the crack tip grows. This is one factor that causes the cracks in the detonation case to arrest early rather than propagate to the end of the tube as observed in the nitrogen case. In the nitrogen loading case, the expansion waves travel at a speed comparable to the crack tip. This suggests that the stress field ahead of the crack will be relatively unaffected by the expansion wave until the cracks arrive at the tube ends.

5.4.3 Energy Storage

Internal pressurization of the tubes is associated with stored energy due to the compressibility of the fluid and the elastic nature of the tube material. This stored energy will be converted into kinetic energy and internal energy of the tube, fluid contents, and surrounding air. A notional energy balance for the process of fracture and tube rupture can be written as

$$\Delta U_{fluid}^{elastic} + \Delta U_{solid}^{elastic} = \Delta E_{fluid}^{K.E.} + \Delta E_{solid}^{K.E.} + \Delta E_{plastic} + \Delta E_{fracture} + \Delta E_{dissipated} \, . \tag{5.3}$$

A similar energy balance was considered by other researchers (Emery et al., 1986, Poynton et al., 1974). One of the main differences between the present study and

the other two studies is the energy associated with the fluid. While the other two considered only the part of fluid energy which does work on the fracturing pipe by assuming a pressure decay profile and a flap displacement pattern, the present study considers maximum energy that is stored in the fluid from a thermodynamic point of view. The energy balance above represents a total energy approach and is different from those that aim to derive the crack driving force (Freund, 1998, Kanninen and Popelar, 1985).

The terms on the left-hand side account for the elastic strain energy stored relative to the reference configuration of the tube and fluid at atmospheric pressure. The terms on the right-hand side include kinetic energy of the tube, energy for large-scale plastic deformation of the flaps, energy required for the fracture process, and dissipation due to heat transfer, etc., after rupture. Only a few of these terms will be estimated in this study.

Thermodynamic considerations can be used to provide upper bounds for stored energy in the fluid. For nitrogen, a perfect gas model $Pv = RT$ can be used and the stored energy estimated by considering isentropic expansion from the initial state (1) to the final state (2) at the pressure of the surrounding atmosphere

$$\Delta s = c_p \ln \frac{T_2}{T_1} - R \ln \frac{P_2}{P_1} = 0 \ , \ c_p = \frac{\gamma R}{\gamma - 1} \ , \ \frac{c_p}{c_v} = \gamma \ . \tag{5.4}$$

The compressibility varies inversely with pressure for an ideal gas

$$K_s = \frac{1}{\gamma P} \tag{5.5}$$

and this has to be taken into account when computing the stored energy for a gas. The simplest way to do that is to use the first law of thermodynamics and evaluate the work done as the change in internal energy during the expansion from state 2 to 1

$$\Delta u = c_v (T_1 - T_2) \ , \tag{5.6}$$

with T_2 computed from Eq. (5.4). The energy change per unit mass during isentropic

expansion of gaseous nitrogen is then

$$\Delta u_{nitrogen}^{elastic} = \frac{P_1 v_1}{\gamma - 1}\left[1 - \left(\frac{P_2}{P_1}\right)^{\frac{\gamma-1}{\gamma}}\right] . \tag{5.7}$$

A similar computation can be carried out for the high-pressure, hot gases behind the detonation wave, taking into account the kinetic energy in the products (Fickett and Davis, 2001).

The stored energy in the hydraulic oil can be computed from the first law of thermodynamics to be

$$\Delta u_{oil}^{elastic} = \int_{v_1}^{v_2} P dv . \tag{5.8}$$

Since the volume change of the liquid is quite small for the pressures being considered, it is easier to work with the pressure and write this as

$$\Delta u_{oil}^{elastic} = -\int_{P_1}^{P_2} v K_s P dP . \tag{5.9}$$

This can be simplified by assuming that the compressibility is constant so that by using the definition of K_s (Eq. (5.1)) and integrating to obtain the volume dependence on pressure,

$$v = v_1 \exp(-K_s(P - P_1)) . \tag{5.10}$$

Expanding in powers of the argument,

$$v \approx v_1(1 - K_s(P - P_1) + \mathcal{O}(K_s(P - P_1))^2 . \tag{5.11}$$

Retaining only the first term in this expansion, one can carry out the integration in Eq. (5.9) to obtain

$$\Delta u_{oil}^{elastic} \approx v_1 K_s \left(\frac{P_1^2 - P_2^2}{2}\right) . \tag{5.12}$$

For comparison, it is better to work on a unit volume basis since the tubes contain a

fixed volume of fluid. For the gaseous nitrogen, this will be

$$\frac{\Delta U^{elastic}_{nitrogen}}{V} = \frac{P_1}{\gamma - 1}\left[1 - \left(\frac{P_2}{P_1}\right)^{\frac{\gamma-1}{\gamma}}\right] = 10 \text{ MJ/m}^3 \, . \tag{5.13}$$

The Fickett-Jacobs thermodynamic cycle computation (Fickett and Davis, 2001, Wintenberger, 2003) for C_2H_4+$3O_2$ detonation products yields

$$\frac{\Delta U^{elastic}_{detonation}}{V} = 5.1 \text{ MJ/m}^3 \, . \tag{5.14}$$

For the hydraulic oil, this will be

$$\frac{\Delta U^{elastic}_{oil}}{V} \approx K_s \left(\frac{P_1^2 - P_2^2}{2}\right) = 15 \text{ kJ/m}^3 \, . \tag{5.15}$$

In these calculations, it was assumed that $\gamma = 1.4$, $P_1 = 6$ MPa, and $P_2 = 0.1$ MPa. The energy stored in the gaseous nitrogen per unit volume is 10^3 times larger than that of the oil.

The elastic energy stored in the tube can be estimated by assuming that the extensions were all in the radial direction. This is a reasonable approximation for most of the tube since the ends were a slip-fit into the flanges, and the pressure on the endplates was balanced by threaded rods. If the hoop stress was the only principal stress, the elastic energy stored per unit volume in the solid before rupture is

$$\frac{1}{2}\sigma\epsilon = \frac{\Delta P^2 R^2}{2Eh^2} \, , \tag{5.16}$$

where $\Delta P = P_1$ - P_2. The rate at which the tube's elastic energy is released during fracture requires an analysis based on the equations of motion and computation of the energy flux into the crack tip. Lacking this, as a first estimate, one can assume that all the elastic energy in a ring of material with volume $(2\pi Rh\Delta a)$ behind the crack tip is released during crack propagation. On this basis, the rate of elastic energy

released per unit crack advance is

$$\frac{\Delta U_{solid}^{elastic}}{\Delta a} \approx \frac{\Delta P^2 R^2}{2Eh^2}(2\pi Rh) = \frac{\pi \Delta P^2 R^3}{Eh} = 16 \text{ J/m} \tag{5.17}$$

for $\Delta P = 6$ MPa. From a fracture mechanics point of view (Broek, 1997), only a fraction of this energy will be used to create fracture surface because there are many other mechanisms for absorbing the stored energy in the fluid and tube. The energy requirement related to crack resistance (per unit crack advance) is

$$\frac{\Delta E_{fracture}}{\Delta a} \geq hG_c \tag{5.18}$$

where G_c is the fracture propagation toughness. Physically, this means that for fracture to occur, the rate of energy flow into the crack tip must be equal to or greater than the fracture propagation toughness. Although G_c was not measured for this study, it can be estimated (Broek, 1997) from the mode-I critical stress intensity of Al6061-T6

$$hG_c \approx h\frac{K_{Ic}^2}{E} = 12 \text{ J/m} \, . \tag{5.19}$$

The energy approximations above are summarized in Table 5.3. The energy stored in the fluid has been converted to energy per unit tube length to allow a more meaningful comparison with the elastic energy and fracture energy. It is clear that from energy considerations, the cracks were significantly shorter for oil loading than nitrogen loading because for the nearly incompressible liquid, a modest amount of stored energy was available to be converted to energy for driving a crack. For the very compressible gases, the stored energy was much larger, by a factor of 10^3, and ample energy was available to create fracture surfaces.

5.5 Conclusions

The differences in the rupture behavior were examined in terms of the physical parameters of the fluids and their influence on the physical processes involved in the

Energy	Det. (J/m)	N_2 (J/m)	Oil (J/m)
Fluid	6.9×10^3	13×10^3	20
Solid	16	16	16
Fracture	12	12	12

Table 5.3: Fluid energy stored per unit tube length compared to elastic solid energy release per unit crack advance and fracture energy expenditure per unit crack advance.

rupture event. The key role of fluid compressibility was highlighted. The striking difference between the results of tests with hydraulic oil and high-pressure gases can be explained in terms of stored energy in the fluid relative to the energy required for fracture surface generation. The initial stress state was an important factor in comparing the nitrogen and detonation cases. A secondary role of sound speed in determining expansion wave propagation was identified as probably being responsible for the observed differences between nitrogen and detonation products. Fluid compressibility is also a significant factor in the venting process that determines the pressure history once the crack begins to open.

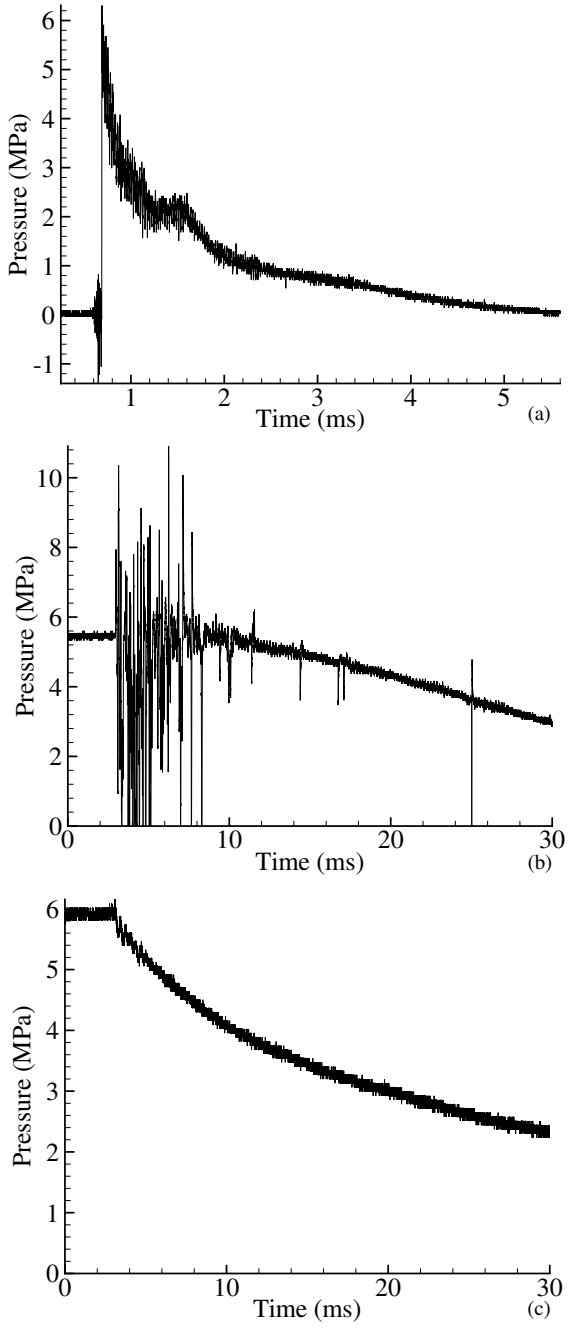

Figure 5.6: Pressure traces for detonation (a), nitrogen (b), and oil (c) loading.

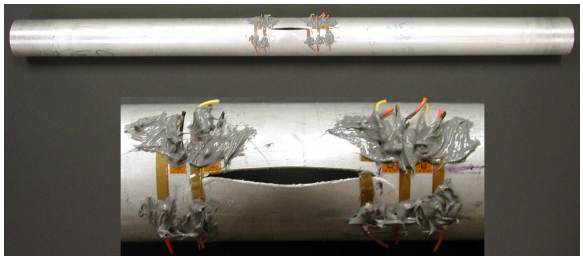

Figure 5.7: Post-test specimen of hydraulic experiment.

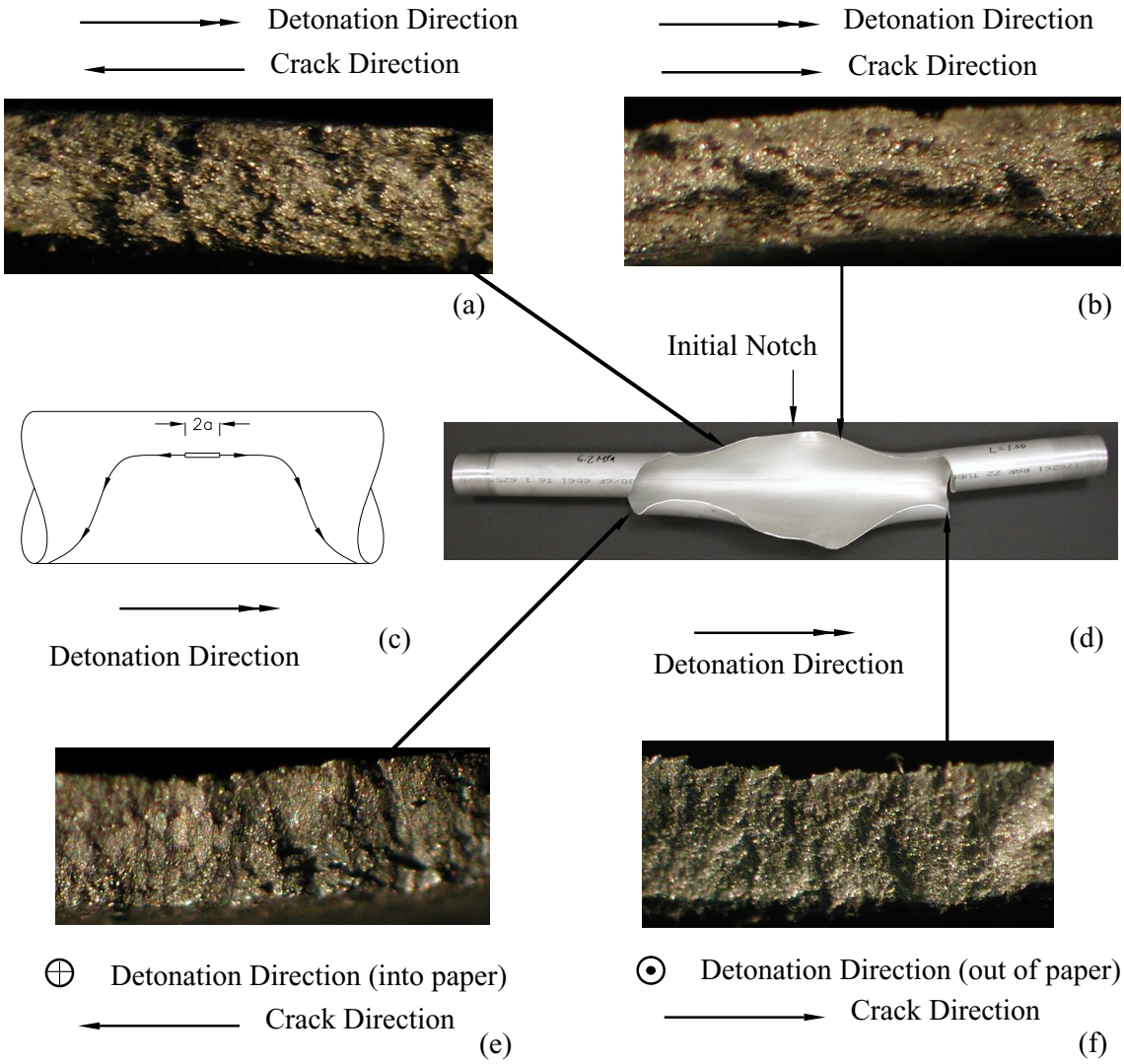

Figure 5.8: Fractographs, post-test specimen, and crack path schematic for a tube fractured under detonation loading.

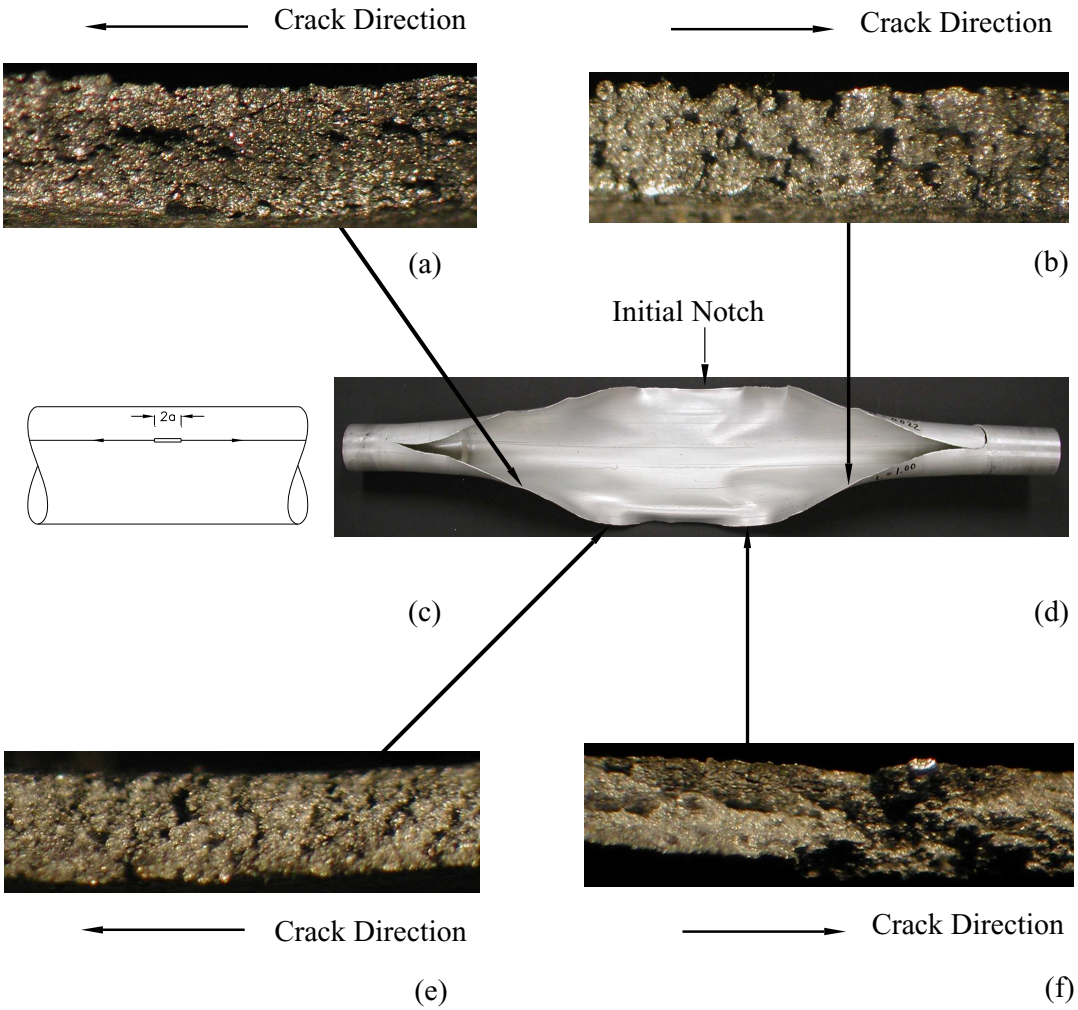

Figure 5.9: Fractographs, post-test specimen, and crack path schematic for a tube fractured under gaseous nitrogen loading.

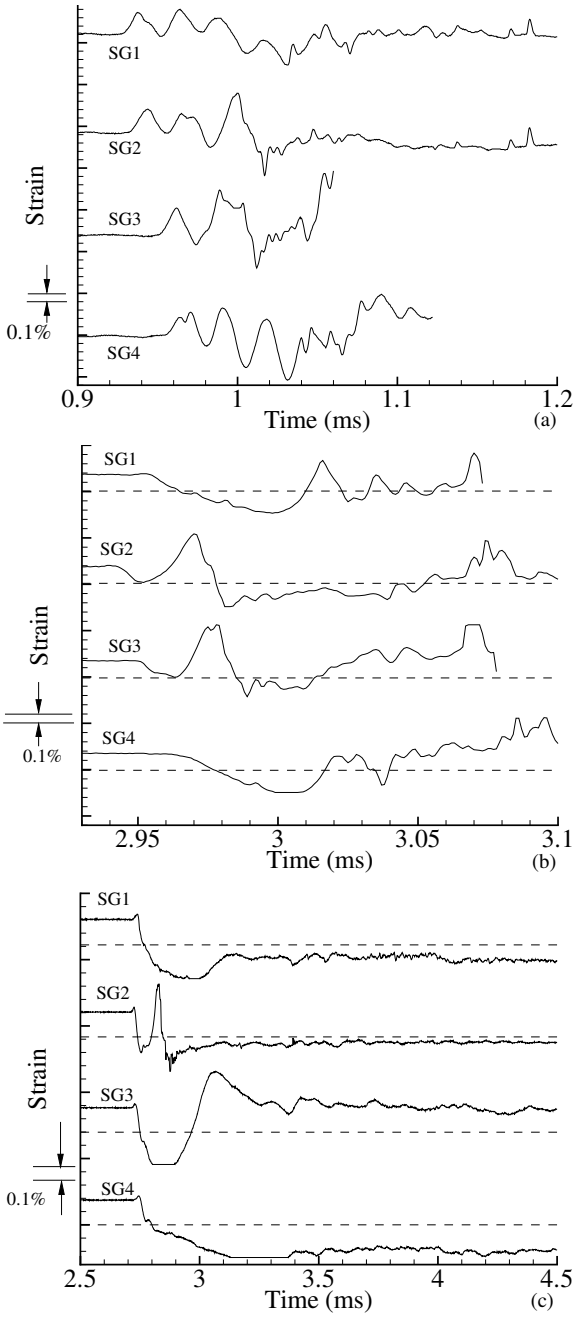

Figure 5.10: Hoop strains for detonation (a), gaseous nitrogen (b), and oil (c) cases. The initial strain is zero in all cases for the detonation case. For the static cases, strains begin at values corresponding to burst. Zero strains are indicated by dashed lines.

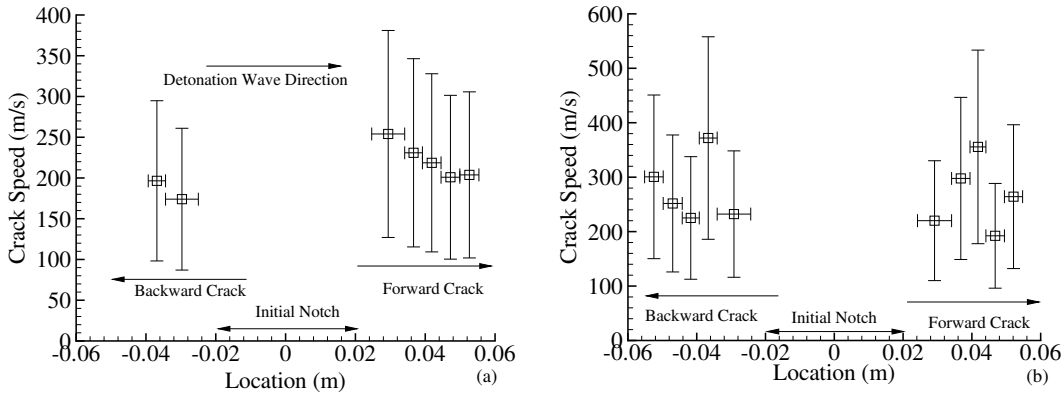

Figure 5.11: Crack speeds for a tube under detonation (a) and gaseous nitrogen (b) loading.

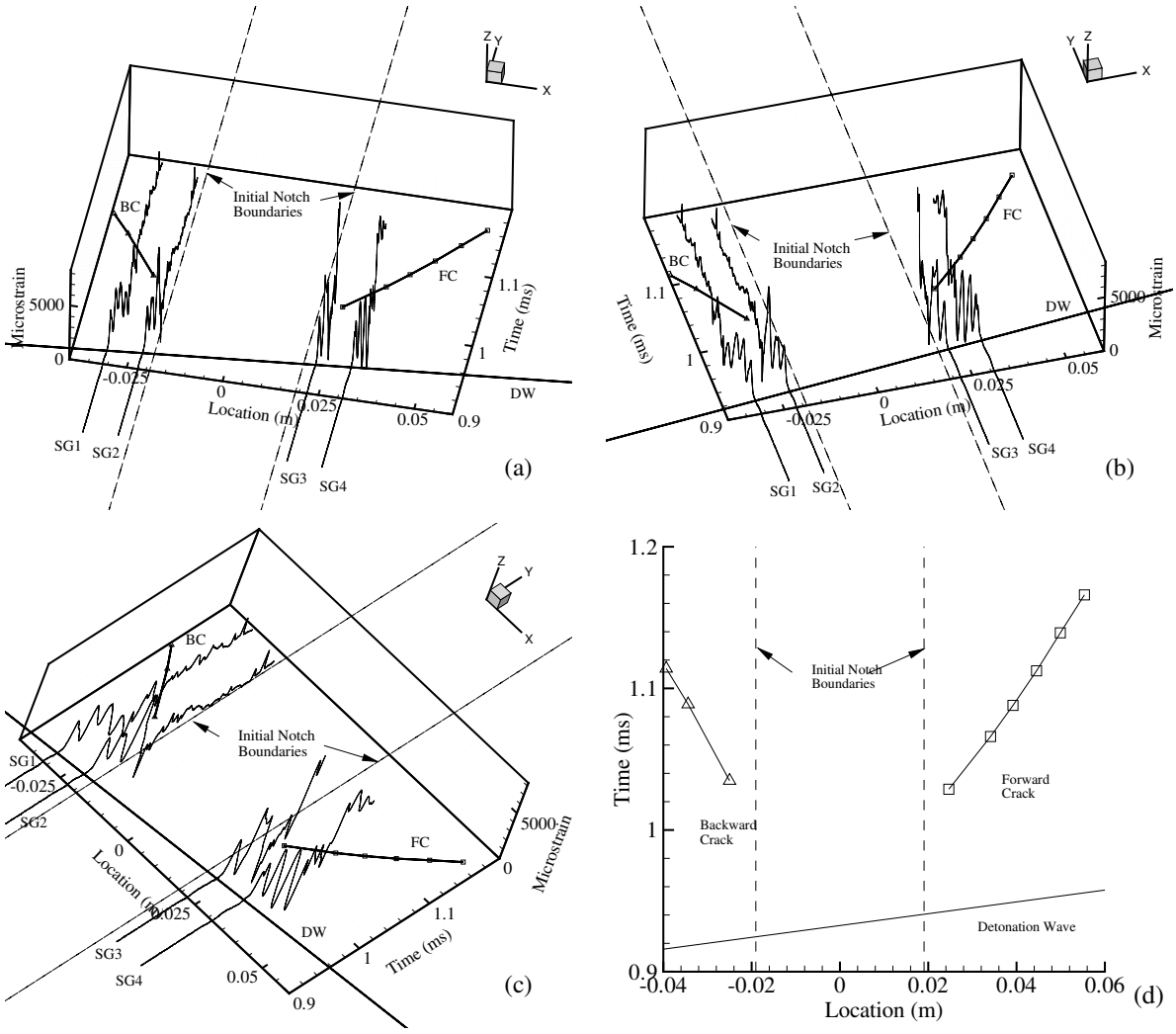

Figure 5.12: Representations of the x-t-strain diagram of a detonation experiment.

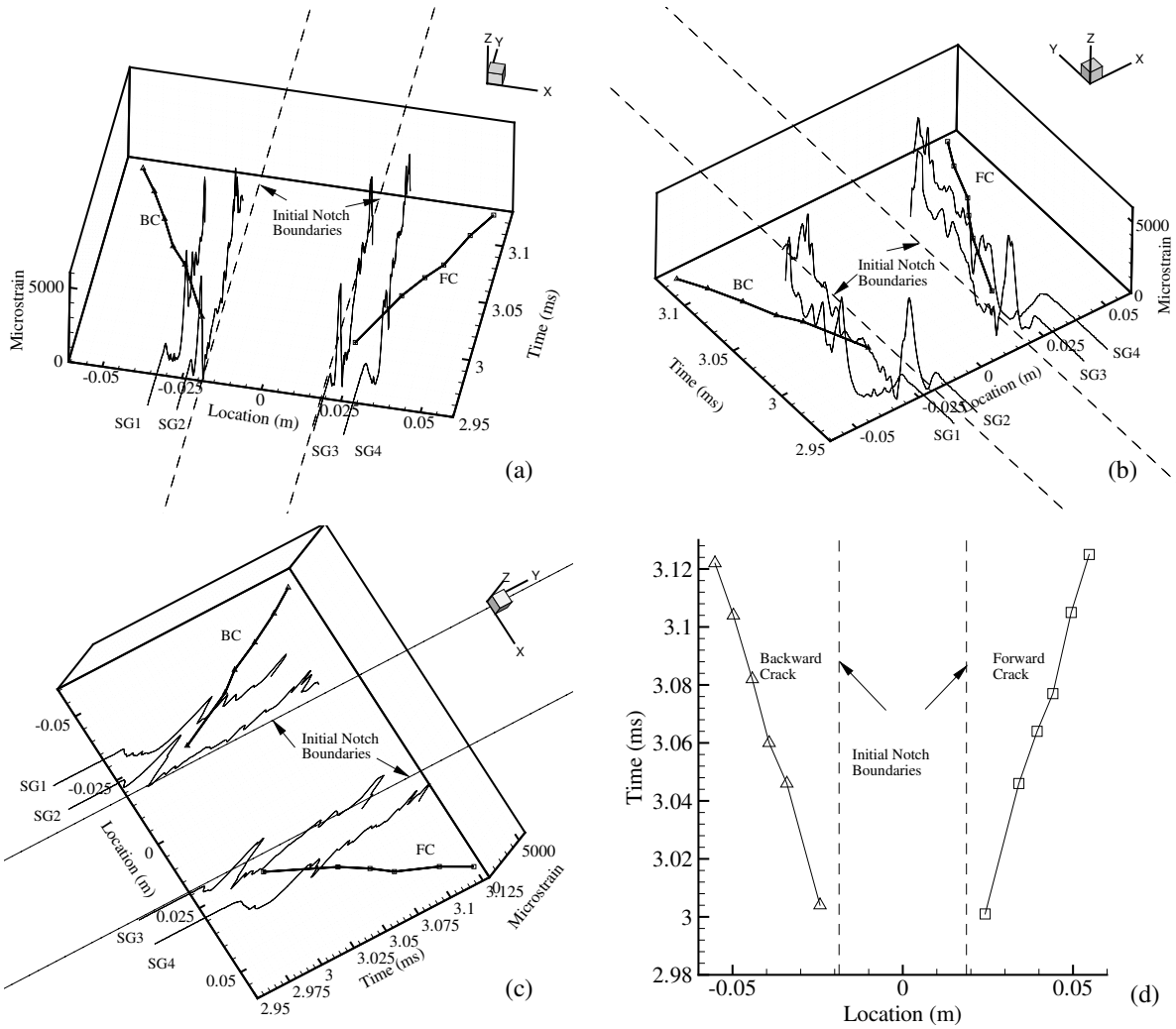

Figure 5.13: Representations of the x-t-strain diagram of a gaseous nitrogen experiment.

Chapter 6

Fracture Response with Applied Torsion

6.1 Introduction

In Chapter 4, the cracks ran without applied stresses. Since there was no control over the crack curving direction, it was nearly impossible to quantify the relation between stress-fields and crack paths. In this chapter, experiments with initial torque will be presented. The torque was applied to induce controlled crack kinking. The detonation pressure, initial crack length, and torque were varied. Strain, crack speed, detonation pressure, blast pressure from the crack opening, and digitized crack paths were recorded. High-speed movies of the rupture were also taken. The increased level of diagnostics allowed better understanding of the rupture events that was not possible in the previous two chapters.

6.2 Experimental Setup

6.2.1 Specimens

The tube specimens were made of aluminum 6061-T6. The walls were 0.89 mm thick and the tubes were 0.914 m long. Thirty-six experiments were performed on a single batch of material. The notch geometry can be found in Tables 6.1 and 6.2, and is also shown in Fig. 4.2. The specimens were roughened by sand-blasting at the surface

where the collets come into contact. This ensured a tight grip and high amounts of torque could be applied.

6.2.2 Test Matrix

As shown in Tables 6.1 and 6.2, the experiments are loosely categorized into series with the main varying parameters being crack length, detonation pressure, and torsion. In each series, the corresponding parameter was varied while the other variables were kept nominally constant (there were a few exceptions). The test mixture used was stoichiometric ethylene and oxygen. The initial pressure was varied to produce different CJ pressures. Table 6.3 shows the diagnostics used for each shot.

6.2.3 Detonation Tube Assembly and Torsion Fixture

6.2.3.1 Torsion Fixture Design

The detonation tube assembly was identical to those in Chapters 4 and 5. However, this time the assembly was mounted to a structural steel I-beam instead of a plywood table, and this is shown in Figs. 6.1 and 6.2. This increases the stiffness of the loading fixture relative to the specimen. Two fixtures applied torque on the specimen through steel blocks and collets. Simple strength of materials calculations showed that the compliance of the specimen was at least two orders of magnitude higher than that of the fixture. Detailed drawings of the setup can be found in Figs. B.1 to B.23.

Several conceptual designs were considered for the torsion fixtures. One conceptual design involved using compact translation and rotation stages from optics. This design allowed convenient translation and rotation of the loading fixtures to eliminate bending and misalignment, but it suffered from a high compliance. Another conceptual design with very high stiffness involved a steel gimbal fixture the size of a bowling ball. It was realized that this fixture was very clumsy to manipulate. The present design was a tradeoff between these two designs. It had the necessary stiffness and yet was not too difficult to manipulate.

Two fixtures were built. The first one (upstream) clamped down the specimen

Shot	L (mm)	$2a$ (mm)	d (mm)	P_{init} (MPa)	U_{cj} (m/s)	P_{cj} (MPa)	Torque (N-m)	Fracture behavior
Crack Length Series								
124	6.4	18.8	0.56	0.150	2395	5.1	131	No rupture
125	6.4	18.8	0.56	0.180	2404	6.1	123	Crack confined in notch
126	12.7	25.1	0.56	0.180	2404	6.1	164	Forward curving and backward bifurcation
149	12.7	25.1	0.56	0.180	2404	6.1	135	Forward and backward curving
127	38.1	50.5	0.56	0.180	2404	6.1	129	Forward curving and backward bifurcation
128	50.8	63.2	0.56	0.180	2404	6.1	135	Forward and backward bifurcation
148	50.8	63.2	0.56	0.180	2404	6.1	135	Forward and backward bifurcation
136	63.5	75.9	0.56	0.180	2404	6.1	136	Forward and backward bifurcation
135	76.2	88.6	0.56	0.180	2404	6.1	136	Forward and backward bifurcation
150	76.2	88.6	0.56	0.180	2404	6.1	135	Forward and backward bifurcation
Detonation Pressure Series								
134	25.4	39.4	0.71	0.100	2376	3.3	141	Short shear cracks
132	25.4	39.4	0.71	0.120	2384	4.0	141	Forward curving and backward bifurcation
133	25.4	39.4	0.71	0.120	2384	4.0	141	Forward curving and backward bifurcation
131	25.4	39.4	0.71	0.150	2395	5.1	141	Forward curving and backward bifurcation
129	25.4	39.4	0.71	0.180	2404	6.1	143	Forward and backward bifurcation
130	25.4	39.4	0.71	0.180	2404	6.1	142	Forward curving and backward bifurcation

Table 6.1: Torsion test matrix.

Shot	L (mm)	$2a$ (mm)	d (mm)	P_{init} (MPa)	U_{cj} (m/s)	P_{cj} (MPa)	Torque (N-m)	Fracture behavior
Torsion Series								
151	25.4	37.8	0.56	0.180	2404	6.1	-135	Forward and backward bifurcation
123	25.4	37.8	0.56	0.150	2395	5.1	-134	Forward curving and backward bifurcation
122	25.4	37.8	0.56	0.120	2384	4.0	-109	No rupture
121	25.4	37.8	0.56	0.180	2404	6.1	-41	Forward and backward curving
119	25.4	37.8	0.56	0.180	2404	6.1	-33	Forward and backward curving
138	25.4	37.8	0.56	0.150	2395	5.1	0	Crack barely left notch
139	25.4	37.8	0.56	0.180	2404	6.1	0	Forward and backward curving
120	25.4	37.8	0.56	0.180	2404	6.1	40	Forward and backward curving
137	25.4	37.8	0.56	0.150	2395	5.1	133	Forward curving and backward bifurcation
152	25.4	37.8	0.56	0.180	2404	6.1	159	Forward and backward bifurcation
153	25.4	37.8	0.56	0.180	2404	6.1	213	Forward and backward bifurcation
154	25.4	37.8	0.56	0.180	2404	6.1	231	Forward and backward bifurcation
Repeat Series								
140	25.4	37.8	0.56	0.165	2400	5.6	135	Forward and backward curving
141	25.4	37.8	0.56	0.165	2400	5.6	136	Forward and backward curving
142	25.4	37.8	0.56	0.165	2400	5.6	136	Forward curving and backward bifurcation
143	25.4	37.8	0.56	0.180	2404	6.1	135	Forward and backward curving
144	25.4	37.8	0.56	0.180	2404	6.1	137	Forward bifurcation and backward curving
146	25.4	37.8	0.56	0.180	2404	6.1	136	Forward and backward curving
145	25.4	37.8	0.56	0.180	2404	6.1	136	Forward and backward curving
147	25.4	37.8	0.56	0.180	2404	6.1	135	Forward and backward bifurcation

Table 6.2: Torsion test matrix (continued).

Shot	SG	CDG	PCB	BG	Video
119	√	√	√	√	
120	√	√	√	√	
121	√	√	√	√	
122	√		√		
123	√		√		
124	√		√	√	
125	√		√	√	
126	√	√	√	√	
127	√	√	√	√	
128	√	√	√	√	
129	√		√	√	
130	√		√	√	
131	√		√	√	
132	√	√	√	√	
133	√		√	√	
134	√	√	√	√	
135	√	√	√	√	
136	√		√	√	
137	√		√		
138			√		
139			√		√
140	√		√		√
141	√		√		√
142	√		√		√
143	√		√		√
144	√		√		√
145	√		√		
146	√		√		√
147	√		√	√	√
148	√		√		√
149	√		√		√
150	√		√		√
151	√		√		√
152	√		√		√
153	√		√		√
154	√		√		√

Table 6.3: Torsion test diagnostics: strain gages (SG), crack detection gages (CDG), piezo-electric gages mounted on detonation tube (PCB), blast gage (BG), and high-speed digital camera (Video).

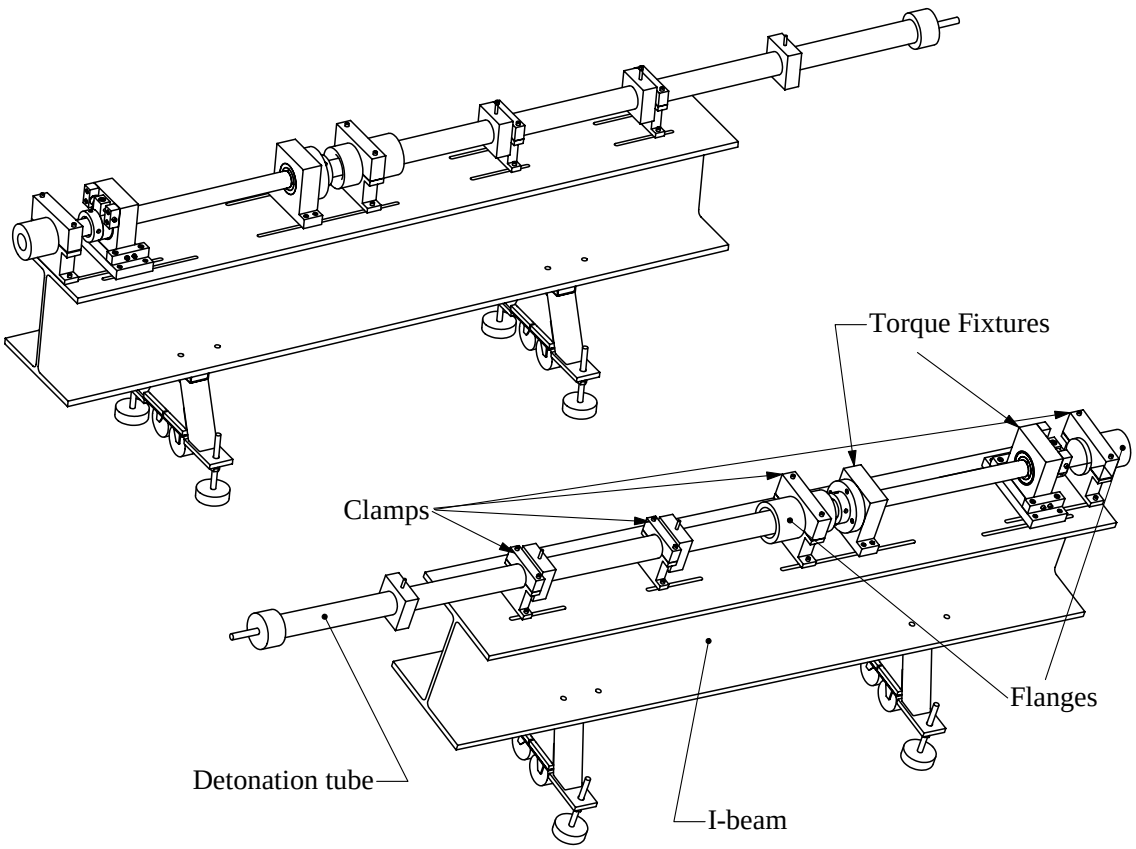

Figure 6.1: Perspective views of the detonation tube assembly and torsion fixture.

and acted as a fixed-end. The second one (downstream) allowed limited motion in six-degrees of freedom due a gimbal, an oil-impregnated bronze bushing, and large tolerances in the fastener through-holes and slots. The specimen's effective test length (measured from the front tip of one collet to the front tip of another) was chosen to be 457 mm. The torsion was applied by loading bolts whose perpendicular distance from the specimen axis (moment-arm) was 5.1 cm. After torsion was applied, these bolts were locked to create a fixed displacement boundary condition.

6.2.3.2 Assembly, Torsion Loading, and Bending Minimization Procedures

Close-ups of the torsion application fixtures can be found in Figs. B.4 ('torsion-end') and B.5 ('fixed-end'). The assembly procedure was based on experience and was de-

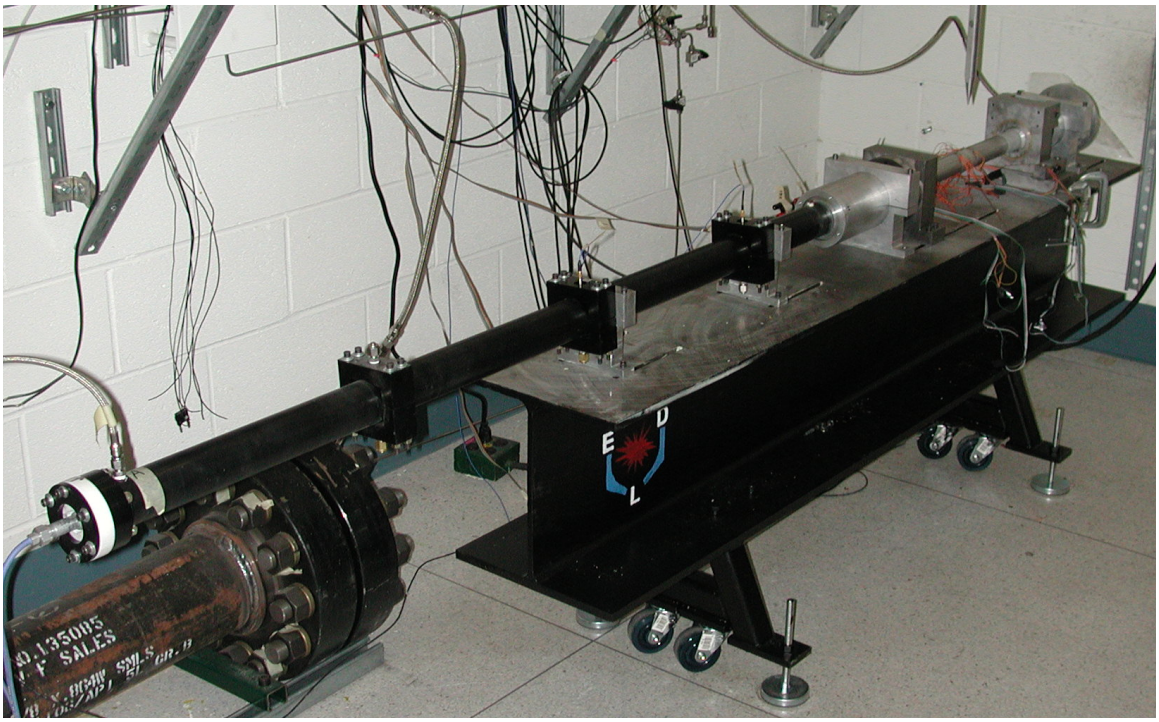

Figure 6.2: Detonation tube assembly and torsion fixture.

signed to minimize bending and maximize torque. Bending minimization sometimes required several realignments of the specimen and fixtures. Bending tolerance was measured in terms of axial strain. The assembly process began with a low bending tolerance. As the assembly progressed and more components were fastened and loaded, higher bending tolerance was allowed. The bending tolerance also increased with the applied torsion. The criterion for bending tolerance was that the bending stresses induced by the fixtures were much lower than the shear stresses. It will be shown later in Sections 6.3.5, 6.3.6, and 6.3.7.1 that this criterion was satisfied because the crack propagation directions were dominated by shear stresses and not by bending stresses.

The assembly and loading procedure is as follows. First, the specimen tube (sandblasted at the collet contact surfaces and instrumented with strain gages, crack detection gages, and Decal grid) was inserted into the collets of the fixed-end assembly and torsion-end assembly. At this point, the flanges were not connected to the specimen tube ends. The flanges should be connected to the specimen only after the

specimen was torqued. The bolts that fastened the fixed-end and torsion-end assemblies should be in place but not tightened. The leads of the strain gages and crack detection gages were soldered and connected. The Wheatstone bridges were balanced (it was crucial at this stage that bolts, collets, and flanges were not fastened so that a nominally stress-free state of the tube was measured). The bolts were then tightened to finger-tight level. The collets were tightened with a wrench. Axial strain readings were taken and the tube bending orientation and magnitude were deduced from beam theory. If the axial strain magnitude exceeded 60 $\mu\epsilon$ (a chosen bending tolerance), the specimen was realigned. This was done by loosening the collets and bolts, displacing the fixed-end and torsion-end assemblies, rotating the gimbal, and inserting appropriate number of shims (typically 0.3 mm thickness each) between the assembly bases and the I-beam to offset the bending. The bolts again were tightened to finger-tight level and the collets were tightened with a wrench.

After a few iterations of realignment, the axial strain magnitude was within the chosen tolerance. The other bolts of the fixtures were tightened with wrenches. The axial strains were measured again and the bending orientation deduced. If the axial strain magnitude exceeded about 100 $\mu\epsilon$ (a chosen bending tolerance), the specimen was realigned by loosening the bolts, displacing the fixed-end and torsion-end assemblies, rotating the gimbal, and inserting appropriate number of shims (typically 0.3 mm thickness each) between the assembly bases and the I-beam to offset the bending. The bolts were tightened to wrench-tight level.

As soon as the strain magnitude was within tolerance, the torsion was applied by advancing the loading bolt mounted on either of the side blocks (Fig. B.22). Either of the loading bolts on the side blocks could be used for loading, and the choice of the bolt determined the direction of torsion. The load was tranferred to the middle block on the gimbal (Fig. B.20). This load, coupled with a moment-arm, became torsion on the specimen. After loading was applied, the free loading bolt on the remaining side block was advanced into contact with the middle block. This contact prevented the collet from rotating once the tube ruptured and unloaded. Nuts were used to lock the two loading bolts into a fixed position. The boundary conditions of the specimens

were then in a displacement-fixed state. Axial strains were again measured and the tolerance at this point was chosen as 250 $\mu\epsilon$ for shots with torsion below 200 N-m and 450 $\mu\epsilon$ for shots with torsion above 200 N-m. Unloading and realignment were necessary if tolerance was exceeded. Torsion was deduced from shear strains measured with a strain gage rosette mounted in the middle of the tube length and 180° away from the notch. Shear strain was calculated by taking the difference in strain between the two outer gages (for example, the difference between the strain of SG1 and SG3 in Fig. A.146) of the three-element 45° rosette.

Next, the flanges were connected to the specimen tube and the detonation tube. The aft flange was sealed by a Mylar diaphragm and the tube assembly was connected to the gas filling station.

6.2.4 Instrumentation

Crack detection gages, strain gages, piezo-electric gages, oscilloscopes, and the LabVIEW program were used in the same way as in Chapter 5. In these experiments, the Phantom V5 CMOS camera (recording at 32000 frames per second for most shots) and a blast gage were also used. The camera was used to photograph the fracture and the blast wave coming out of the crack opening. The orientation of the notch is shown in Table A.1 and Figs. A.70 to A.72. For shots with crack detection gages (without the camera), the notch faced the ceiling. For shots in which the tube was rotated so that the notch was aligned with the camera, the line of sight was inclined at 10° to the horizontal. The blast gage was used to measure the pressure at some distance away from the notch. Unless otherwise stated, the blast gage was mounted at 24 cm above the notch. Strain gage rosettes, mounted 180° away from the notch, were also used to measure the shear strains.

6.3 Results and Discussion

The events associated with the rupture can be best understood by first examining the cines in Fig. 6.10 and Figs. A.55 to A.69. In the cines where the notch faces the

camera, the light from the detonation products came through the crack openings. The shape of the crack and the location of the crack tip can be seen clearly. Under the influence of the shear stress, the forward and backward cracks kinked according to the stress fields. As they propagated further, they either branched or curved. Figs. A.1 to A.32 show the digitized crack paths.

Since there was no theory or numerical simulation to guide the test matrix design, it was nearly impossible in the beginning to know how to choose the torque, detonation pressure, and flaw geometry. After many shots, patterns slowly emerged and the test matrix can be categorized loosely into crack length, detonation pressure, and torsion series.

6.3.1 Crack Length Series

The most obvious trends were made by the crack length series, in which the flaw size was varied from $2a = 18.8$ mm to 88.6 mm. The first thing to notice is that under nominally identical torsion and detonation pressure, as the crack length increased (Shots 149, 128, 143 to 148, 136, 135, 150), there is an increasing tendency for cracks to branch. This is due to the fact that by increasing the initial flaw length, there is a higher stress intensity factor and energy release rate to drive more cracks. The same trend has been observed in Chapter 4, except that, in the present experiments, the incipient cracks differ by kinking under the influence of torsion. Moreover, as the initial notch length increases, so does the blast pressure (measured 24 cm above the notch, Fig. 6.3). The blast pressure appears to be a linear function of initial flaw length for these flaw sizes.

6.3.2 Pressure Series

From Shots 129 thru 134, the detonation pressure was varied while other parameters were kept nominally constant. It is natural to expect that the blast coming out of the crack opening scales with the detonation pressure. Fig. 6.4 shows the blast strength as a function of detonation pressure. There is some non-repeatibility for Shots 132

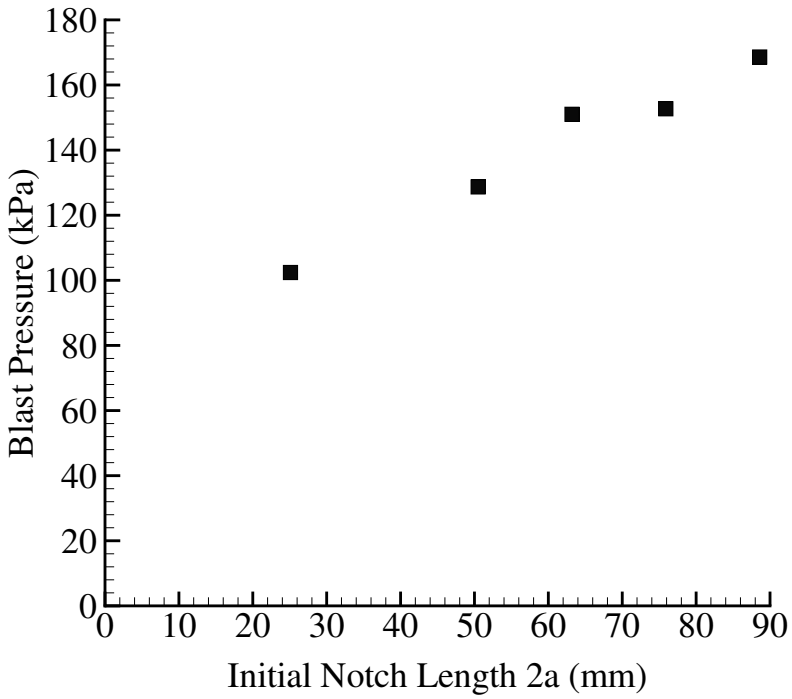

Figure 6.3: Blast gage pressure as a function of initial flaw length.

and 133 (P_{cj} = 4.0 MPa) and Shots 129 and 130 (P_{cj} = 6.1 MPa). The difference could be caused by variations in crack initiation time and crack speed.

A more interesting trend, however, is how fracture behavior was influenced by the detonation pressure while the other variables were kept nominally the same. The first trend to notice is that the cracks became shorter as the detonation pressure was reduced. Also, as the detonation pressure was decreased from Shot 130 to 134, the initial forward kinking angle increased (Table 6.4). The trend can be explained in terms of the ratio K_I/K_{II}. As the detonation pressure drops, the hoop stress decreases, and K_I/K_{II} decreases with increasing kink angle. Section 6.3.5 extends this trend for other shots with torsion.

6.3.3 Torsion Series

When the magnitude of torsion was below 100 N-m (Shots 119 to 121), the incipient crack kinking did not seem to follow the principle stress direction. It was only after the

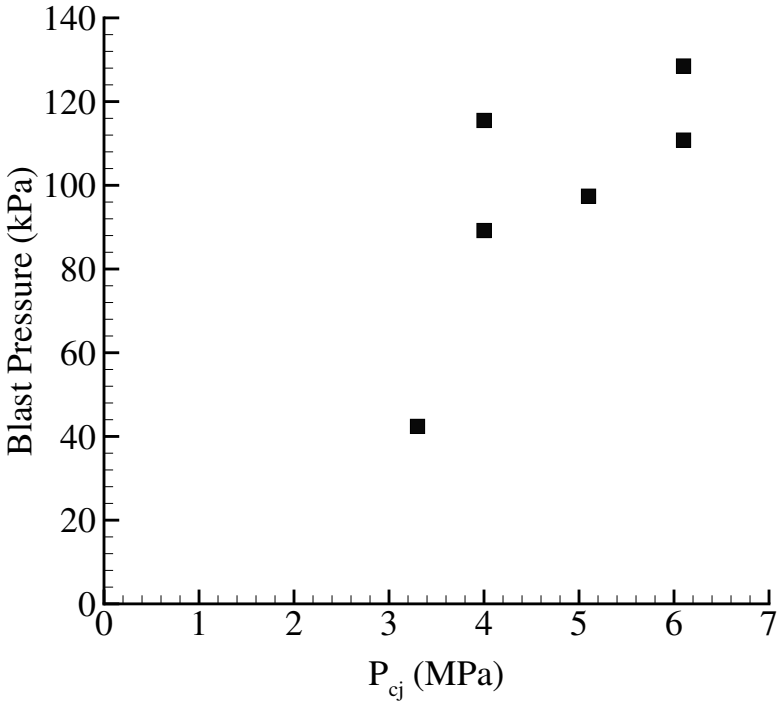

Figure 6.4: Blast gage pressure as a function of detonation pressure.

Shot	P_{cj} (MPa)	Forward Incipient Crack Kink Angle (degrees)
130	6.1	7
131	5.1	13
132	4.0	40
133	4.0	36
134	3.3	50

Table 6.4: Forward crack kink angle increases as detonation pressure drops.

torsion magnitude was increased above 100 N-m that both the forward and backward incipient cracks kinked according to the principle stresses. This can be explained by the fact that the hoop stresses caused by the detonation wave were so much larger than the shear stresses for torques below 100 N-m that this was not enough to kink the cracks.

Reversing the torsion not only reverses the incipient kink angle, but the subsequent curving crack paths were also reversed in direction. This can be seen by comparing the crack paths of Shots 147 (Fig. A.25) and 151 (Fig. A.29), which were the same in the number of branching cracks and nominally identical in every parameter except

the sign of the torsion. From these crack paths, it is clear that the initial static torsion had an influence on the crack path after the specimen ruptured and increased in its compliance.

6.3.4 Repeat Series

Experiments with repeated initial conditions and loading were performed. The reader is referred to Tables 6.1 and 6.2 for the initial conditions. Repeat conditions were imposed for Shots 140 thru 142 and Shots 143 thru 147. Additional couples of repeats include 128 and 148, 135 and 150, and 132 and 133.

Examination of the crack paths shows that the incipient crack kink angles were fairly repeatable, but the overall crack paths were not very repeatable. The kink angles for different repeated sets are compared in Table 6.5. In Sets 1 and 2, the notch was oriented in a fixed direction with respect to the fixture. In Set 3, the notch was rotated between shots to see if rotational symmetry of the experiment was preserved. It was found that the greatest variation in kink angle was produced when the tube was rotated 90° (Shot 146).

Shot	Backward Crack (deg.)	Forward Crack (deg.)	Comments
Set No. 1: P_{cj} *= 4.0 MPa, Nominal Torque = 141 N-m,* $2a$ *= 39.4 mm*			
132		40	
133		36	
Set No. 2: P_{cj} *= 5.6 MPa, Nominal Torque = 136 N-m,* $2a$ *= 37.8 mm*			
140	16	27	
141	17	26	
142	22	16	
Set No. 3: P_{cj} *= 6.1 MPa, Nominal Torque = 136 N-m,* $2a$ *= 37.8 mm*			
143	30	20	Notch aligned with camera (0°)
144	26	15	Notch aligned with camera (0°)
145	22	24	Notch rotated 180°
146	60	11	Notch rotated 90°
147		25	Notch rotated 270°

Table 6.5: Repeatability of incipient crack kinking angles.

6.3.5 Incipient Crack Kinking Angle and Mixed-Mode Fracture

The incipient crack kinking angle (measured from the tip of the notch) is governed by the ratio of mode I to mode II. If the tube can be modeled as a flat plate with an initially through-crack, then the stress intensity factors may be estimated as

$$K_I = \sigma\sqrt{\pi a} = \frac{\Phi P_{cj} R\sqrt{\pi a}}{h} \tag{6.1}$$

and

$$K_{II} = \tau\sqrt{\pi a}, \tag{6.2}$$

where τ is the shear stress. This leads to

$$\frac{K_I}{K_{II}} = \frac{\Phi P_{cj} R}{h\tau}. \tag{6.3}$$

A plot of this ratio against the kink angle is shown in Fig. 6.5. The crack kinking angle for static two-dimensional mixed-mode loading (using the local $k_{II} = 0$ criterion) from numerical data by Melin (1994) is plotted as solid lines for comparison. There is a fair scatter, given the very approximate nature of estimating the dynamic K_I.

6.3.6 Reflected Shear Wave

The fracture events after incipient crack kinking at the notch tips can be explained by wave mechanics. As the crack tips propagated, release waves were sent at shear wave speeds (3100 m/s) from the crack opening to both ends of the tube. Once fracture occurred, it took 147 μs for shear waves to travel from the center of the tube to the loading devices and back. Since the tube was clamped at the torsion fixtures, these release waves reflected as shear waves that are in *opposite* sign to the originally applied torque. However, since other flexural waves were present, the sign reversal was not

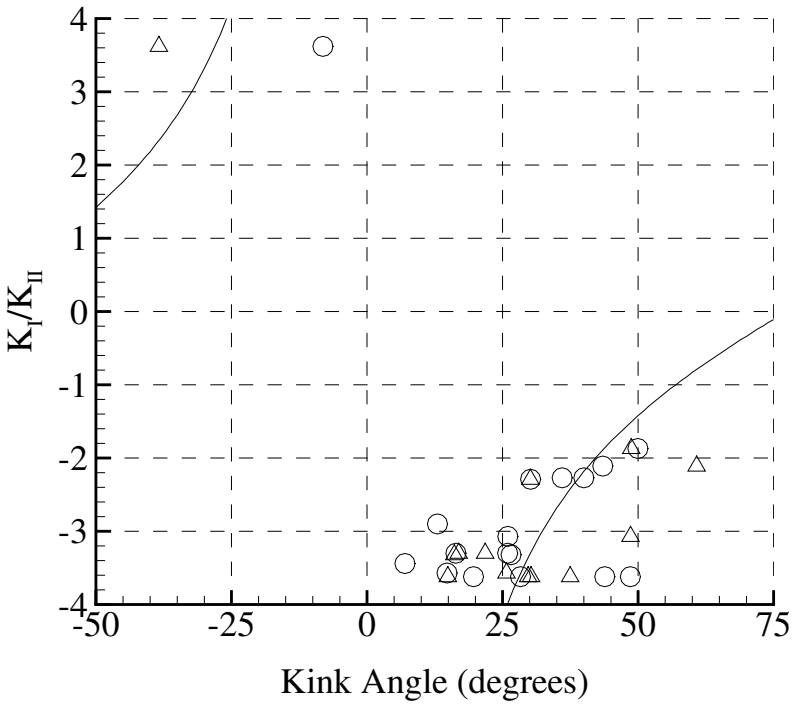

Figure 6.5: K_I/K_{II} versus crack kinking angle. Circles: forward cracks. Deltas: backward cracks. Solid lines: numerical data from Melin (1994) using a local $k_{II} = 0$ criterion.

'clean' (compared to, say, the longitudinal stresses in one-dimensional Hopkinson bar experiments). When these reflected shear wave fronts met in the middle of the tube, they superpose in magnitude. The consequence of shear reversal was that sometimes the cracks changed direction (Shots 140, Fig. A.18, and 143, Fig. A.21), or that additional cracks, kinking in directions opposite to the original ones, initiated from the notch tips. The dynamic shear and axial strains were captured by strain gage rosettes opposite to the notch and these are plotted in Figs. A.149 to A.180.

6.3.7 The Role of Other Prestresses

6.3.7.1 Bending

In Chapter 4, fixture-induced bending stress (T-stress) was measured and used to explain crack curving. Significant torque was applied in the present experiments and it was shown clearly in Section 6.3.5 that K_I/K_{II} had a predominant effect on

the initial kinking angle. Yet, in Table 6.5, it was shown that sometimes the crack kinking angle was very non-repeatable (e.g., Set 3, Shot 146). It was suspected that the bending-induced T-stress was the cause of the variance.

Static axial strains were measured prior to each shot from 143 to 146 (corresponding to Set 3 in Table 6.5). These axial strains were measured at 90° and 180° away from the notch. Using a strength of materials approach, the bending moment, inclination of the neutral plane, and the bending-induced axial stress at the fibre along the notch were calculated. Fig. 6.6 shows the sign convention for the calculations and Table 6.6 shows a comparison between the various stresses. It can be seen that 1) since Shot 146 does not have a large positive T, the bending alone cannot explain why this shot's kink angles had such a high difference from the other companion shots; 2) the inclination of the neutral plane did not change according to the rotation of the tube (refer to Table 6.5 for the rotation angles); and 3) even when the tube specimen orientation was fixed with respect to the fixture between Shots 143 and 144, both the neutral plane inclination and bending moment changed significantly, indicating that bending was not reproducible between change of specimens.

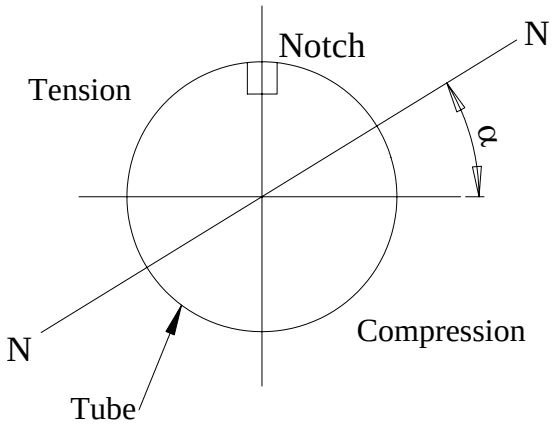

Figure 6.6: Sign convention for bending-induced axial stresses in Table 6.6. N-N indicates the neutral plane. Detonation direction is out of paper.

Shot	α (deg.)	M (N-m)	T (MPa)	$\Phi P_{cj}R/h$ (MPa)	τ (MPa)
143	132	19	-11.6	277	-77
144	162	5	-4.6	277	-78
145	95	11	-0.9	277	-77
146	106	17	-4.1	277	-77
147	3	4	3.7	277	-77

Table 6.6: Comparison of bending stress at the notch (T), dynamic hoop stress ($\Phi P_{cj}R/h$), and shear stress (τ). M is the bending moment and α is the inclination of the neutral plane.

6.3.7.2 Compression

The collets at the torsion fixtures generated compressive stresses on the specimen. However, the compression decayed very quickly along the tube length and did not influence crack paths. The influence was calculated analytically and it was found that compressive axial and hoop stresses decayed to negligible values within half a tube diameter away from the collet. This was verified by measurements of hoop strains near the collet. Compressive hoop strains right next to the collet after tightening were measured to attain 600 $\mu\epsilon$. At about 6 cm along the tube length away from the collet, the measured hoop strains dropped to about 40 $\mu\epsilon$.

6.3.8 Crack Speed

The measured crack speeds were highly transient and sometimes even appeared to be oscillatory. This is related to the highly oscillatory nature of the flexural waves which were observed many times in previous chapters. Crack speeds were measured by crack detection gages for Shots 119 to 136 (Figs. A.33 to A.41), and by the Phantom camera for Shots 139 to 154 (Figs. A.42 to A.54). Since only four crack detection gages were mounted next to each notch tip, there were three data points at most for the crack speed plots using crack detection gages. Whenever branching cracks occurred from a crack tip, the crack detection gage data had to be discarded because it was not certain which of the two crack tips's speeds the gages were measuring. The data presented for crack detection gages were, hence, for single crack fronts only.

No particularly striking trend is discerned in these plots. High crack speeds (close

to 300 m/s) were measured for certain cracks. They include those that ran within the notch (Shot 141, Fig. A.44), cracks that were about to branch, and cracks that began to curve and go into predominantly mode III. Slow crack speeds (below 50 m/s) were measured for Shot 134 (where the P_{cj} was as low as 3.3 MPa).

6.3.9 Blast Wave

The orientation of the notch is shown in Table A.1 and Figs. A.70 to A.72. The initial notch was oriented towards the ceiling in Shot 147 and towards the I-beam in Shot 146 to examine the shape of the blast. The blast initially appeared as an oblique jet 20° from the vertical axis (Fig. A.61 to A.63). The jet direction was consistent with the flow direction inside the tube.

Three shots (119 to 121) were performed with the same flaw size ($2a = 37.8$ mm) and detonation pressure ($P_{cj} = 6.1$ MPa), but with the blast gage at different vertical distances from the notch. The blast pressure, ΔP, varied inversely with the gage distance from the notch (Fig. 6.7).

Blast pressure traces can be found in Figs. A.73 to A.89. There was some contamination due to the diffracted shock wave emerging from the aft end of the specimen tube. Figure A.76, for Shot 124 with no rupture, shows the magnitude of pressure (9 kPa at 3 ms) measured at the gage caused by the diffracted shock wave. Figure A.77 shows the blast pressure for Shot 125 with the crack confined within the notch. Distinct pressure pulses with smooth rises can be seen, with the one at 1.7 ms corresponding to the crack opening, and the one at 3 ms corresponding to the diffracted shock wave from the tube end. All other pressure traces indicate shock waves with abrupt pressure rises.

6.3.10 Comparison of Finite-Element Simulation and Experiment

Shot 148 was selected for numerical simulation. The simulation was performed using the commercial code LS-Dyna V. 960. Since three-dimensional shell elements were

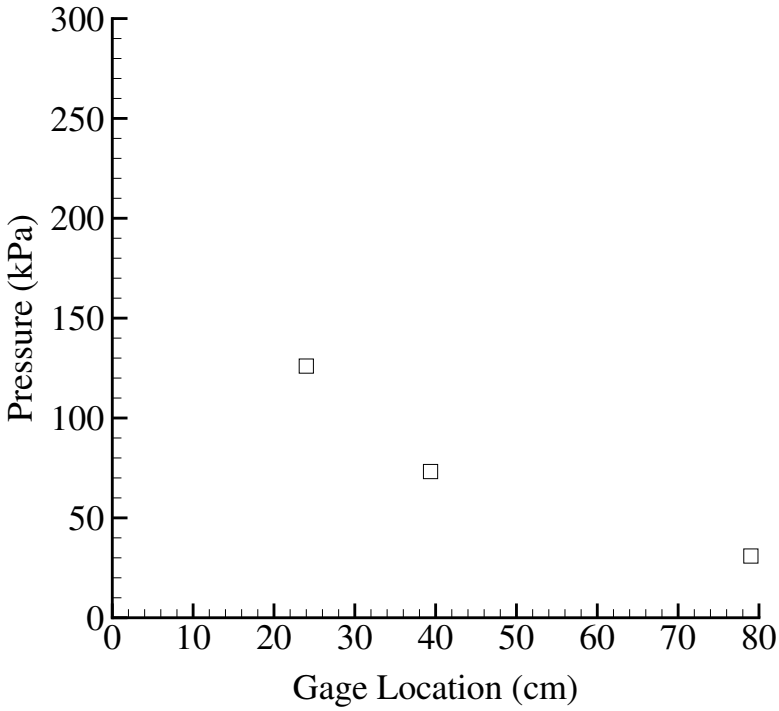

Figure 6.7: Blast gage pressure as a function of distance from the notch.

used, the inital flaw was modeled as a through-crack. This was done by untying nodes at predetermined places. There were 403712 elements used. The mesh size was 376 micron by 382 micron. The detonation was modeled as a traveling pressure load with a linear decay. The material was modeled as an isotropic elastic-plastic model (Material Type 3). The stress strain curve was modeled bilinearly. The material was set to yield at 275 MPa, and elements were set to fail (erode) at a failure strain of 12% and a failure stress of 310 MPa. Only 457.2 mm of the tube length was simulated because this was the distance between the torsion fixtures in the experiment. The simulated tube was fixed at the upstream end and a distributed moment was applied at the downstream end. Significant material damping was applied to remove the transient torsional stresses. After two milliseconds of damping, the tube reached steady stress state, the damping was turned off, and the traveling load was applied.

Results from finite-element simulation of Shot 148 are shown in Figs. 6.8 and 6.9. Contours of maximum shear stress are plotted. The interframe time shown here is 20 μs. The cine from the experiment is shown in Fig. 6.10. The interframe time for the

cine is 31 μs.

It can be seen that the simulation captured the general qualitative fracture behavior in the experiment. Two sets of branched cracks are seen to form from the forward and backward crack tips. The forward crack is seen to kink before branching. However, the crack speeds in the simulation were much higher than those in the experiment. Also, the crack paths were different.

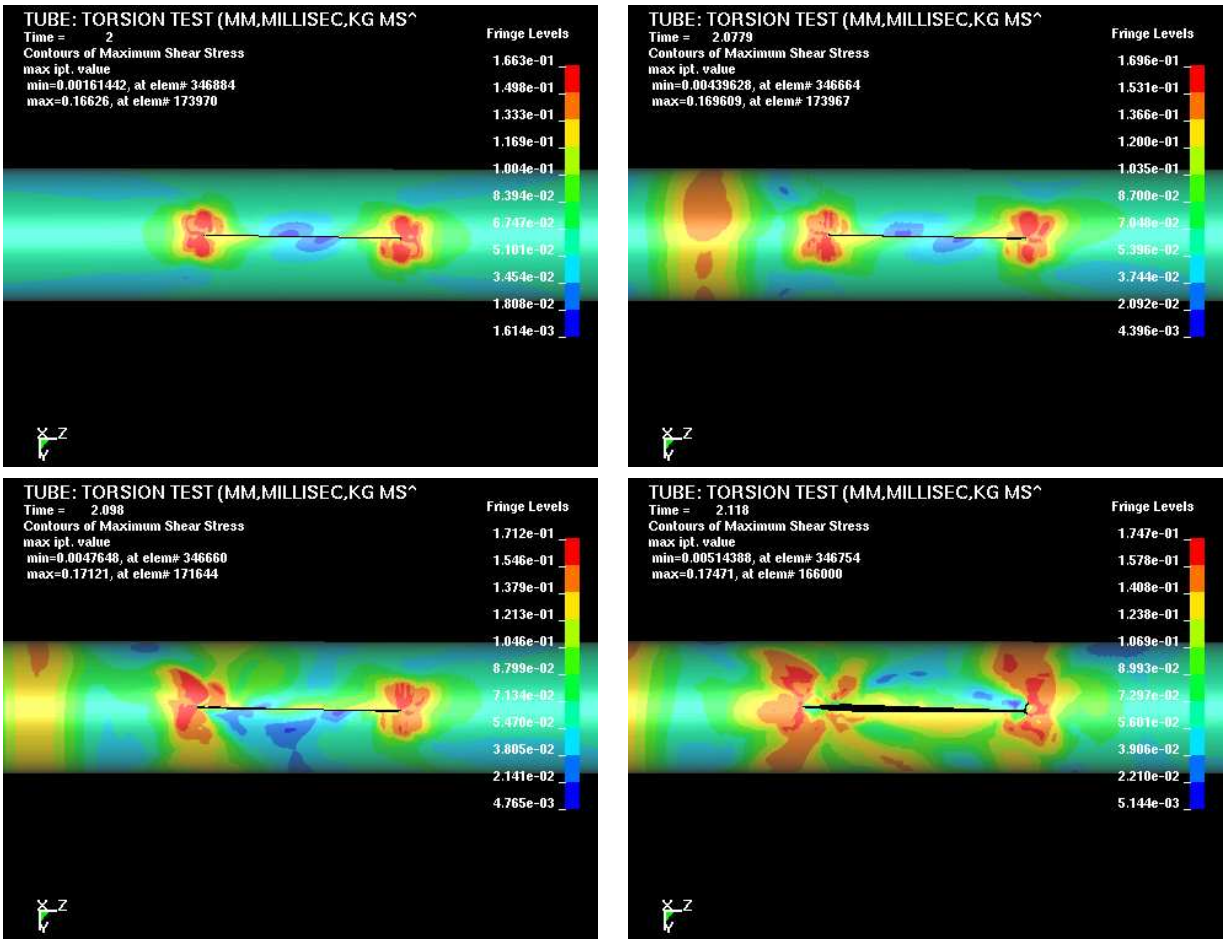

Figure 6.8: Fracture simulation of Shot 148. The first frame shows the initial stress state after the tube was torqued. In the second frame (upper right), the stress front (coincident with the detonation front) is seen approaching the backward crack tip. Contours of maximum shear stress are plotted. Color scale represents stress in GPa.

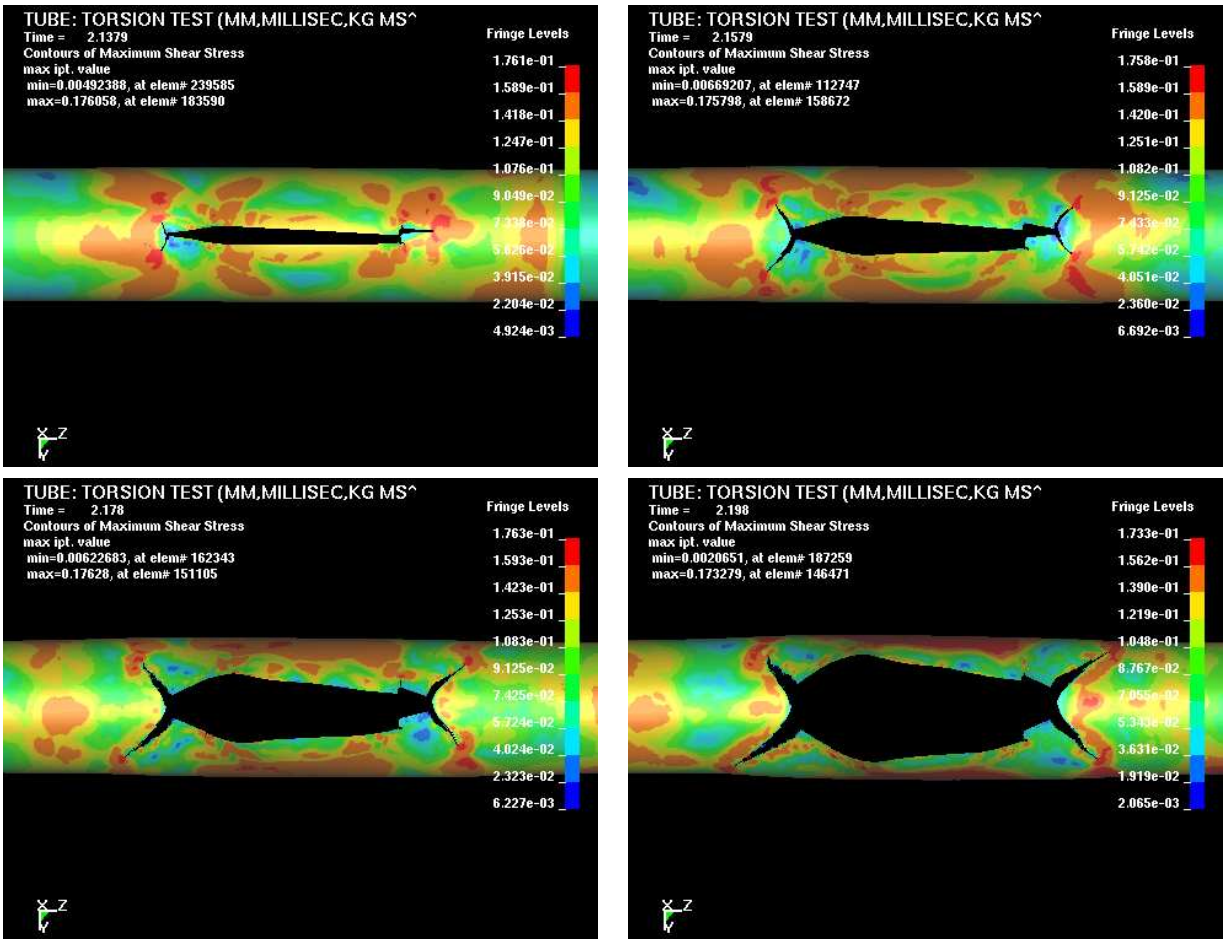

Figure 6.9: Fracture simulation of Shot 148 (continued).

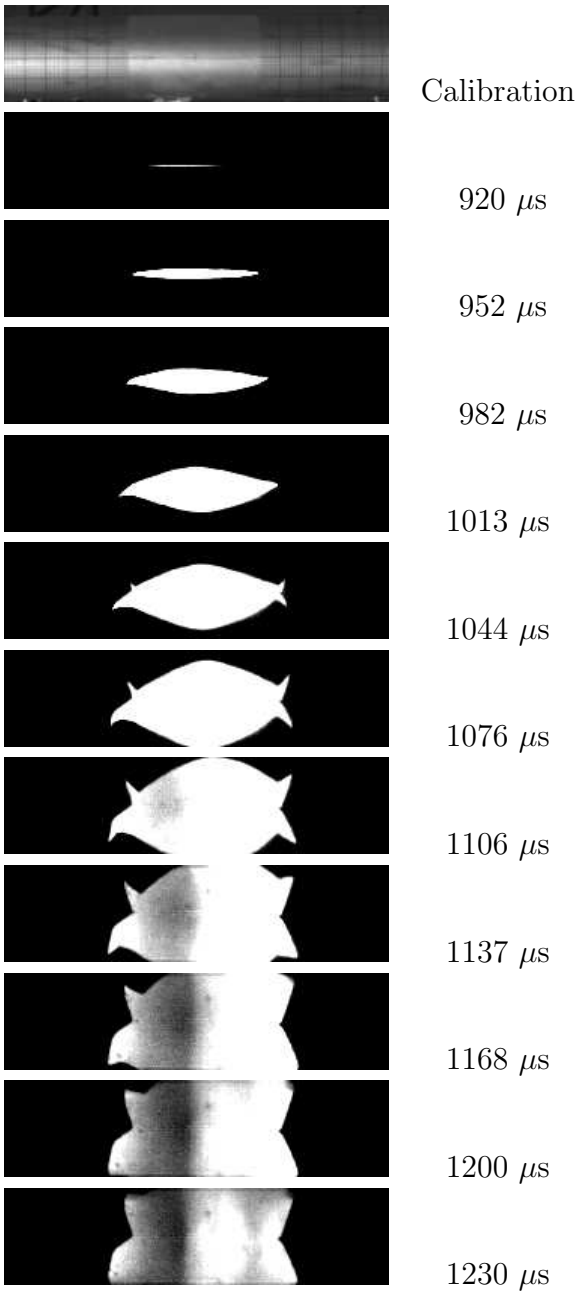

Figure 6.10: Shot 148.

6.3.11 Uncertainty Considerations

The uncertainty associated with crack speeds depends on the diagnostics. For crack detection gage measurements, the uncertainty in speed is about ±100 m/s (an upper bound considering the spacing between the gages). For the camera measurements,

the uncertainty depends on the pixel size. The cracks that faced the camera were imaged with 256 × 56 pixels. This translated to about 0.7 mm per pixel typically. Uncertainty in the crack tip location from the cines was about ±1 pixel, giving an uncertainty in the crack speed of about ±50 m/s typically.

The post-test specimens were often highly deformed, making accurate crack kinking angle measurements difficult. A conservative estimate on the uncertainty of kink angle is ±5°.

6.4 Conclusions

Fracture experiments were performed with torsional loading in an attempt to control the crack paths. Both the experimental setup and diagnostics were much improved from those in previous chapters. As a result, much better understanding of the fracture and blast events was attained.

The control was highly successful in the initial stages of fracture, with incipient cracks kinking at expected directions under the combined detonation-induced hoop stress and torque-induced shear stress loading. Cracks reversing curving directions were observed in some cases. In others, cracks initiated at the notch tips at a later time with reversed kinking directions. Both these phenomena were consistent in terms of timing and the sign of shear waves that reflected from the torsion devices.

Blast waves that emerged from the crack opening were registered as weak shocks at pressure gages. The blast waves were initially seen as jets at angles consistent with the flow direction of the detonation products.

Fair repeatibility was achieved for incipient crack kinking angles. An analysis on the bending stress did not show that T-stress was the main cause of variance in the crack kinking angles. Other uncertainties (material, machining, etc.) may be the reason, but these uncertainties could not be quantified with present techniques. Once the crack tips travel beyond one tube diameter of the notch tip, the crack paths became, in general, much less repeatable.

An attempt was made to numerically simulate the fracture process. Although

the process was simulated without regard to the fluid-structural interaction, with a very simple plastic strain failure criterion, and with a mesh much coarser than those in more accurate crack propagation simulations, the crack branching behavior was captured. This successfully shows how much simplification can be made to obtain the basics of the fracture process.

Chapter 7

Conclusions and Recommendations

7.1 Summary

A wealth of quantitative and visual experimental data on gaseous detonation-driven fracture of tubes, never available before in the open literature, was obtained. The new results of this experimental and numerical study will be extremely important to future fracture mechanics-based design of systems under gaseous detonation loading, and to simulation experts who want to challenge themselves with simulating this type of complicated fluid-structure-fracture interaction phenomena.

This investigation began with the linear elastic response having CJ speeds near the material shear wave speed. One important new result was that a resonance in transverse shear near the shear wave speed, similar to the flexural resonance at the first critical load speed, was found numerically. The study continued with observations in fracture without intentionally applied static loading. Crack branching and helical curving were observed for different initial flaw sizes. A fracture threshold model, first of its kind for gaseous detonation-loaded tubes, was developed and compared well with experimental data. Next, crack speeds, fracture behavior, and strain of detonation-loaded specimens were compared, for the first time, with specimens quasi-statically loaded by gaseous nitrogen and hydraulic oil. With the specimen geometry, flaw geometry, and pressure magnitude nominally identical, the difference in results was striking, and these were analyzed in terms of fluid mechanics and energy storage.

An I-beam supported loading assembly was constructed to apply torque onto the

specimen to control the crack curving direction. Such combination of controlled loading and geometry had never been attempted before in fracture experiments. Under large torques, the cracks were forced to kink according to mixed-mode loading conditions. High-speed movies of the fracture events were invaluable in interpreting the quantitative data including strain, crack speed, pressure, blast shape, and fracture sequence. After initial kinking, some cracks were observed to reverse curving directions under the influence of reflected shear waves that were measured by strain gage rosettes. In many cases, additional cracks initiated at the notch tips because of these reflected waves. The flow coming out of the crack opening was observed to be a jet at an angle consistent with the detonation product flow direction. Crack speeds ranging from 20 to 350 m/s were measured, and the difference in crack speed was attributed to the mode of fracture and detonation pressure. A simulation was performed using the conditions from one of the torque-controlled fracture experiments. The simulated fractures were directly compared with the experimentally observed ones. The simulated fracture behavior was found to be qualitatively consistent with experiment.

7.2 Future Work

The next most productive step will probably involve simultaneously imaging the crack flaps, crack fronts, detonation wave front, and the shock waves with transparent specimens and better optical techniques. Examples of results of a preliminary visual experiment involving polycarbonate under gaseous detonation loading can be seen in Figs. 7.1 and 7.2. The detonation front is clearly visible, followed by the rupture initiating from the initial axial flaw.

Future flow measurements may include optical flow visualization based on interferometric or shadowgraph methods. The three-dimensional nature of the flow field will require simultaneous multi-axis, time-resolved visualization. The location of the crack tips can be visualized using optical measuring systems such as caustics. A proposed setup for simultaneous visualization is shown in Fig. 7.3 for a transparent rupturing tube specimen, such as polycarbonate. It involves two light beams

with one going through the tube (Optical Path 1), which reveals the caustic at the crack tip due to a Poisson contraction effect and the detonation wave front inside the tube. This will yield information about the crack tip position, crack velocity, and the crack's interaction with the detonation wave front. The other beam (Optical Path 2), perpendicular to the first one, illuminates the crack flaps and the emerging detonation products. This will yield information about the boundary conditions for the shock-flap interaction. Pictures can be obtained from an additional (third) beam (not shown) parallel to the axis of the tube. A high-speed camera can be used to record images created by tiling information from different optical paths into a single segmented image. Conventional piezo-electric pressure transducers can be used to record pressures inside and outside of the tubes. Simultaneous, multi-axis visualization in this fashion will inevitably yield a new level of understanding of gaseous detonation-driven tube fracture.

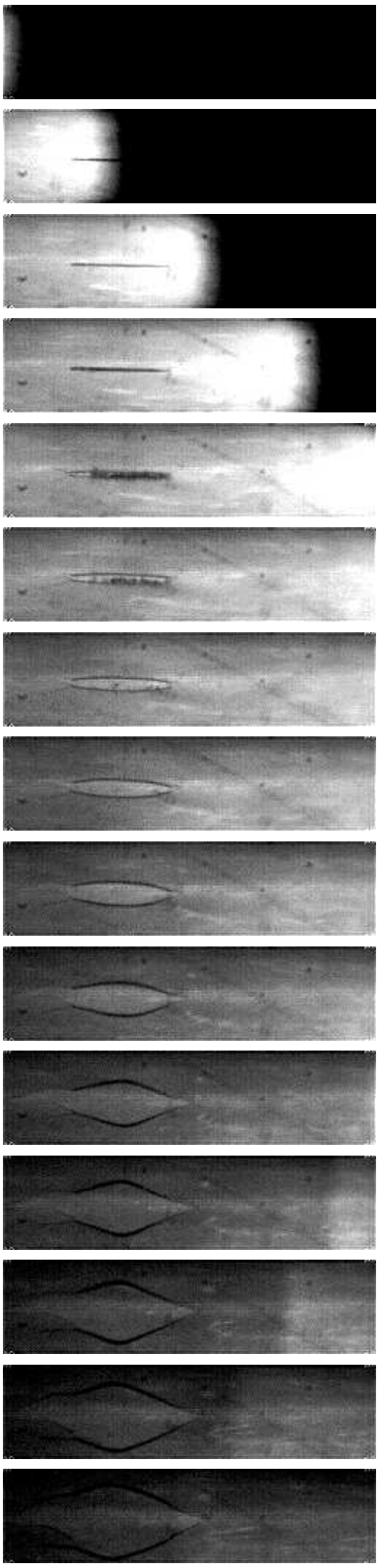

Figure 7.1: Polycarbonate specimen with an initial axial flaw rupturing under gaseous detonation loading. Interframe time is 31 μs.

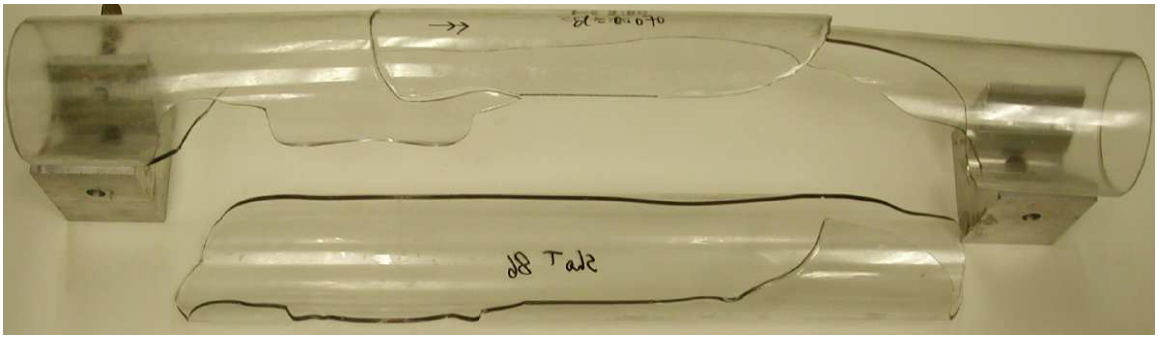

Figure 7.2: Polycarbonate specimen after fracture.

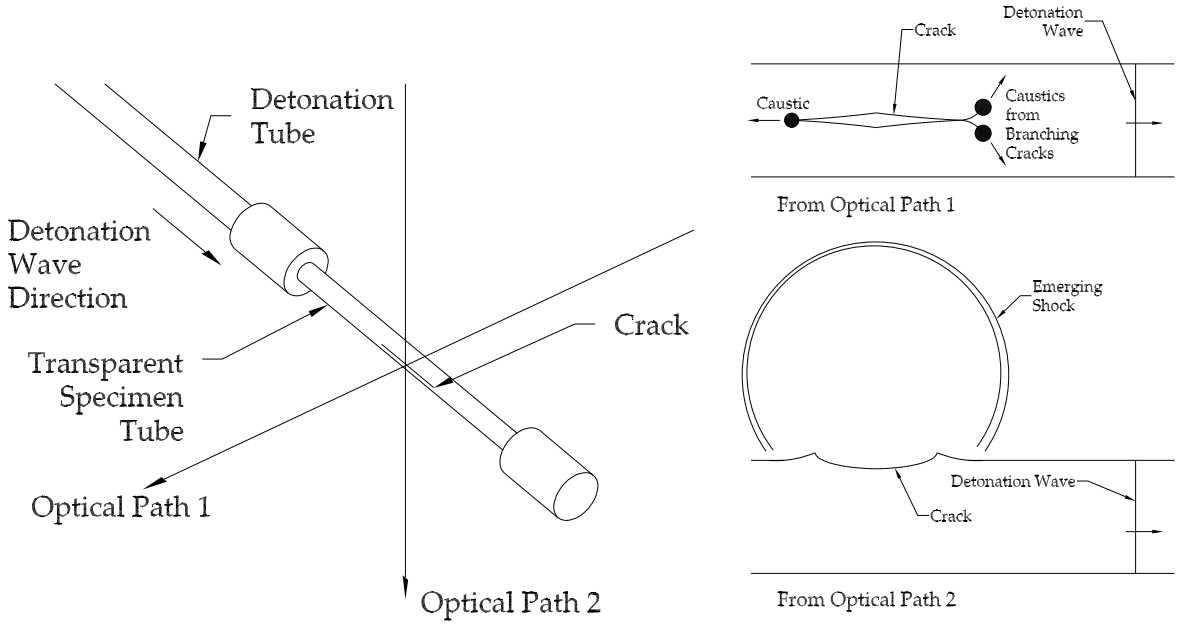

Figure 7.3: Proposed visualization.

Bibliography

M. Aivazis, B. Goddard, D. Meiron, M. Ortiz, J. C. Pool, and J. Shepherd. ASCI alliance center for simulation of dynamic response in materials FY 2001. Technical report, California Insititute of Technology, 2001. 5

ASME. *ASME Boiler and Pressure Vessel Code - An International Code*. The American Society of Mechanical Engineers, New York, NY, 2000. Section VIII, Div. 1 (Part UG-100), Div. 2 (Article T-4). 93

J. M. Austin. *The role of instability in gaseous detonation*. PhD thesis, California Institute of Technology, 2003. 7

H. Baaser and D. Gross. Crack analysis in ductile cylindrical shells using Gurson's model. *International Journal of Solids and Structures*, 37:7093–7104, 2000. 27

M. R. Baum. The development of the breach generated by axial rupture of a gas-pressurized steel pipe. *Journal of Pressure Vessel Technology*, 104(4):253–261, 1982a. 21

M. R. Baum and M. J. H. Elston. Pneumatic rupture of a brittle pipe: the depressurization transient adjacent to the ruptured zone. *Journal of Pressure Vessel Technology*, 103(3):287–293, 1981. 21, 29

M.R. Baum. The relationship between breach development and the depressurization transient during axial rupture of a gas-pressurized steel pipe. *Journal of Pressure Vessel Technology*, 104(1):20–24, 1982b. 21, 30

W. T. Becker and R. J. Shipley. *ASM Handbook, 10th ed., Vol. 11: Failure Analysis and Prevention*. American Society for Metals, 2002. 94

W.M. Beltman, E.N. Burcsu, J.E. Shepherd, and L. Zuhal. The structural response of cylindrical shells to internal shock loading. *Journal of Pressure Vessel Technology*, 121:315–322, 1999. 9, 17, 34, 43

W.M. Beltman and J.E. Shepherd. Linear elastic response of tubes to internal detonation loading. *Journal of Sound and Vibration*, 252(4):617–655, 2002. 8, 9, 17, 34, 35, 39, 43, 71, 96, 100

K. B. Broberg. *Cracks and Fracture*. Academic Press, 1999. 10

D. Broek. *Elementary Engineering Fracture Mechanics*. Kluwer academic publishers, fourth revised edition, 1997. 10, 11, 104

J. Brossard and J. Renard. Mechanical effects of gaseous detonations on a flexible confinement. In J. R. Bowen, editor, *Gasdynamics of detonations and explosions: technical papers from the seventh International Colloquium on Gasdynamics of Explosions and Reactive Systems*, Progress in astronautics and aeronautics, v.75, pages 108–121, Göttingen, Federal Republic of Germany, August 1979. AIAA. 17

M. R. Cain and R. J. Hall. Pressure vessel burst test study. *ASME PVP-Vol. 277, Recertification and Stress Classification Issues*, pages 29–44, 1994. 21

T. W. Chao and J. E. Shepherd. Fracture response of externally-flawed cylindrical shells to internal gaseous detonation loading. In M. Fisher and A. Holdo, editors, *ASME Pressure Vessels and Piping Conference, Emerging Technologies in Fluids, Structures, and Fluid-Structure Interactions, PVP Vol. 446-2*, pages 85–98. ASME, 2002. 23

T. W. Chao and J. E. Shepherd. Comparison of fracture response of preflawed tubes under internal static and detonation loading. In W. Cheng and S. Itoh, editors, *ASME Pressure Vessels and Piping Conference, Emerging Technologies in Fluids, Structures, and Fluid-Structure Interactions, PVP Vol. 460*, pages 129–144. ASME, 2003. 23

T. W. Chao, J. E. Shepherd, and F. Schauer. Experimental investigation of thermomechanical fatigue crack propagation in pulse detonation engines. Unpublished Data, 2003. 3

C.-S. Chen. *Crack growth simulation and residual strength prediction in thin shell structures*. PhD thesis, Cornell University, 1999. 26

C.-S. Chen, P. A. Wawrzynek, and A. R. Ingraffea. Methodology for fatigue crack growth and residual strength prediction with applications to aircraft fuselages. *Computational Mechanics*, 19(6):527–532, 1997. 26

C.-S. Chen, P. A. Wawrzynek, and A. R. Ingraffea. Prediction of residual strength and curvilinear crack growth in aircraft fuselages. *AIAA Journal*, 40(8):1644–1652, 2002. 27

B. Cotterell and J.R. Rice. Slightly curved or kinked cracks. *International Journal of Fracture*, 16(2):155–169, 1980. 77, 78

M.C. de Malherbe, R.D. Wing, A.J. Laderman, and A.K. Oppenheim. Response of a cylindrical shell to internal blast loading. *Journal of Mechanical Engineering Science*, 8(1):91–98, 1966. 17

A. R. Duffy, G. M. McClure, R. J. Eiber, and W. A. Maxey. Fracture design practice for pressure piping. In H. Liebowitz, editor, *Fracture: An Advanced Treatise, Vol. 5*, pages 159–232. Academic Press, 1969. 18, 30

A. F. Emery, Y. H. Chao, A. S. Kobayashi, and W. J. Love. Numerical modeling of full-scale pipe rupture tests. *Journal of Pressure Vessel Technology*, 114:265–270, 1992. 25, 26

A. F. Emery, A. S. Kobayashi, W. J. Love, B. W. Place, C. Lee, and Y. H. Chao. An experimental and analytical investigation of axial crack propagation in long pipes. *Engineering Fracture Mechanics*, 23(1):215–226, 1986. 19, 25, 26, 30, 32, 100

A. F. Emery, W. J. Love, and A. S. Kobayashi. Elastic crack propagation along a pressurized pipe. *Journal of Pressure Vessel Technology*, pages 2–7, 1976. 30

A. F. Emery, M. Perl, W. J. Love, and A. S. Kobayashi. On the motion of an axial through crack in a pipe. *Journal of Pressure Vessel Technology*, 103:281–286, 1981. 25, 26, 32

L. Engle and H. Klingele. *An Atlas of Metal Damage*. Prentice-Hall, Englewood Cliffs, N.J., 1981. 94

W. Fickett and W. C. Davis. *Detonation: Theory and Experiment*. Dover, 2001. 7, 102, 103

E. S. Folias. A finite crack in a pressurized cylindrical shell. *International Journal of Fracture Mechanics*, 1:104–113, 1965. 15, 31

E. S. Folias. Failure of pressurized vessels. In G. P. Cherepanov, editor, *Fracture: A Topical Encyclopedia of Current Knowledge*, chapter 12, pages 275–288. Krieger publishing company, 1998. 15

L. B. Freund. *Dynamic Fracture Mechanics*. Cambridge University Press, 1998. 10, 12, 13, 14, 22, 32, 101

L. B. Freund, D. M. Parks, and J. R. Rice. Running ductile fracture in a pressurized line pipe. In *Mechanics of Crack Growth, ASTM STP 590*, pages 243–262. American Society for Testing and Materials, Philadelphia, 1976. 29

L.B. Freund and D.M. Parks. Discussion. *Journal of Pressure Vessel Technology*, 98 (4):323–324, 1976. 29

R. W. Gurney. The initial velocities of fragments from bombs, shell and grenades. U.S. Army Ballistic Laboratory, BRL Report 405, 1943. 33

G. T. Hahn, M. Sarrate, M. F. Kanninen, and A. R. Rosenfield. A model for unstable shear crack propagation in pipes containing gas pressure. *International Journal of Fracture*, 9(2):209–222, 1973. 14, 30, 31

G. T. Hahn, M. Sarrate, and A. R. Rosenfield. Criteria for crack extension in cylindrical pressure vessels. *International Journal of Fracture Mechanics*, 5:187–210, 1969. 31

T. H. Hyde and A. Yaghi. An experimental investigation of dynamic crack propagation. *Journal of Strain Analysis*, 30(3):175–183, 1995. 22

A. G. Ivanov, L. I. Kochkin, L. V. Vasilev, and V. S. Kustov. Explosive rupture of tubes. *Combustion Explosion and Shock Waves*, 10(1):112–116, 1974. 23

K.D. Ives, A.K. Shoemaker, and R.F. McCartney. Pipe deformation during a running shear fracture in line pipe. *Journal of Engineering Materials and Technology*, 96 (4):309–317, 1974. 20

M. F. Kanninen. Research in progress on unstable crack propagation in pressure vessels and pipelines. *International Journal of Fracture Mechanics*, 6:94–95, 1970. 31

M. F. Kanninen and P. E. O'Donoghue. Research challenges arising from current and potential applications of dynamic fracture mechanics to the integrity of engineering structures. *International Journal of Solids and Structures*, 32(17/18):2423–2445, 1995. 5, 12, 23, 25, 28

M. F. Kanninen and C. H. Popelar. *Advanced Fracture Mechanics*. Oxford University Press, New York, 1985. 10, 13, 101

M. F. Kanninen, S. G. Sampath, and C. Popelar. Steady-state crack propagation in pressurized pipelines withouth backfill. *Journal of Pressure Vessel Technology*, 98 (1):56–65, 1976. 29, 30, 31

J. F. Kiefner, W. A. Maxey, R. J. Eiber, and A. R. Duffy. Failure stress levels of flaws in pressurized cylinders. In *ASTM STP 536, Progress in Flaw Growth and Fracture Toughness Testing, Proceedings of the 1972 National Symposium on Fracture Mechanics*, 1973. 18, 31

A. S. Kobayashi, A. F. Emery, W. J. Love, and Y. H. Chao. Subsize experiments and numerical modeling of axial rupture of gas transmission lines. *Journal of Pressure Vessel Technology*, 110:155–160, 1988. 20, 25, 26

M. Kosai, A. Shimamoto, C. T. Yu, A. S. Kobayashi, and P. W. Tan. Axial crack propagation and arrest in a pressurized cylinder: an experimental-numerical analysis. *Experimental Mechanics*, 39(4):256–264, 1999. 20, 25, 26

V. Koundy, S. Renevey, B. Marini, and A. Combescure. Effects of torsional buckling on the cleavage failure of low-alloy steel tension pipe specimens. *Journal of Pressure Vessel Technology*, 120:256–261, 1998. 23, 27

A. Lam and M. Zielonka. Fracture response of externally flawed thin-walled plastic tubes to gaseous detonation loading. Ae104c Report, Graduate Aeronautical Laboratories, California Institute of Technology, Pasadena, California 91125, 2002. 23

E.R. Lancaster and S.C. Palmer. Burst pressures of pipes containing dents and gouges. *Proceedings of the Institution of Mechanical Engineers Part E-Journal of Process Mechanical Engineering*, 210(E1):19–27, 1996a. 22

E.R. Lancaster and S.C. Palmer. Strain concentrations in pressurized dented pipes. *Proceedings of the Institution of Mechanical Engineers Part E-Journal of Process Mechanical Engineering*, 210(E1):29–38, 1996b. 22

W. J. Love, A. F. Emery, and A. S. Kobayashi. Fracture in straight pipes under large deflection conditions–part i: structural deformation. *Journal of Pressure Vessel Technology*, 99:122–127, 1977a. 26, 29, 30

W. J. Love, A. F. Emery, and A. S. Kobayashi. Fracture in straight pipes under large deflection conditions–part ii: pipe pressures. *Journal of Pressure Vessel Technology*, 99:128–136, 1977b. 26, 29, 30

W. A. Maxey, J. F. Kiefner, R. J. Eiber, and A. R. Duffy. Ductile fracture initiation, propagation, and arrest in cylindrical vessels. In *ASTM STP 514, Fracture Tough-*

ness, Proceedings of the 1971 National Symposium on Fracture Mechanics PART II, 1971. 18, 31

W.A. Maxey, R.J. Podlasek, R.J. Eiber, and R.J. Duffy. Paper 16: Observations on shear fracture propagation behavior. In *Institution of Gas Engineers Symposium on Crack Propagation in Pipelines*, Newcastle-Upon-Tyne, England, 1974. 18, 31

G. M. McClure, A. R. Duffy, and R. J. Eiber. Fracture resistance in line pipe. *Journal of Engineering for Industry*, 81:265–278, 1965. 18

S. Melin. Accurate data for stress intensity factors at infinitesimal kinks. *Journal of Applied Mechanics*, 61(2):467–470, 1994. xx, 125, 126

N. F. Mott. Fragmentation of shell cases. In *Proceedings of the Royal Society of London Series A-Mathematical and Physical Sciences*, volume 189, pages 300–308, 1947. 24, 33

J.C. Newman, Jr., M. A. James, and U. Zerbst. A review of the ctoa/ctod fracture criterion. *Engineering Fracture Mechanics*, 70(3-4):371–385, 2003. 26

J.C. Newman, Jr. and I. S. Raju. An empirical stress-intensity factor equation for the surface crack. *Engineering Fracture Mechanics*, 15(1-2):185–192, 1981. 52, 54

NTSB. National Transportation Safety Board aircraft accident report, Aloha Airlines Flight 243, Boeing 737-200, N 73711, near Maui, April 28, 1988. NTSB/AAR-89/03, 1989. 26

P. E. O'Donoghue, S. T. Green, M. F. Kanninen, and P. K. Bowles. The development of a fluid/structure interaction model for flawed fluid containment boundaries with applications to gas transmission and distribution piping. *Computers and Structures*, 38(5/6):501–513, 1991. 24

P.E. O'Donoghue and Z. Zhuang. A finite element model for crack arrestor design in gas pipelines. *Fatigue and Fracture of Engineering Materials and Structures*, 22 (1):59–66, 1999. 25

L.S. Ong, A.K. Soh, and J.H. Ong. Experimental and finite-element investigation of a local dent on a pressurized pipe. *Journal of Strain Analysis for Engineering Design*, 27(3):177–185, 1992. 22

D.M. Parks and L.B. Freund. On the gasdynamics of running ductile fracture in a pressurized line pipe. *Journal of Pressure Vessel Technology*, 100(1):13–17, 1978. 29

C. H. Popelar, P. C. Gehlen, and M. F. Kanninen. Dynamic crack propagation in precracked cylindrical vessels subjected to shock loading. *Journal of Pressure Vessel Technology*, 103:155–159, 1981. 28

D. O. Potyondy. *A methodology for simulation for curvilinear crack growth in pressurized shells*. PhD thesis, Cornell University, 1993. 22, 26

D. O. Potyondy, P. A. Wawrzynek, and A. R. Ingraffea. Discrete crack growth analysis methodology for through cracks in pressurized fuselage structures. *International Journal for Numerical Methods in Engineering*, 38(10):1611–1633, 1995. 26

W. A. Poynton, R. W. E. Shannon, and G. D. Fearnehough. The design and application of shear fracture propagation studies. *Journal of Engineering Materials and Technology*, 96(4):323–329, 1974. 32, 100

H. Reismann. Response of a pre-stressed cylindrical shell to moving pressure load. In S. Ostrach and R.H. Scanlon, editors, *Eighth Midwest Mechanics Conference*, pages 349–363. Pergamon Press, 1965. 17

W.C. Reynolds. The element potential method for chemical equilibrium analysis: implementation in the interactive program STANJAN. Technical report, Mechanical Engineering Department, Stanford University, 1986. 58, 91

J. R. Rice. A path independent integral and the approximate analysis of strain concentrations by notches and cracks. *Journal of Applied Mechanics*, 35:379–386, 1968. 31

S. Roy, S. Grigory, M. Smith, M. F. Kanninen, and M. Anderson. Numerical simulations of full-scale corroded pipe tests with combined loading. *Journal of Pressure Vessel Technology*, 119:457–466, 1997. 23, 27

F. Schauer. Private communication. 2003. 3

A. Shimamoto, M. Kosai, and A. S. Kobayashi. Axial crack propagation and crack kinking criteria in pressurized fuselage. *JSME International Journal*, 41(3):256–264, 1998. 20, 25, 26

A.K. Shoemaker and R.F. McCartney. Displacement consideration for a ductile propagating fracture in line pipe. *Journal of Engineering Materials and Technology*, 96 (4):318–322, 1974. 19, 20

T.E. Simkins. Resonance of flexural waves in gun tubes. Technical Report ARCCB–TR–87008, US Army Armament Research, Development and Engineering Center, Watervliet, N.Y. 12189–4050, July 1987. 9, 17, 28

M. Singh, H. R. Suneja, M. S. Bola, and S. Prakash. Dynamic tensile deformation and fracture of metal cylinders at high strain rates. *International Journal of Impact Engineering*, 27:939–954, 2002. 23, 33

P. M. B. Slate, M. J. W. Billings, and P. J. A. Fuller. The rupture behavior of metals at high strain rates. *Journal of the Institute of Metals*, 95:244–251, 1967. 23

R. A. Strehlow. *Combustion Fundamentals*. McGraw-Hill, 1984. 7

S. Tang. Dynamic response of a tube under moving pressure. In *Proceedings of the American Society of Civil Engineers*, volume 5, pages 97–122. Engineering Mechanics Division, October 1965. 8, 9, 17, 34, 37, 43, 44, 46, 71, 96

G. I. Taylor. The fragmentation of tubular bombs. In *Scientific Papers of G. I. Taylor, Vol. III*, pages 387–390. Cambridge Press, Cambridge, 1963. 33

K. Thielsch. *Defects and Failures in Pressure Vessels and Piping*. Reinhold, New York, 1965. 94

G.O. Thomas. The response of pipes and supports generated by gaseous detonations. *Journal of Pressure Vessel Technology*, 124:66–73, 2002. 17

J. T. Tzeng. Dynamic fracture of composite overwrap cylinders. *Journal of Reinforced Plastics and Composites*, 19(1):2–14, 2000. 27

D. L. Wesenberg and M. J. Sagartz. Dynamic fracture of 6061-T6 aluminum cylinders. *Journal of Applied Mechanics*, 44(4):643–646, 1977. 23, 24

J.G. Williams and G.P. Venizelos. A perturbation analysis of rapid crack propagation in pressurised pipe. *International Journal of Fracture*, 94(2):161–176, 1998. 32

E. Wintenberger. Private communication. 2003. 103

E. Wintenberger and J. E. Shepherd. A model for the performance of air-breathing pulse detonation engines. In *39th AIAA/ASME/SAE/ASEE Joint Propulsion Conference and Exhibit, Huntsville, Al, AIAA 2003-4511*, 2003. xiv, 3

W. C. Young. *Roark's Formulas For Stress And Strain*. McGraw-Hill, 1989. 42

Z. Zhuang. *The development of finite element methods for the investigation of dynamic crack propagation in gas pipelines*. PhD thesis, University College Dublin, Ireland, 1995. 24

Z. Zhuang and P.E. O'Donoghue. Determination of material fracture toughness by a computational/experimental approach for rapid crack propagation in PE pipe. *International Journal of Fracture*, 101(3):251–268, 2000a. 23, 25

Z. Zhuang and P.E. O'Donoghue. The recent development of analysis methodology for rapid crack propagation and arrest in gas pipelines. *International Journal of Fracture*, 101(3):269–290, 2000b. 25

Appendix A

Data from Torsion Experiments

Due to the large number of plots and figures generated from the torsion experiments, it was decided that rather than inserting all the plots and figures into Chapter 6, organizing them here will make it easier to read. In this section, selected crack paths, crack speeds, cines, blast pressure, strain traces, and post-test specimen photographs are presented in chronological order.

A.1 Crack Paths

The crack paths were plotted as circumferential location from the notch against axial location from the center of the notch. Presented this way, the crack paths are drawn as if the tube specimens were slit open axially and laid flat. The crack paths were hand-traced onto transparent sheets of plastic and then digitized. Detonation wave direction is from left to right.

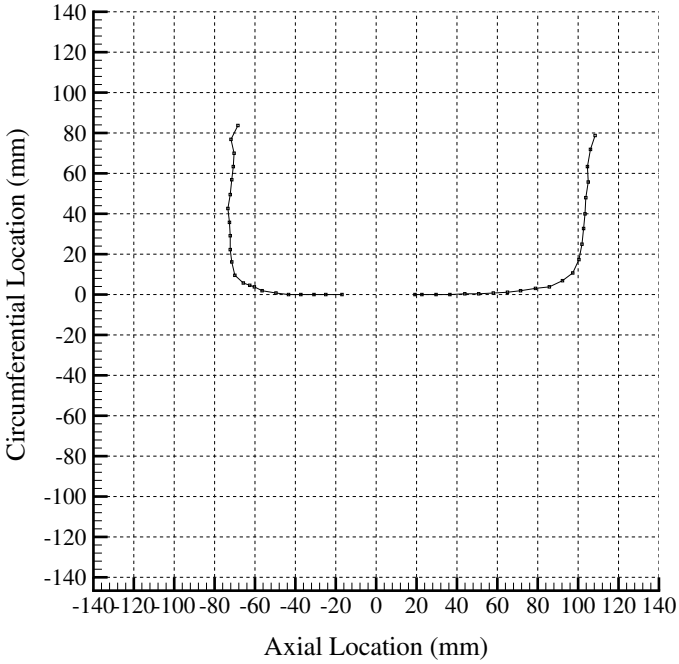

Figure A.1: Shot 119 crack paths.

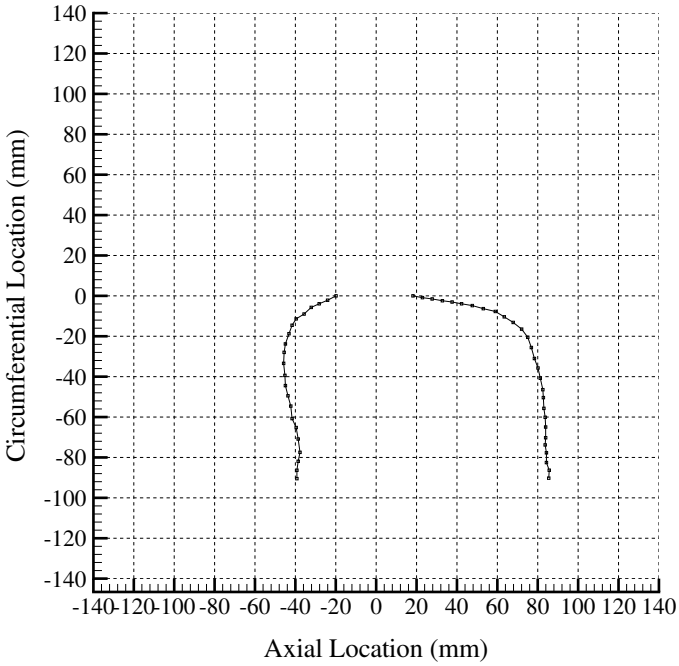

Figure A.2: Shot 120 crack paths.

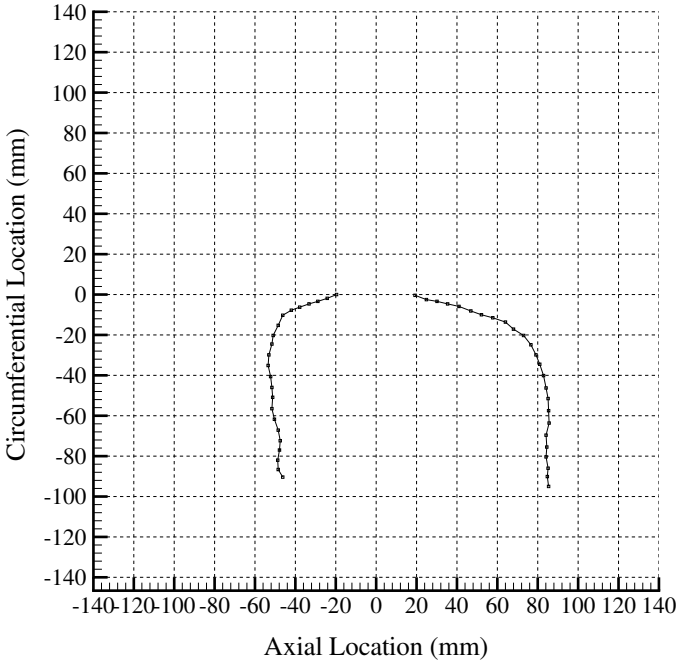

Figure A.3: Shot 121 crack paths.

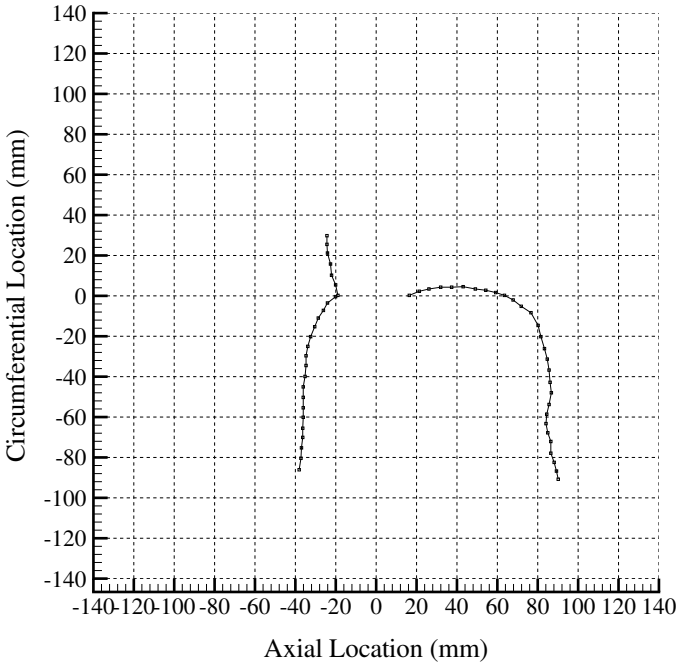

Figure A.4: Shot 123 crack paths.

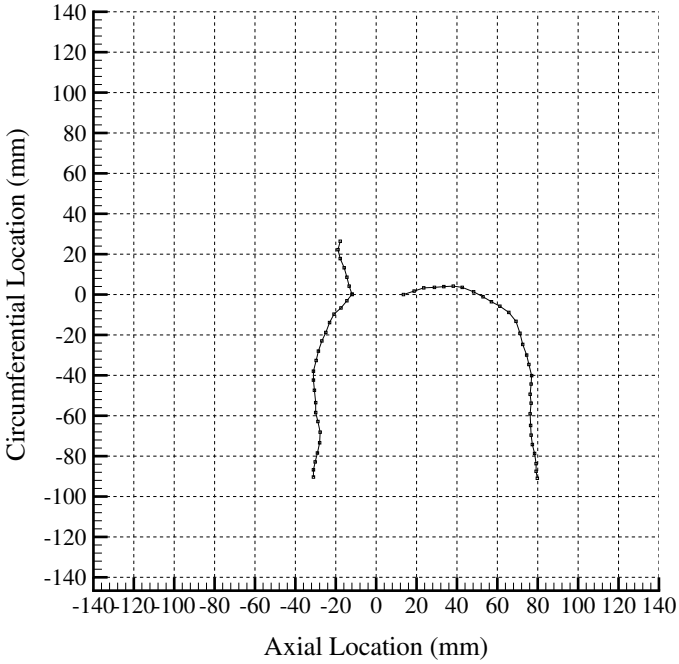

Figure A.5: Shot 126 crack paths.

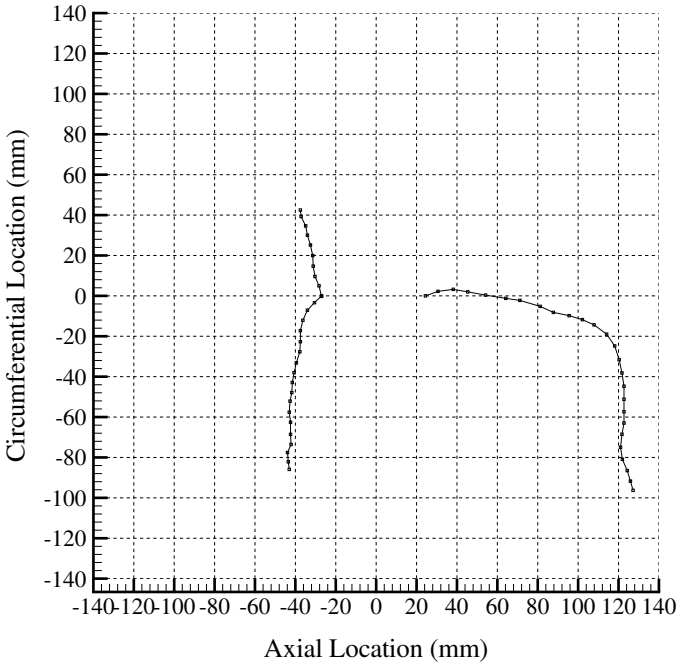

Figure A.6: Shot 127 crack paths.

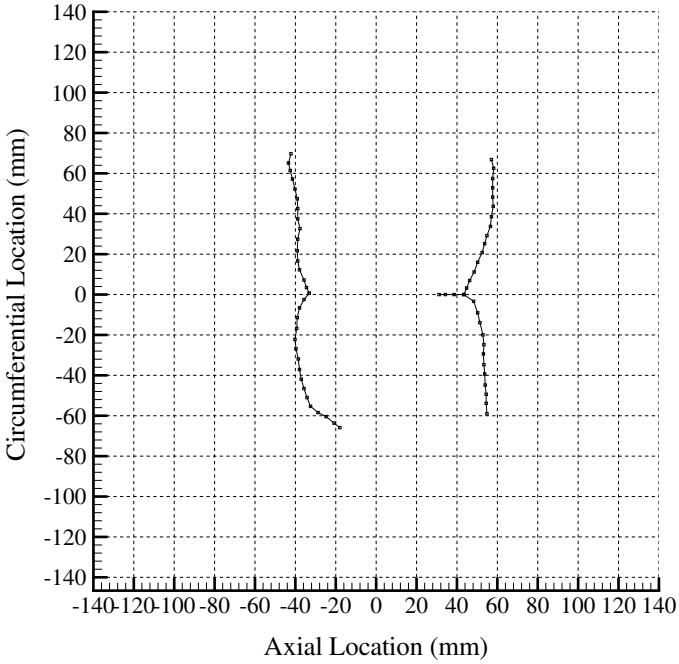

Figure A.7: Shot 128 crack paths.

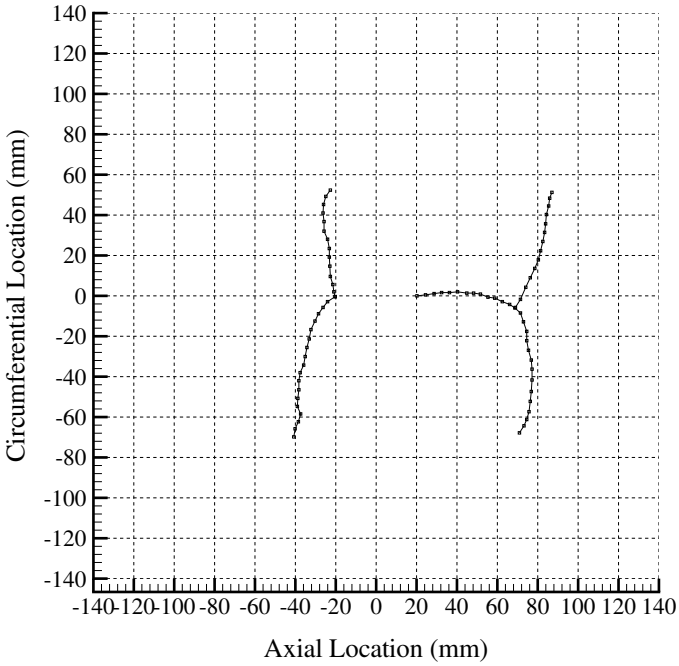

Figure A.8: Shot 129 crack paths.

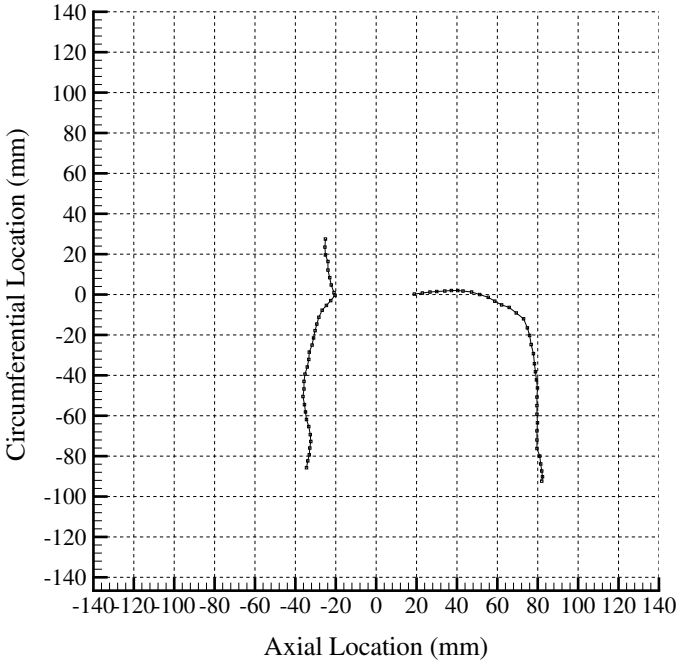

Figure A.9: Shot 130 crack paths.

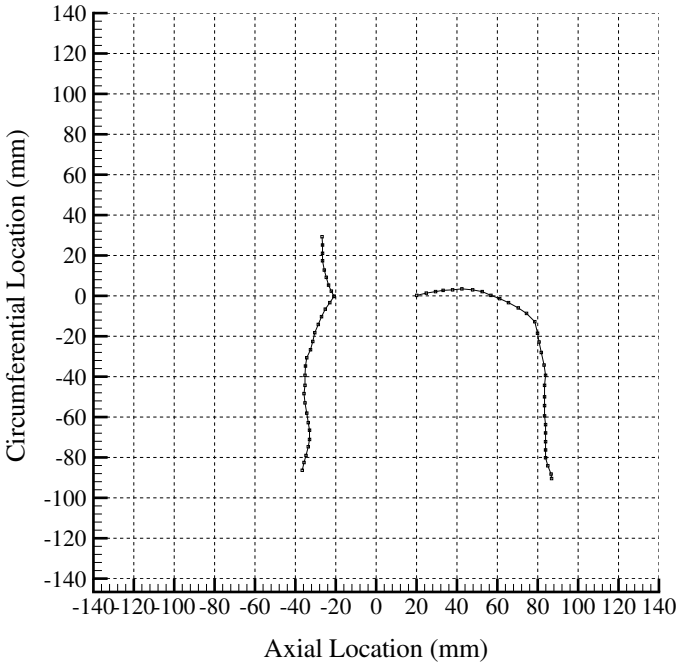

Figure A.10: Shot 131 crack paths.

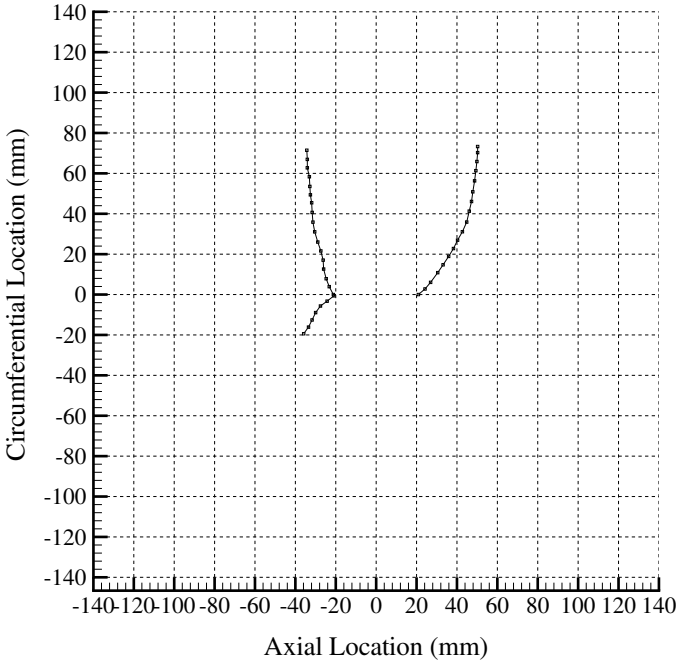

Figure A.11: Shot 132 crack paths.

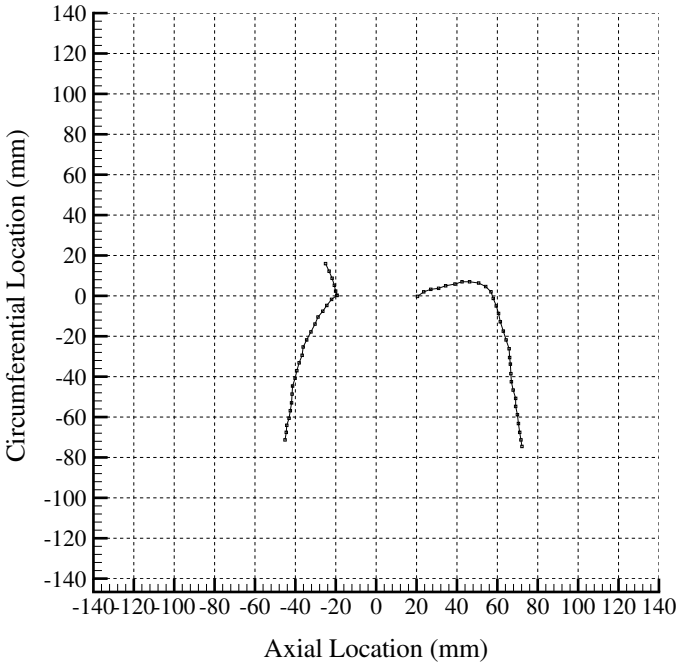

Figure A.12: Shot 133 crack paths.

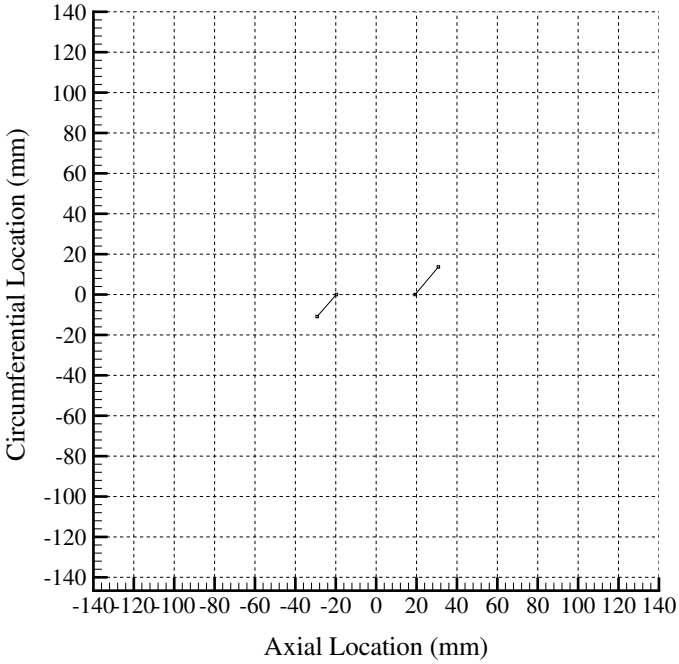

Figure A.13: Shot 134 crack paths.

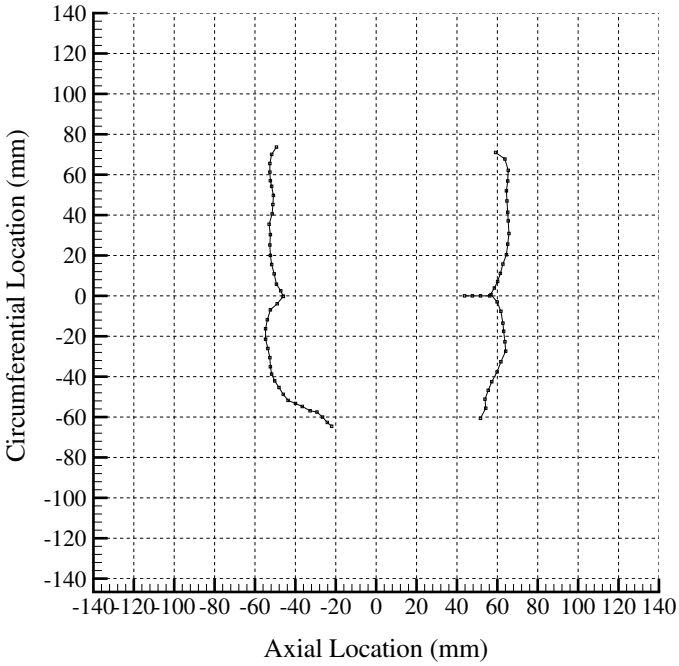

Figure A.14: Shot 135 crack paths.

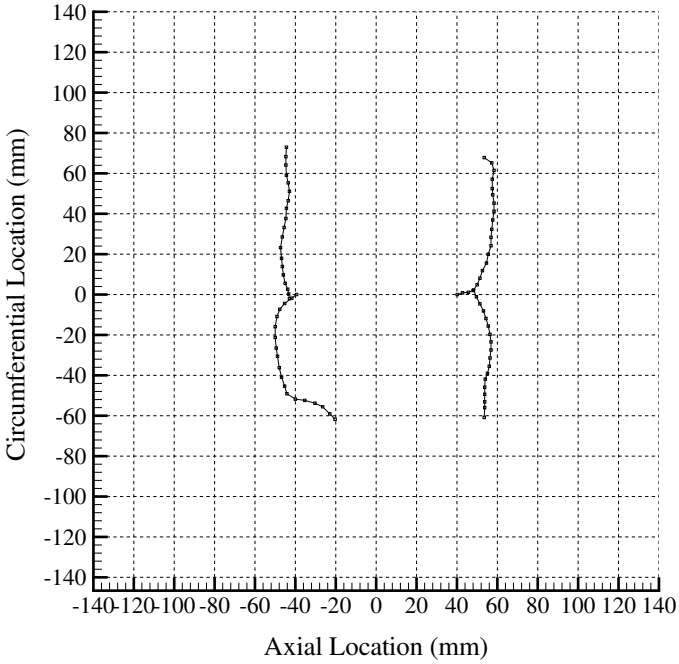

Figure A.15: Shot 136 crack paths.

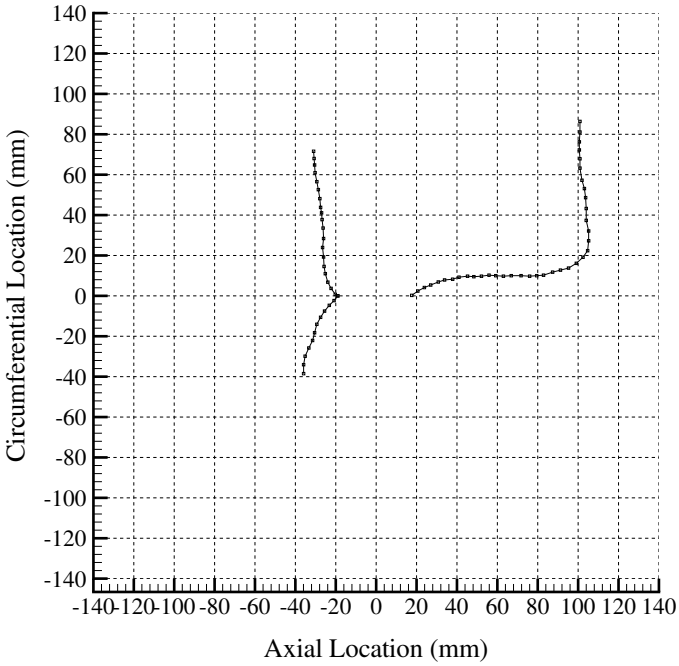

Figure A.16: Shot 137 crack paths.

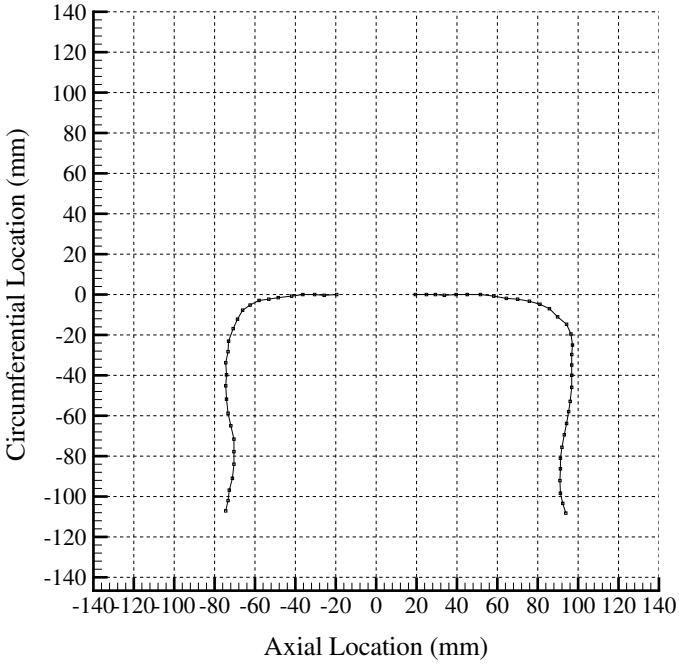

Figure A.17: Shot 139 crack paths.

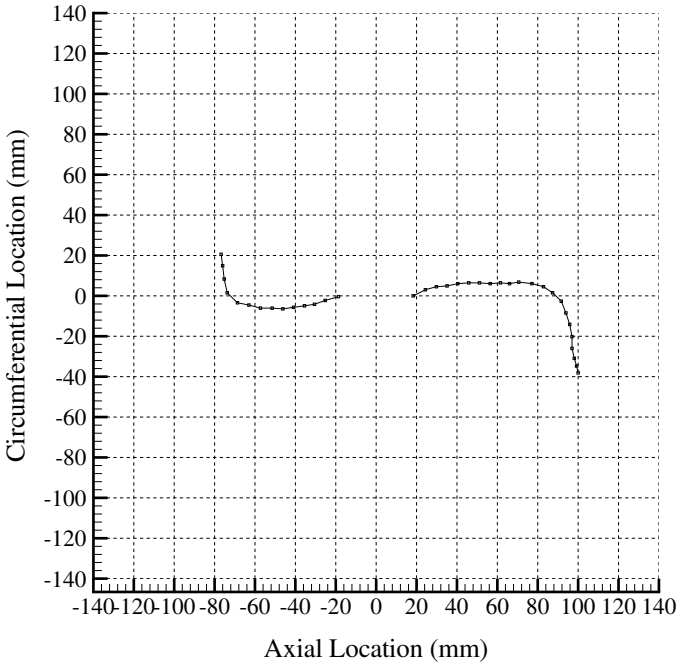

Figure A.18: Shot 140 crack paths.

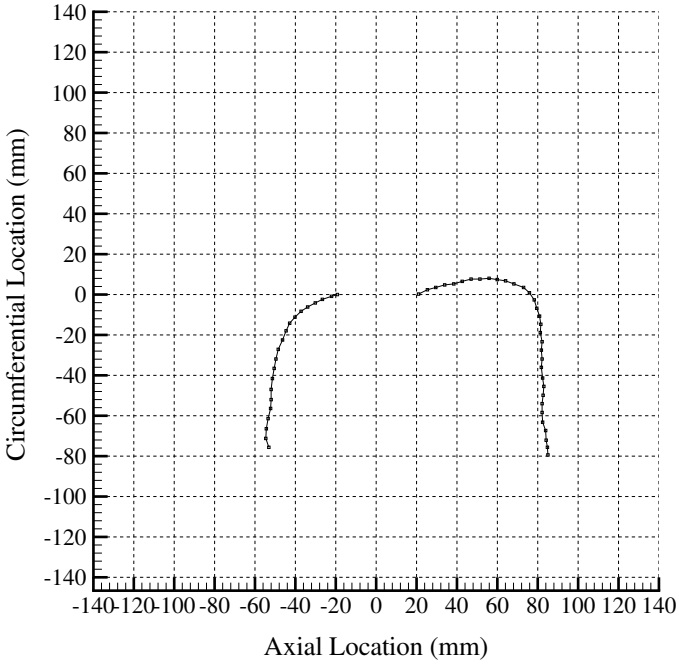

Figure A.19: Shot 141 crack paths.

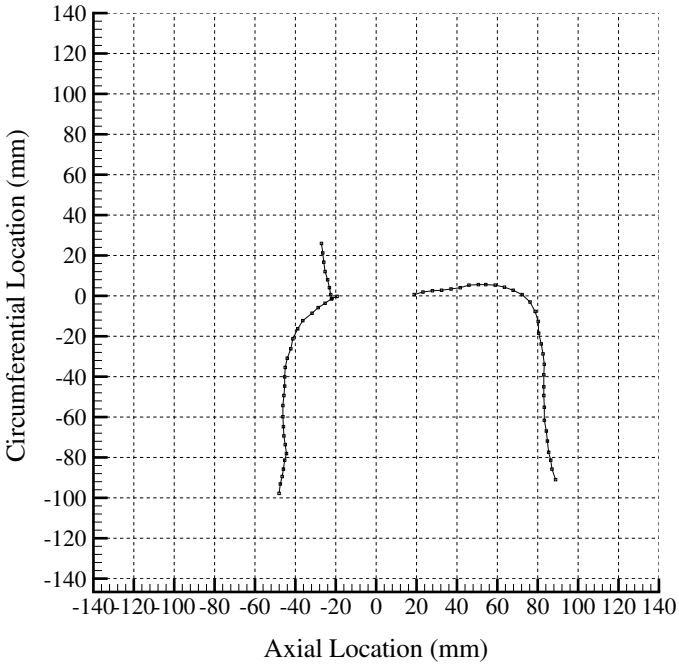

Figure A.20: Shot 142 crack paths.

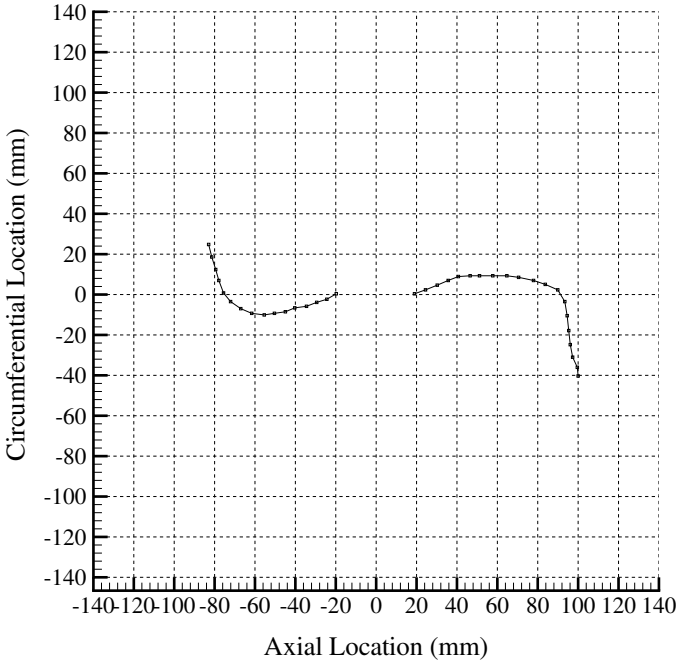

Figure A.21: Shot 143 crack paths.

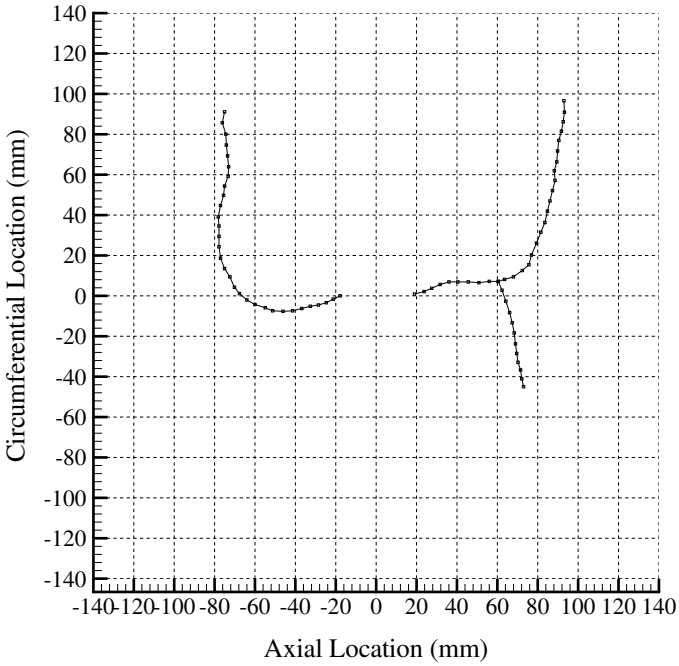

Figure A.22: Shot 144 crack paths.

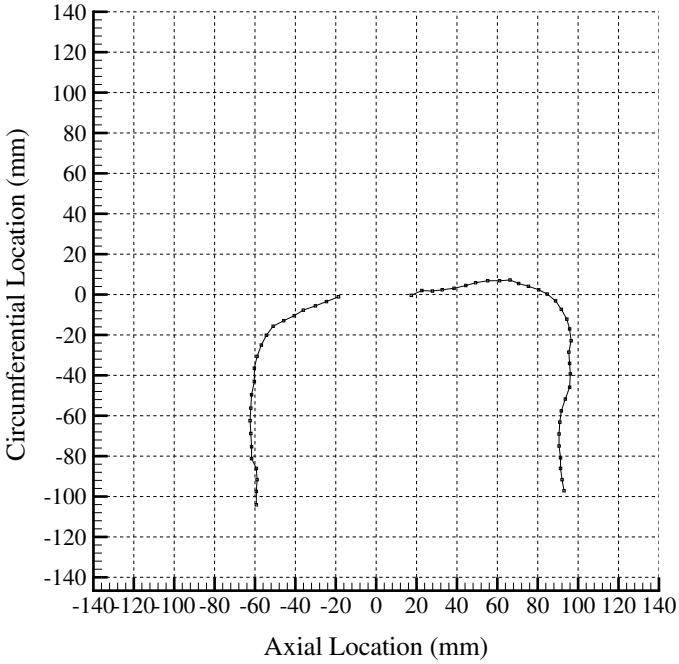

Figure A.23: Shot 145 crack paths.

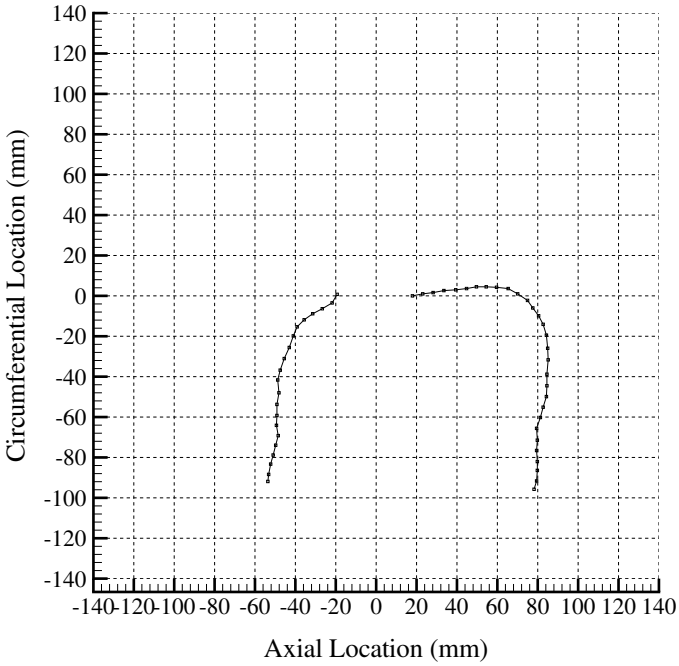

Figure A.24: Shot 146 crack paths.

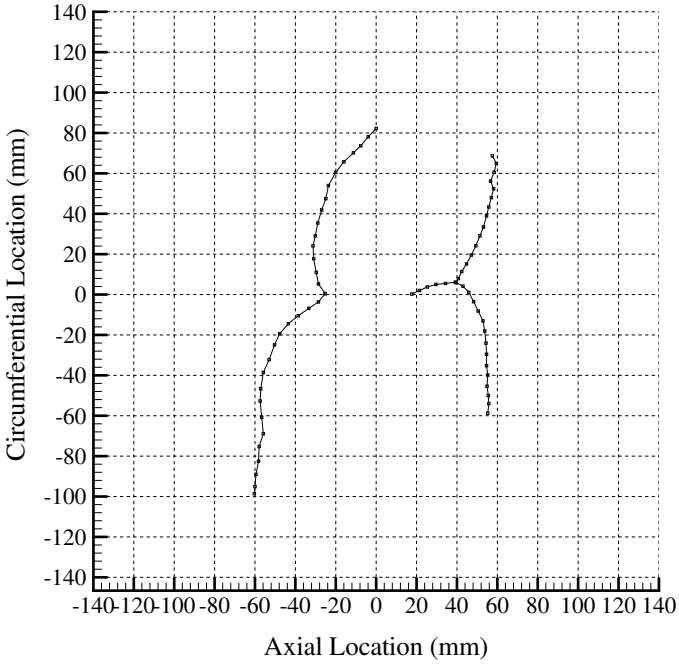

Figure A.25: Shot 147 crack paths.

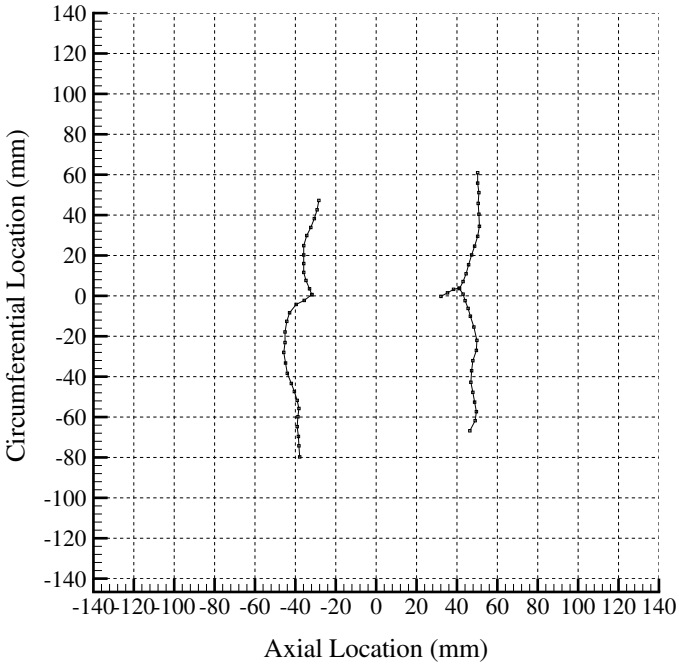

Figure A.26: Shot 148 crack paths.

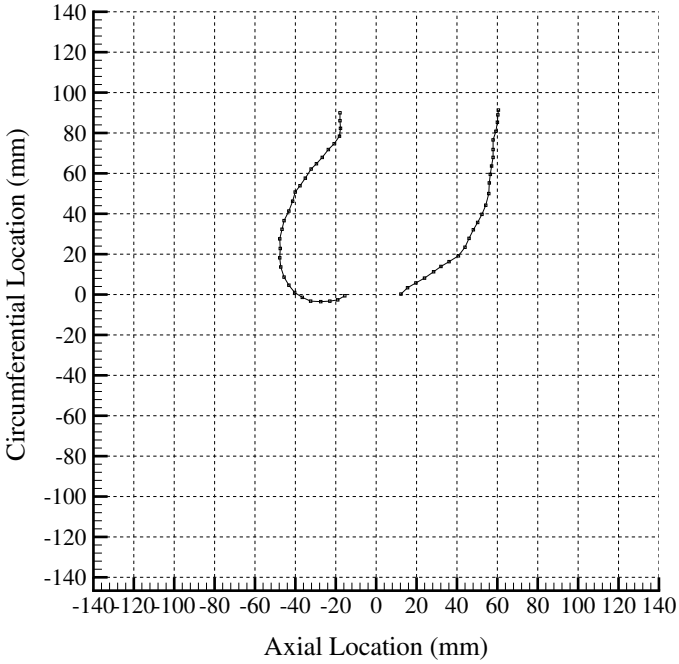

Figure A.27: Shot 149 crack paths.

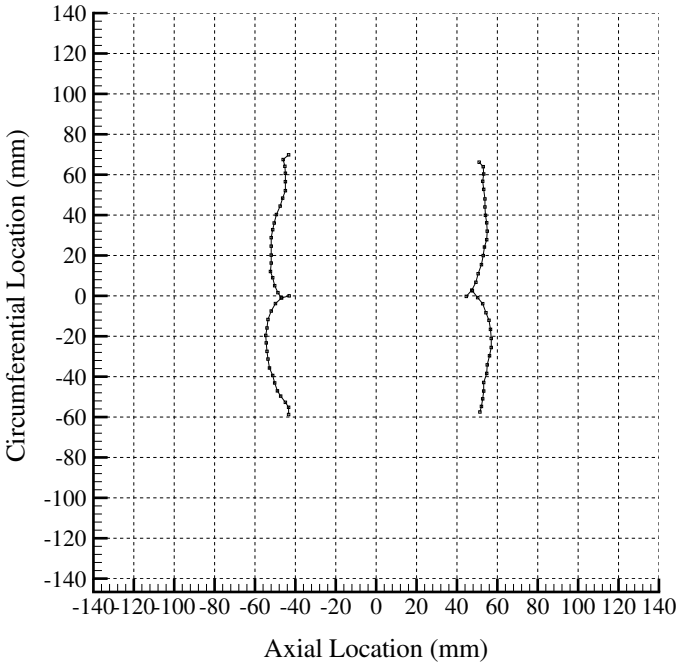

Figure A.28: Shot 150 crack paths.

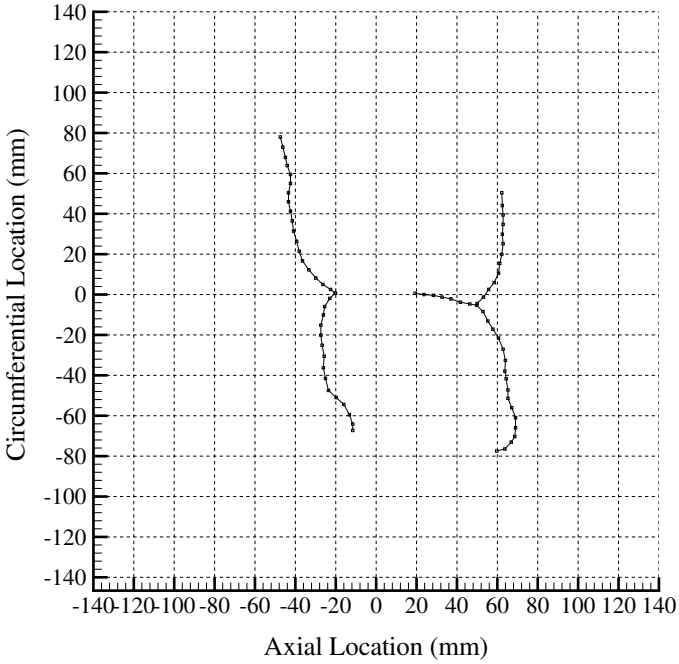

Figure A.29: Shot 151 crack paths.

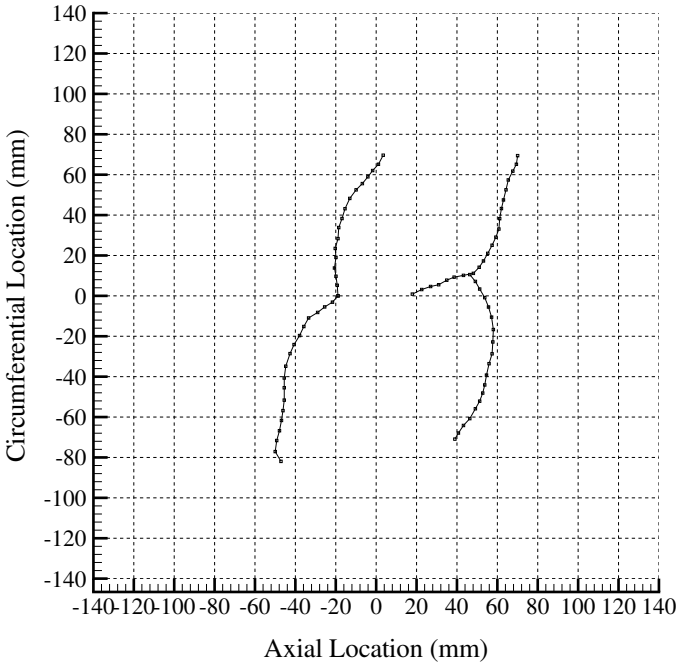

Figure A.30: Shot 152 crack paths.

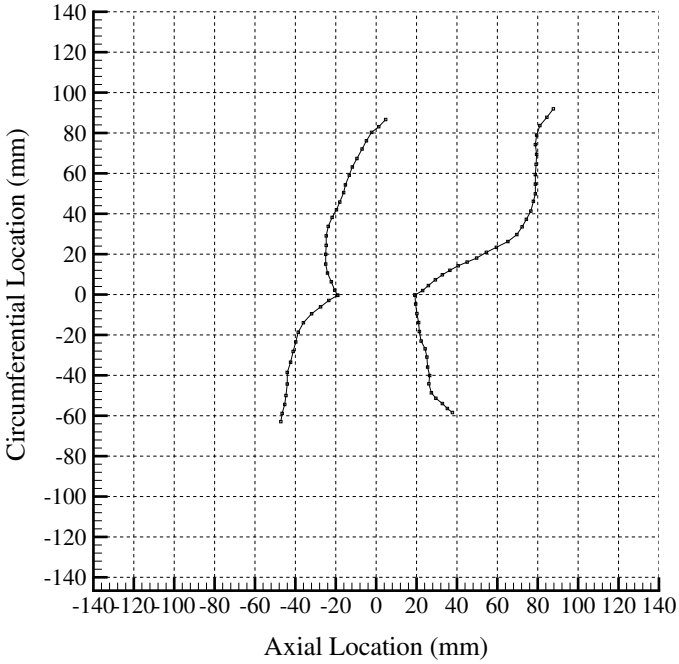

Figure A.31: Shot 153 crack paths.

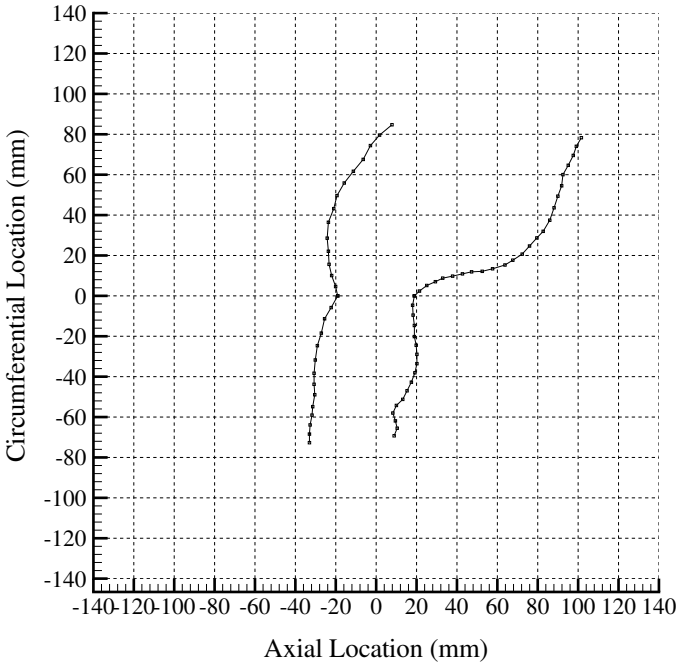

Figure A.32: Shot 154 crack paths.

A.2 Crack Speeds

Crack speeds are plotted against axial location (zero being the center of the notch). Solid squares represent backward upper cracks, open deltas represent backward lower cracks, solid diamonds represent forward upper cracks, and open circles represent forward lower cracks. Detonation wave direction is from left to right.

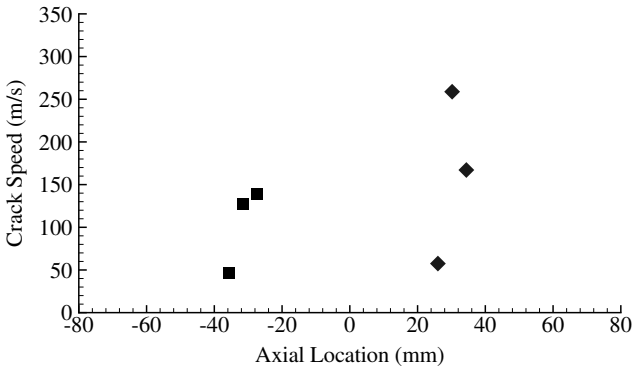

Figure A.33: Shot 119 crack speeds.

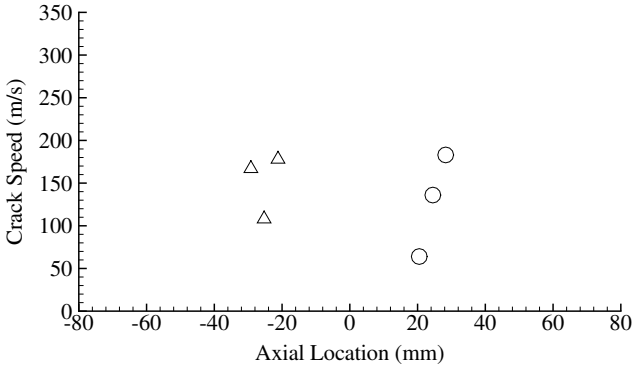

Figure A.34: Shot 120 crack speeds.

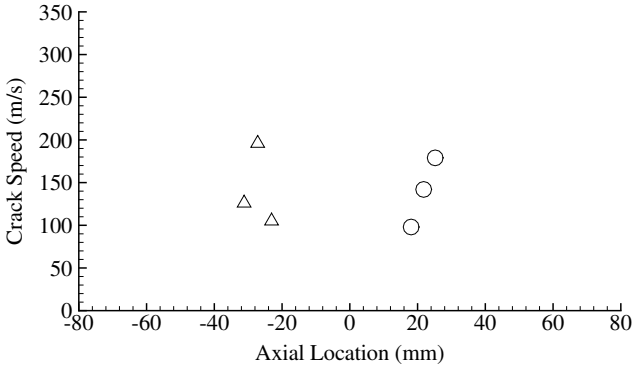

Figure A.35: Shot 121 crack speeds.

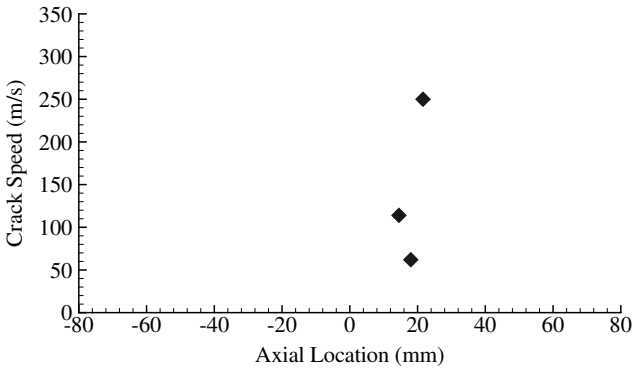

Figure A.36: Shot 126 crack speeds.

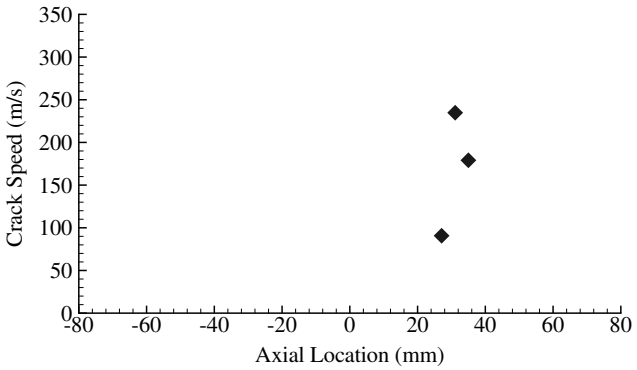

Figure A.37: Shot 127 crack speeds.

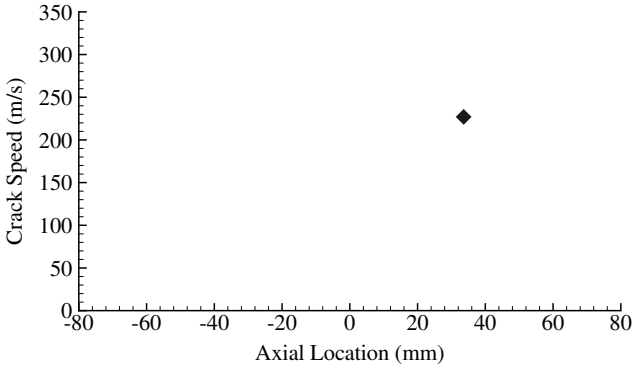

Figure A.38: Shot 128 crack speeds.

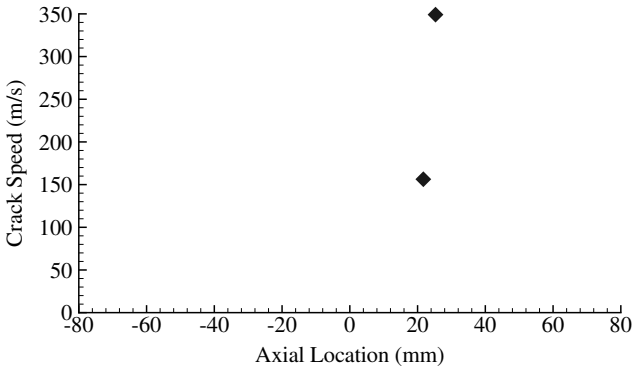

Figure A.39: Shot 132 crack speeds.

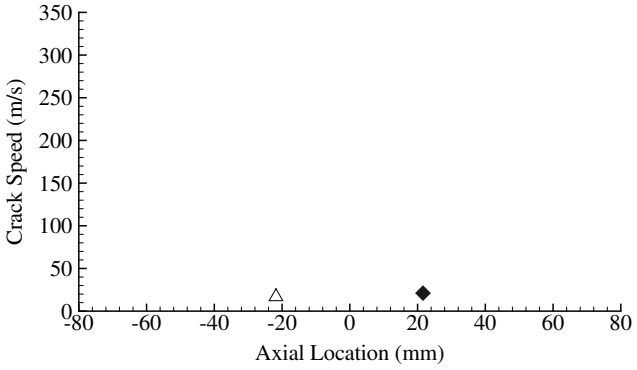

Figure A.40: Shot 134 crack speeds.

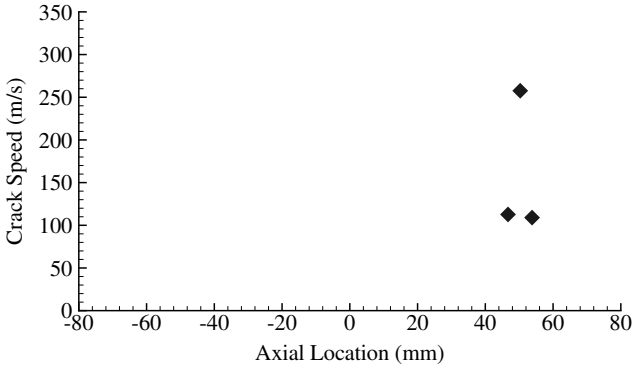

Figure A.41: Shot 135 crack speeds.

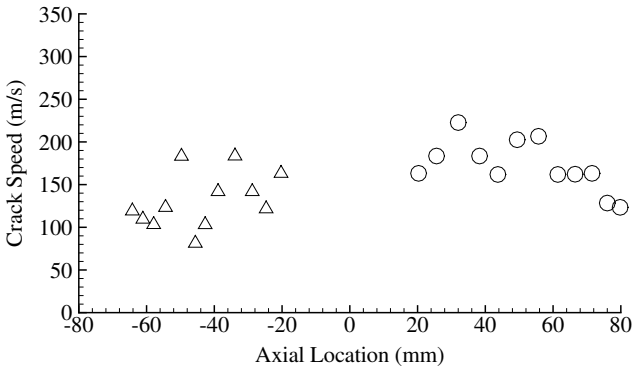

Figure A.42: Shot 139 crack speeds.

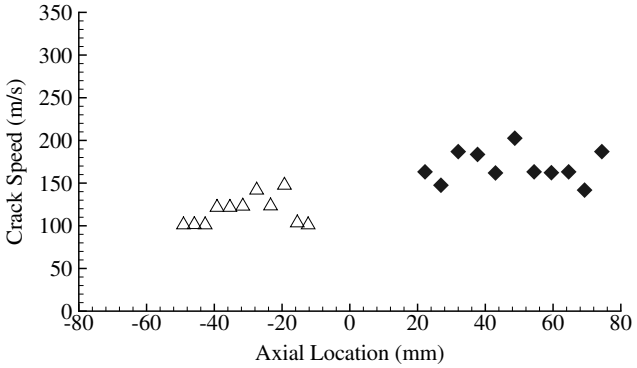

Figure A.43: Shot 140 crack speeds.

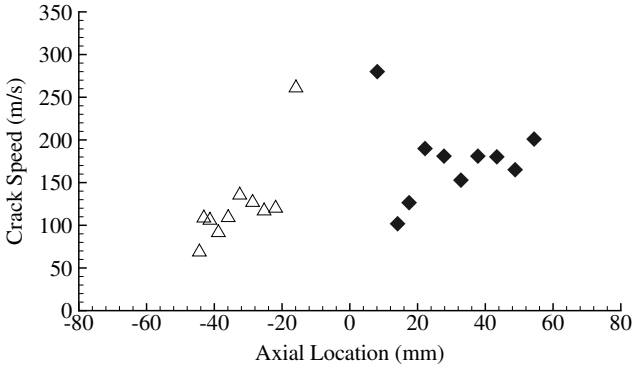

Figure A.44: Shot 141 crack speeds.

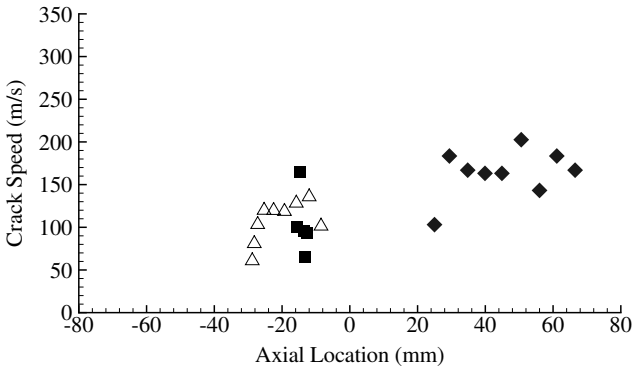

Figure A.45: Shot 142 crack speeds.

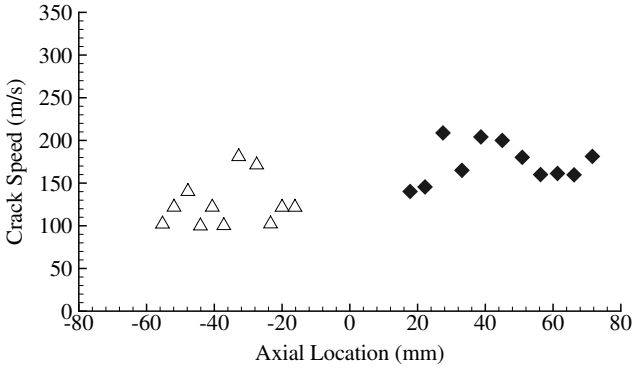

Figure A.46: Shot 143 crack speeds.

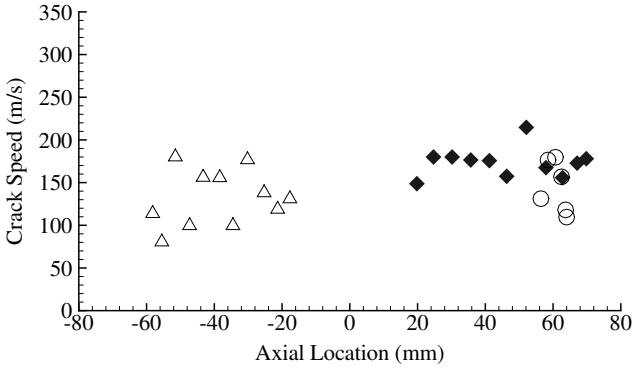

Figure A.47: Shot 144 crack speeds.

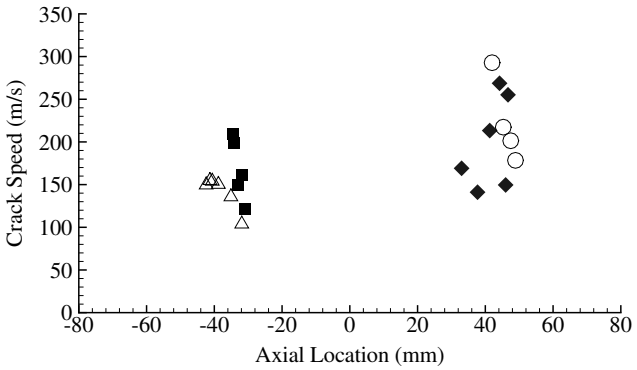

Figure A.48: Shot 148 crack speeds.

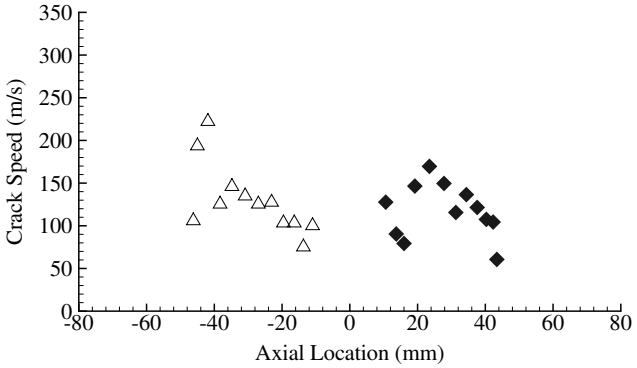

Figure A.49: Shot 149 crack speeds.

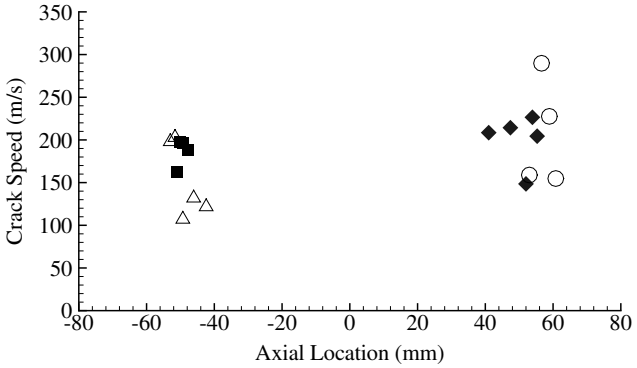

Figure A.50: Shot 150 crack speeds.

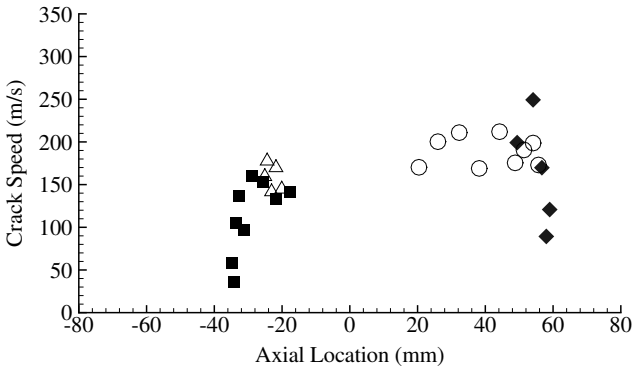

Figure A.51: Shot 151 crack speeds.

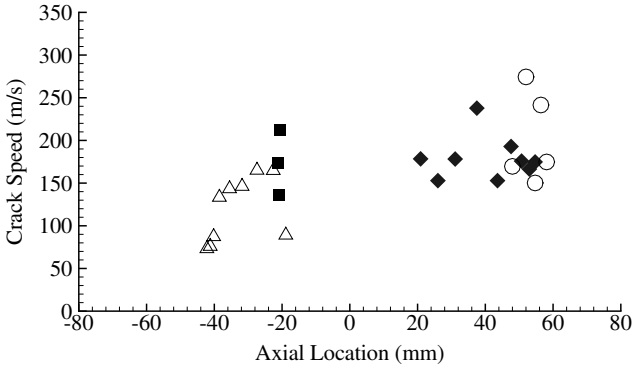

Figure A.52: Shot 152 crack speeds.

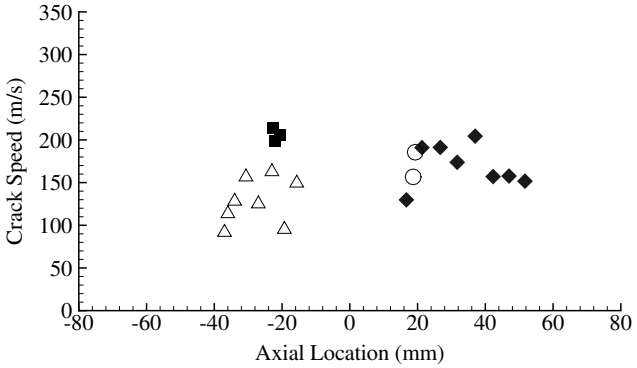

Figure A.53: Shot 153 crack speeds.

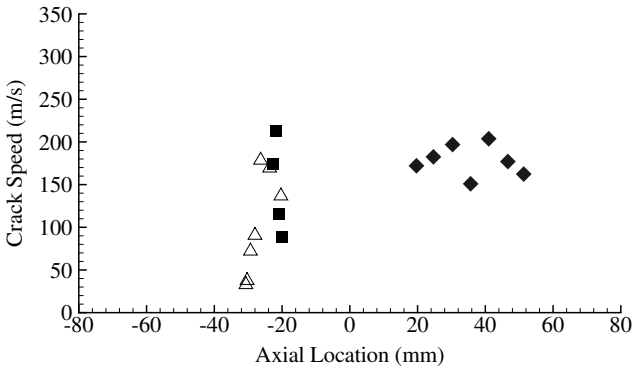

Figure A.54: Shot 154 crack speeds.

A.3 Cines

The cines are adjusted to maximize the contrast between the luminous detonation products and the dark crack flaps so that the crack tips can be clearly seen. The cines are organized in such a fashion that they can be read like $x-t$ diagrams. Time zero corresponds to the ignition spark in the detonation tube.

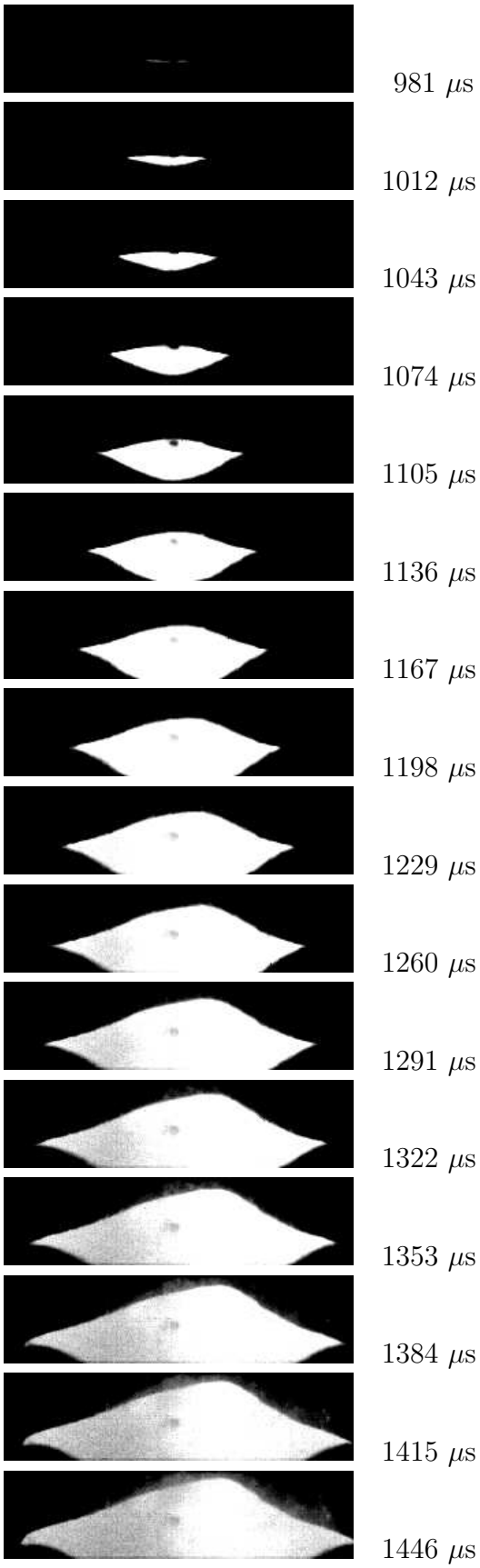

Figure A.55: Shot 139.

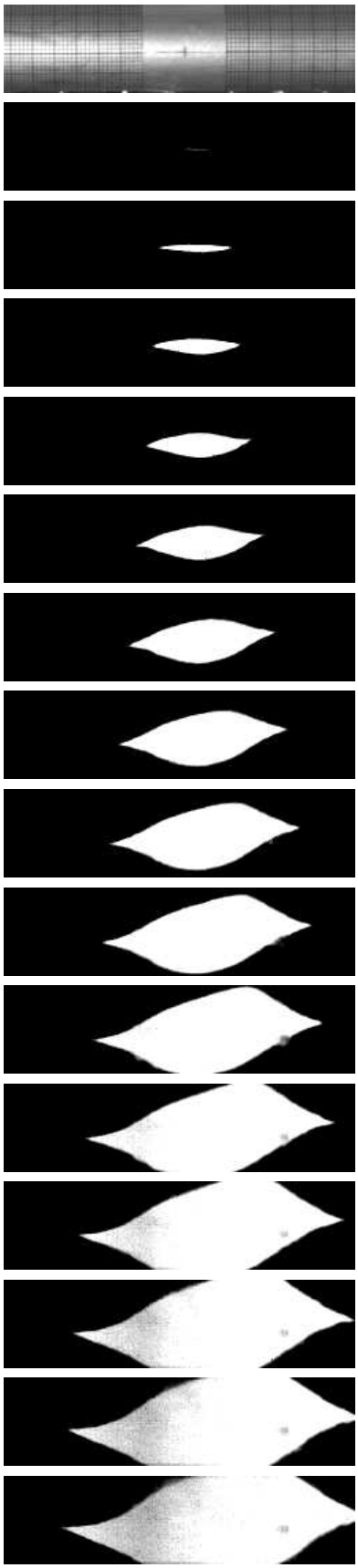

Figure A.56: Shot 140.

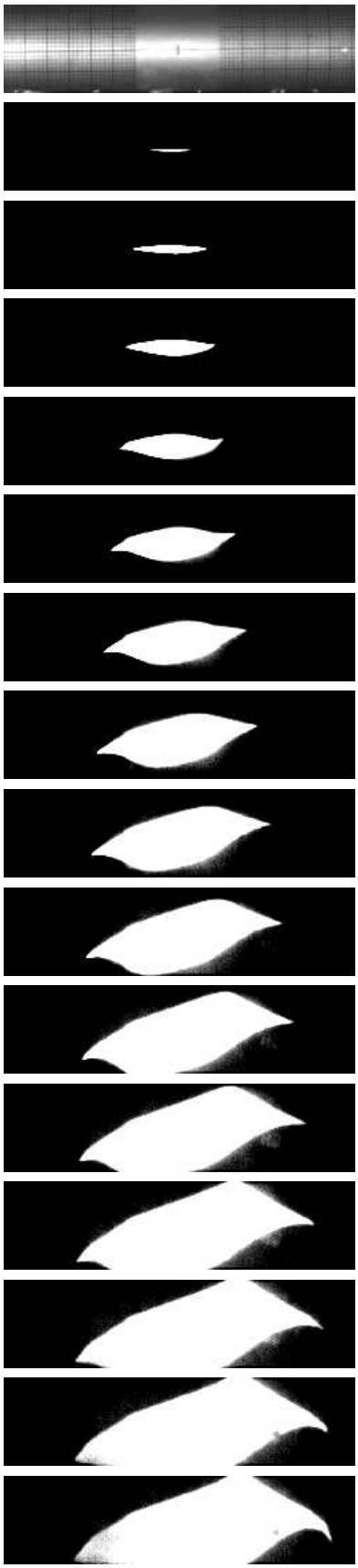

Figure A.57: Shot 141.

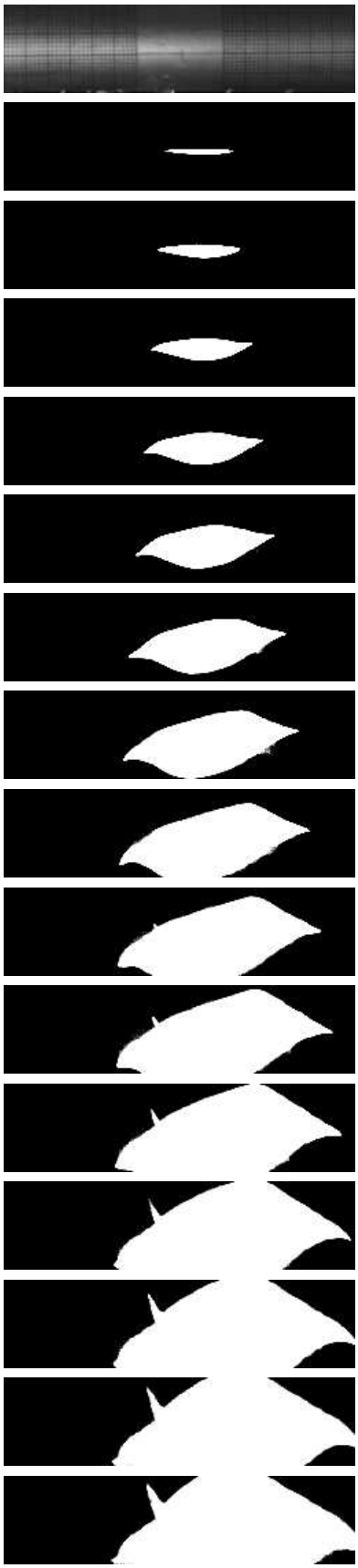

Figure A.58: Shot 142.

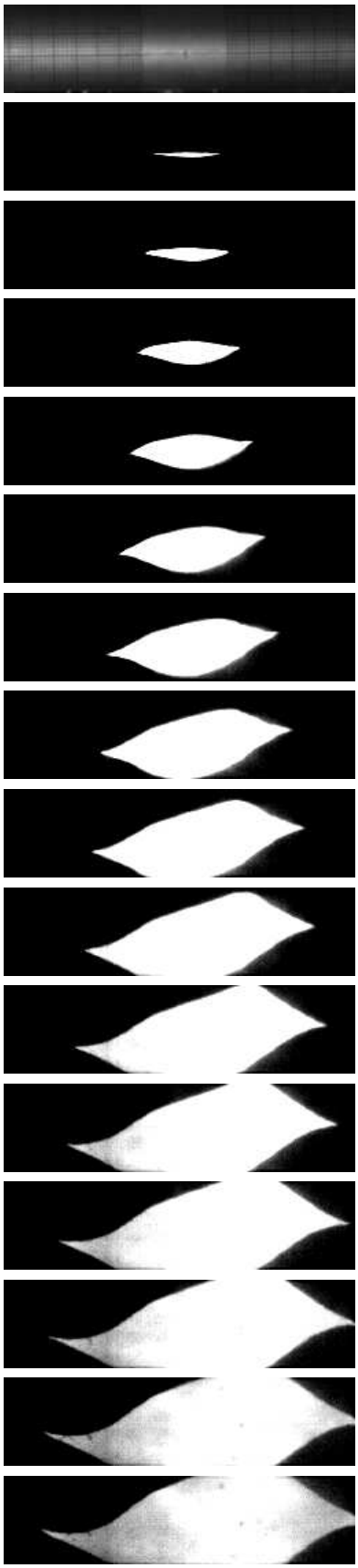

Figure A.59: Shot 143.

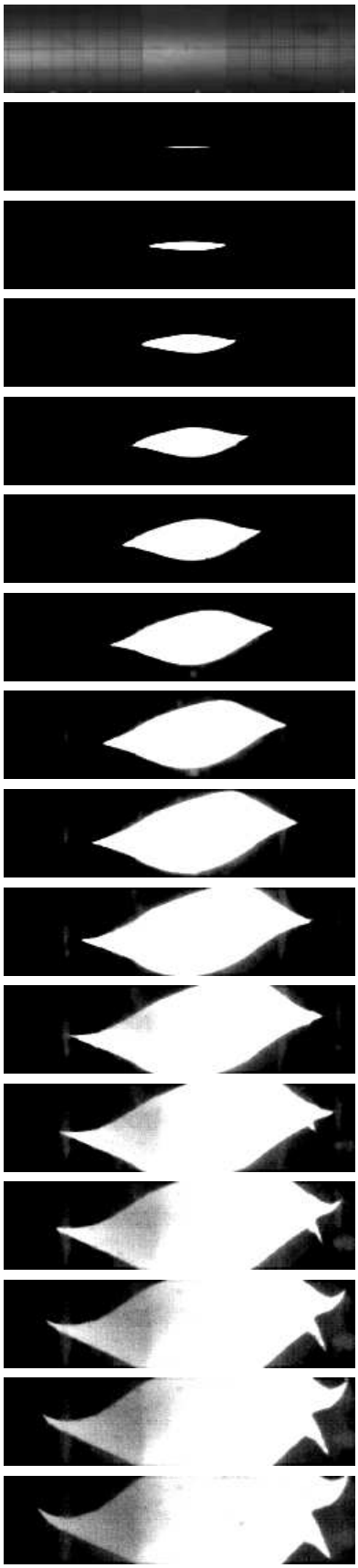

Figure A.60: Shot 144.

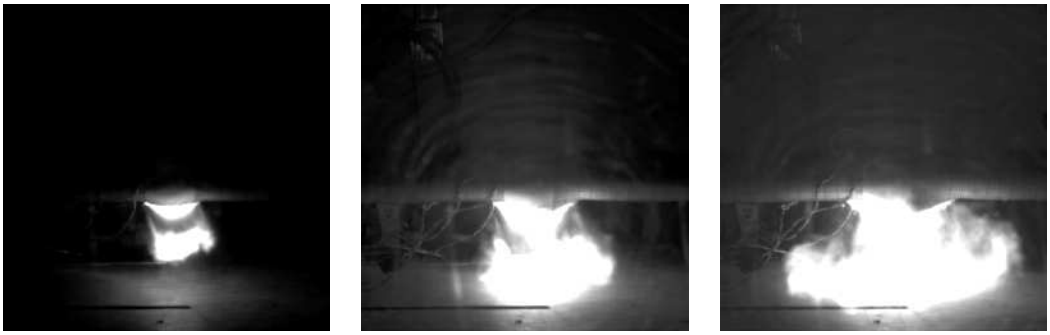

996 μs

1085 μs

1174 μs

1264 μs

1352 μs

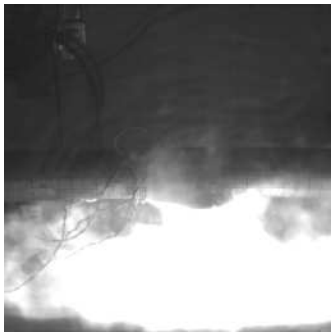

1441 μs

1530 μs

1620 μs

1708 μs

1797 μs

1886 μs

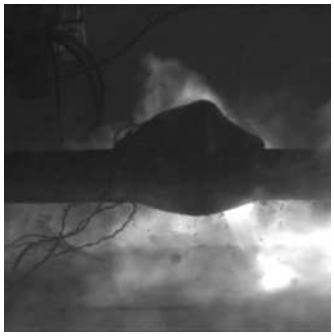

1976 μs

Figure A.61: Shot 146.

2064 μs

2153 μs

2242 μs

2332 μs

2420 μs

2509 μs

2598 μs

2688 μs

2776 μs

2865 μs

2954 μs

3044 μs

Figure A.62: Shot 146 (continued.)

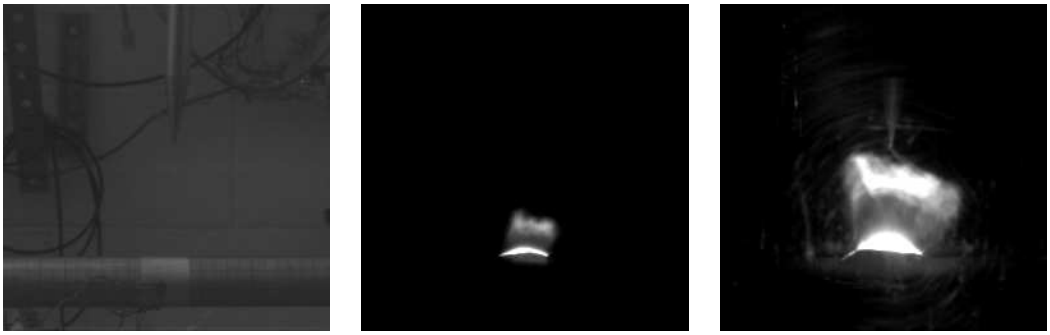
Calibration

994 μs

1083 μs


1172 μs

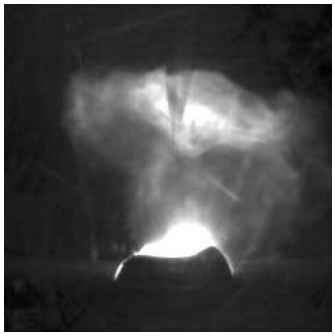
1261 μs

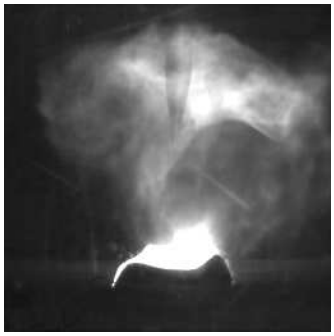
1350 μs

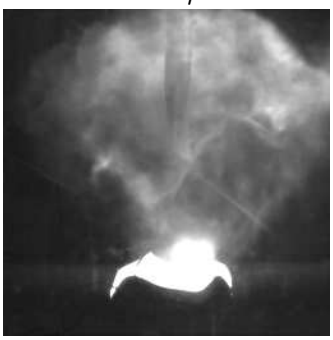
1439 μs

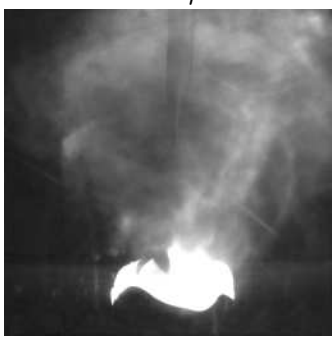
1528 μs


1617 μs


1706 μs


1795 μs

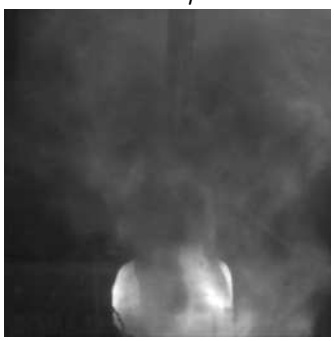
1884 μs

Figure A.63: Shot 147.

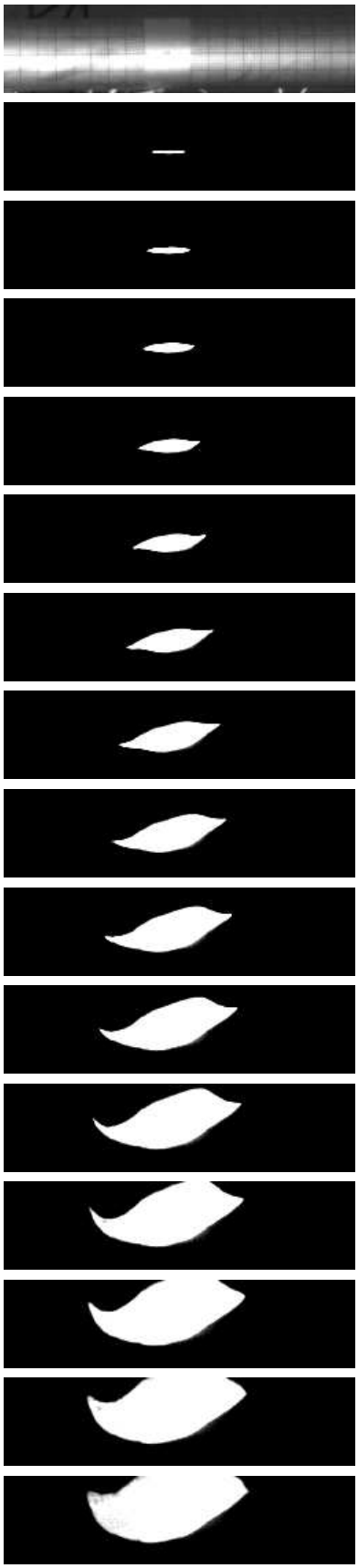

Figure A.64: Shot 149.

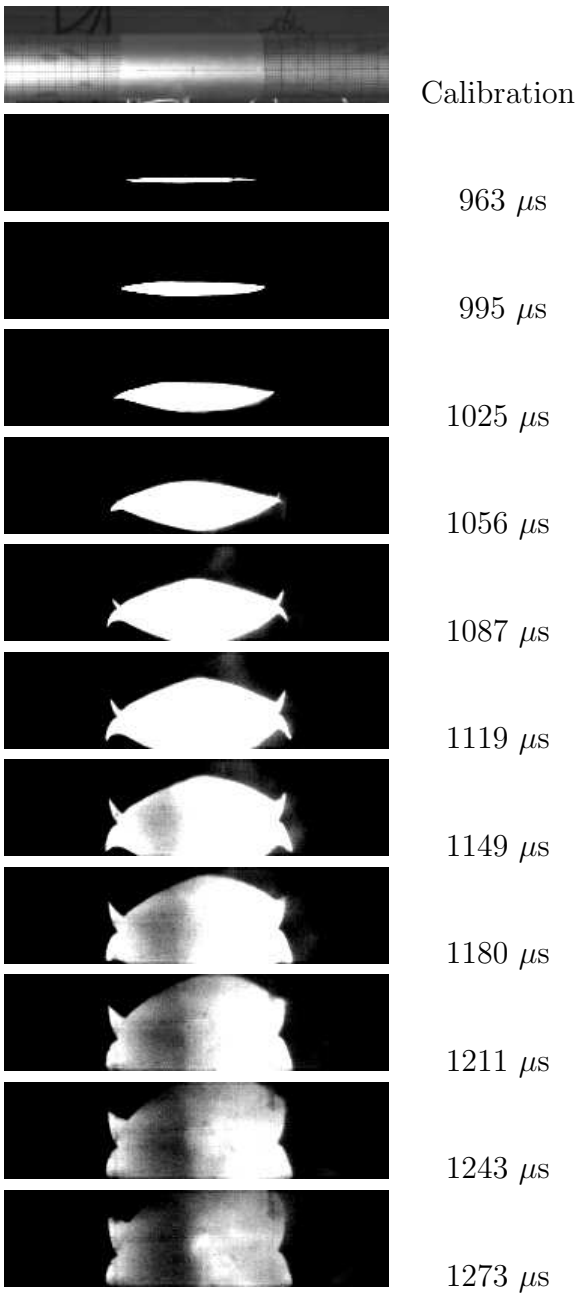

Figure A.65: Shot 150.

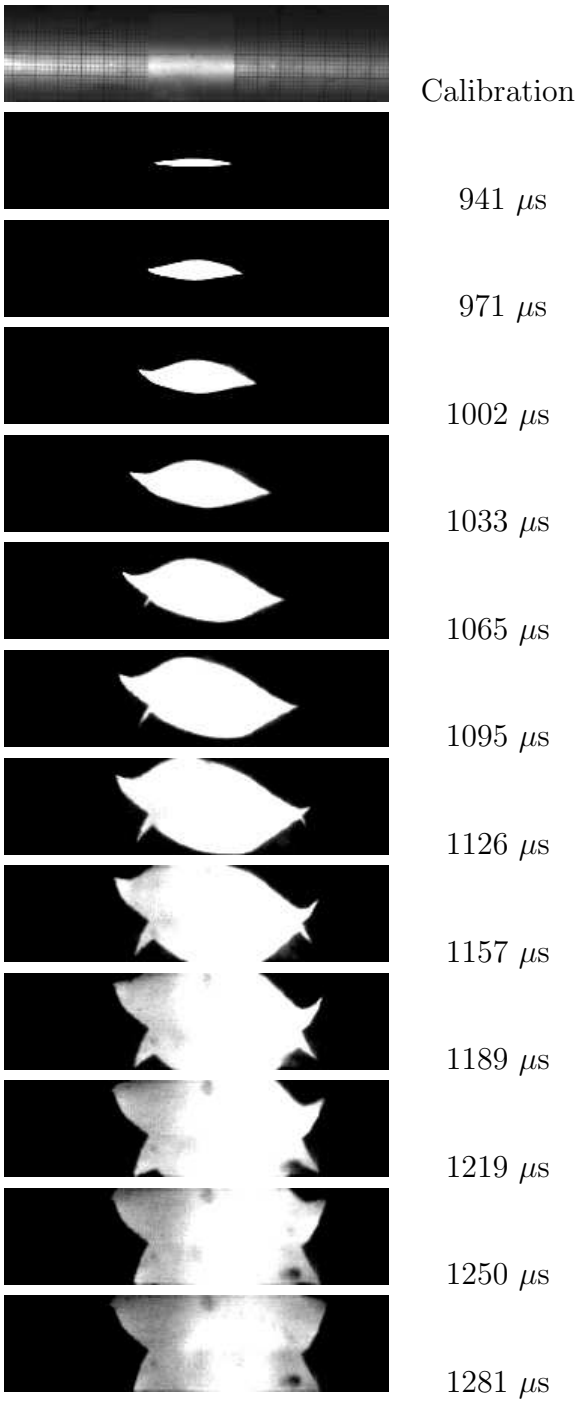

Figure A.66: Shot 151.

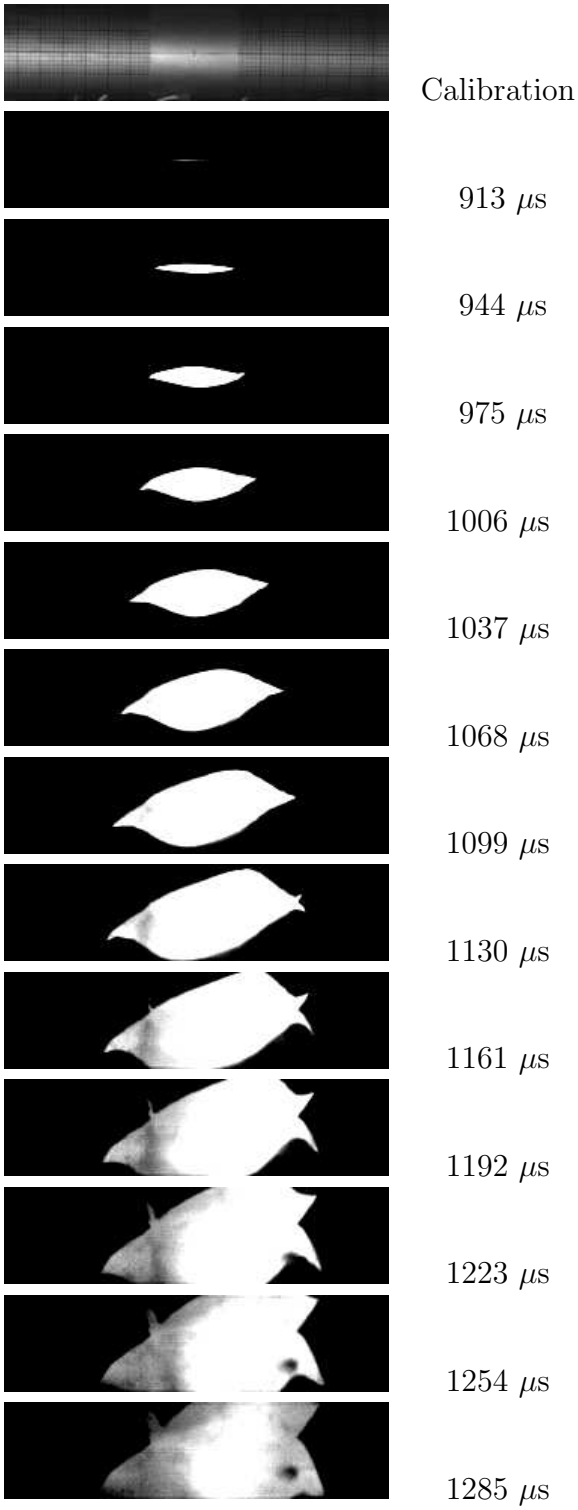

Figure A.67: Shot 152.

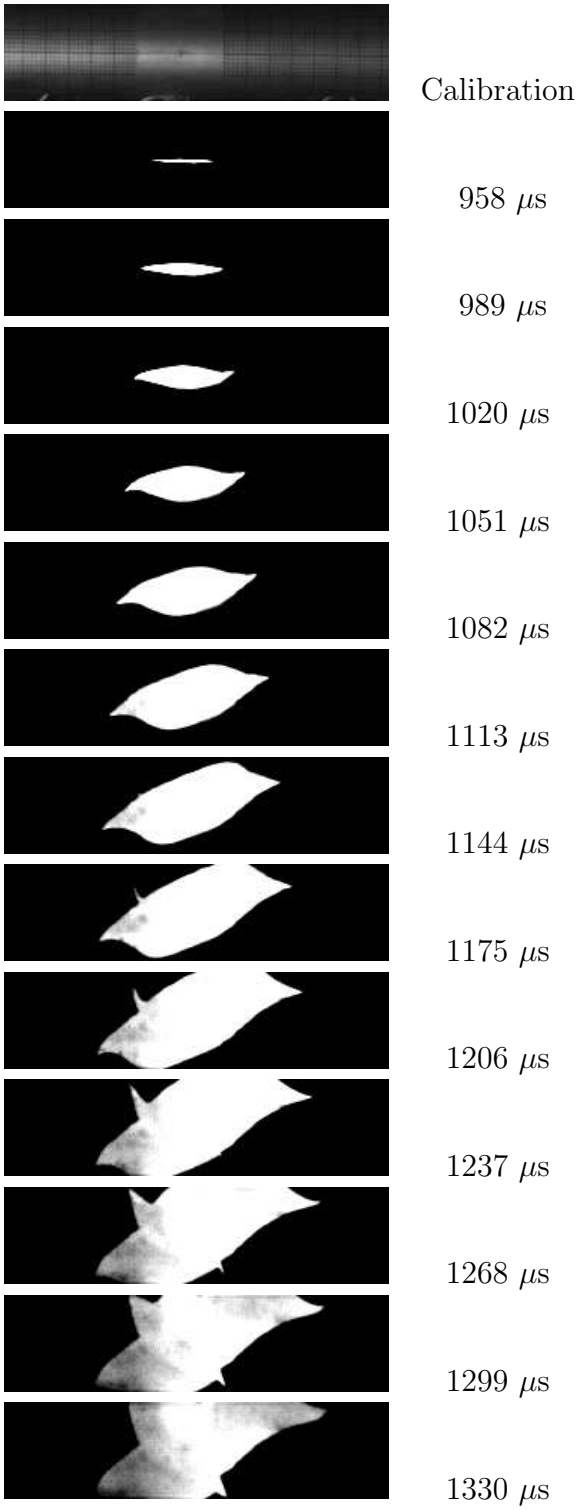

Figure A.68: Shot 153.

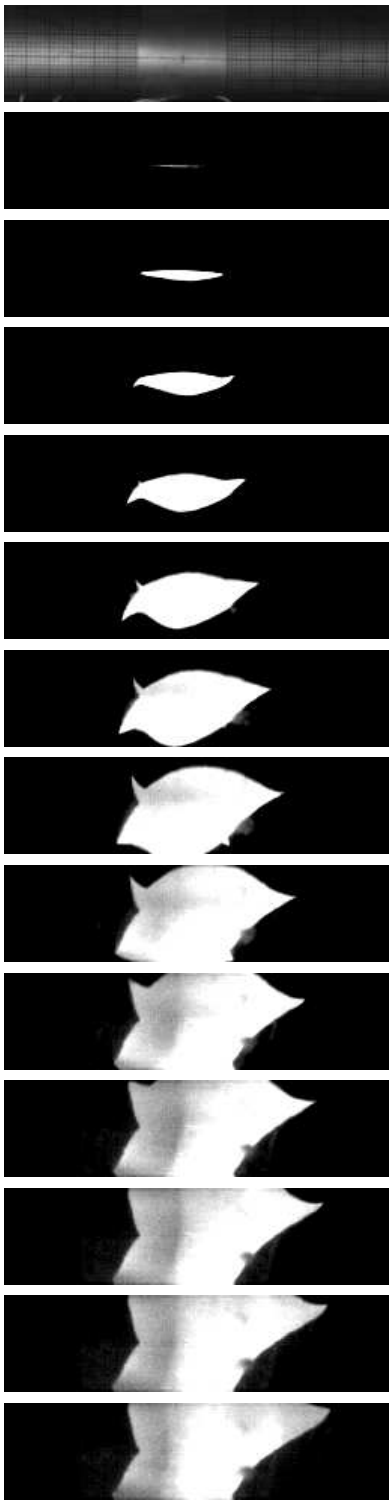

Figure A.69: Shot 154.

A.4 Rupture Blast Pressure

Except Shots 119 and 120, the blast gages were located 24 cm vertically above the notch. For Shot 119, the gage was located at 79 cm and for Shot 120, the gage was located at 39 cm. Time zero corresponds to the ignition spark in the detonation tube. Table A.1 and Figs. A.70 to A.72 show the blast gage and wall locations and notch orientation. As discussed in Section 6.3.9, the disturbances caused by the diffracted shock wave from the tube end and the reflected wave from the walls were small and did not arrive until 3 ms.

Shot	θ (deg.)	$b1$ (cm)	$b2$ (cm)	$b3$ (cm)
119	0	79	53	103
120	0	39	53	104
121	0	24	53	104
122	0			
123	0			
124	0	24	53	104
125	0	24	53	104
126	0	24	53	104
127	0	24	53	104
128	0	24	53	104
129	0	24	53	104
130	0	24	53	104
131	0	24	53	104
132	0	24	51	104
133	0	24	53	104
134	0	24	53	104
135	0	24	51	104
136	0	24	51	104
137	80			
138	80			
139	80			
140	80			
141	80			
142	80			
143	80			
144	80			
145	260			
146	170			
147	350	24	53	104
148	80			
149	80			
150	80			
151	80			
152	80			
153	80			
154	80			

Table A.1: Blast gage and wall locations and notch orientation.

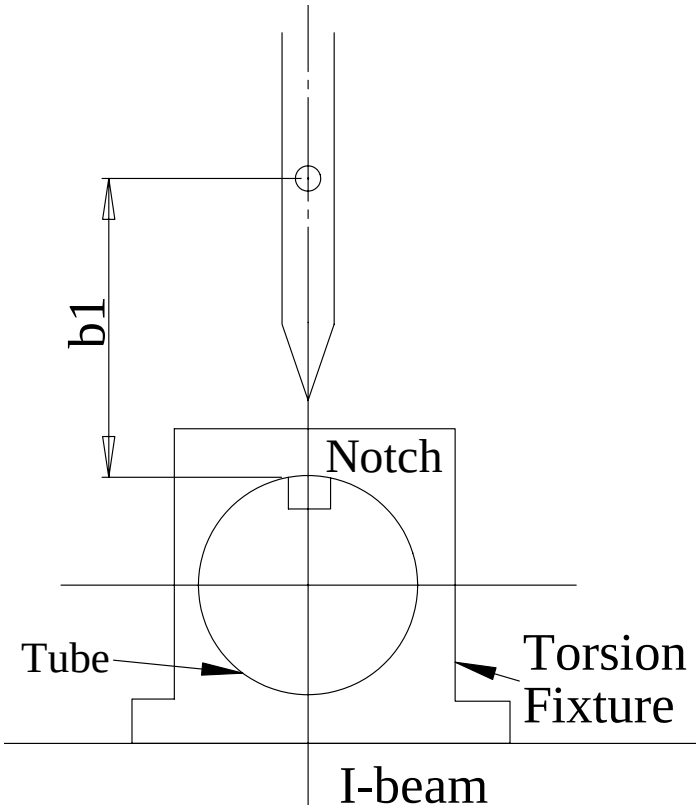

Figure A.70: Blast gage location for Shots 119 to 136. Detonation direction is out of paper.

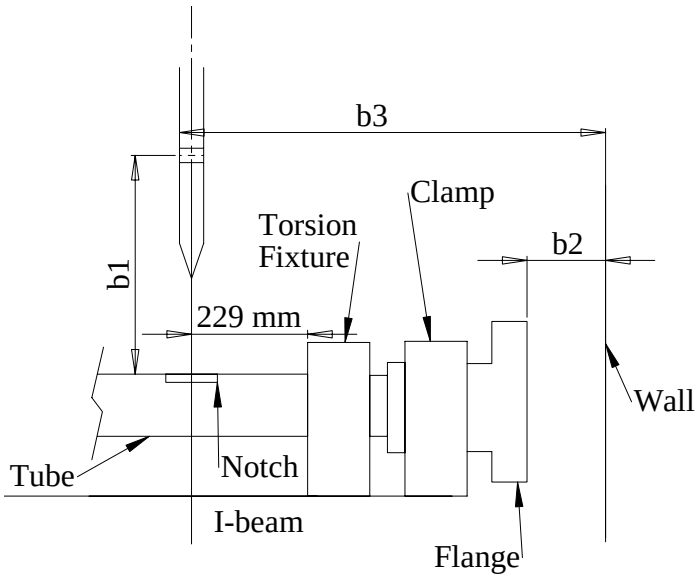

Figure A.71: Blast gage location. Detonation direction is from left to right.

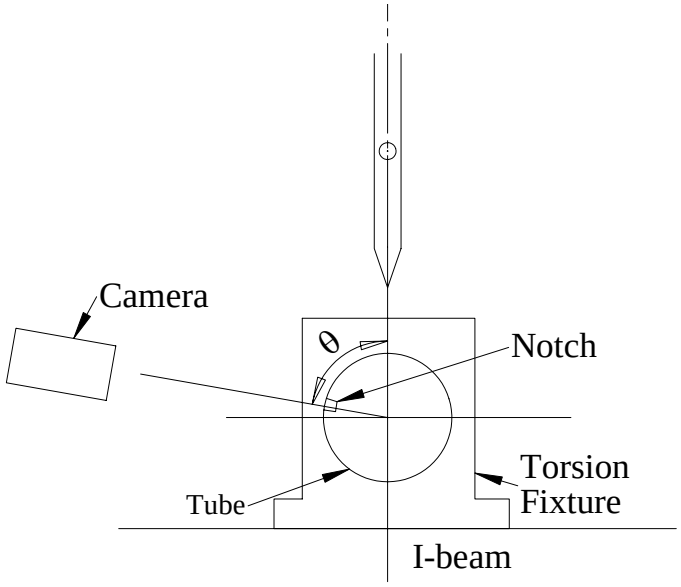

Figure A.72: Camera location for Shots 137 to 154. Detonation direction is out of paper.

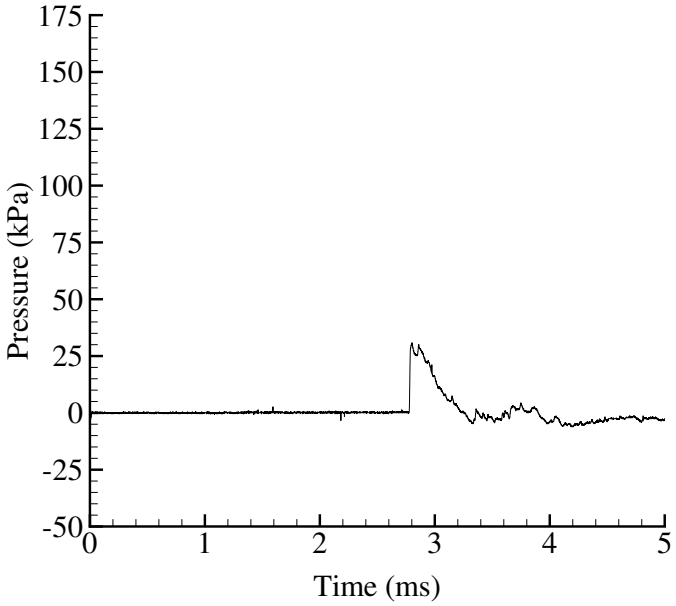

Figure A.73: Shot 119 blast pressure.

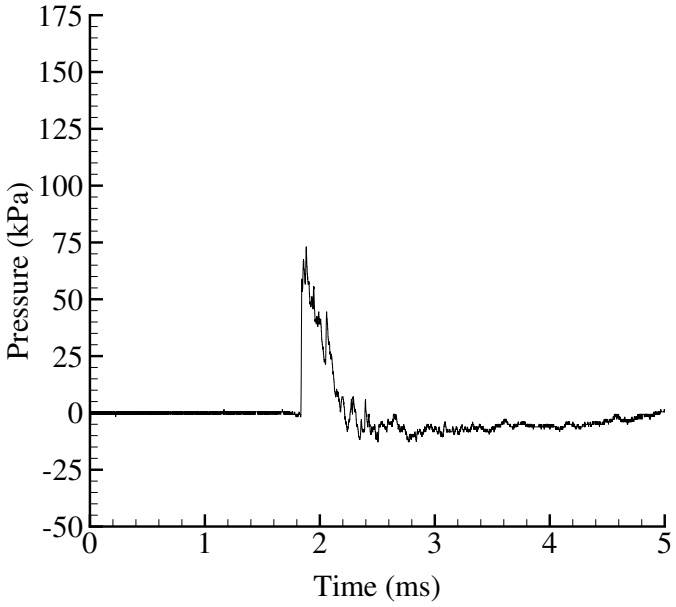

Figure A.74: Shot 120 blast pressure.

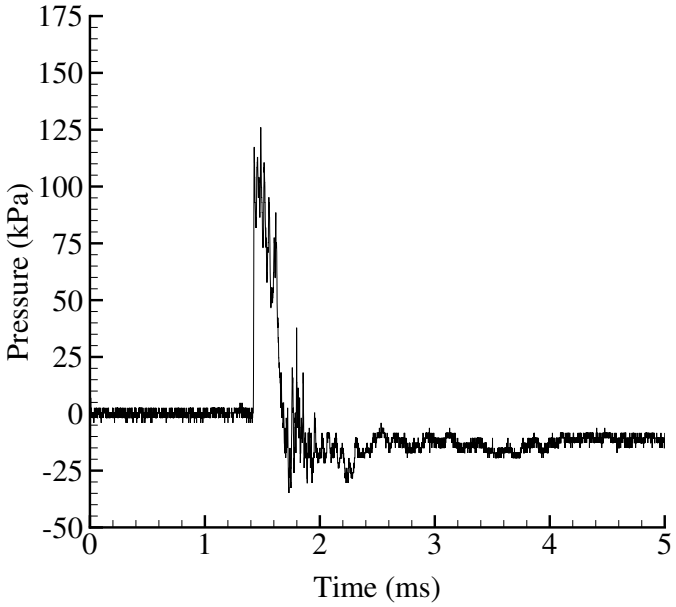

Figure A.75: Shot 121 blast pressure.

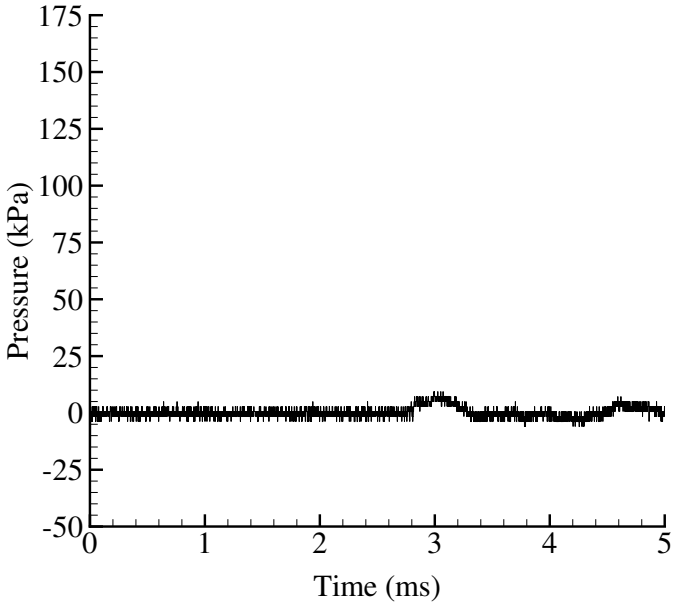

Figure A.76: Shot 124 blast pressure.

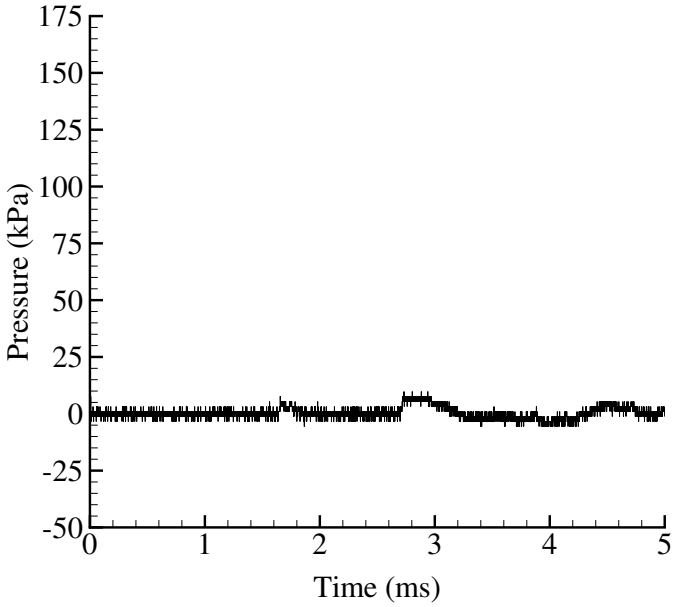

Figure A.77: Shot 125 blast pressure.

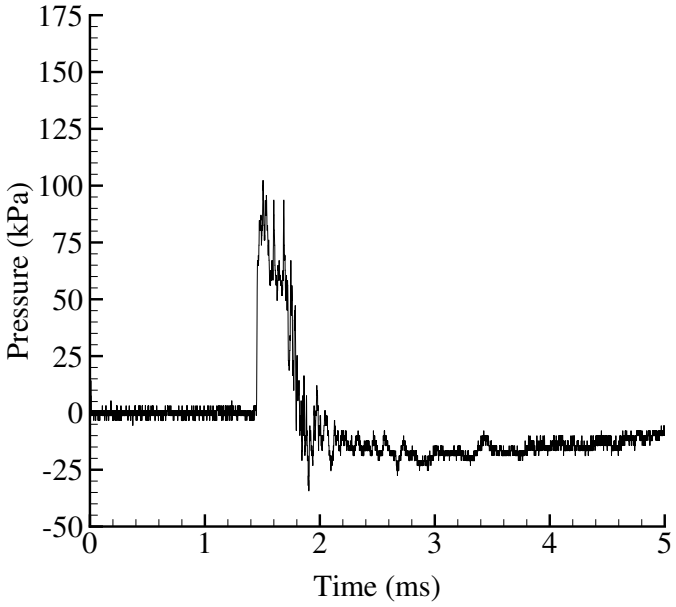

Figure A.78: Shot 126 blast pressure.

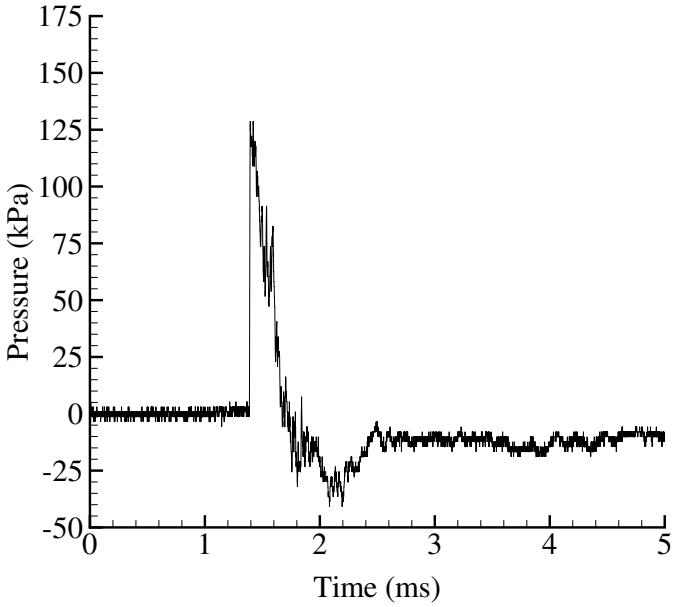

Figure A.79: Shot 127 blast pressure.

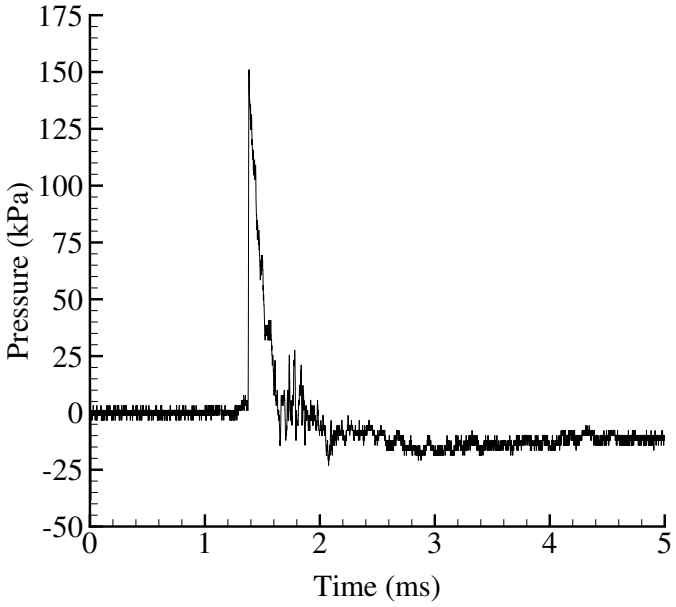

Figure A.80: Shot 128 blast pressure.

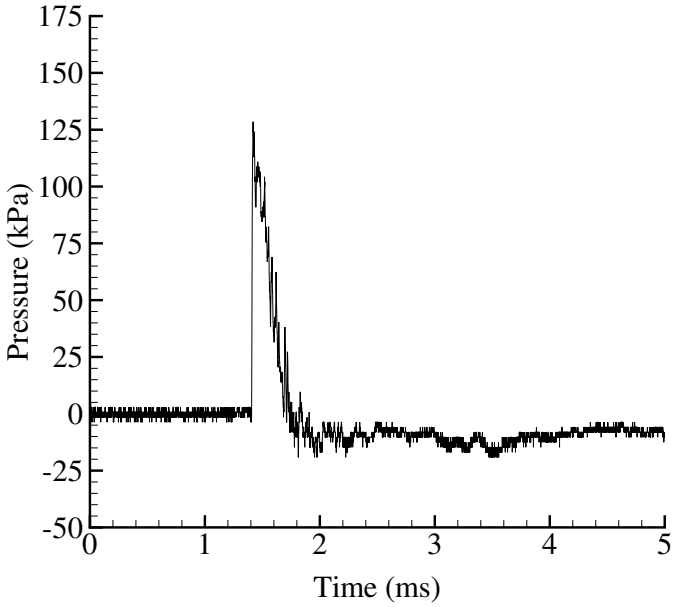

Figure A.81: Shot 129 blast pressure.

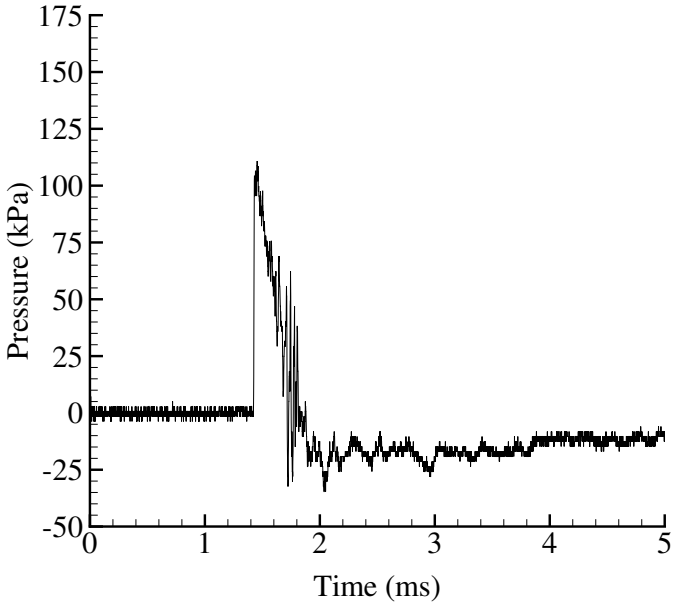

Figure A.82: Shot 130 blast pressure.

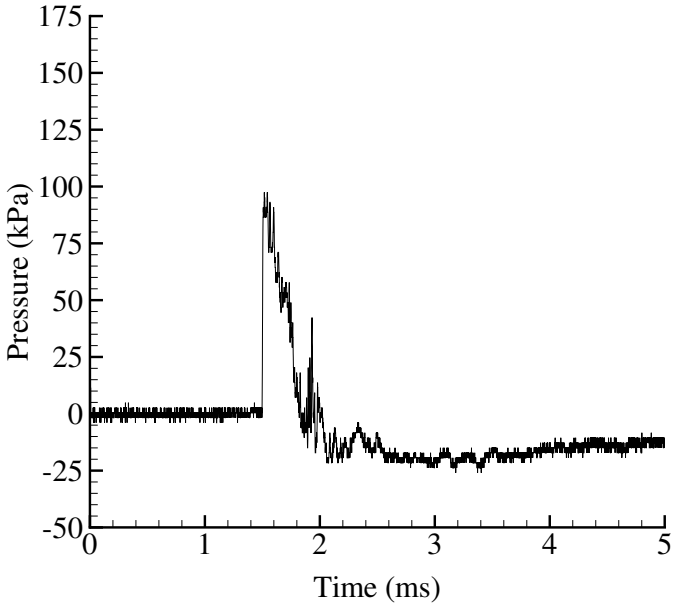

Figure A.83: Shot 131 blast pressure.

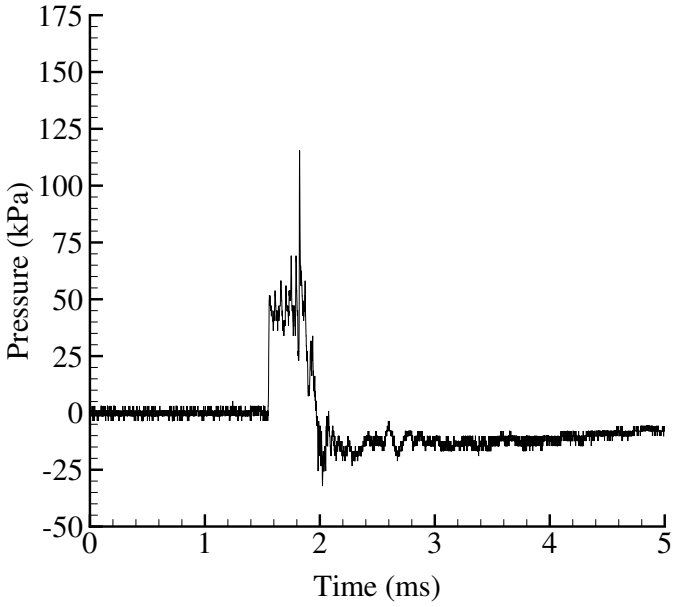

Figure A.84: Shot 132 blast pressure.

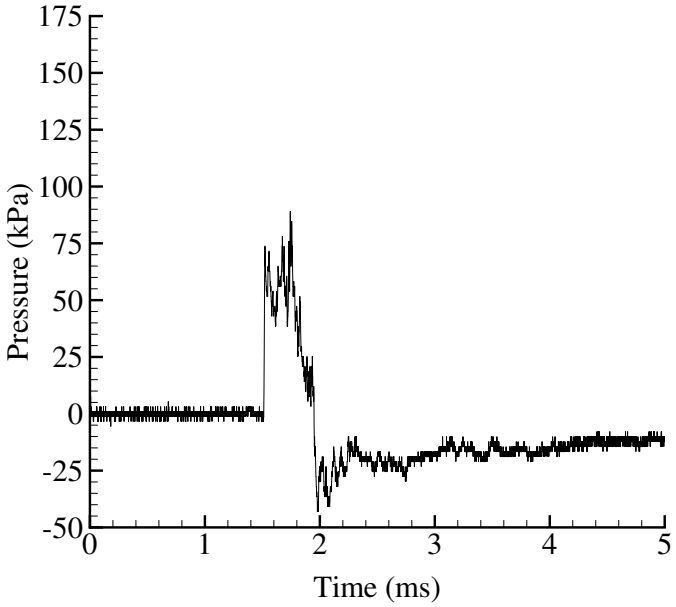

Figure A.85: Shot 133 blast pressure.

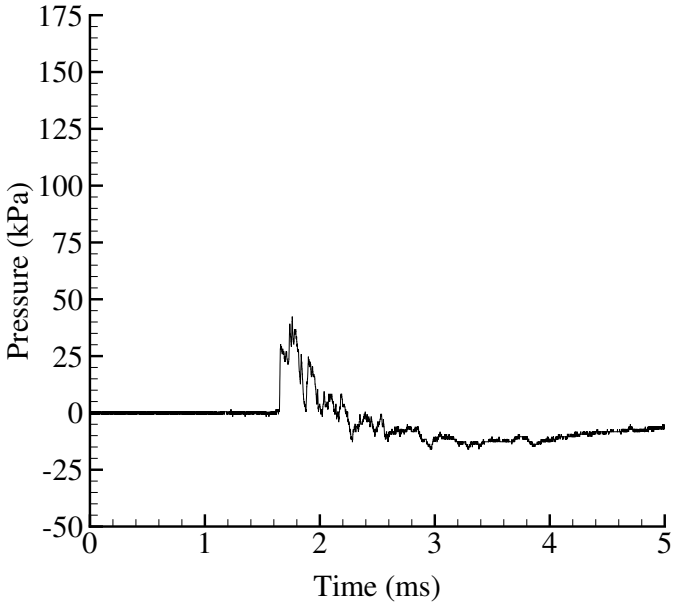

Figure A.86: Shot 134 blast pressure.

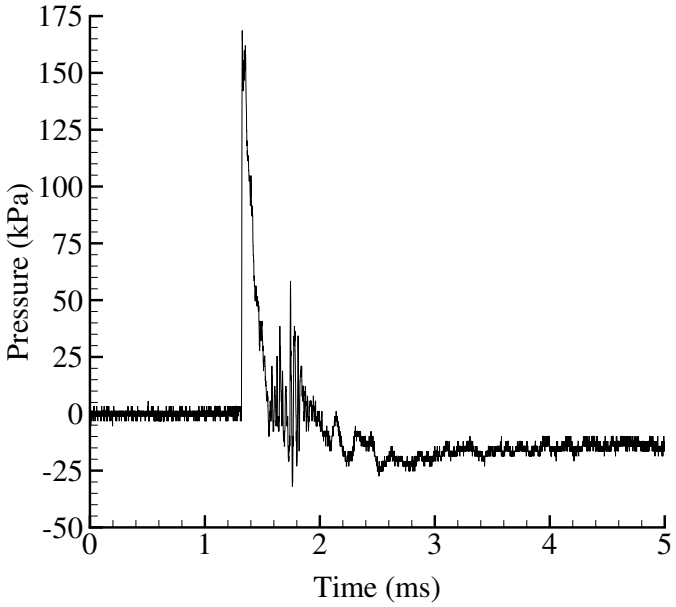

Figure A.87: Shot 135 blast pressure.

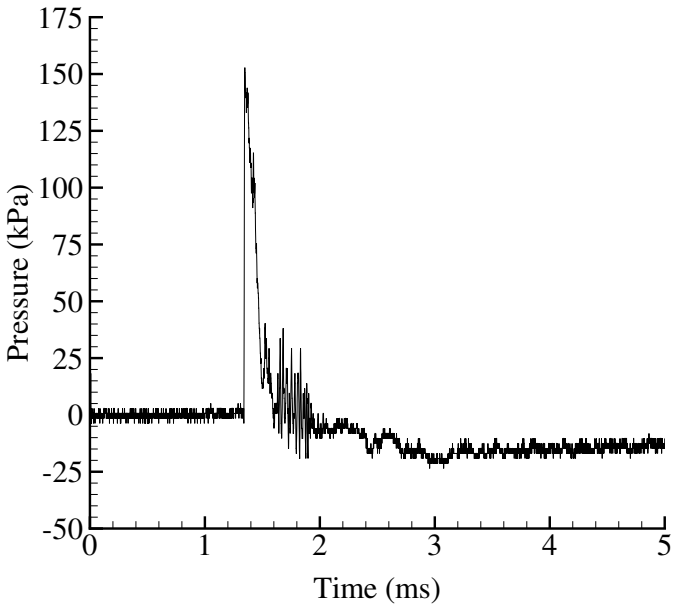

Figure A.88: Shot 136 blast pressure.

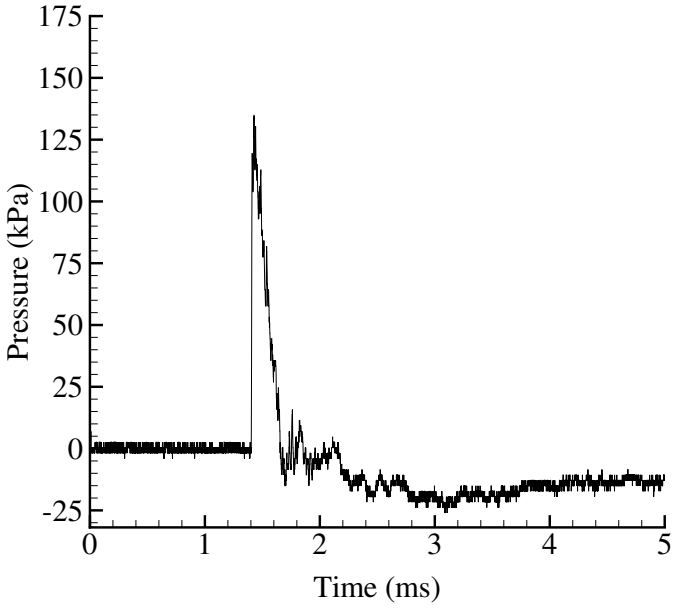

Figure A.89: Shot 147 blast pressure.

A.5 Strain Traces

A.5.1 Hoop strain and Axial Strain Near The Notch

Figures A.90 to A.91 and Table A.2 show the locations for strain gages mounted outside the tube near the notch.

Shot	$s5$	$s6$	$s7$
119	22	21	n/a
120	17	11	15
121	18	11	15
122	17	11	16
123	17	11	16
124	7	3	7
125	7	3	7
126	11	6	11
127	23	18	22
128	29	25	29
129	18	12	17
130	18	13	17
131	17	13	17
132	17	13	17
133	18	13	17
134	17	13	17
135	42	38	42
136	35	30	34

Table A.2: Strain gage locations (all dimensions are in mm.)

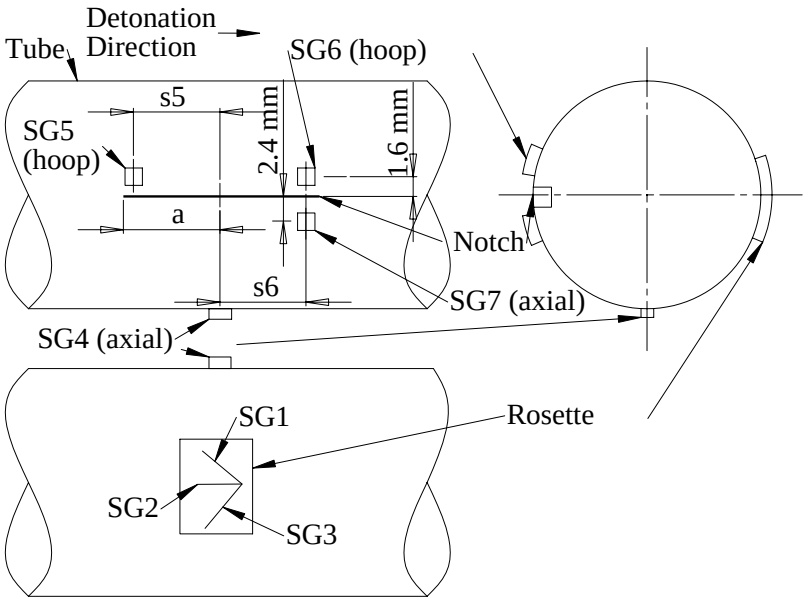

Figure A.90: Strain gage location for Shot 119.

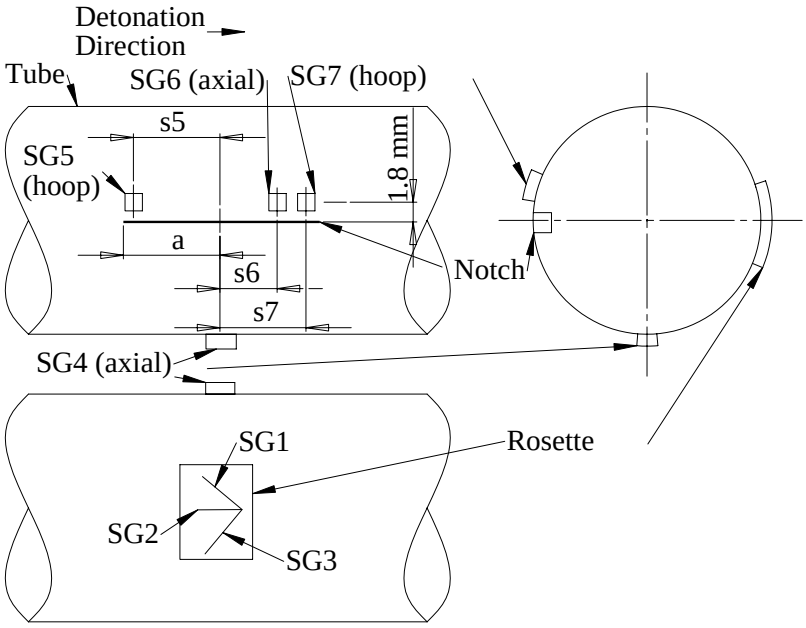

Figure A.91: Strain gage location for Shots 120 to 136.

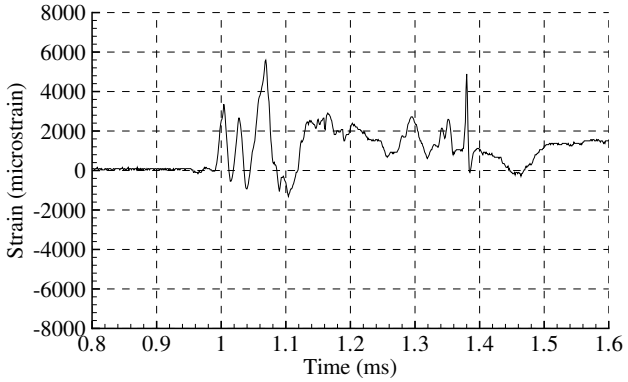

Figure A.92: Shot 119 SG5 (hoop) strain.

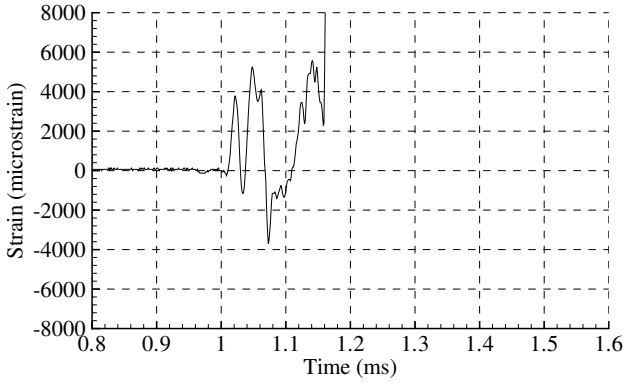

Figure A.93: Shot 119 SG6 (hoop) strain.

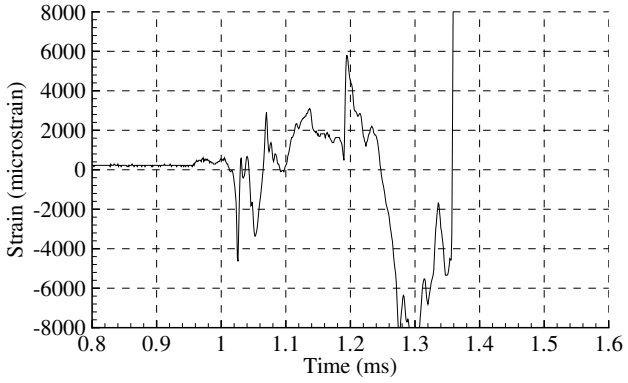

Figure A.94: Shot 119 SG7 (axial) strain.

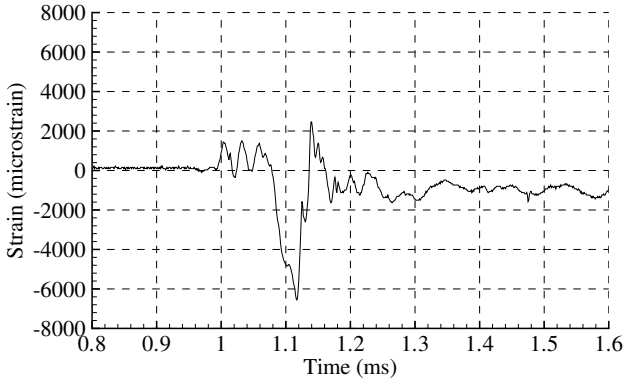

Figure A.95: Shot 120 SG5 (hoop) strain.

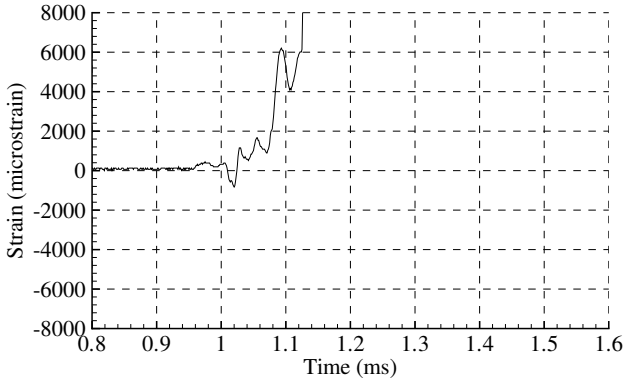

Figure A.96: Shot 120 SG6 (axial) strain.

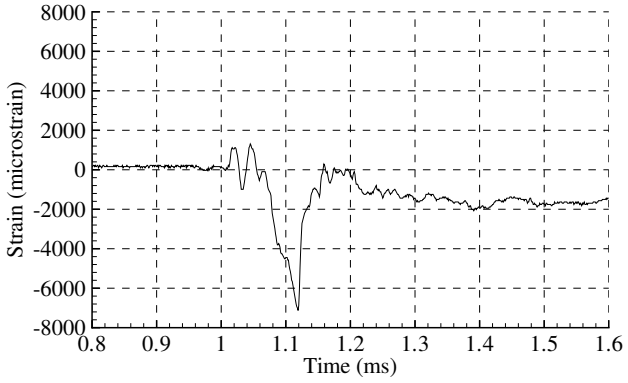

Figure A.97: Shot 120 SG7 (hoop) strain.

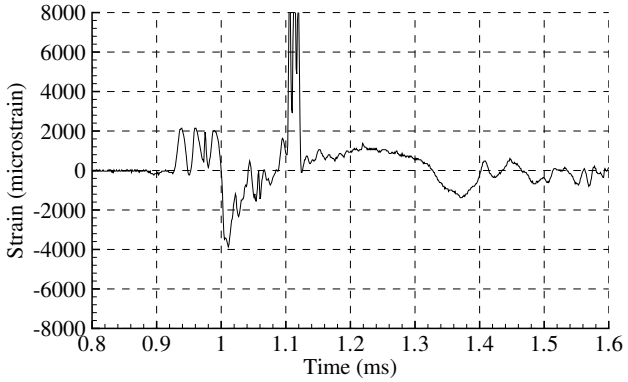

Figure A.98: Shot 121 SG5 (hoop) strain.

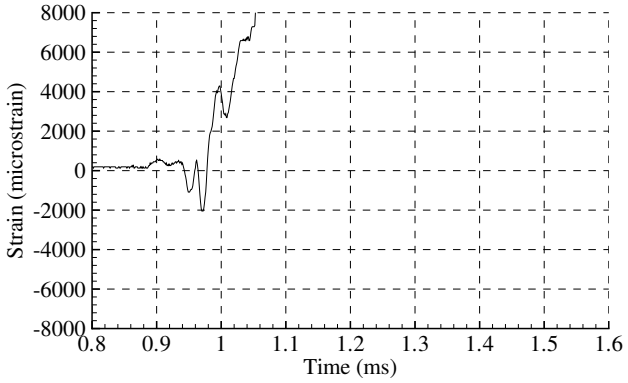

Figure A.99: Shot 121 SG6 (axial) strain.

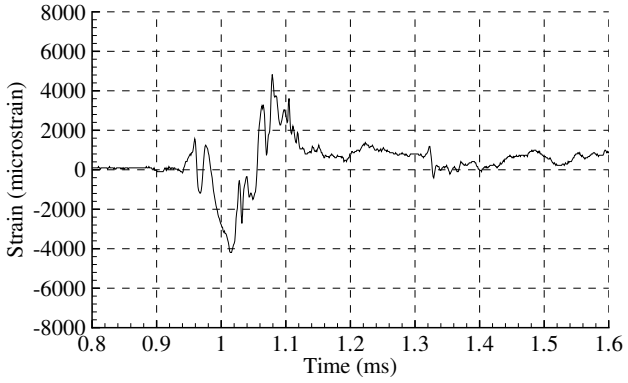

Figure A.100: Shot 121 SG7 (hoop) strain.

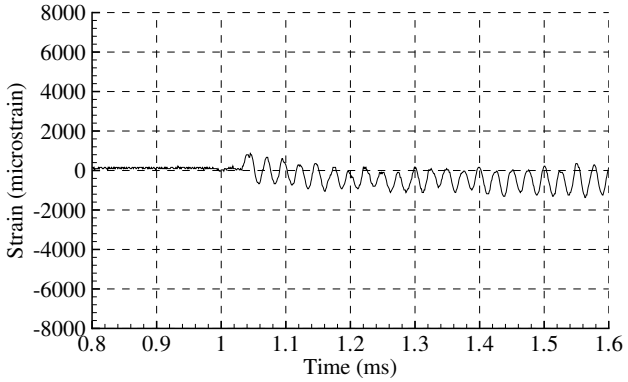

Figure A.101: Shot 122 SG5 (hoop) strain.

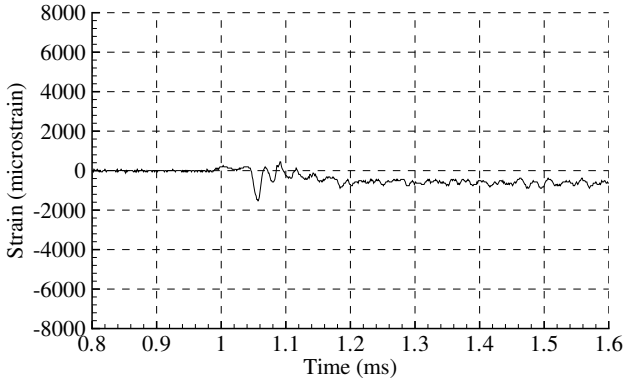

Figure A.102: Shot 122 SG6 (axial) strain.

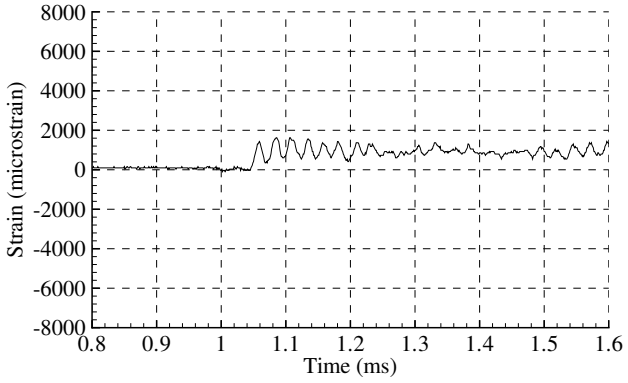

Figure A.103: Shot 122 SG7 (hoop) strain.

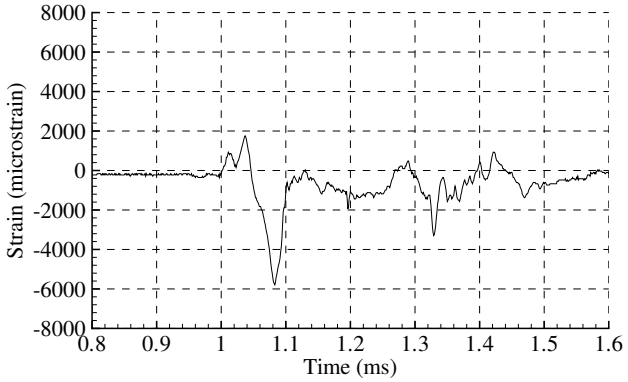

Figure A.104: Shot 123 SG5 (hoop) strain.

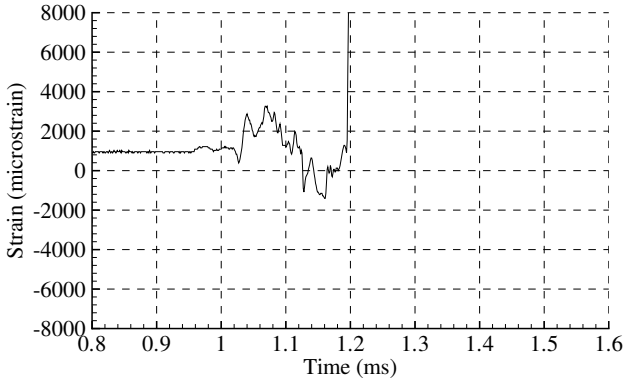

Figure A.105: Shot 123 SG6 (axial) strain.

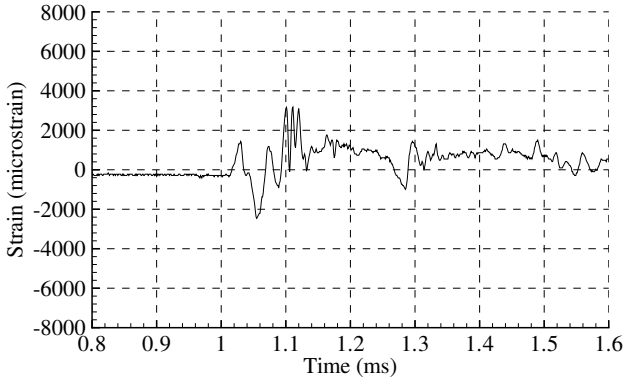

Figure A.106: Shot 123 SG7 (hoop) strain.

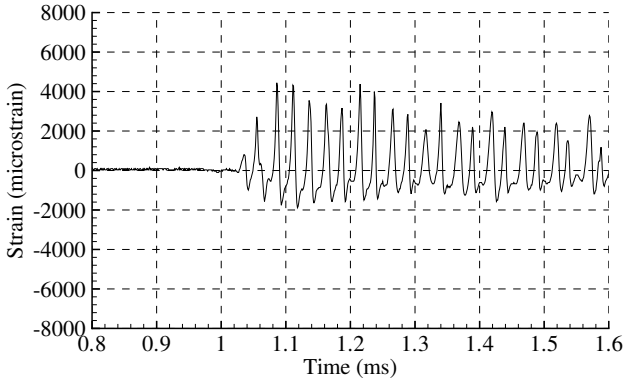

Figure A.107: Shot 124 SG5 (hoop) strain.

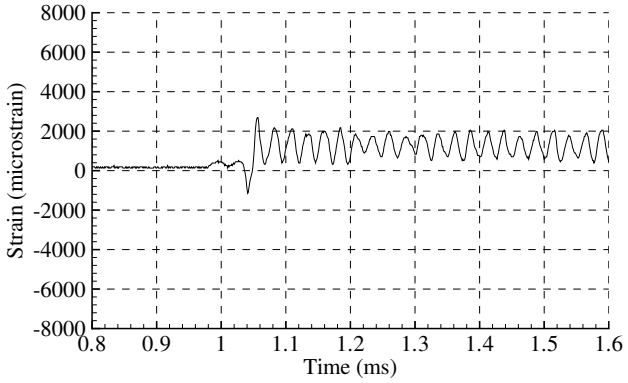

Figure A.108: Shot 124 SG6 (axial) strain.

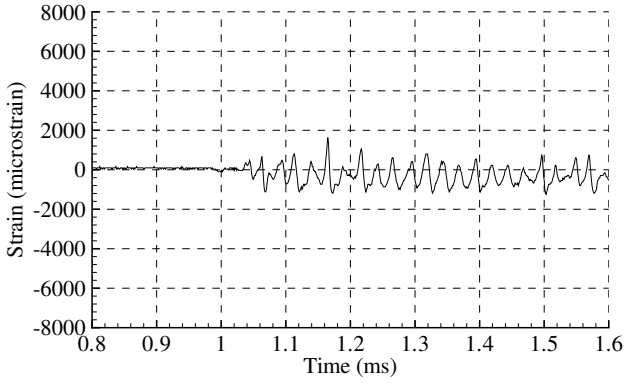

Figure A.109: Shot 124 SG7 (hoop) strain.

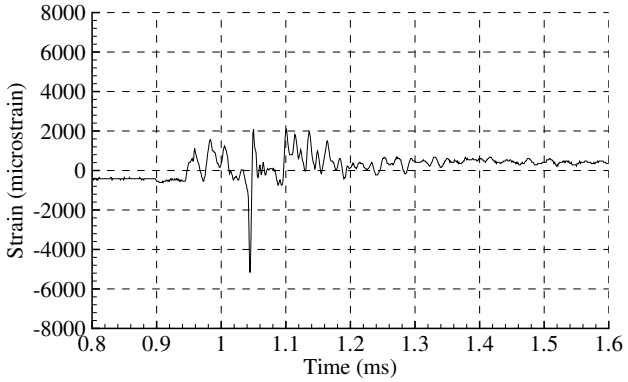

Figure A.110: Shot 125 SG5 (hoop) strain.

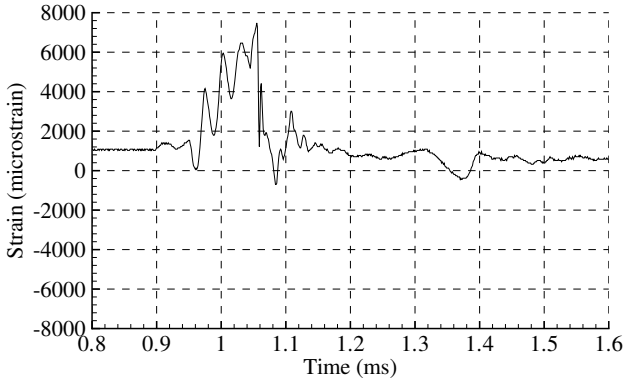

Figure A.111: Shot 125 SG6 (axial) strain.

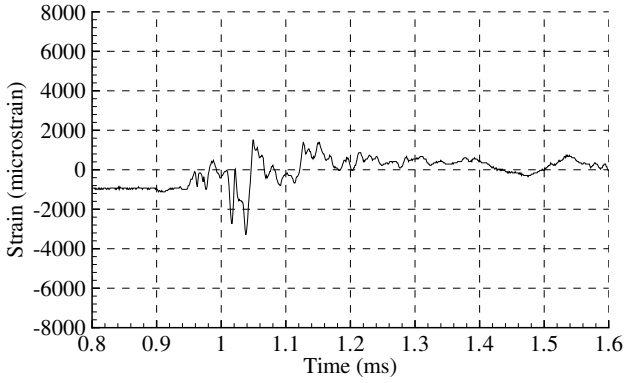

Figure A.112: Shot 125 SG7 (hoop) strain.

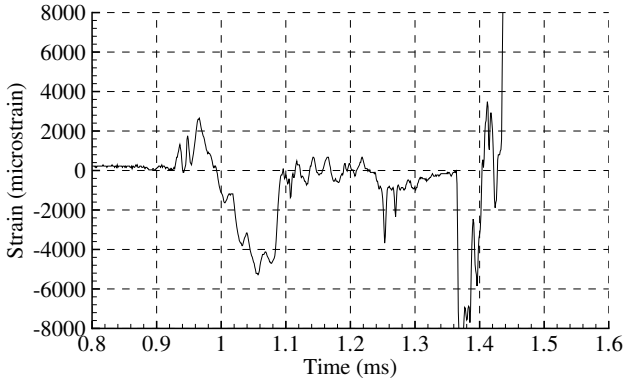

Figure A.113: Shot 126 SG5 (hoop) strain.

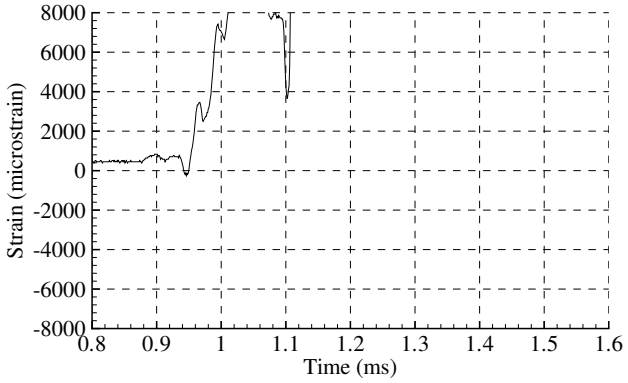

Figure A.114: Shot 126 SG6 (axial) strain.

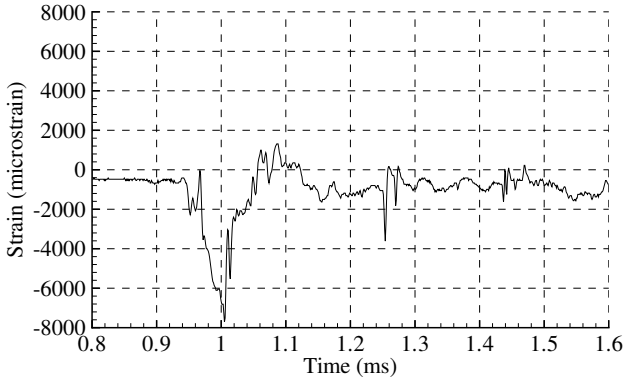

Figure A.115: Shot 126 SG7 (hoop) strain.

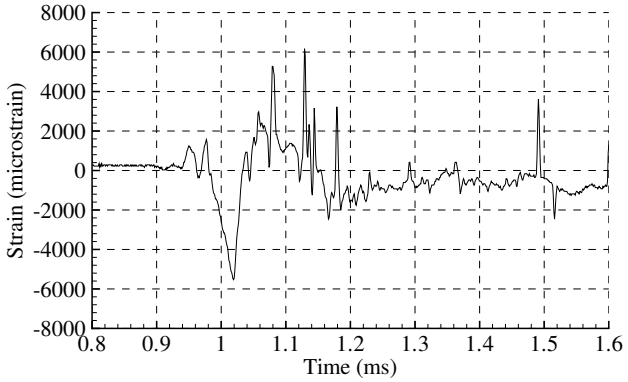

Figure A.116: Shot 127 SG5 (hoop) strain.

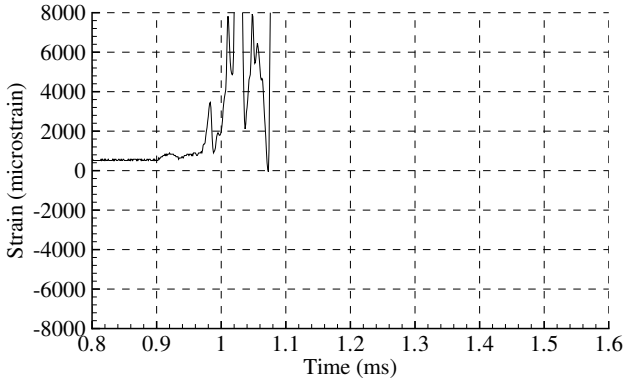

Figure A.117: Shot 127 SG6 (axial) strain.

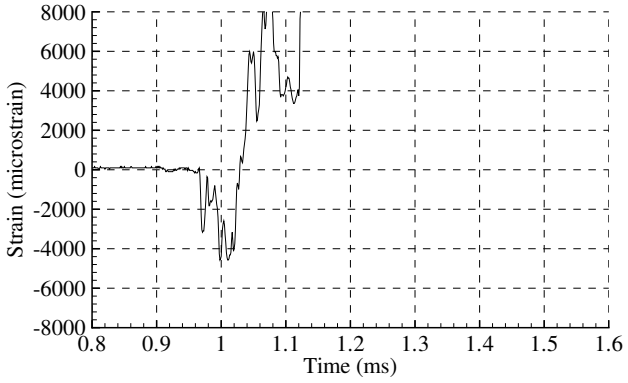

Figure A.118: Shot 127 SG7 (hoop) strain.

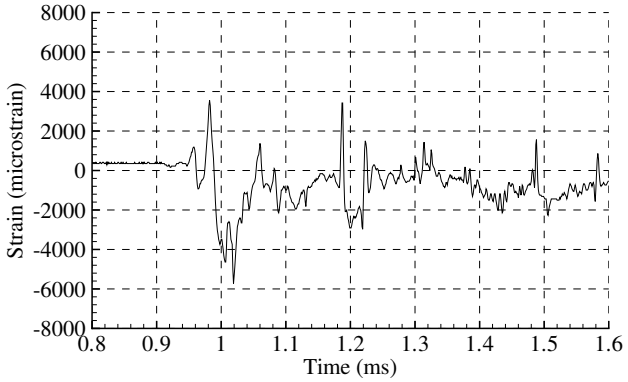

Figure A.119: Shot 128 SG5 (hoop) strain.

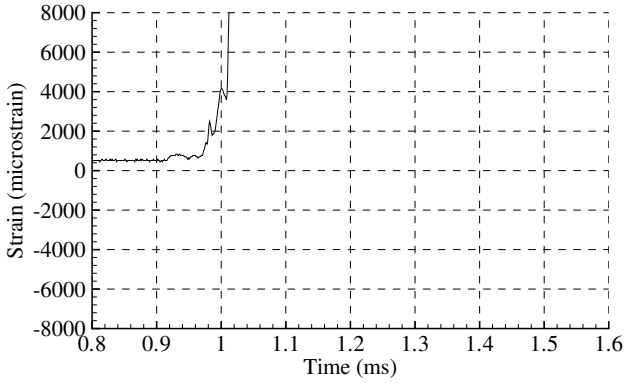

Figure A.120: Shot 128 SG6 (axial) strain.

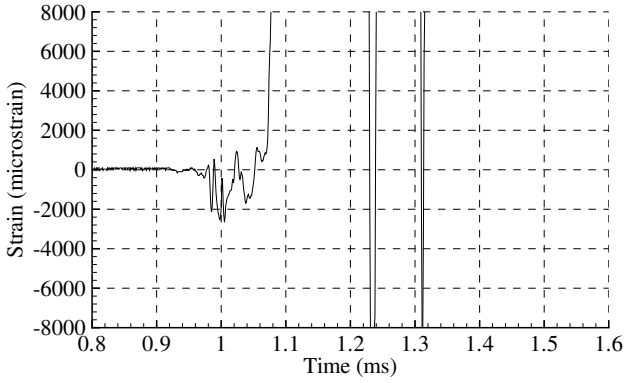

Figure A.121: Shot 128 SG7 (hoop) strain.

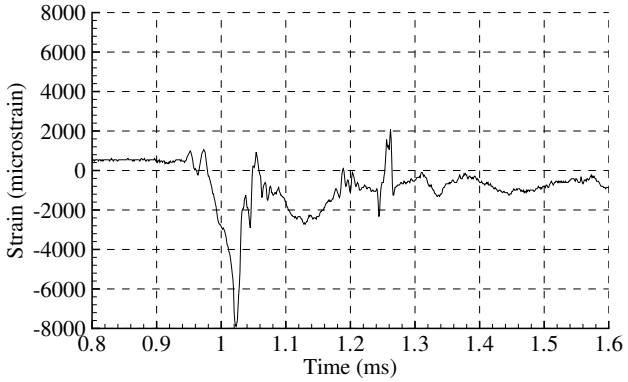

Figure A.122: Shot 129 SG5 (hoop) strain.

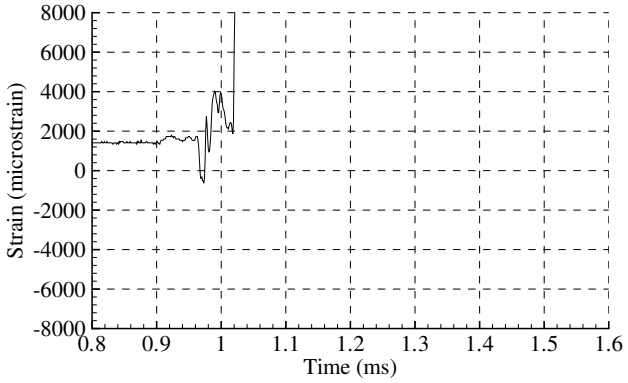

Figure A.123: Shot 129 SG6 (axial) strain.

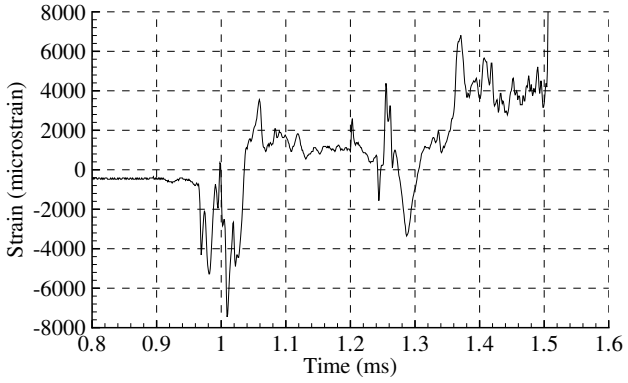

Figure A.124: Shot 129 SG7 (hoop) strain.

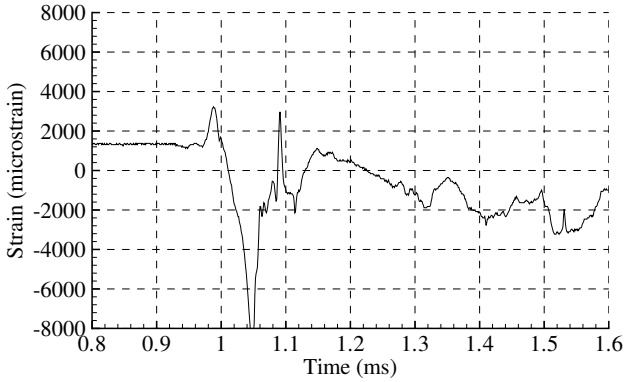

Figure A.125: Shot 130 SG5 (hoop) strain.

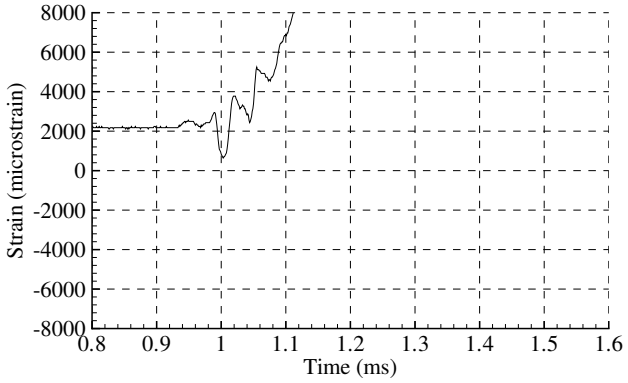

Figure A.126: Shot 130 SG6 (axial) strain.

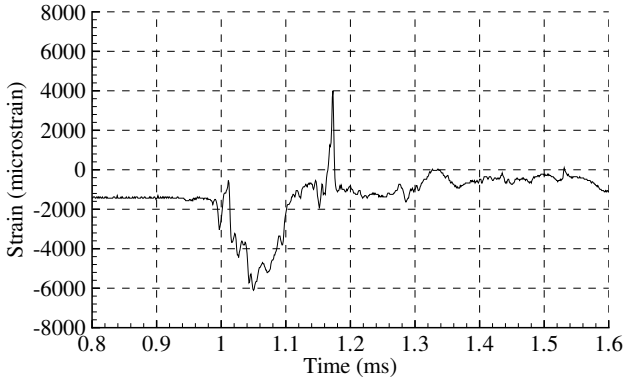

Figure A.127: Shot 130 SG7 (hoop) strain.

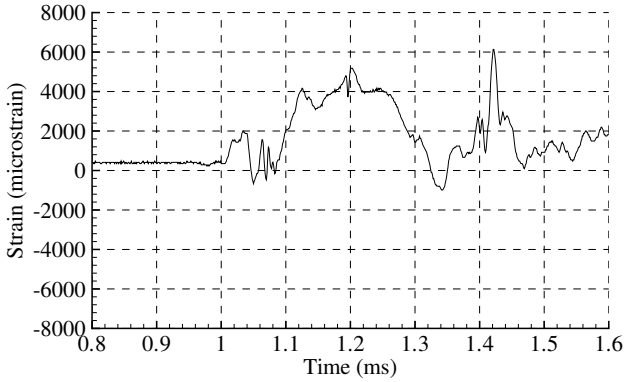

Figure A.128: Shot 131 SG5 (hoop) strain.

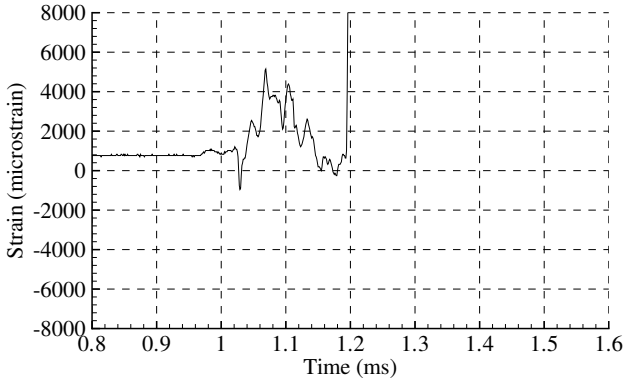

Figure A.129: Shot 131 SG6 (axial) strain.

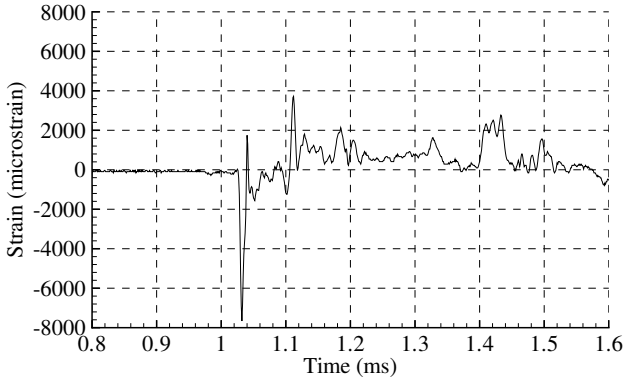

Figure A.130: Shot 131 SG7 (hoop) strain.

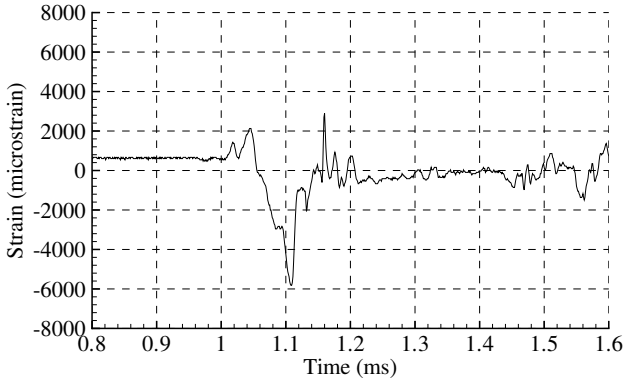

Figure A.131: Shot 132 SG5 (hoop) strain.

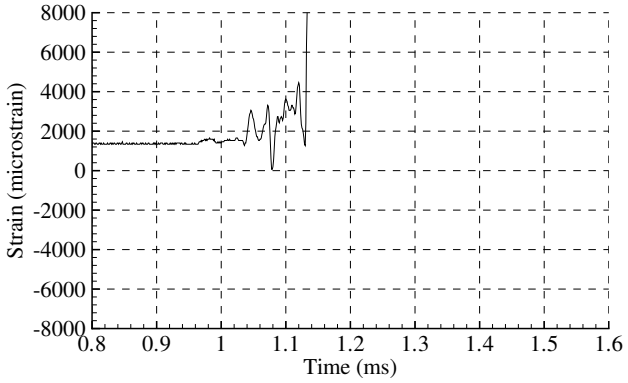

Figure A.132: Shot 132 SG6 (axial) strain.

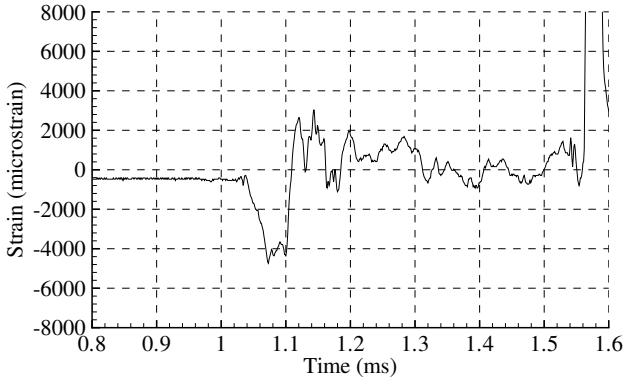

Figure A.133: Shot 132 SG7 (hoop) strain.

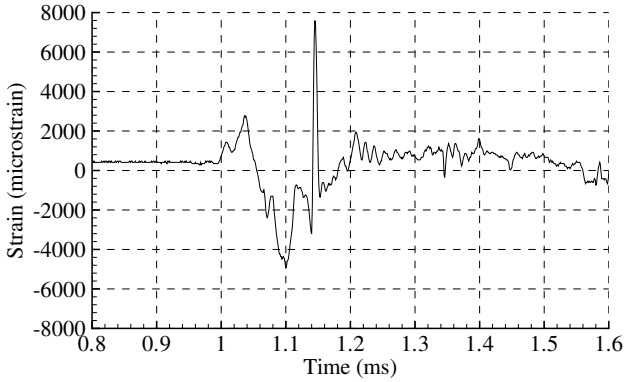

Figure A.134: Shot 133 SG5 (hoop) strain.

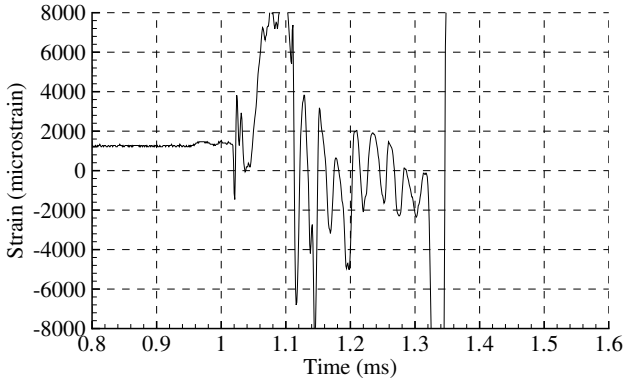

Figure A.135: Shot 133 SG6 (axial) strain.

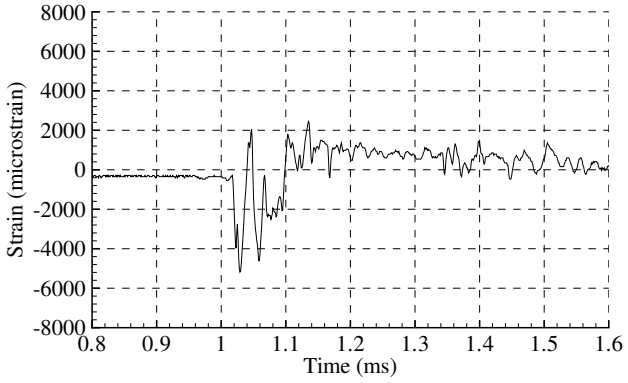

Figure A.136: Shot 133 SG7 (hoop) strain.

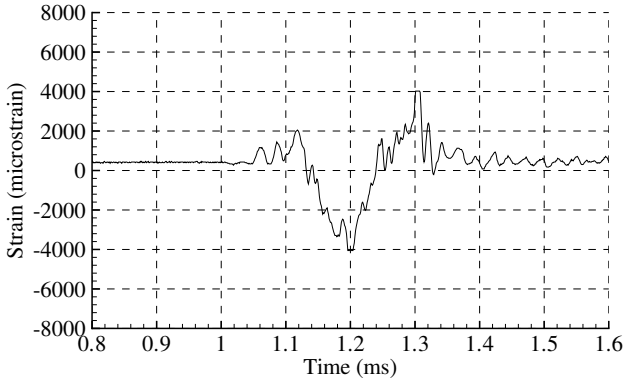

Figure A.137: Shot 134 SG5 (hoop) strain.

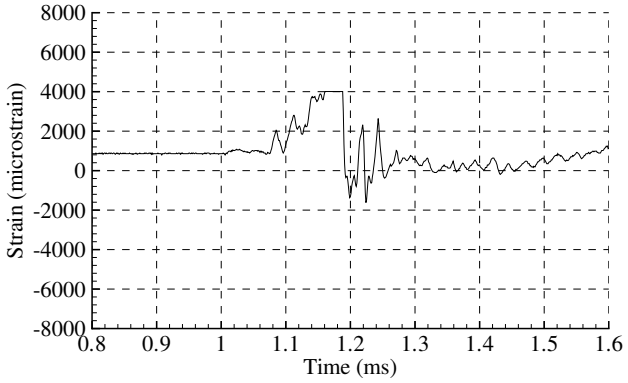

Figure A.138: Shot 134 SG6 (axial) strain.

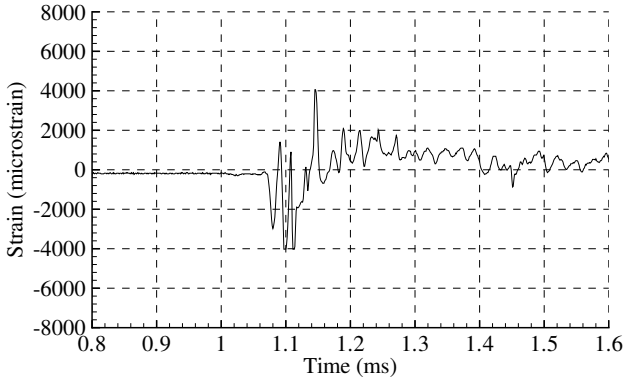

Figure A.139: Shot 134 SG7 (hoop) strain.

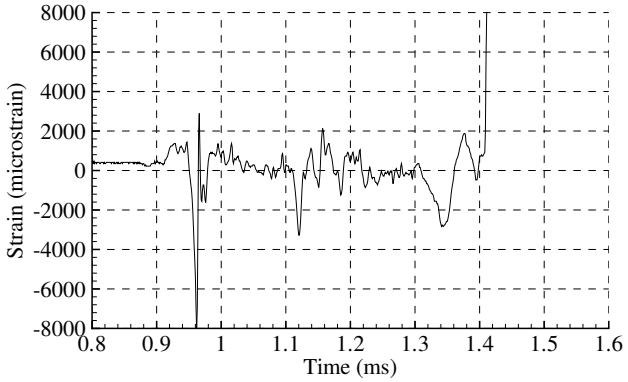

Figure A.140: Shot 135 SG5 (hoop) strain.

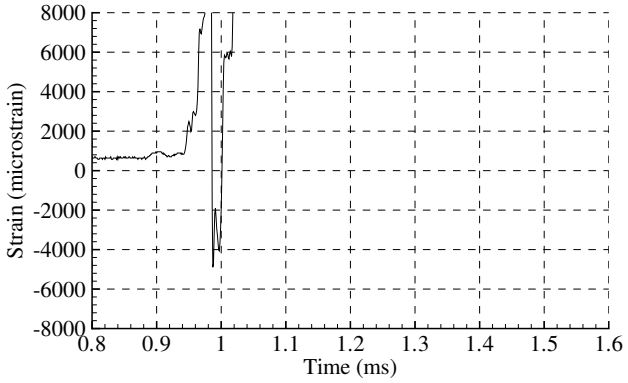

Figure A.141: Shot 135 SG6 (axial) strain.

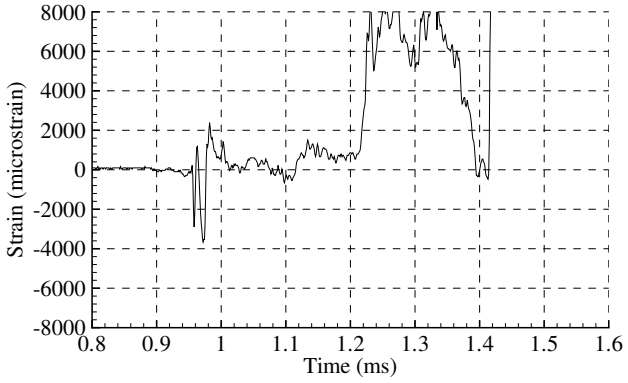

Figure A.142: Shot 135 SG7 (hoop) strain.

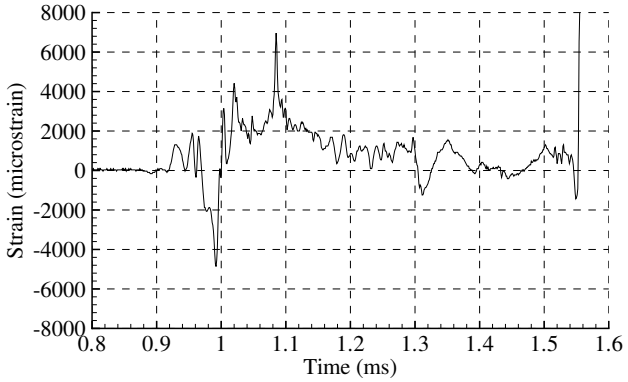

Figure A.143: Shot 136 SG5 (hoop) strain.

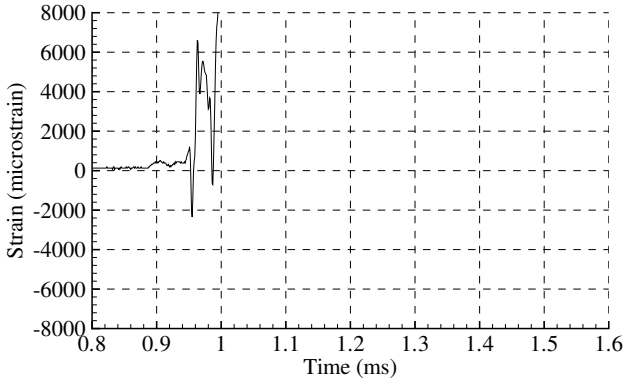

Figure A.144: Shot 136 SG6 (axial) strain.

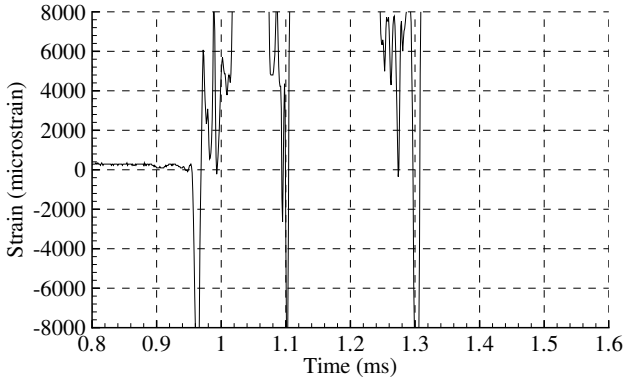

Figure A.145: Shot 136 SG7 (hoop) strain.

A.5.2 Strain Gage Rosettes

Shear and axial strain histories from strain gage rosettes are shown here. Solid lines represent data from the strain gage rosette located in the middle of the tube length, opposite the notch. Dotted lines represent data from the second strain gage rosette, located 11.43 cm (one quarter of the effective specimen length) downstream from the first rosette and at the same circumferential location. Time zero corresponds to the ignition spark in the detonation tube. Figures A.146 to A.148 show the locations for the strain gage rosettes.

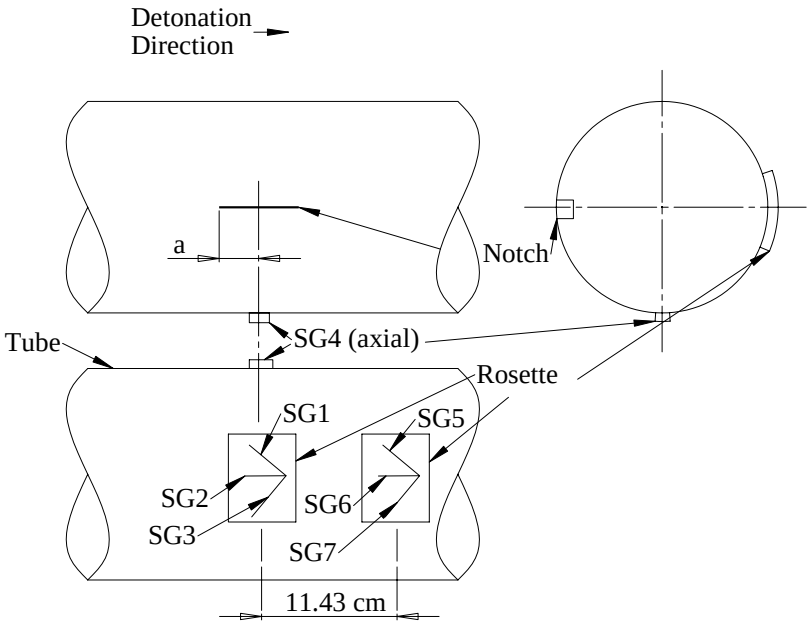

Figure A.146: Strain gage location for Shots 137, 140 to 143, and 148 to 153.

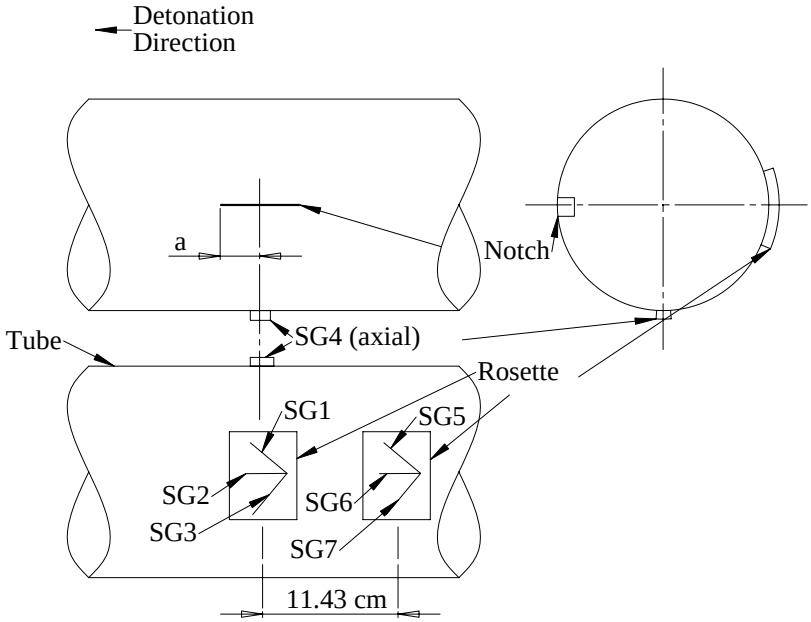

Figure A.147: Strain gage location for Shot 144 (note that in this figure the detonation direction is from right to left).

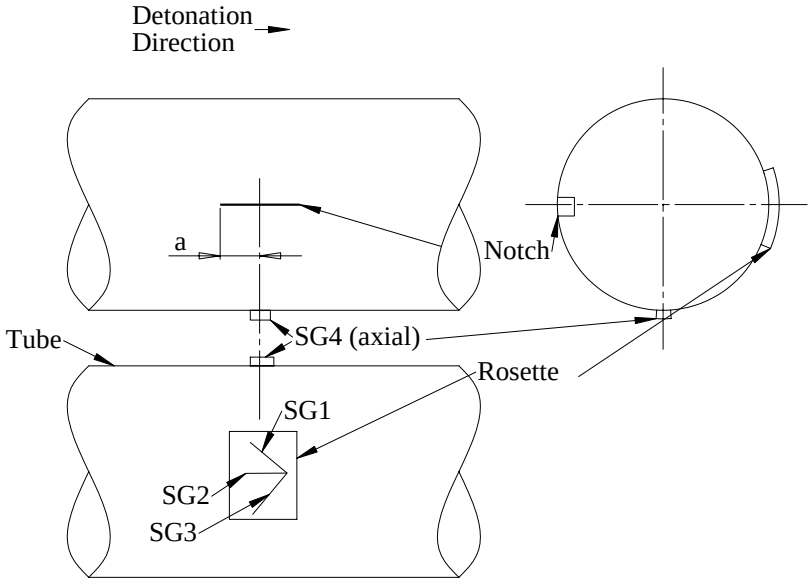

Figure A.148: Strain gage location for Shots 145 to 147, and 154.

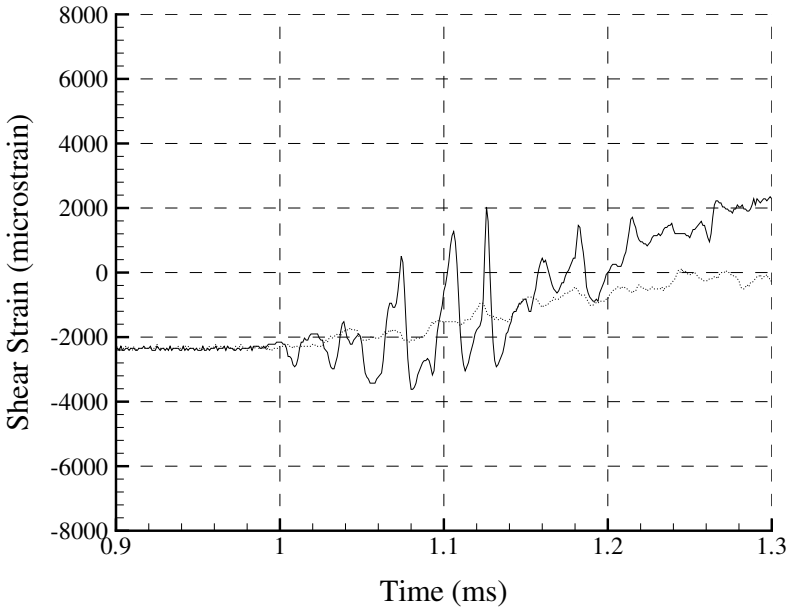

Figure A.149: Shot 137 shear strain.

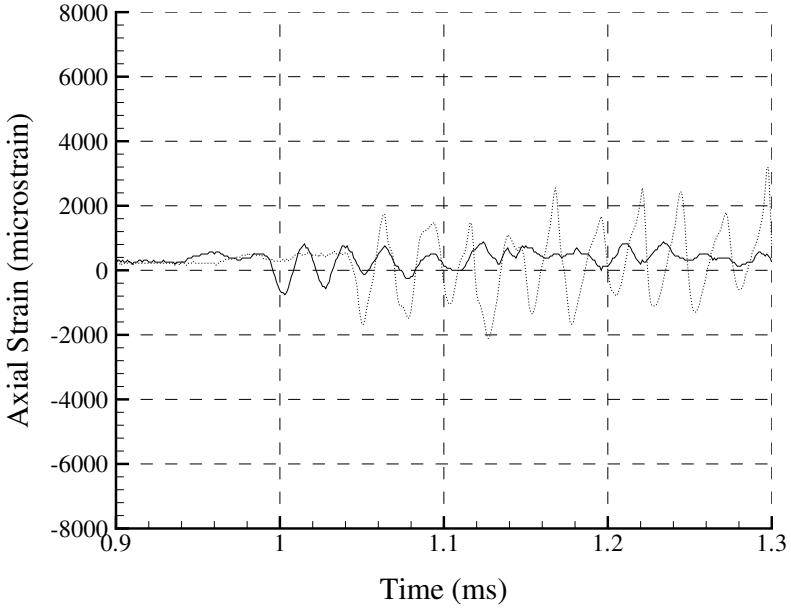

Figure A.150: Shot 137 axial strain.

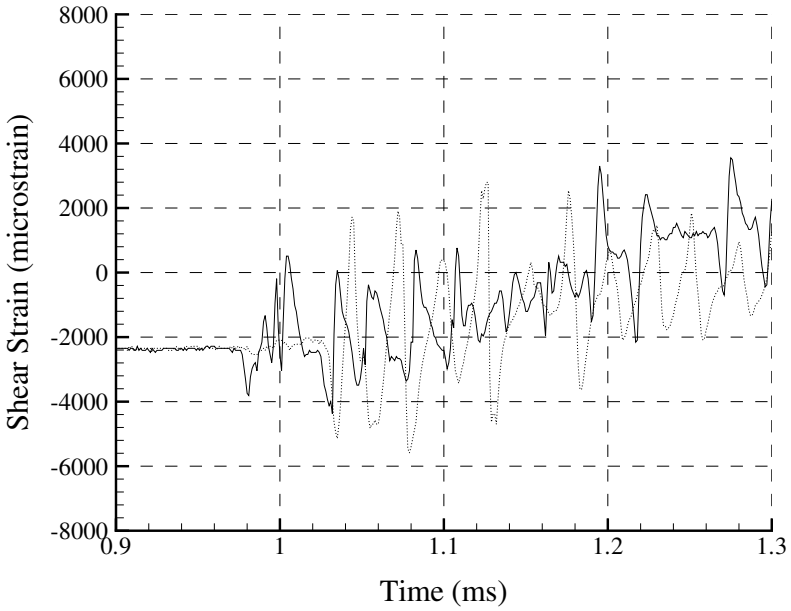

Figure A.151: Shot 140 shear strain.

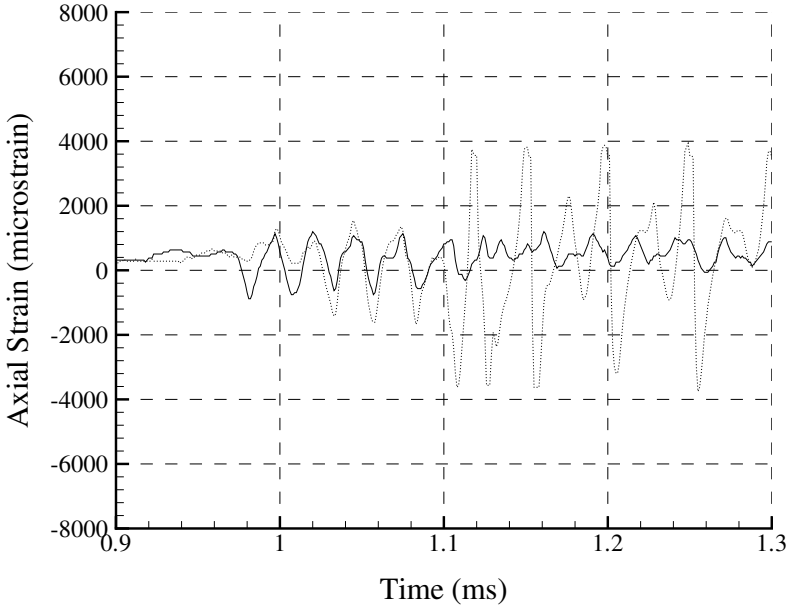

Figure A.152: Shot 140 axial strain.

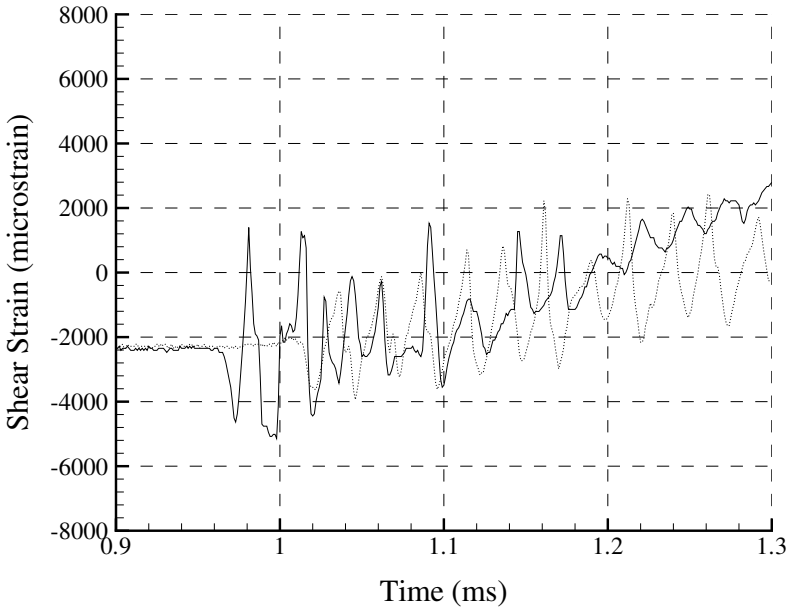

Figure A.153: Shot 141 shear strain.

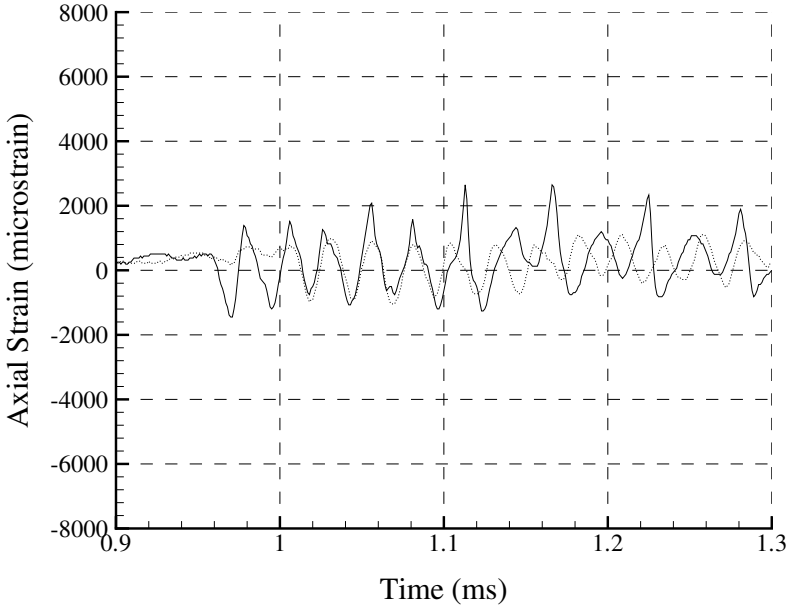

Figure A.154: Shot 141 axial strain.

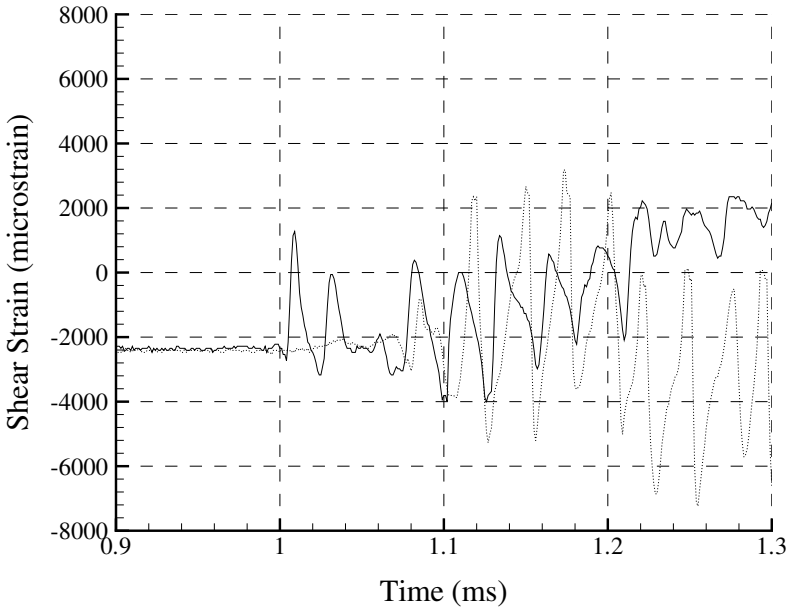

Figure A.155: Shot 142 shear strain.

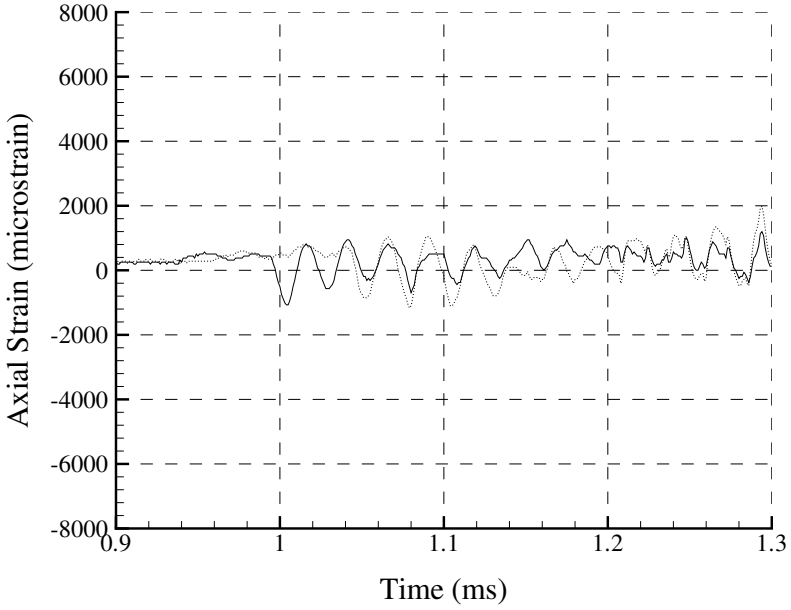

Figure A.156: Shot 142 axial strain.

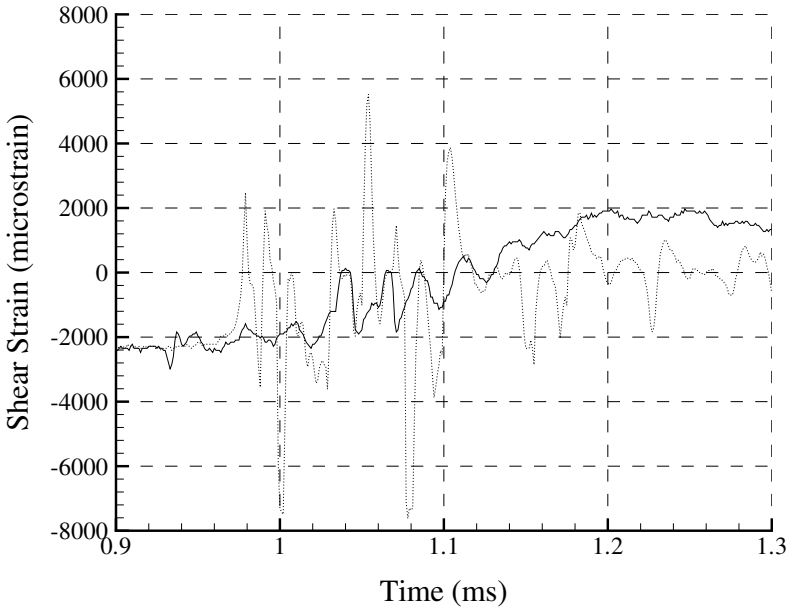

Figure A.157: Shot 143 shear strain.

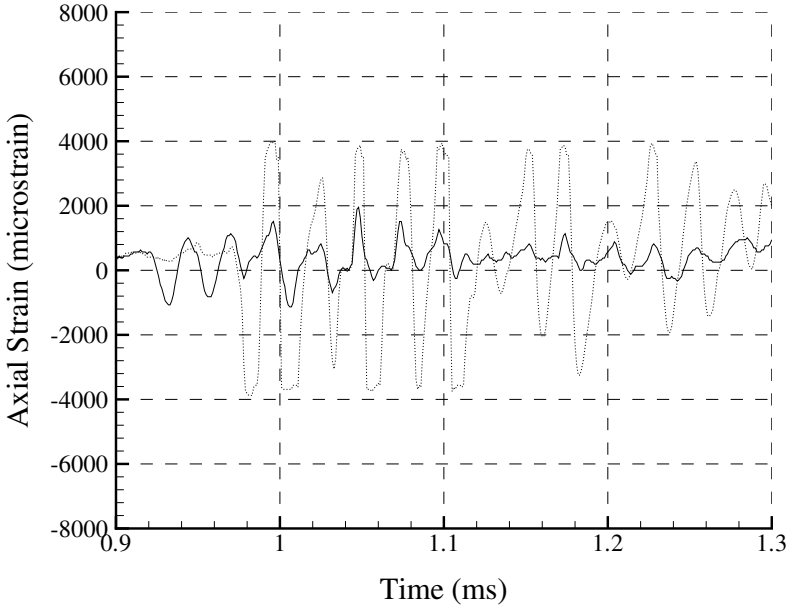

Figure A.158: Shot 143 axial strain.

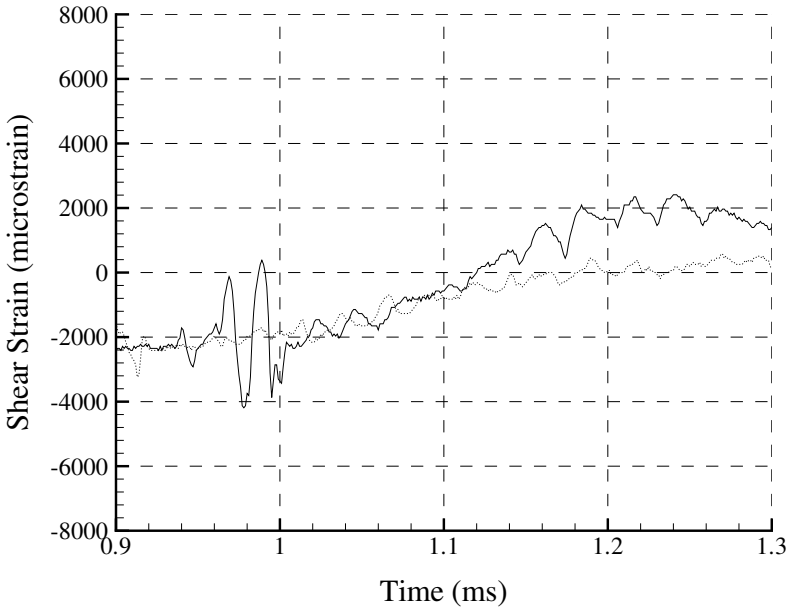

Figure A.159: Shot 144 shear strain.

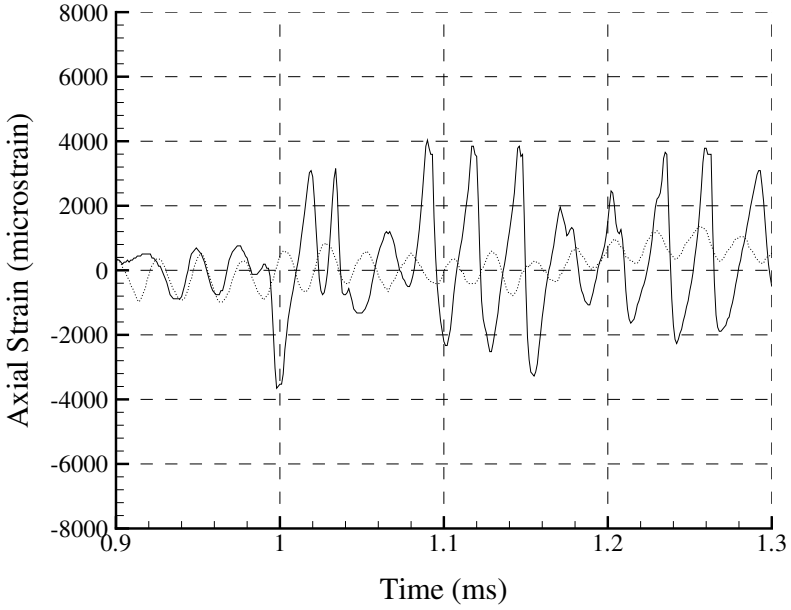

Figure A.160: Shot 144 axial strain.

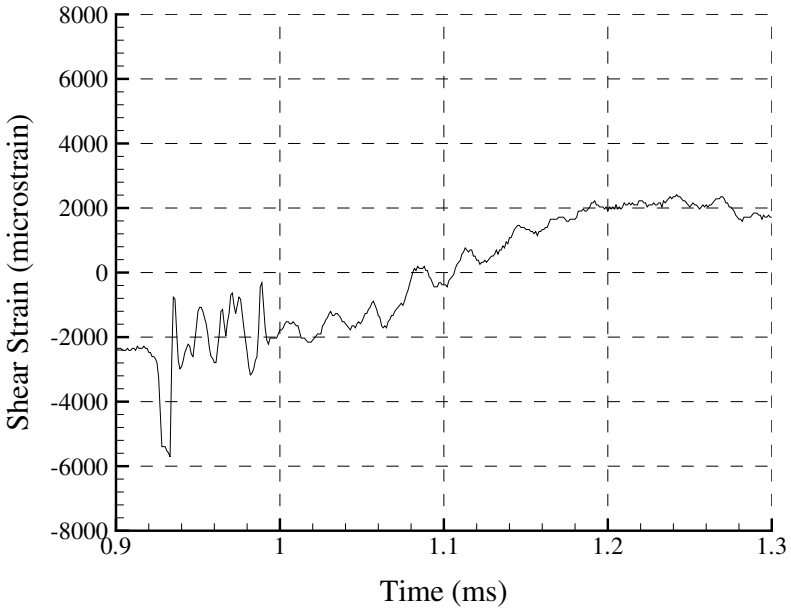

Figure A.161: Shot 145 shear strain.

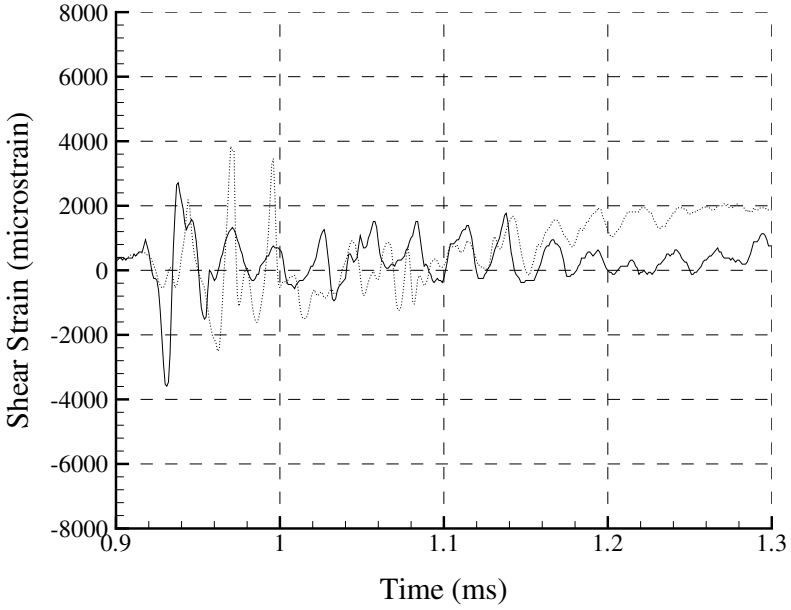

Figure A.162: Shot 145 axial strain.

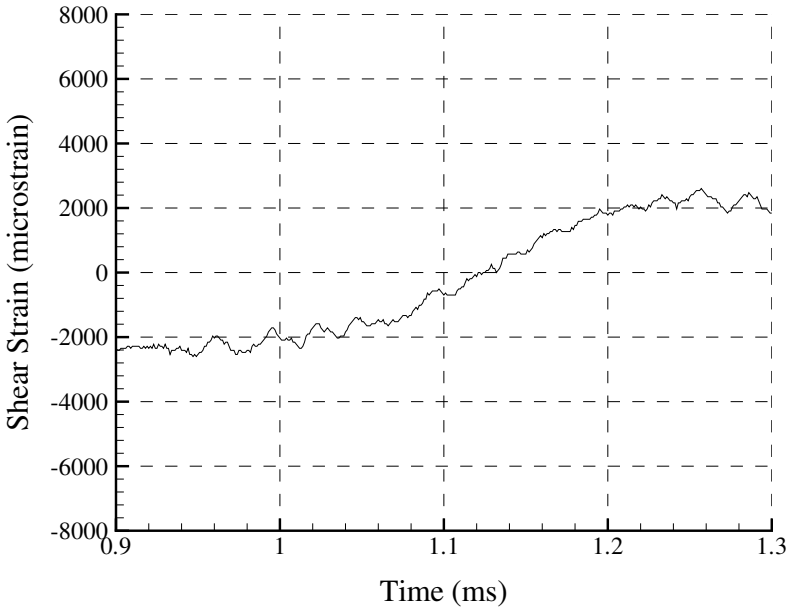

Figure A.163: Shot 146 shear strain.

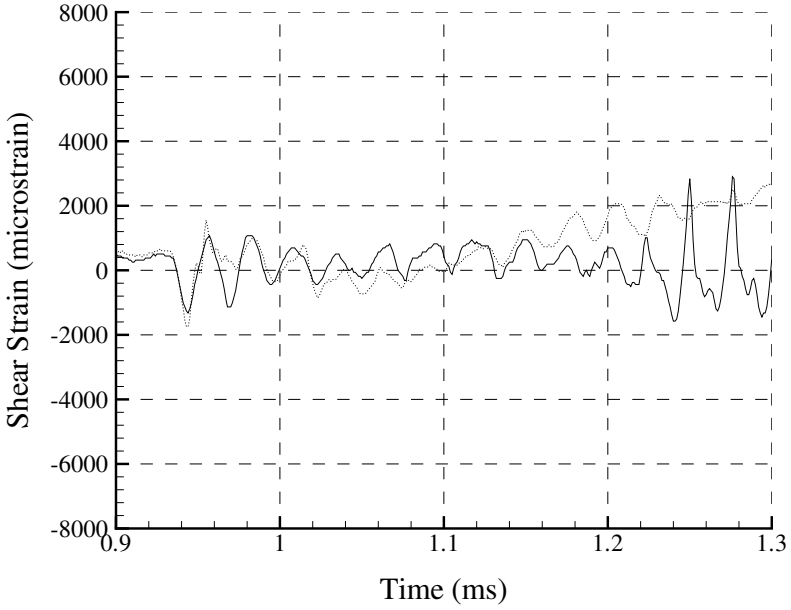

Figure A.164: Shot 146 axial strain.

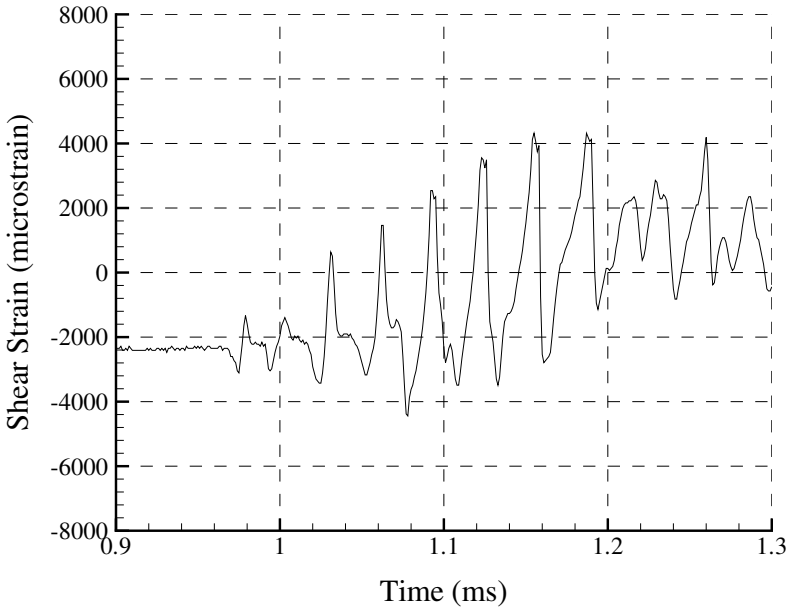

Figure A.165: Shot 147 shear strain.

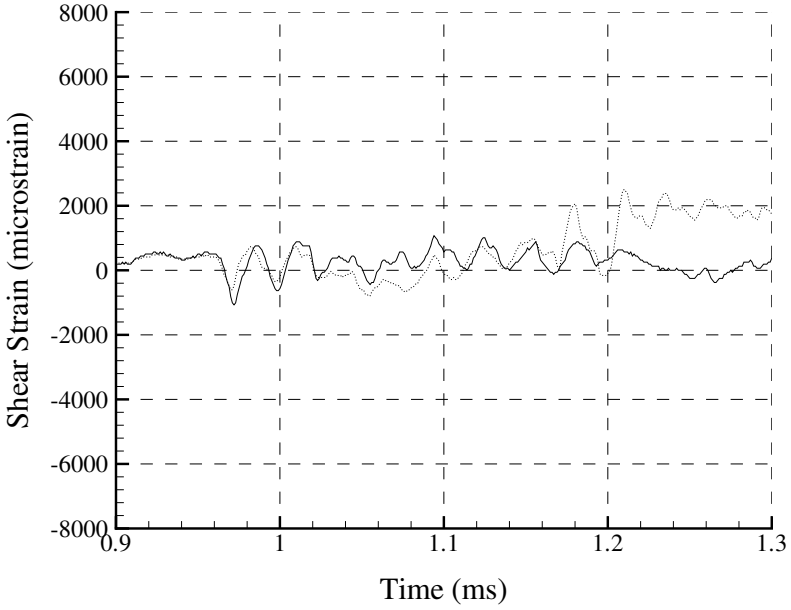

Figure A.166: Shot 147 axial strain.

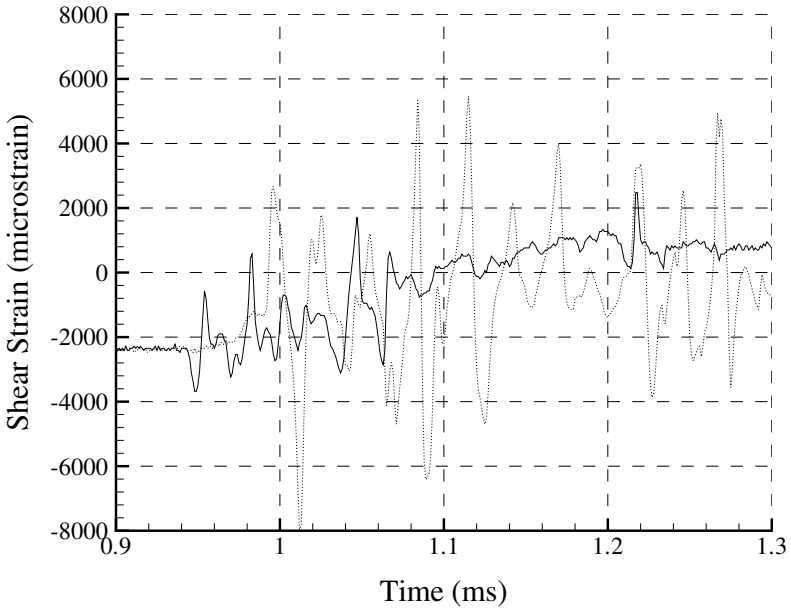

Figure A.167: Shot 148 shear strain.

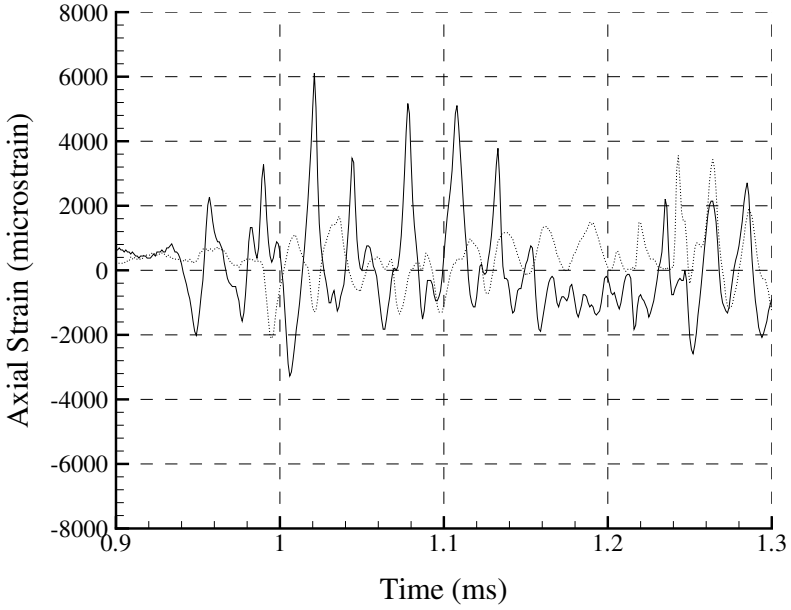

Figure A.168: Shot 148 axial strain.

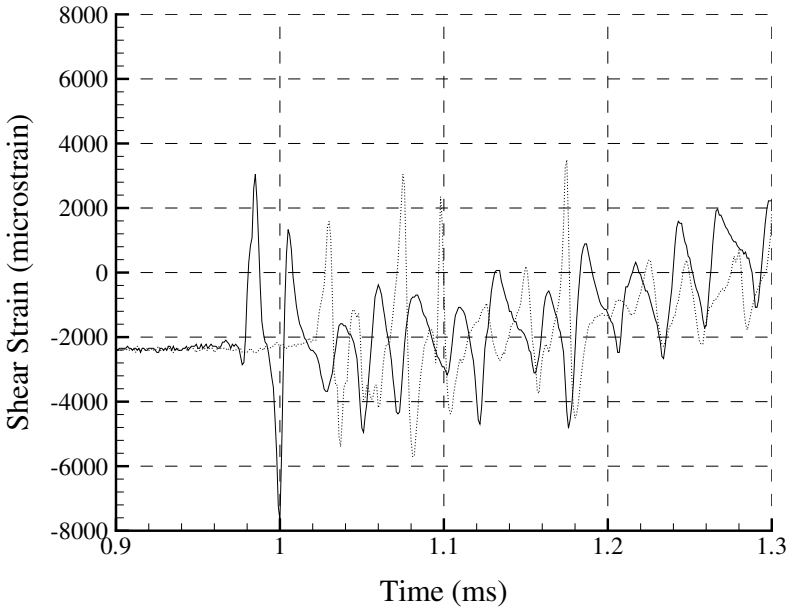

Figure A.169: Shot 149 shear strain.

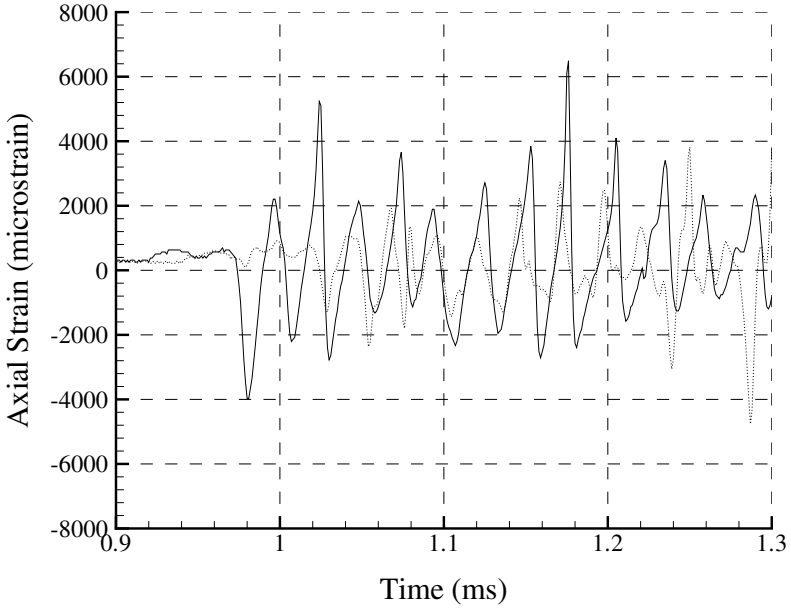

Figure A.170: Shot 149 axial strain.

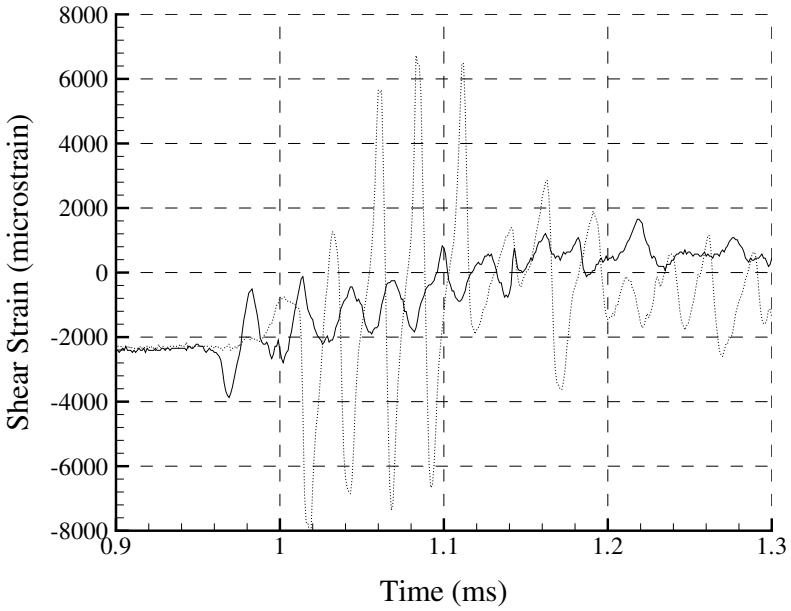

Figure A.171: Shot 150 shear strain.

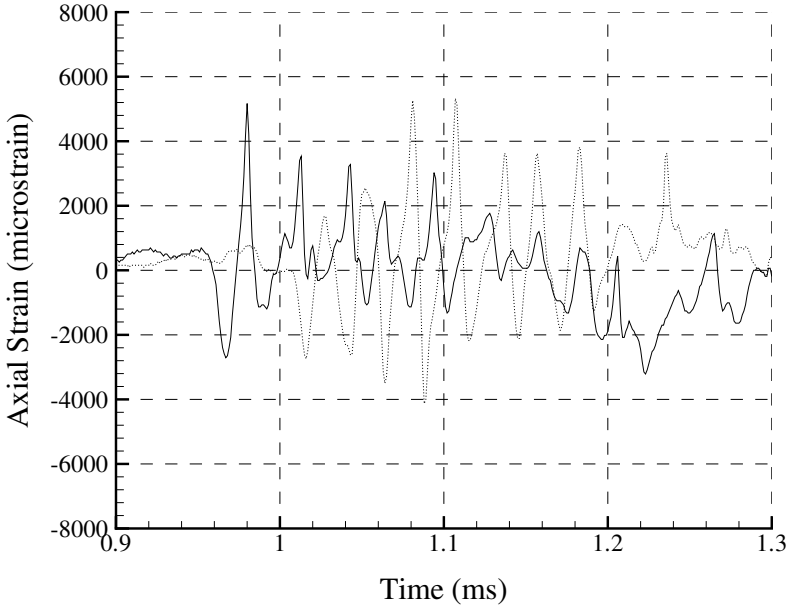

Figure A.172: Shot 150 axial strain.

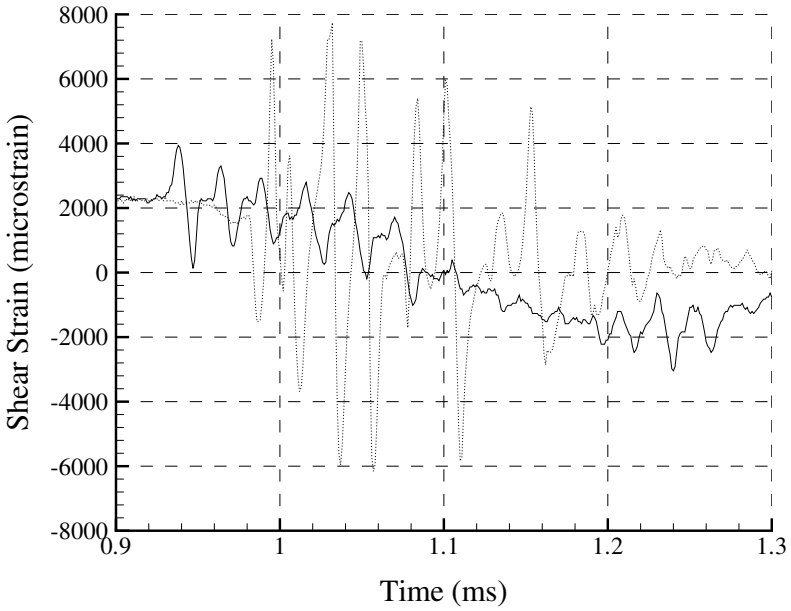

Figure A.173: Shot 151 shear strain.

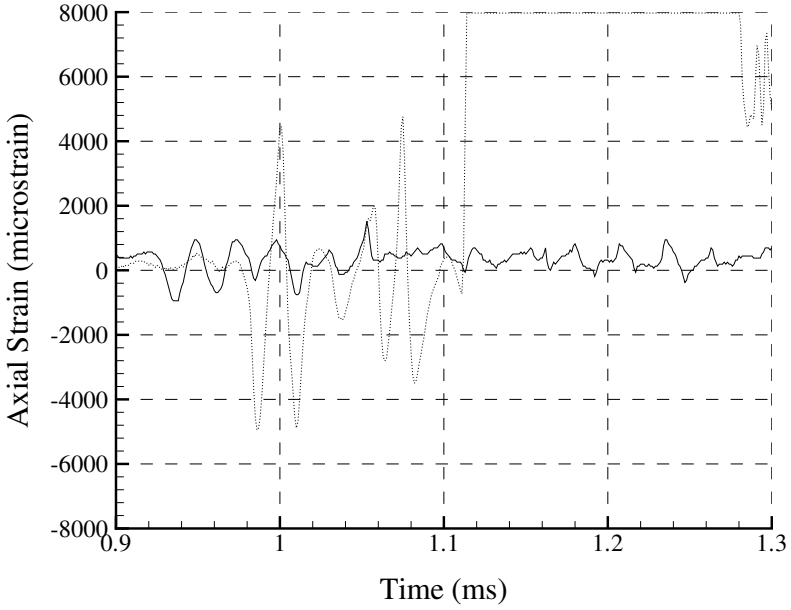

Figure A.174: Shot 151 axial strain.

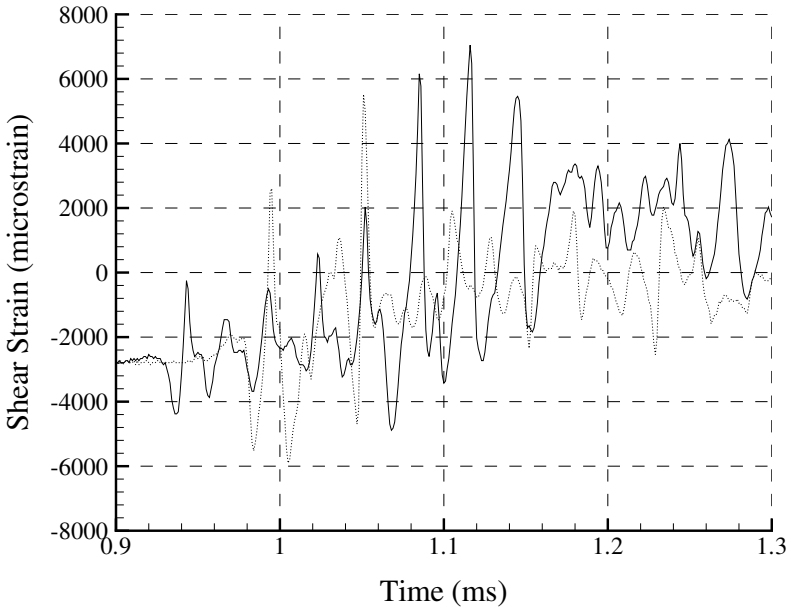

Figure A.175: Shot 152 shear strain.

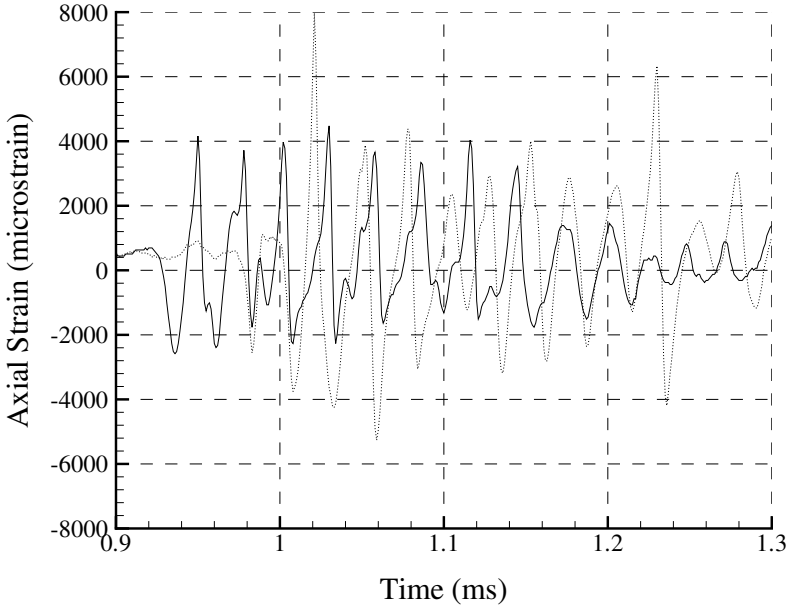

Figure A.176: Shot 152 axial strain.

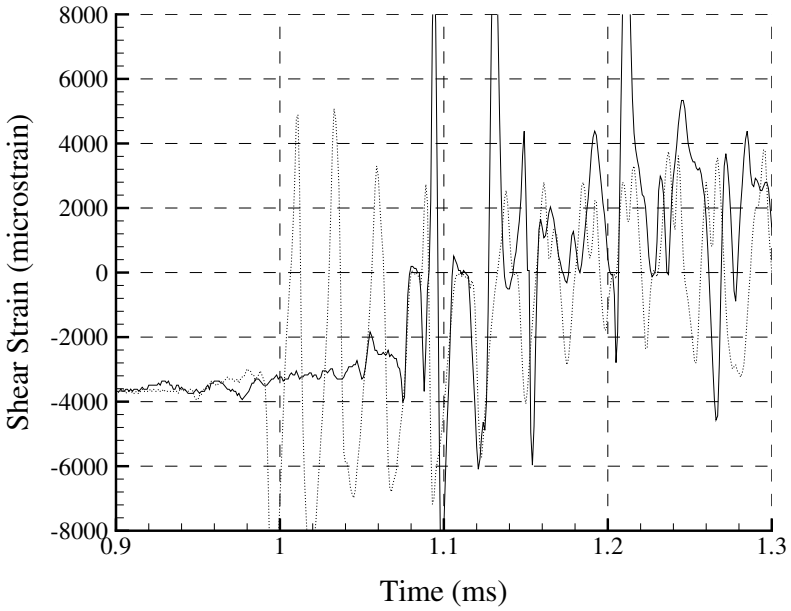

Figure A.177: Shot 153 shear strain.

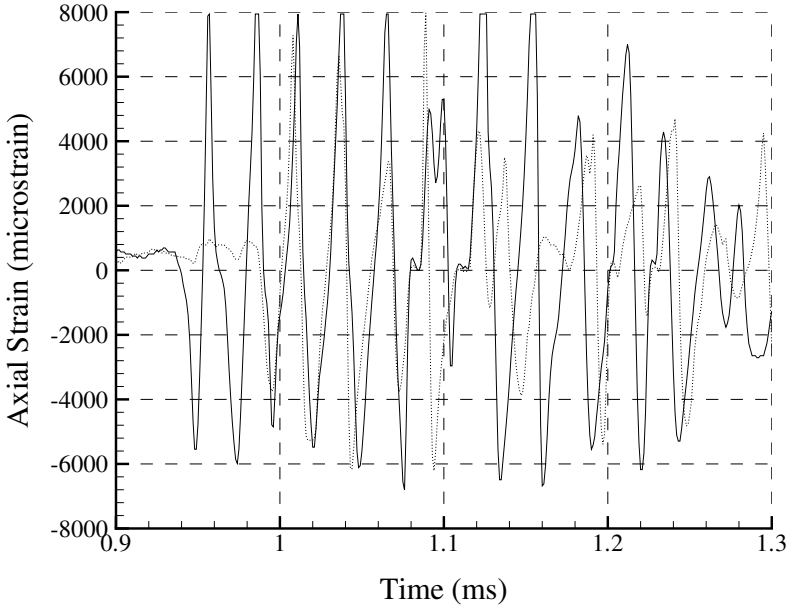

Figure A.178: Shot 153 axial strain.

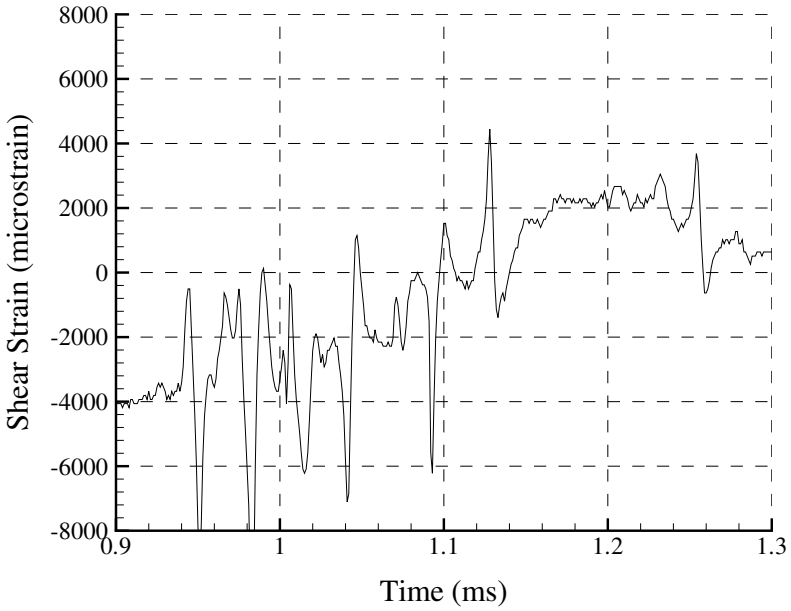

Figure A.179: Shot 154 shear strain.

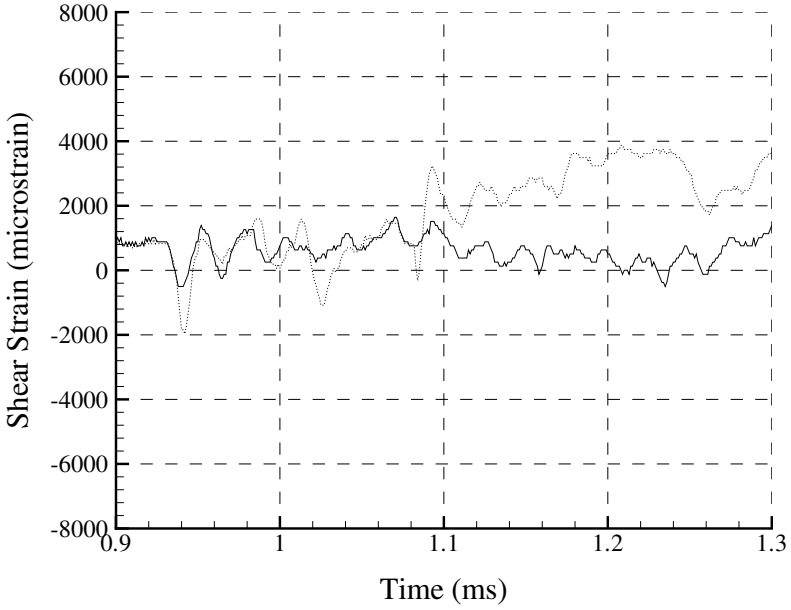

Figure A.180: Shot 154 axial strain.

A.6 Post-test Specimens

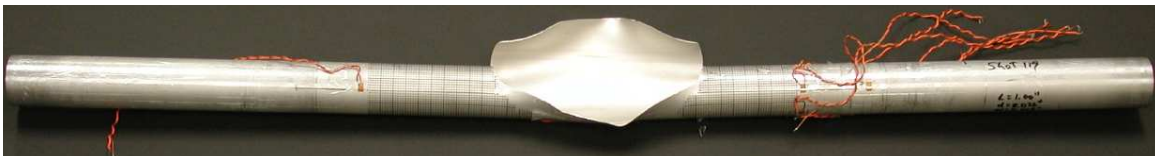

Figure A.181: Shot 119.

Figure A.182: Shot 120.

Figure A.183: Shot 121.

Figure A.184: Shot 123.

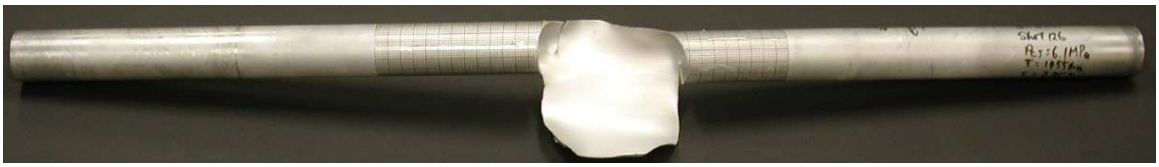

Figure A.185: Shot 126.

Figure A.186: Shot 127.

Figure A.187: Shot 128.

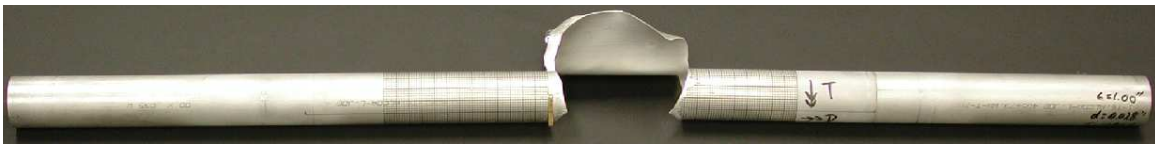

Figure A.188: Shot 129.

Figure A.189: Shot 130.

Figure A.190: Shot 131.

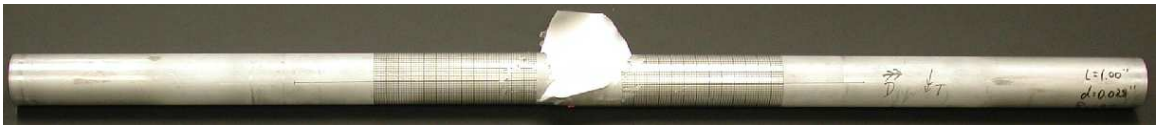

Figure A.191: Shot 132.

Figure A.192: Shot 133.

Figure A.193: Shot 134.

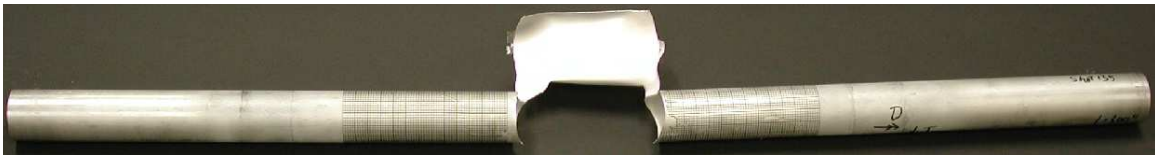

Figure A.194: Shot 135.

Figure A.195: Shot 136.

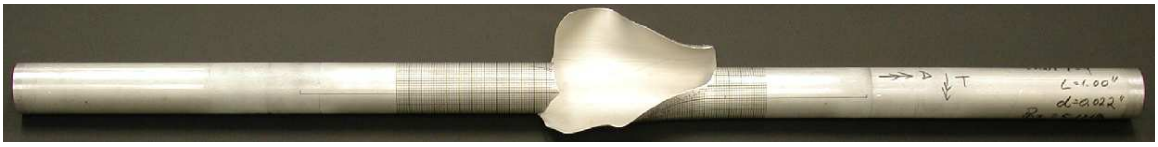

Figure A.196: Shot 137.

Figure A.197: Shot 139.

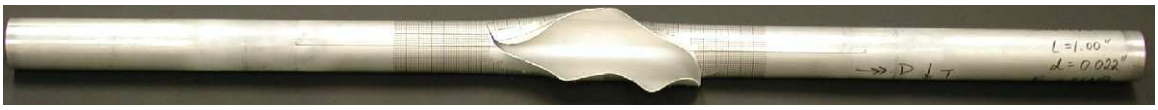

Figure A.198: Shot 140.

Figure A.199: Shot 141.

Figure A.200: Shot 142.

Figure A.201: Shot 143.

Figure A.202: Shot 144.

Figure A.203: Shot 145.

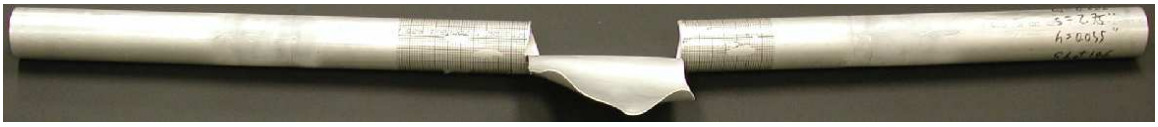

Figure A.204: Shot 146.

Figure A.205: Shot 147.

Figure A.206: Shot 148.

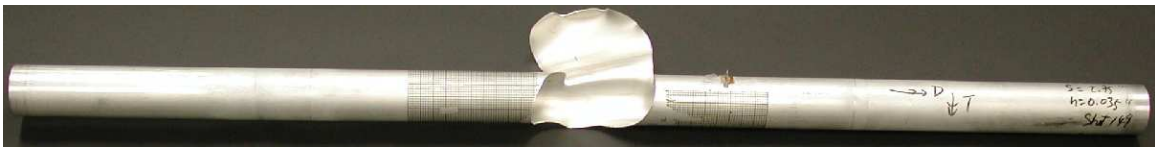

Figure A.207: Shot 149.

Figure A.208: Shot 150.

Figure A.209: Shot 151.

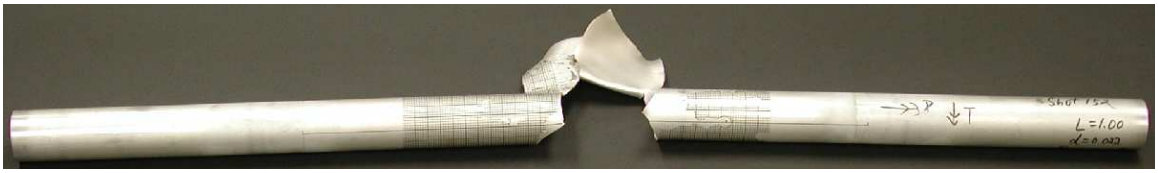

Figure A.210: Shot 152.

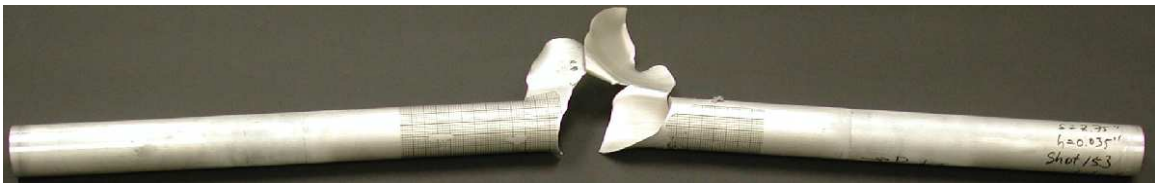

Figure A.211: Shot 153.

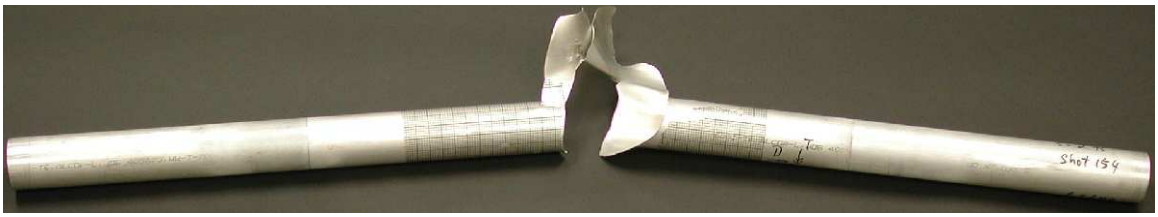

Figure A.212: Shot 154.

Appendix B

Engineering Drawings Of Torsion Experiment Setup

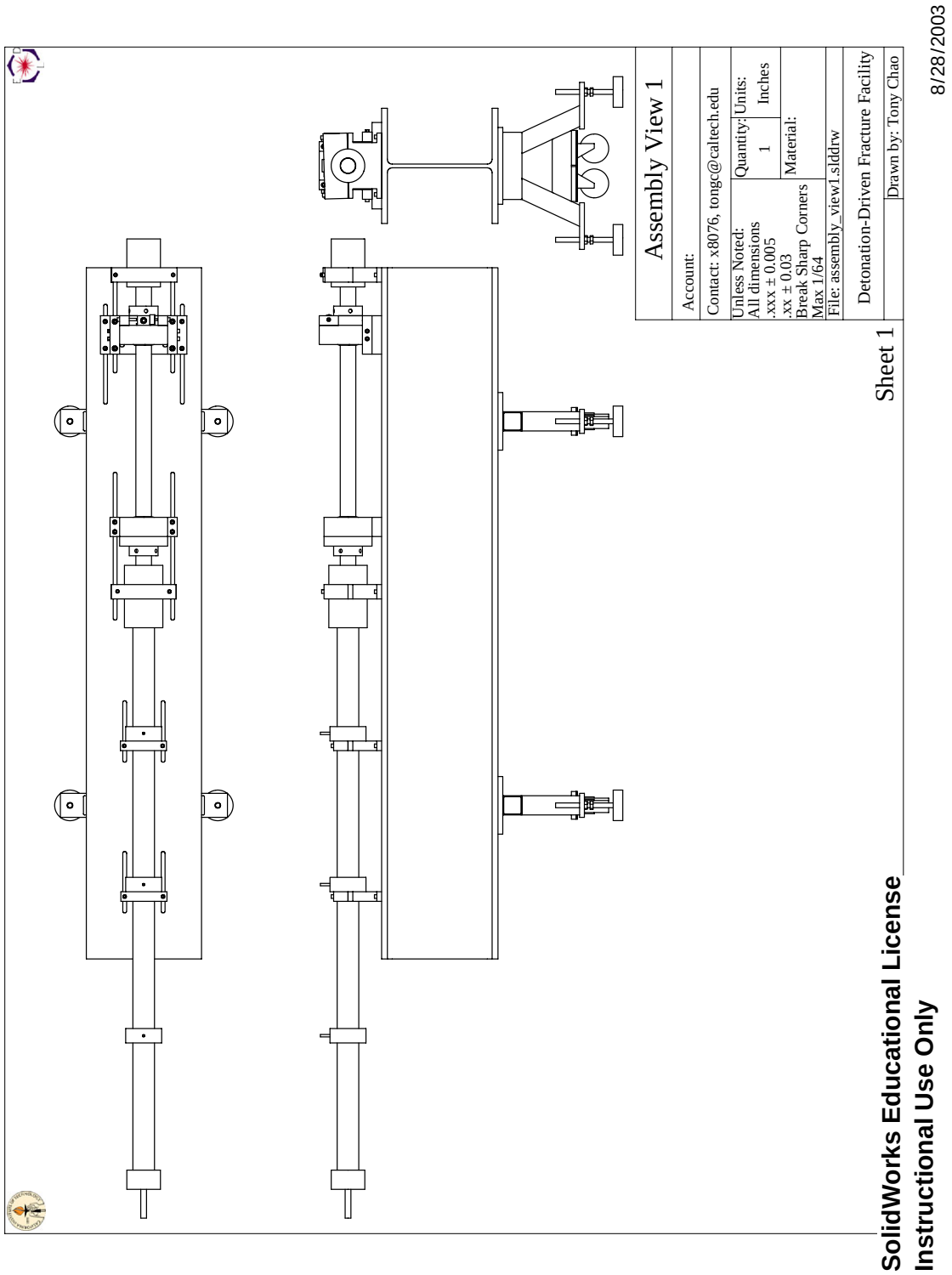

Figure B.1: Assembly view 1.

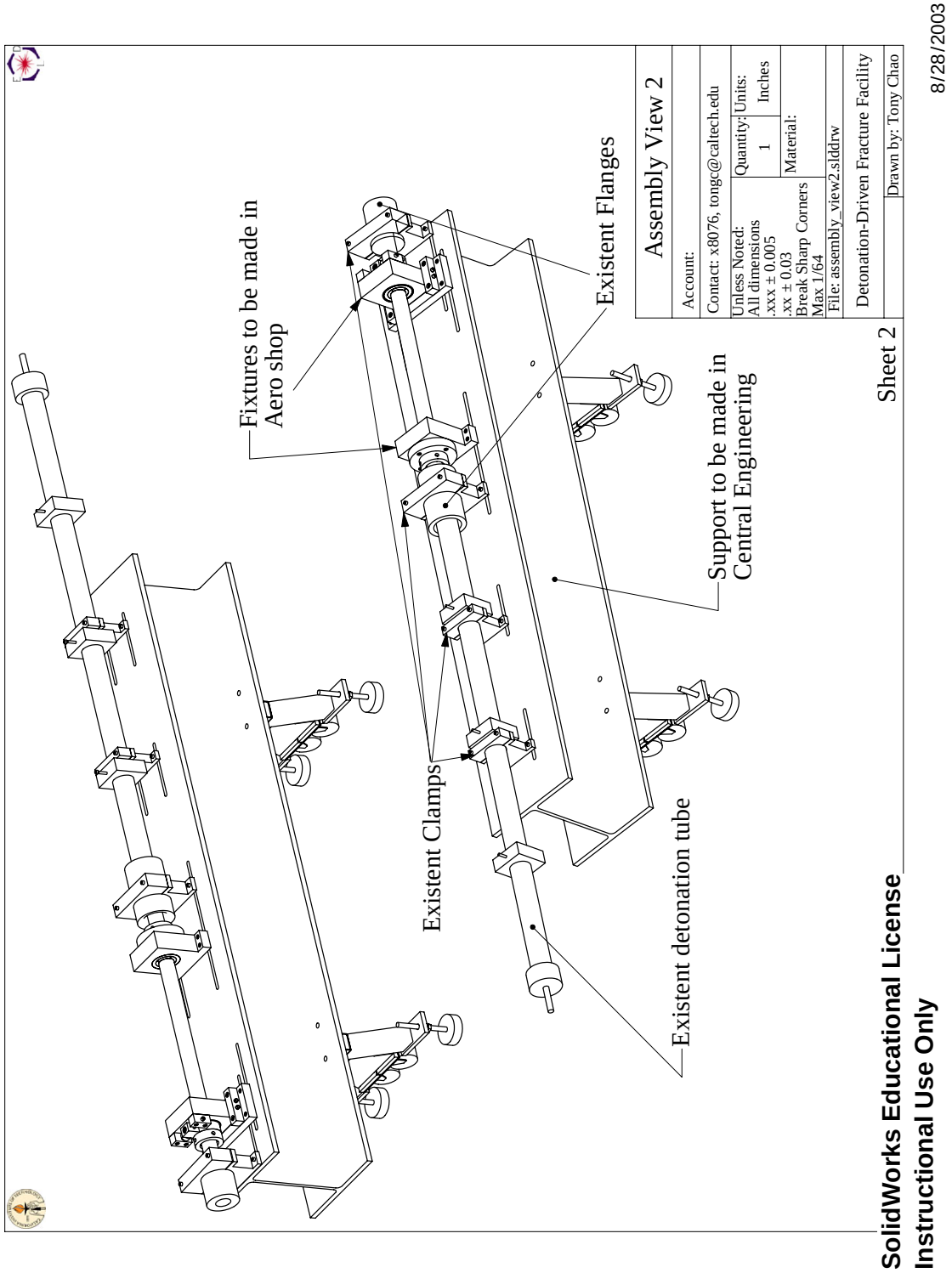

Figure B.2: Assembly view 2.

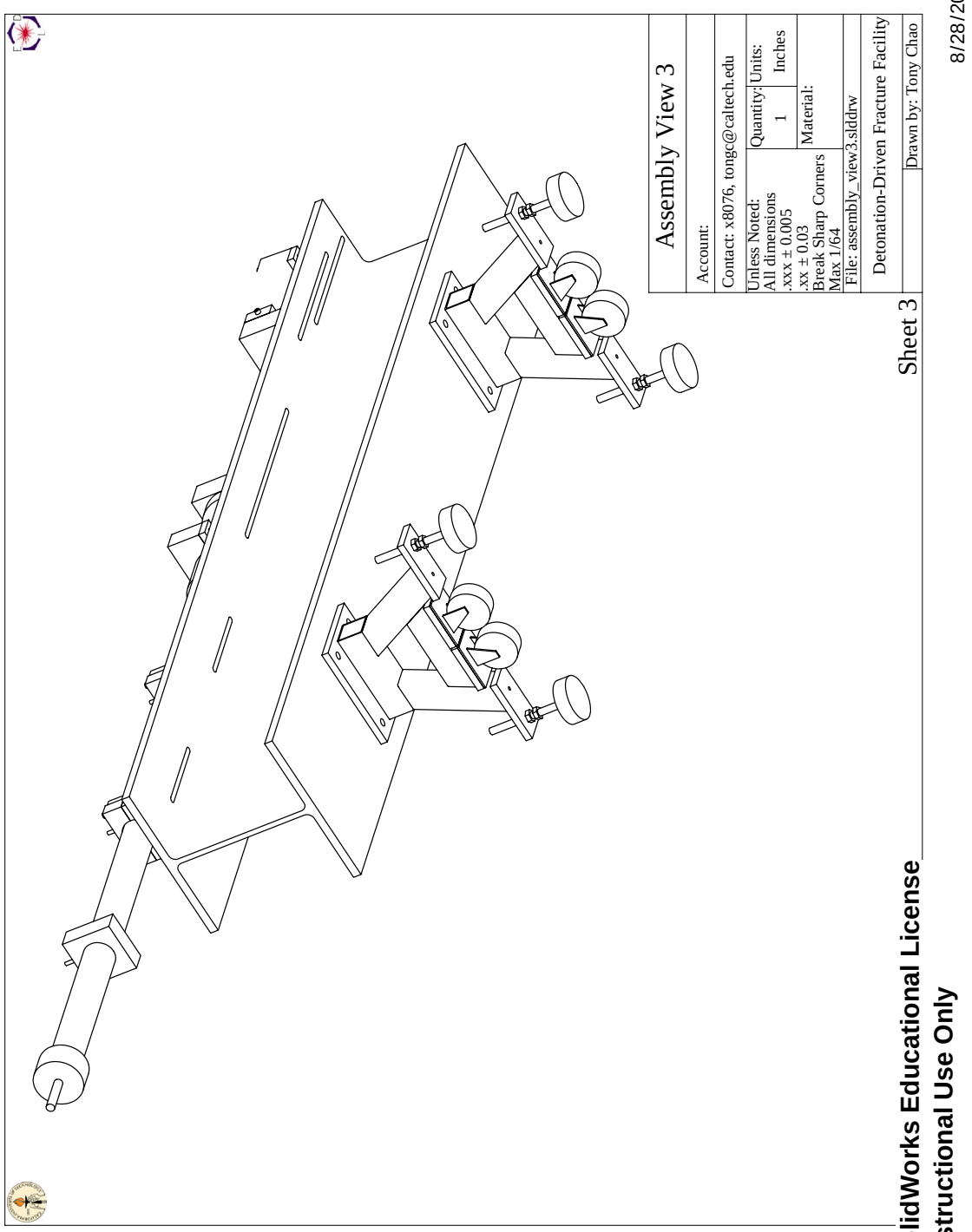

Figure B.3: Assembly view 3.

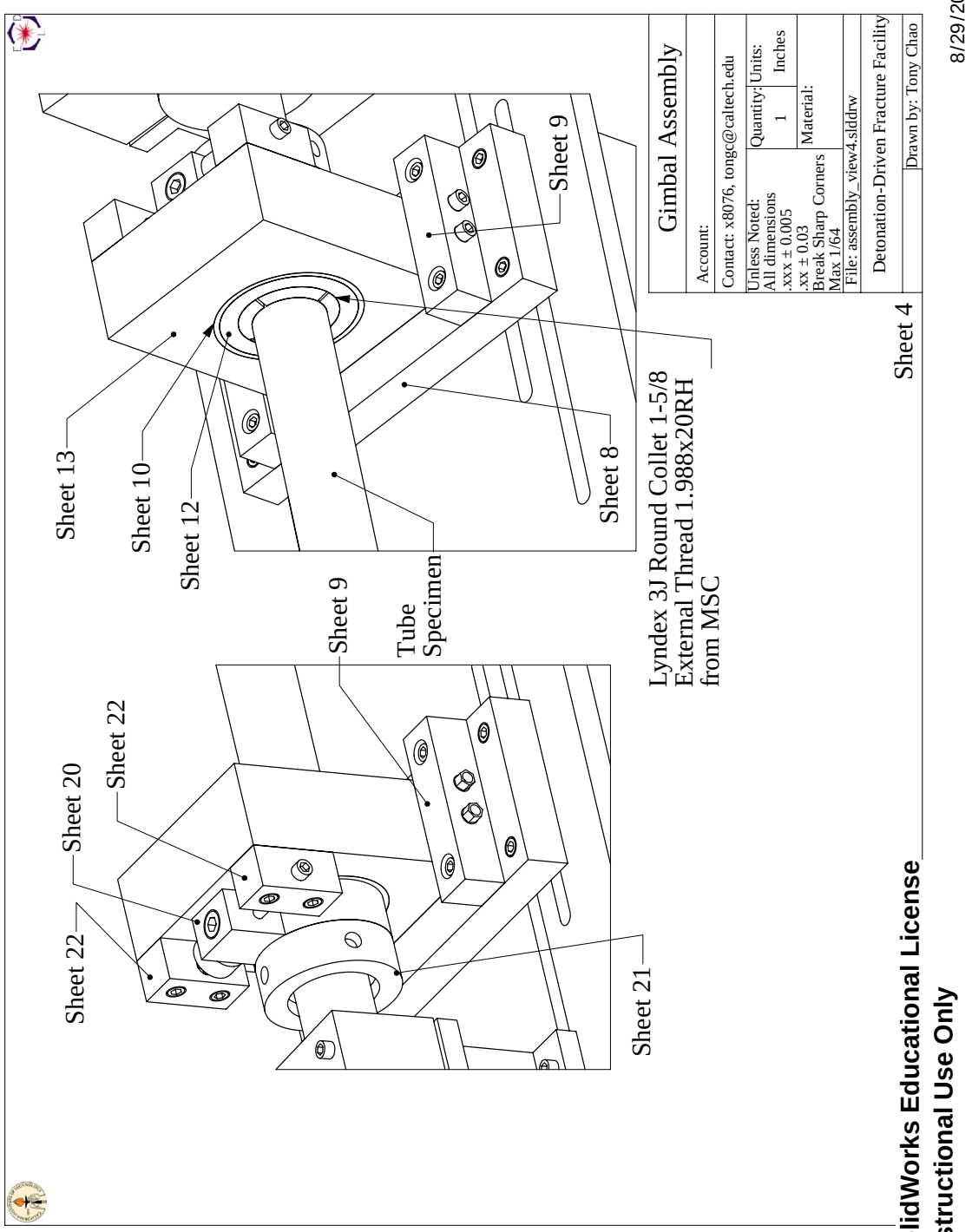

Figure B.4: Torsion-end assembly.

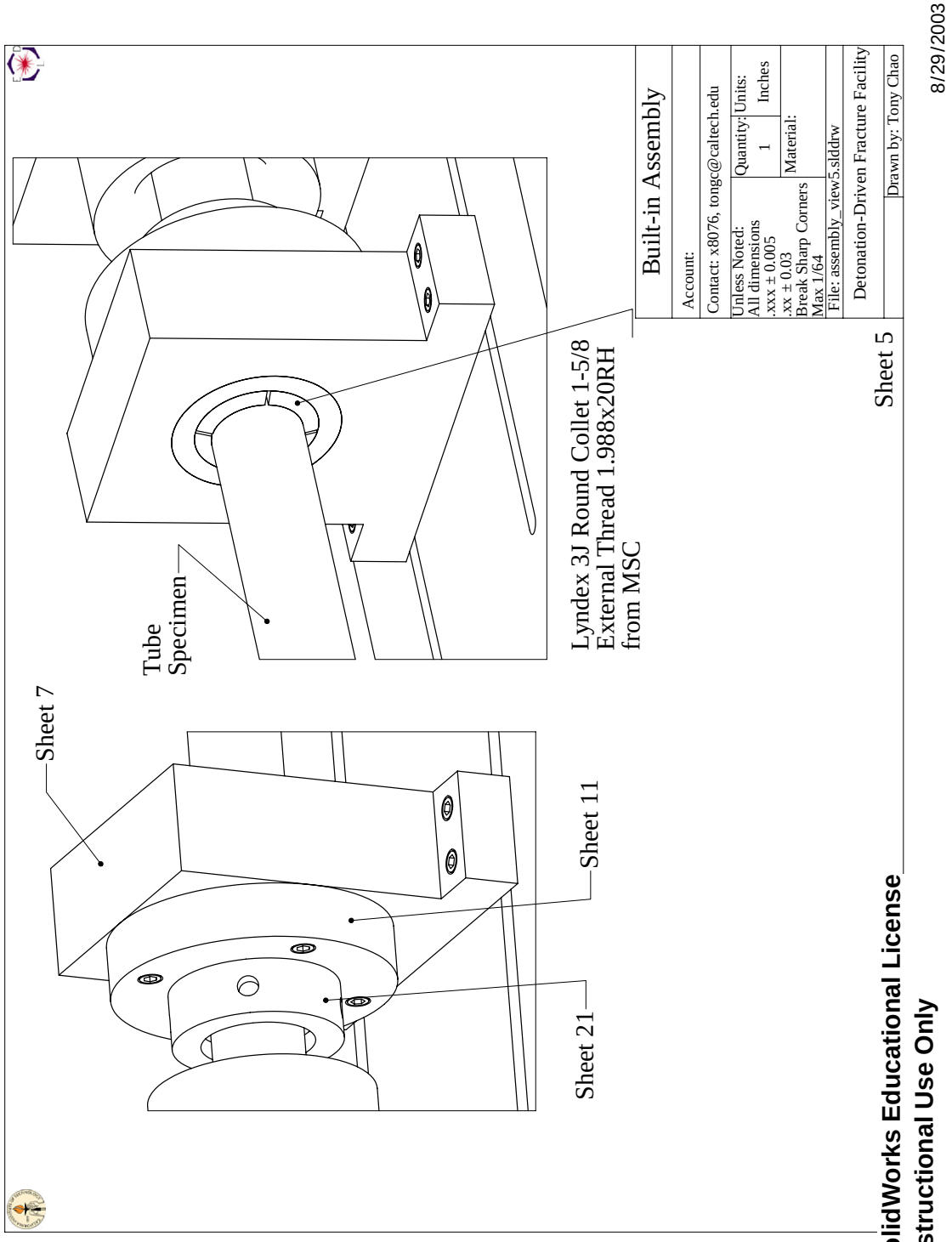

Figure B.5: Fixed-end assembly.

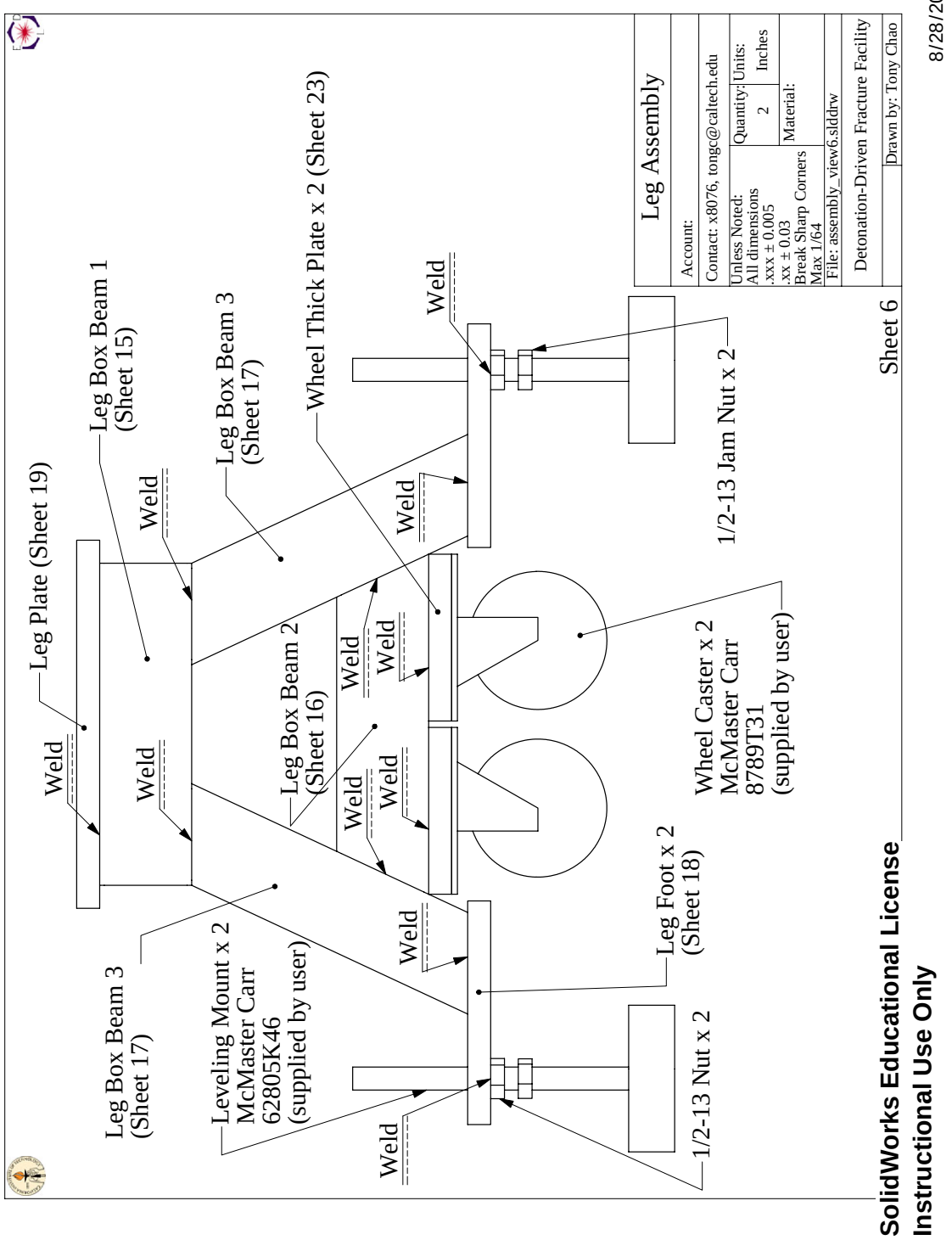

Figure B.6: I-beam leg assembly.

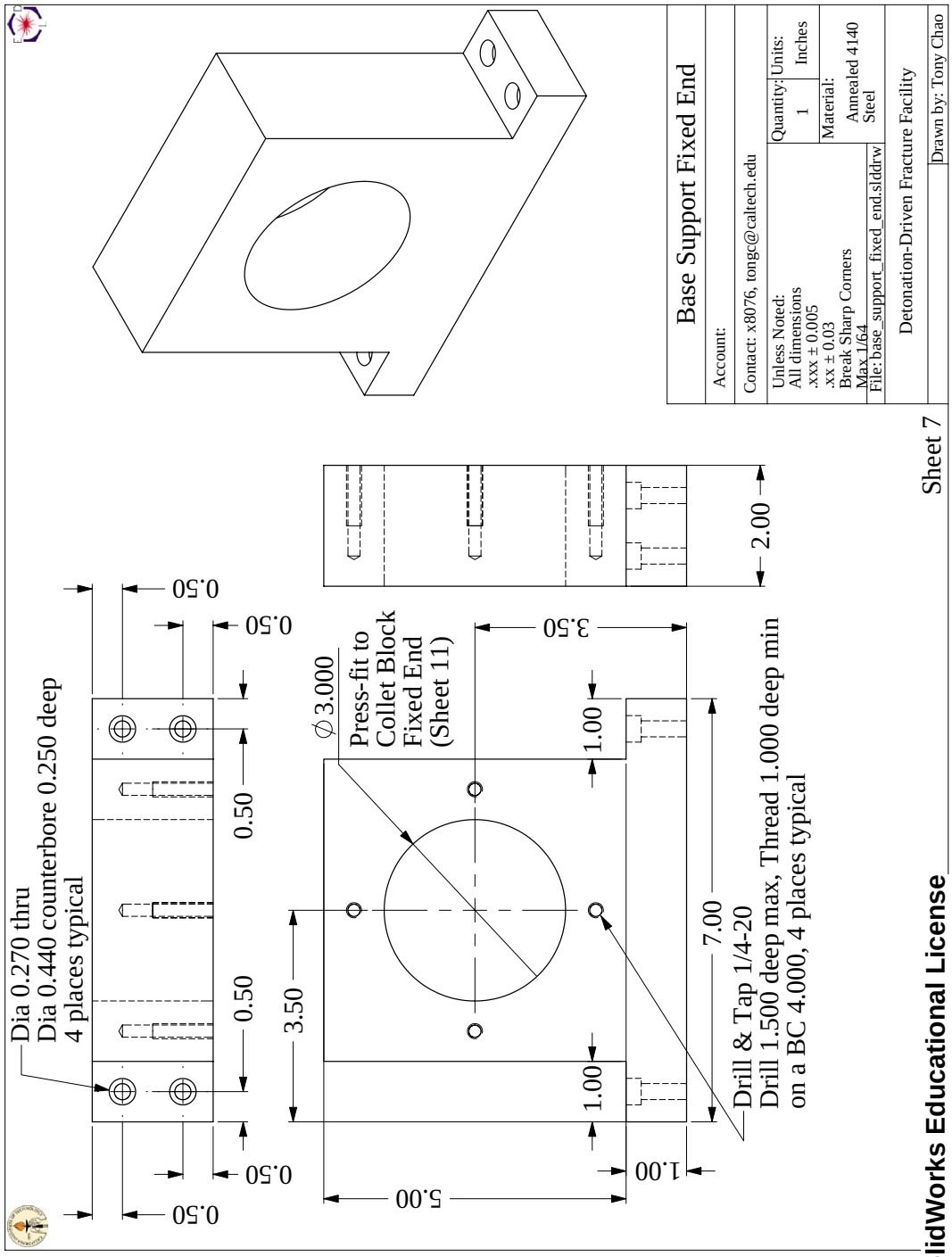

Figure B.7: Fixed-end base.

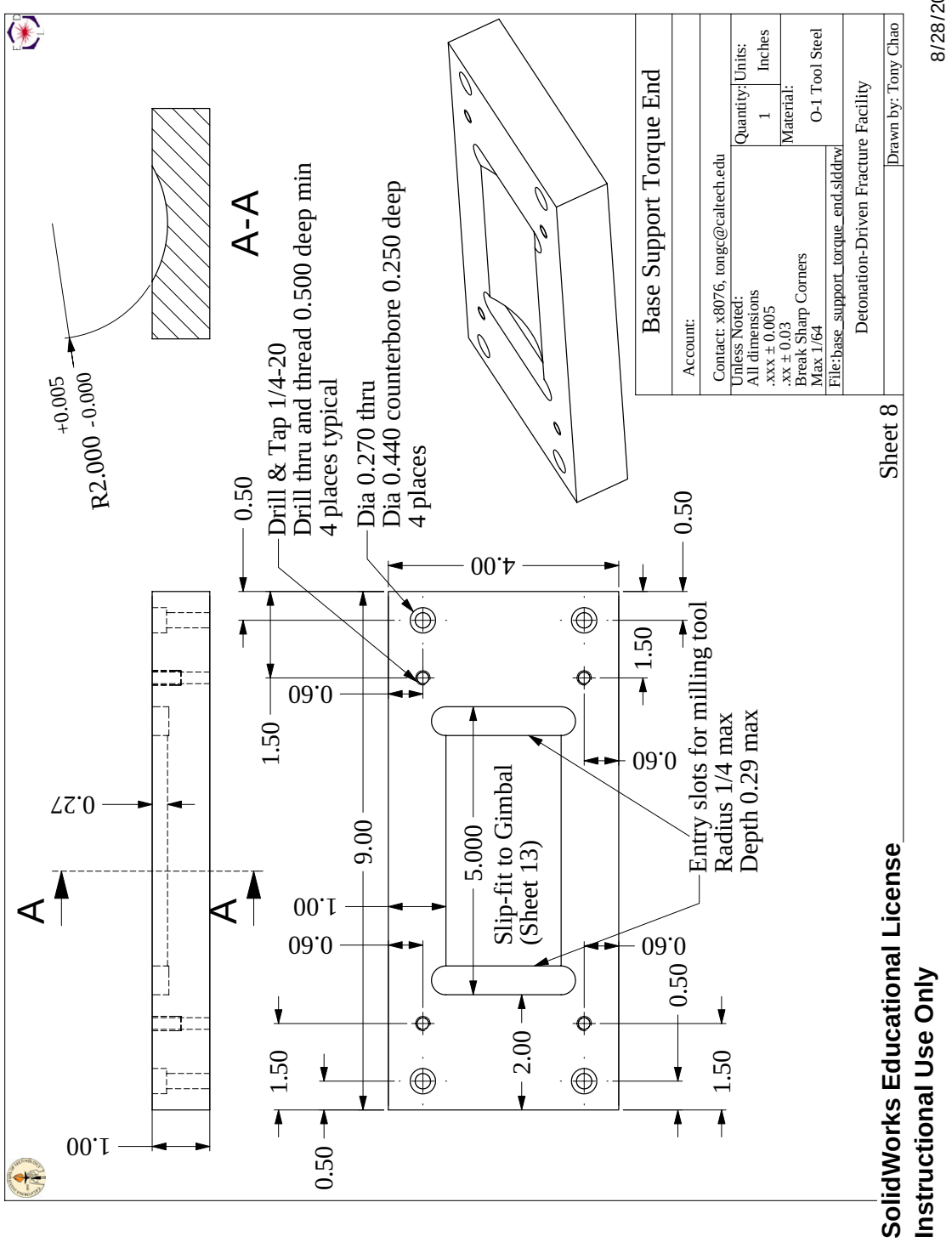

Figure B.8: Torsion-end base.

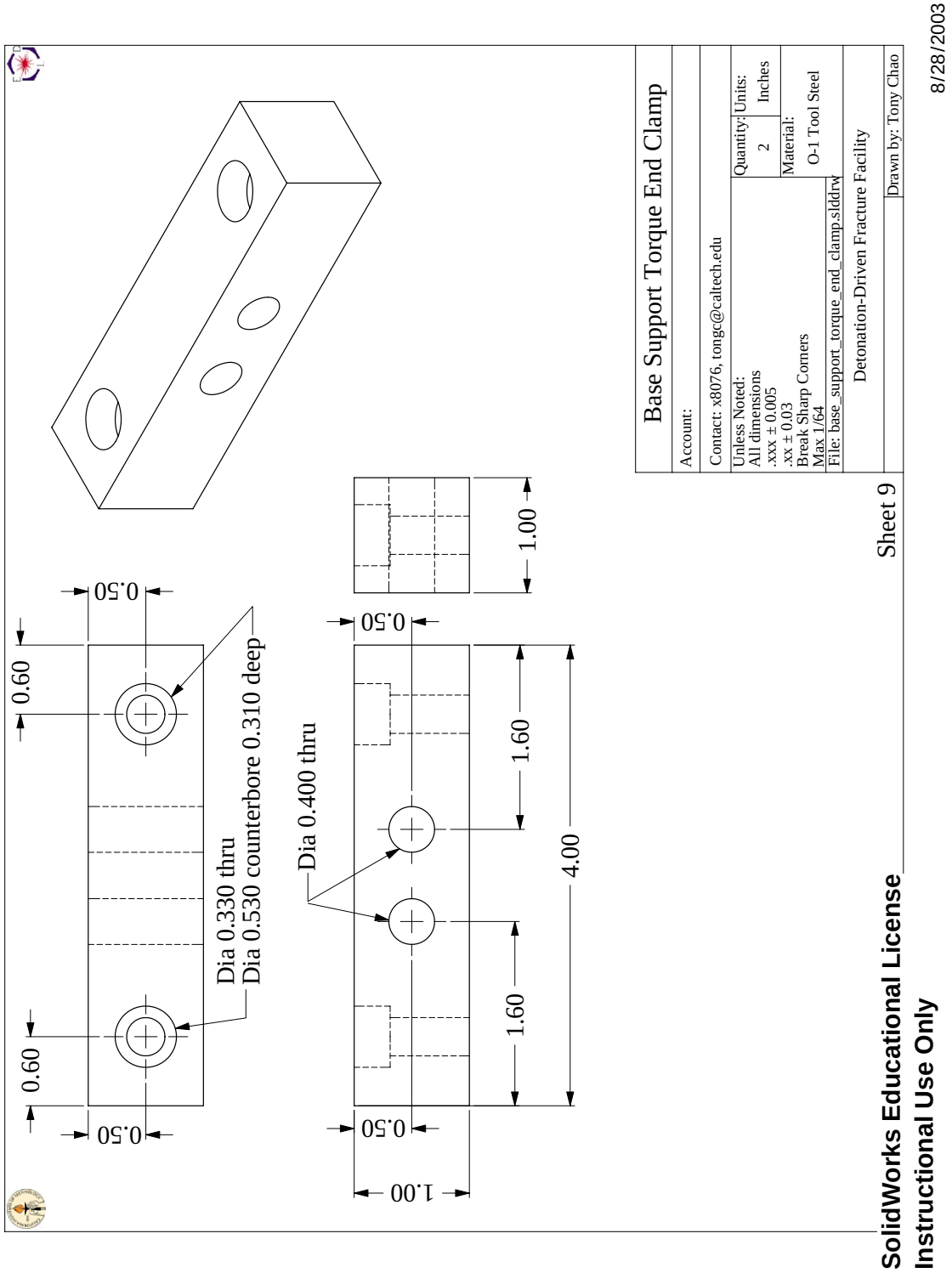

Figure B.9: Clamp for the torque-end of base.

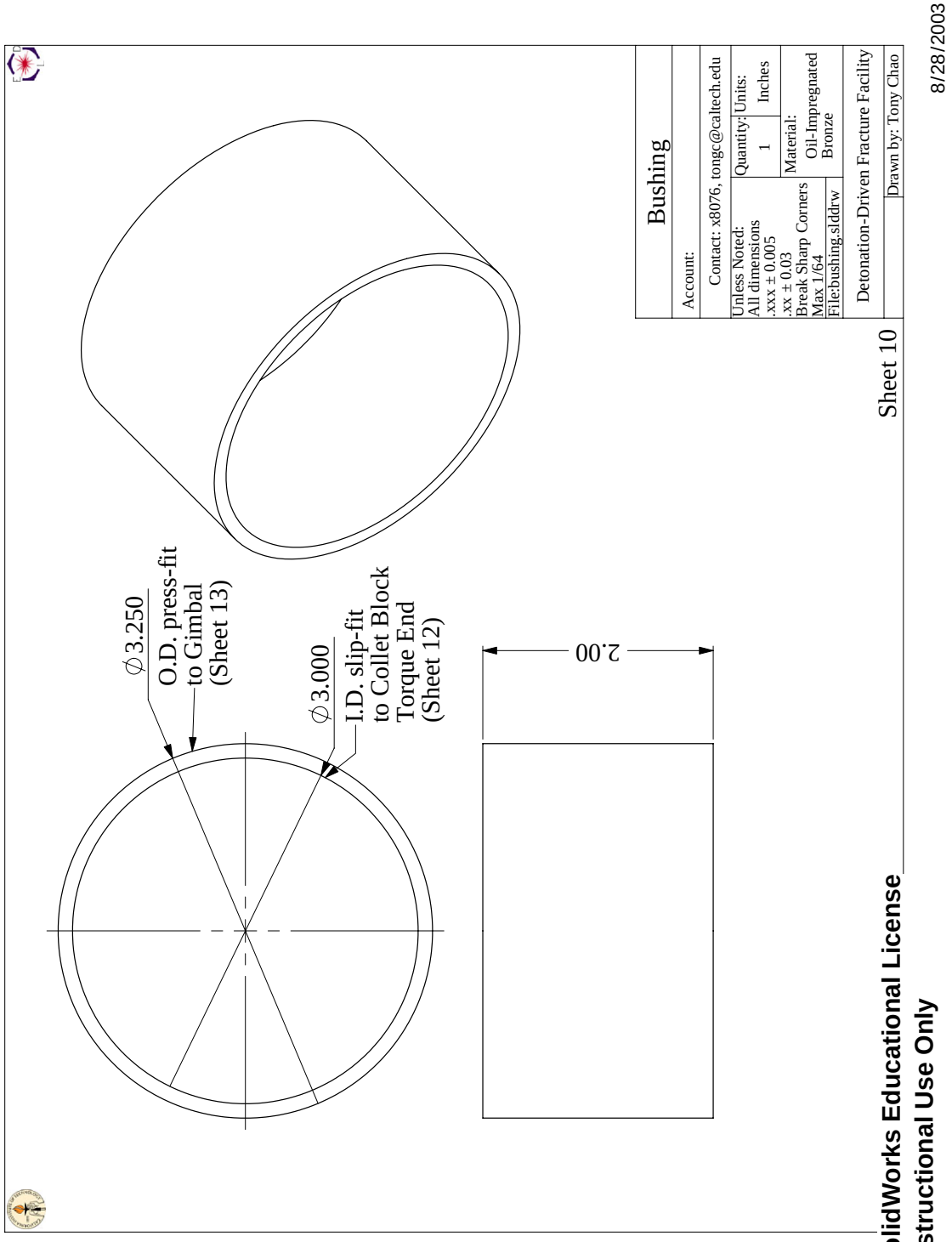

Figure B.10: Bushing for collet.

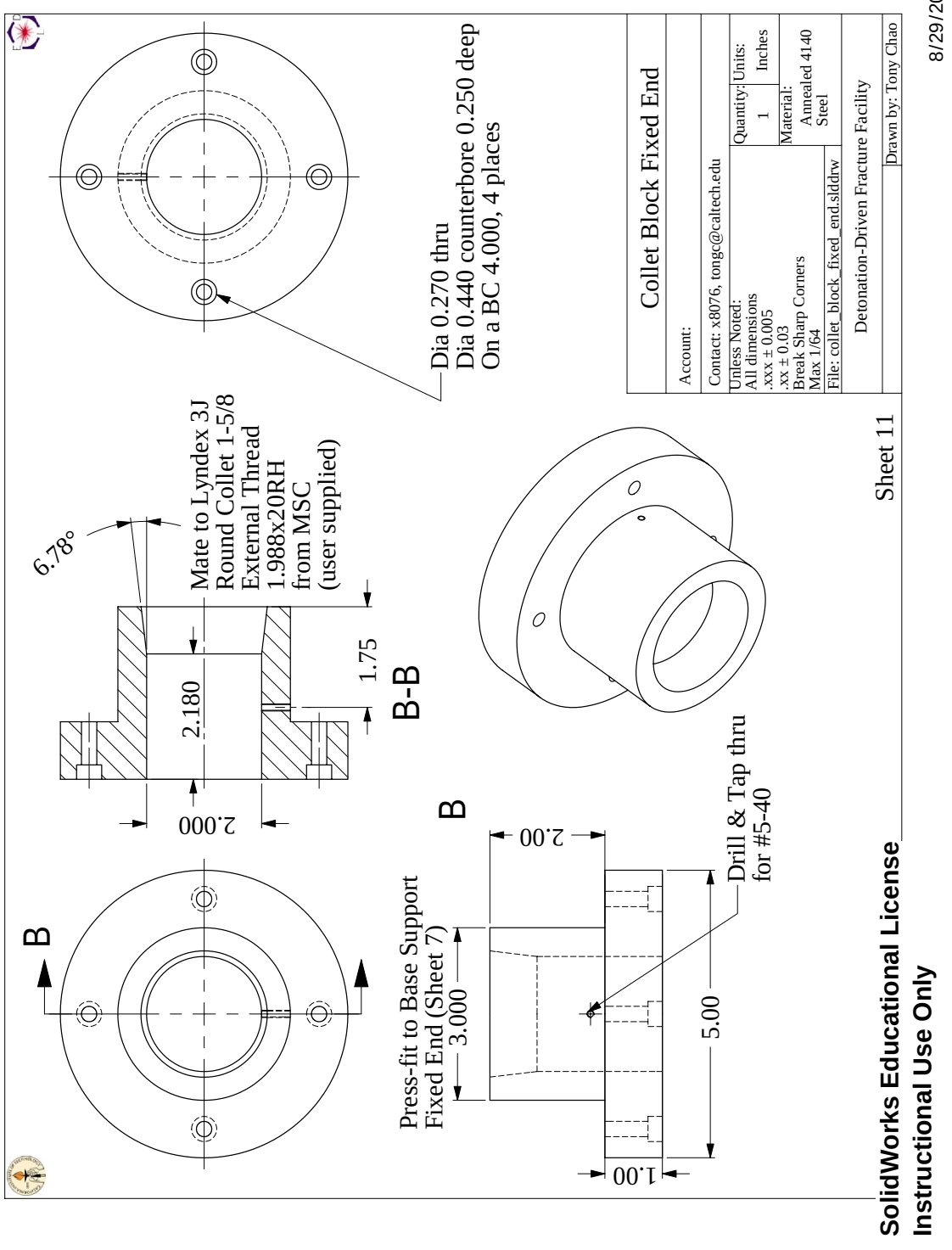

Figure B.11: Fixed-end collet block.

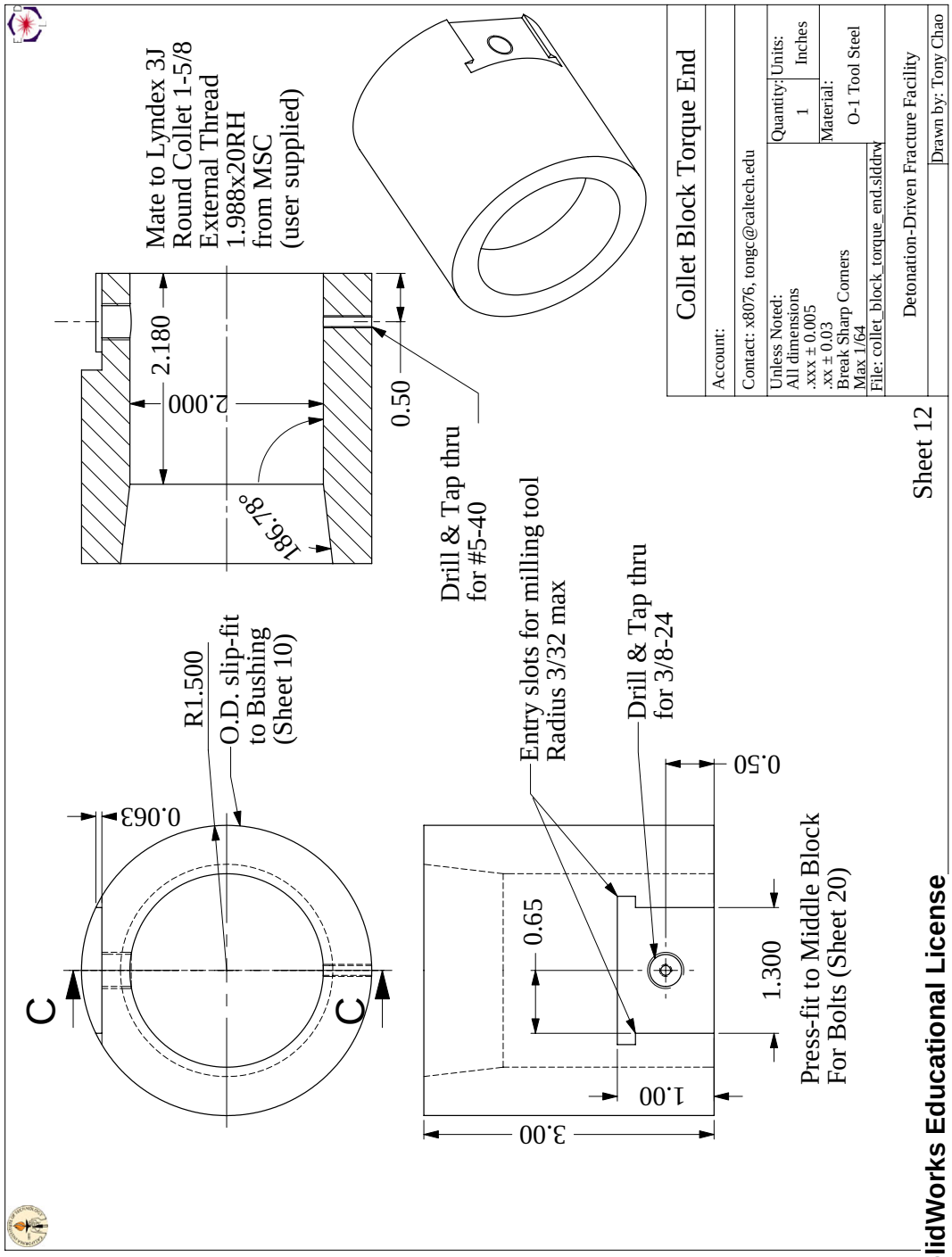

Figure B.12: Torque-end collet block.

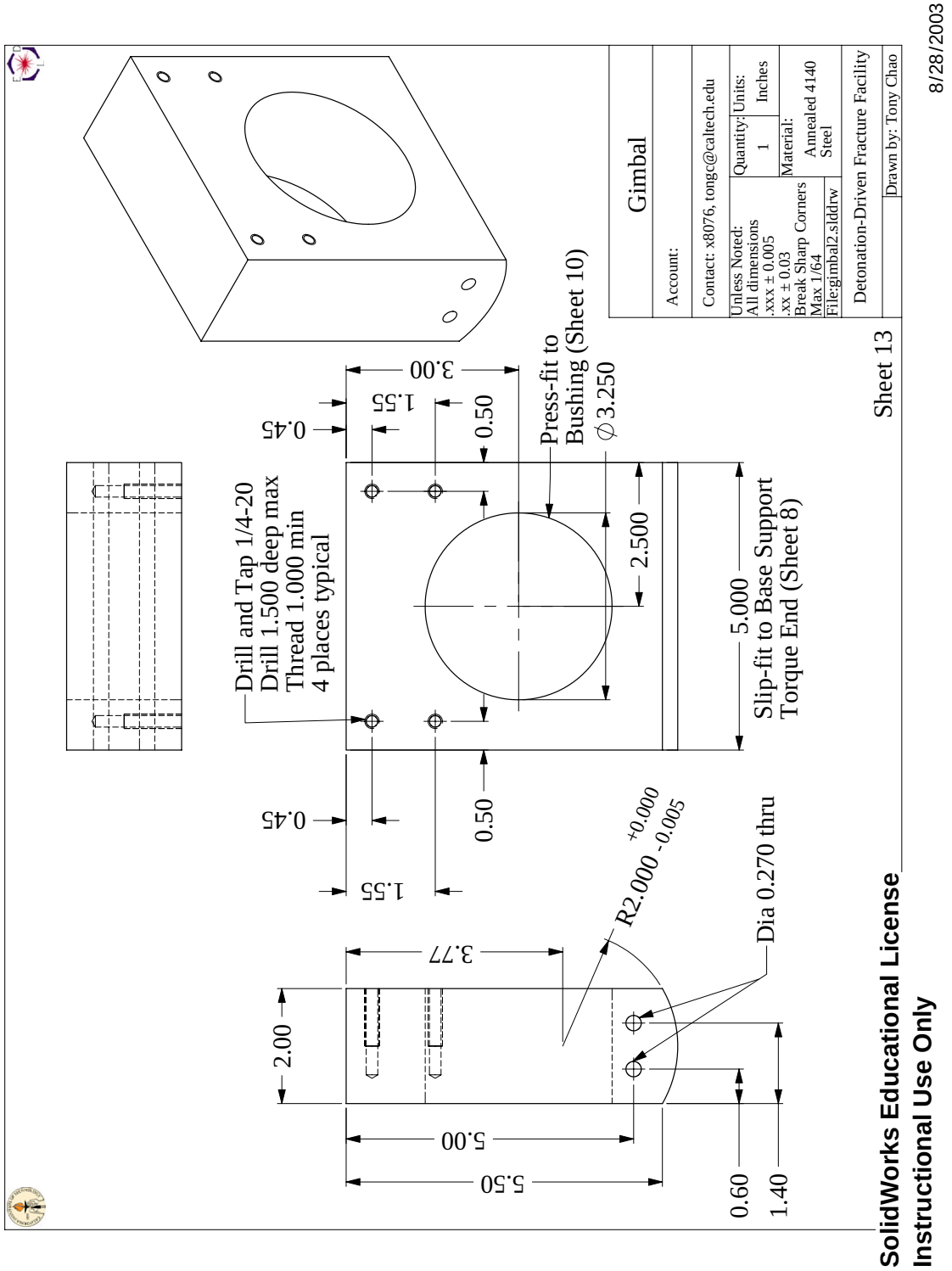

Figure B.13: Gimbal.

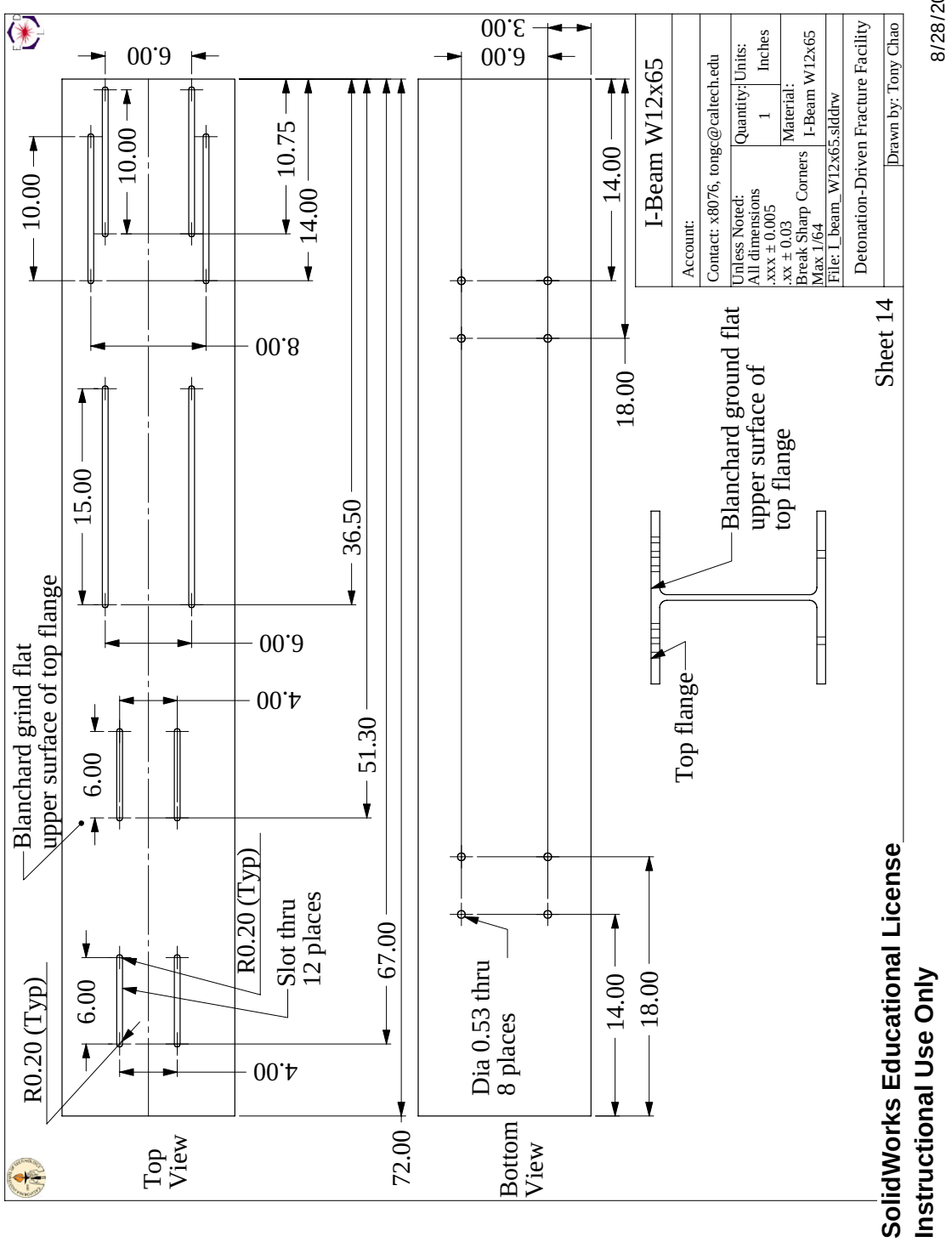

Figure B.14: I-beam.

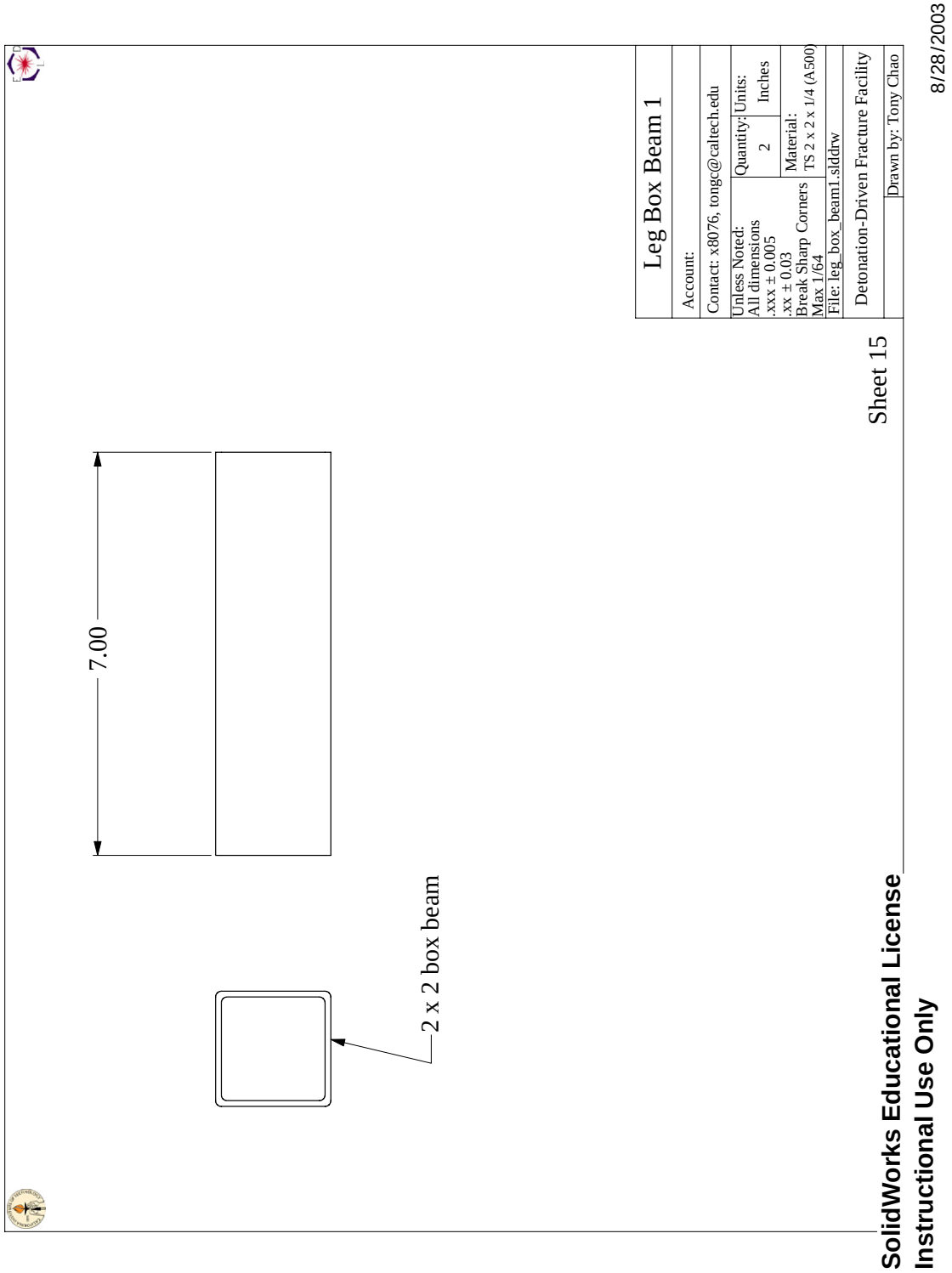

Figure B.15: I-beam leg box beam 1.

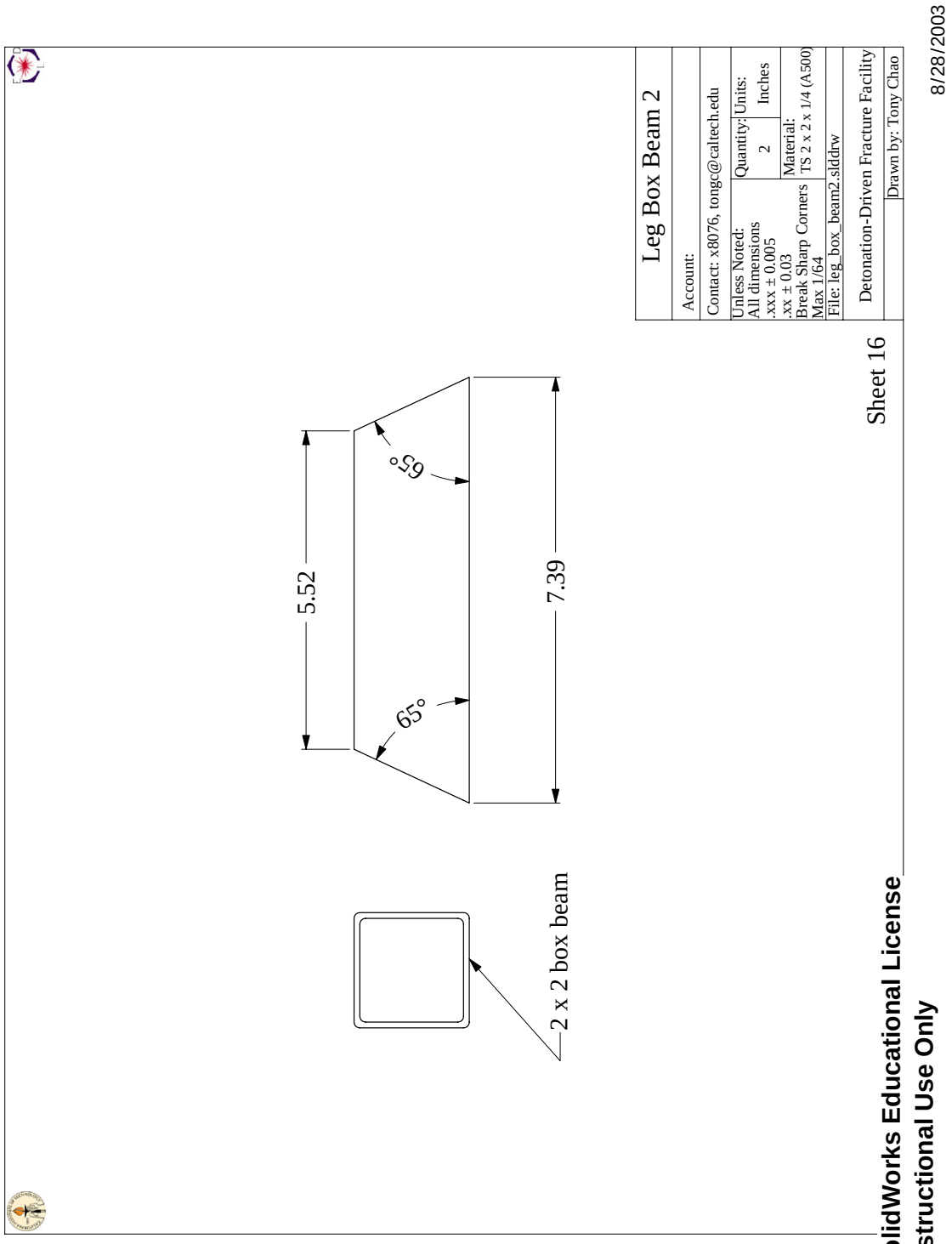

Figure B.16: I-beam leg box beam 2.

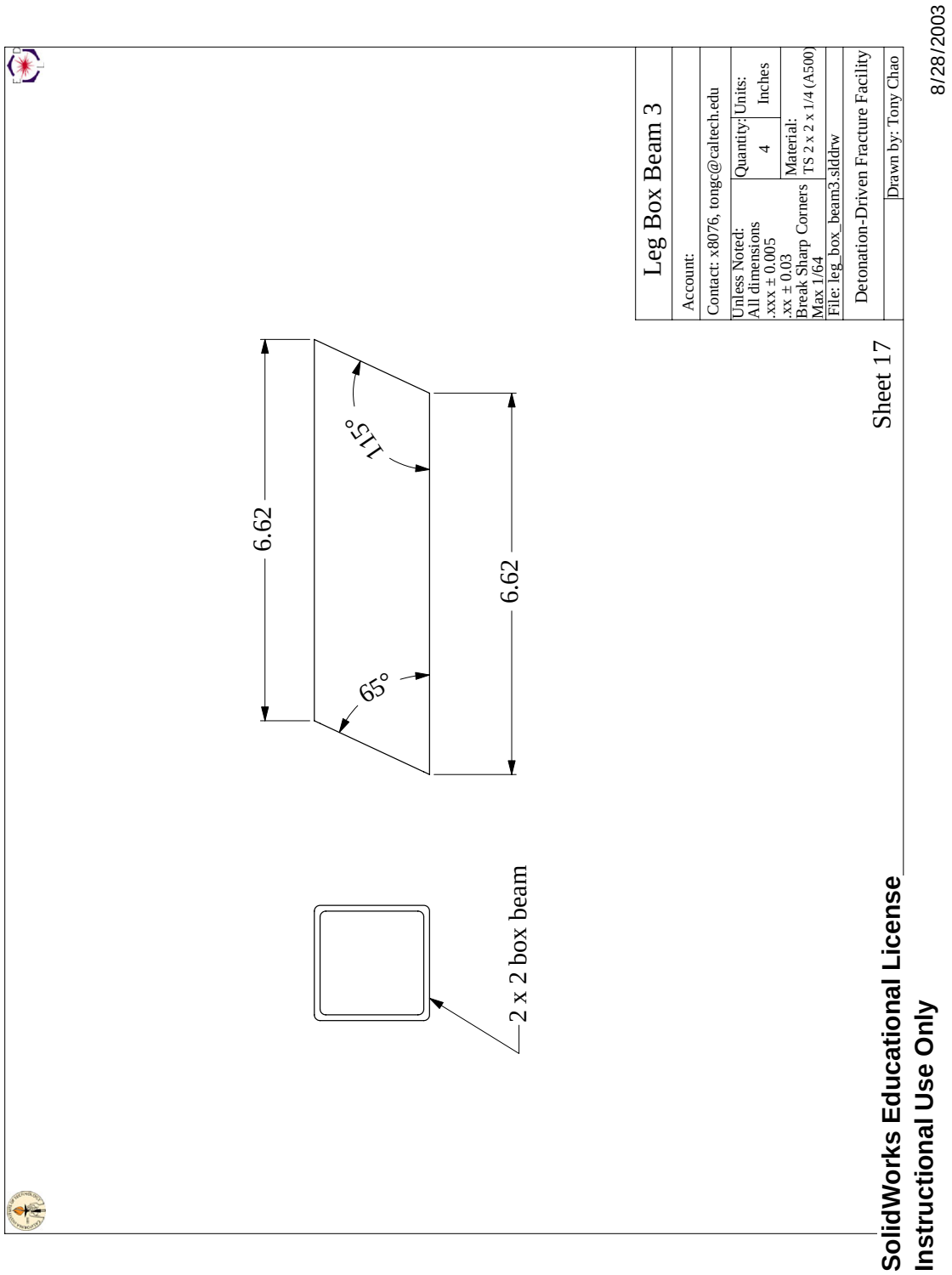

Figure B.17: I-beam leg box beam 3.

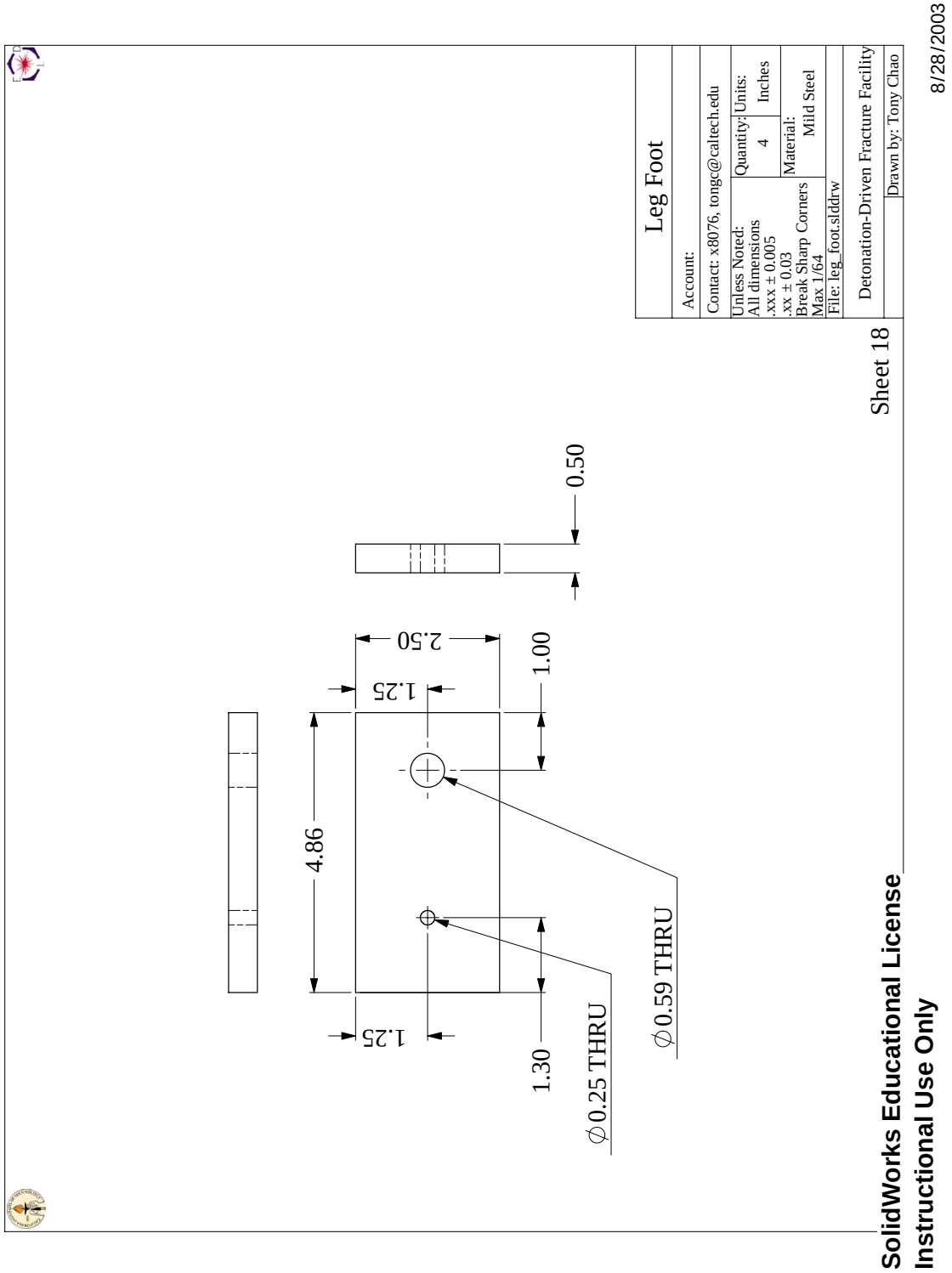

Figure B.18: Foot for I-beam leg.

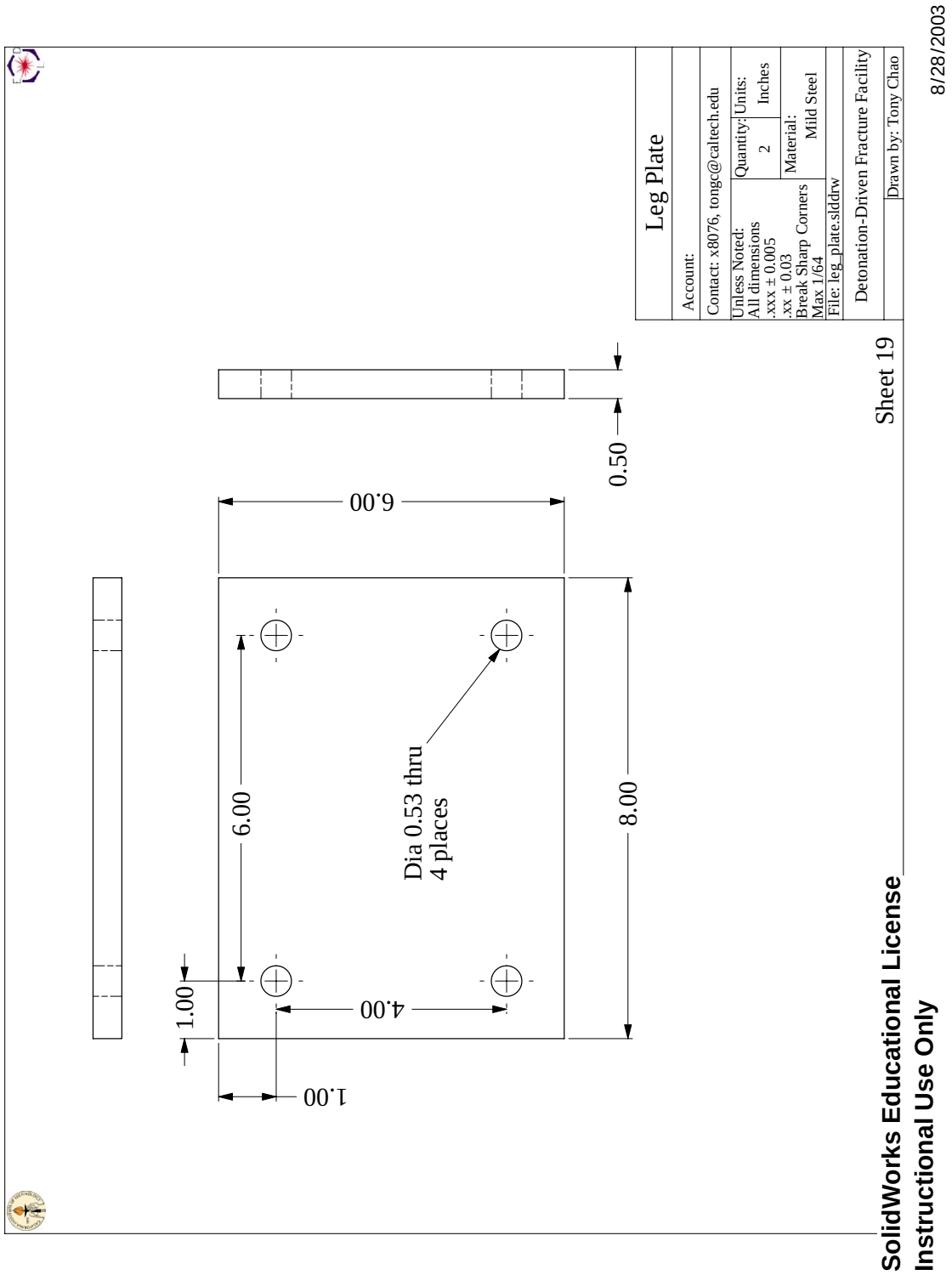

Figure B.19: Plate for I-beam leg.

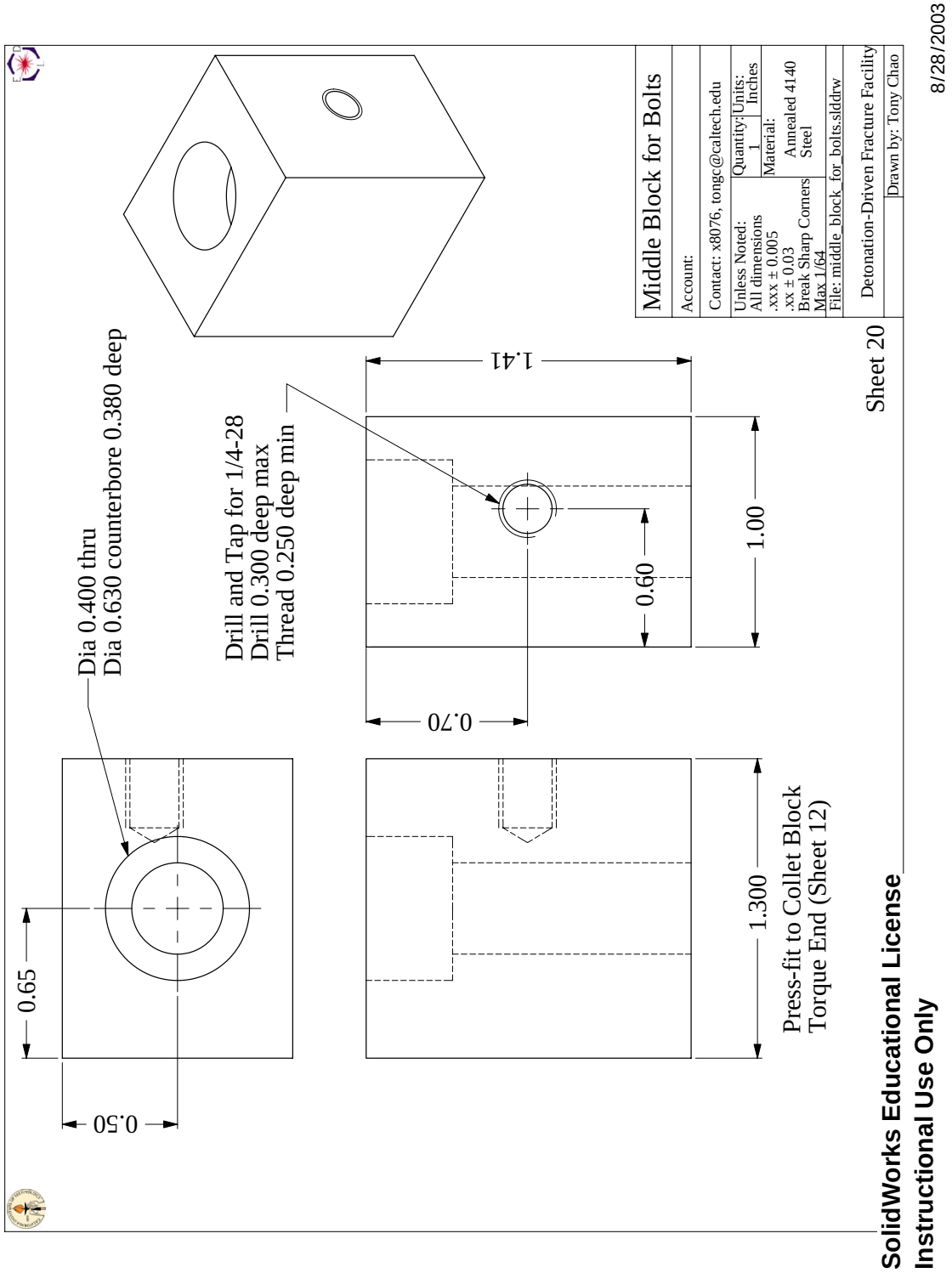

Figure B.20: Middle block on gimbal.

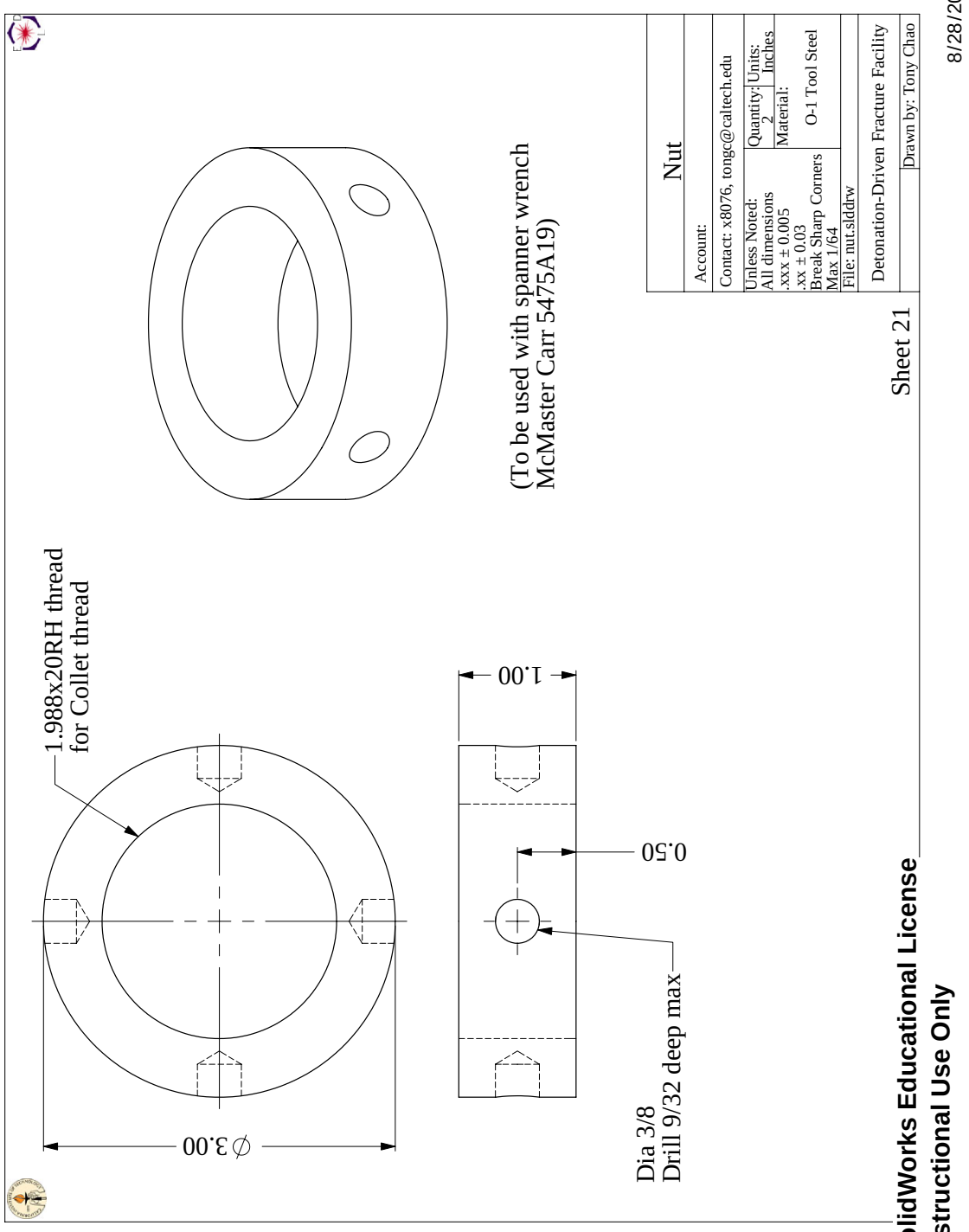

Figure B.21: Nut for tightening collet.

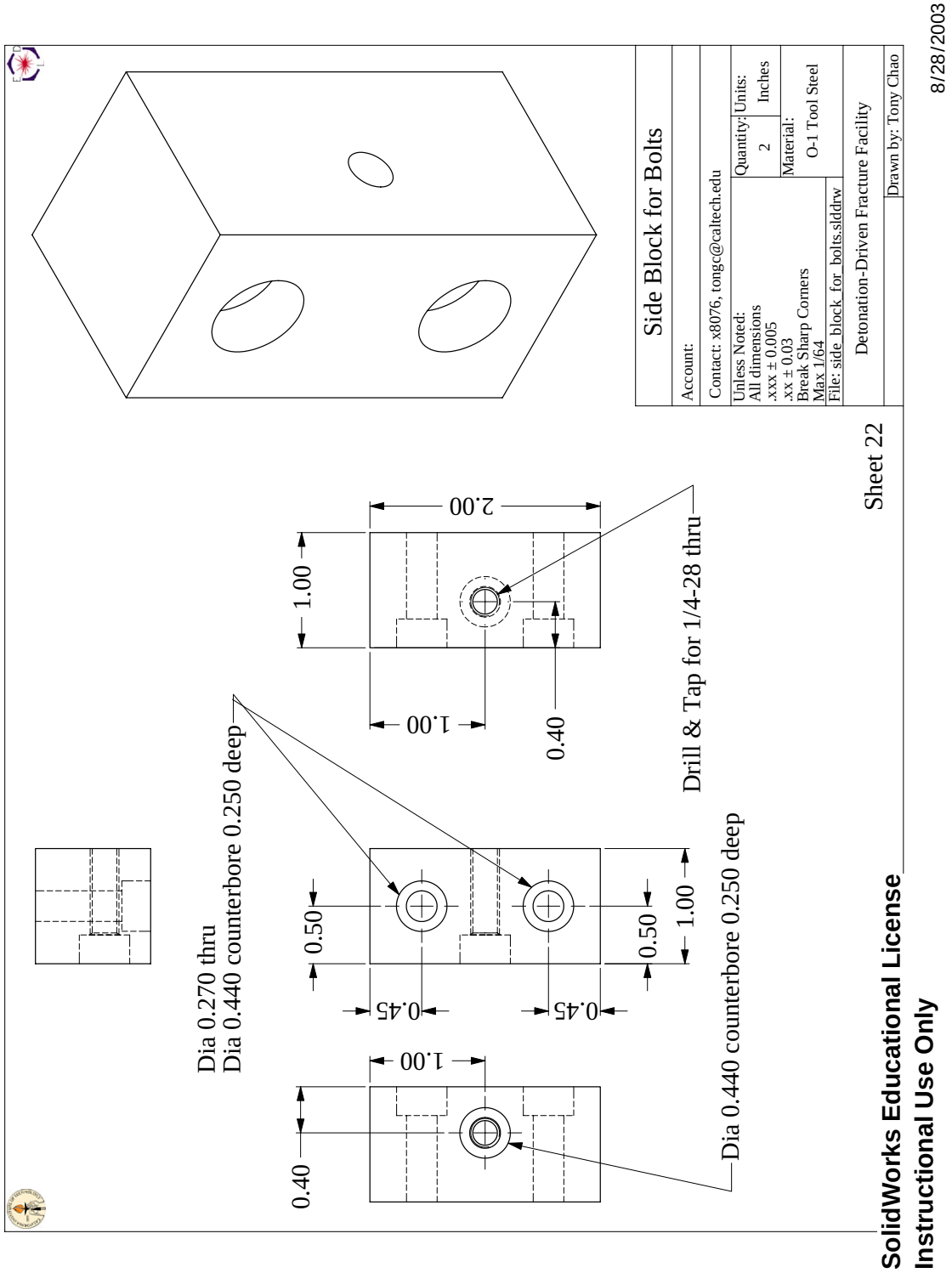

Figure B.22: Side block on gimbal.

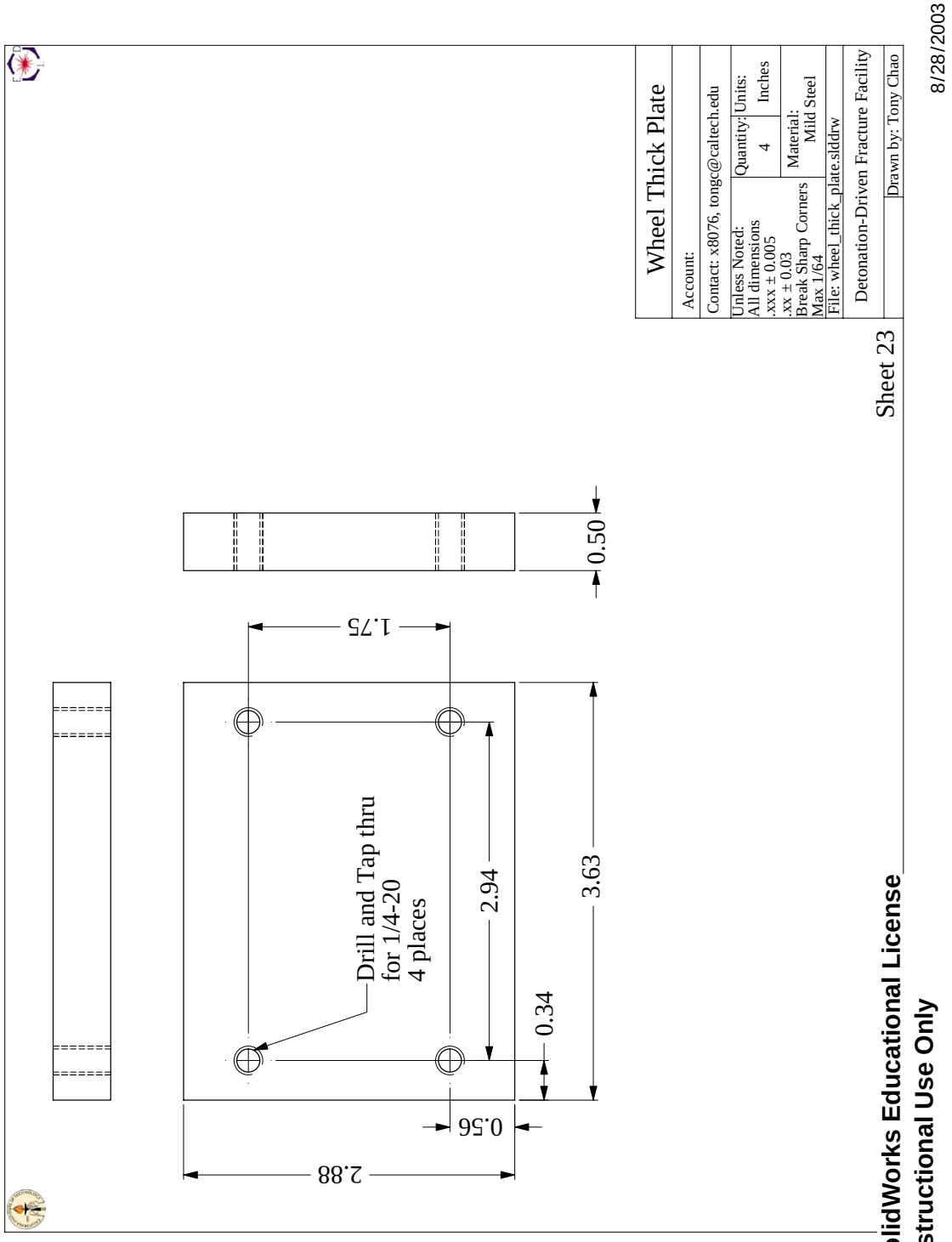

Figure B.23: Plate for I-beam.